Bluff-Body Wake Encounter and Tandem Wing-Tail Wake Dynamics in Forced Harmonic Pitch

Tan Kin Jon, Benjamin

Submitted in fulfilment of the requirements for the
Degree of Doctor of Philosophy

School of Engineering
College of Science and Engineering
University of Glasgow

August 2020

To my parents,
for their unconditional love.

Acknowledgements

It is my privilege to have been jointly-supervised by Drs. Henrik Hesse, Victor Wang Peng Cheng, Sutthiphong Srigrarom, and Euan McGookin throughout this journey.

I cannot express enough thanks to Dr Henrik for undertaking the responsibility as the primary supervisor during the final year of study. Although the time we had was limited, the difference he made is immeasurable. The meticulousness he demonstrated through constructive criticisms to continuously improve and elevate all aspects of my work is invaluable and something that I greatly appreciate. Thank you for being such a wonderful supervisor. Our weekly lunchtimes is something that I will miss.

I would also like to offer my deepest gratitude to Dr Victor, who has always been going above and beyond the call of his duties for me. I am extremely grateful to have met him as a supervisor for my undergraduate final year project, where the work has evolved to its state today. He has always been an excellent mentor and a role model, and is a source of motivation and inspiration. His knowledge and expertise in the realm of CFD and aerodynamics pushed me to persevere and overcome many challenges. Thank you for believing in me.

The scholarship and funding provided to support this study, along with the multiple conferences and training programmes is gratefully acknowledged. This was possible through the partnership between the University of Glasgow Singapore, AviationLearn Pte. Ltd., and the Economic Development Board of Singapore under the Industrial Postgraduate Programme (EDB-IPP). A substantial amount of time was spent at AviationLearn throughout these years, and the friendships and experiences gained there are things that I treasure.

Most importantly, I will not be where I am today without my family. My parents, David and Irene, have worked tirelessly even in their golden years to provide for the family. My siblings, Kensyn and Lynn, are also pillars of support and encouragement. Their own families have also brought so much joy to everyone. Finally, to Jingyi, thank you for being a continuous source of love and happiness. I look forward to the coming chapters of our lives!

Abstract

Wake phenomena and its encounter with downstream bodies are of engineering importance as it can affect aerodynamic loads. This can induce unfavourable—or even dangerous—conditions to aircraft through a loss of lift, or stability and control. Such scenarios range from the local interactions between an aircraft wing and its empennage, to wakes emanated from buildings acting on a helicopter fuselage downstream. Therefore, wake physics must be evaluated to predict any consequential aerodynamic effects. Furthermore, accurately modelling turbulent wake regimes are challenging, as obtaining physically meaningful data requires high-fidelity techniques. In this thesis, canonical cases under static and dynamic conditions focusing on wake encounters are investigated computationally to address these concerns. This is achieved using a Detached-Eddy Simulation (DES) approach that will be validated with a static case before expanding to include overset methods to induce dynamic grid motion on a tandem configuration.

Validation is performed by investigating the vortex shedding behaviour and wake characteristics of a separated flow over a square beam bluff-body. Spectral analyses of surface-forces reveal von Kármán street dynamics with frequency correlations in the freestream-parallel and cross-stream directions. Metrics are verified against benchmark experimental data, where a considerable aerodynamic impact is implied by both first- and second-moment wake statistics up to a measured downstream distance of six characteristic lengths. The extent of numerical treatment is further demonstrated through validation of its shear-stresses, an auto-correlation function of point-probed velocities, while coherence is observed as peak frequencies correspond to surface vortex shedding frequency. This case is then subsequently used as a wake generator for the investigation of its aerodynamic impact downstream.

A NACA0012 wing-section is placed three characteristic lengths downstream for insights on the aerodynamic effects of the bluff-body wake encounter. Time-averaged surface-forces on the wing-section are evaluated against a wake-free condition of the airfoil for reference. The wake encounter demonstrates a decrease in overall pressure distribution from wake-induced separation, with a strong correlation in lift response with the bluff-body vortex shedding dynamics. Instantaneous contours reveal flow behaviour resembling those expected of heave dynamics caused by the alternating vortex street. As oscillatory lift characteristics are induced, the work proposes approximating this response with the Sear's and Theodorsen's functions represented as a relative harmonic motion to the wake based on reduced frequency.

Finally, expanding this framework to include overset grids accomplishes dynamic motion for forced harmonic pitching on a tandem wing-tail configuration. This subjects the horizontal stabilizer to a wake induced by pitch oscillations of its main wing located upstream. As this is a single rigid system with a rotational centre on the wing chord, it is observed that the moment arm translates to a coupled pitch-heave motion at the tail. In addition, a separated wake with characteristic leading and trailing edge vortices (LEV/TEVs) is emanated from the wing at the higher angles-of-attack in the harmonic pitch cycles. This leads to a direct correlation in wing-tail dynamics where the tail lift response can be distinguished into two components; the combination of its pitch-heave directly contributed by the tail moment arm, and a gust component by periodically encountering the separated wing wake. The combination of these mechanisms synthesises the tails response from both forced harmonic motion and wing wake interaction, and is shown to be significant to the entire (wing-tail) system. This contributes to novel insights on wake interactions, as the computational framework advances the understanding of tandem aerodynamic relationships under dynamic conditions.

Keywords *vortex shedding, wake dynamics, wake encounter, bluff-body, tandem flows, forced harmonic motion, overset grid, OpenFOAM*

Contents

List of Tables

List of Figures

Nomenclature

Symbols

$\mathbf{a}$	General vector property
a_P	Central coefficient
a_N	Central coefficient for neighbour N
a_{ij}	Anisotropic component of Reynolds stress tensor
a_{ij}^{sgs}	Subgrid scale anisotropic component of Reynolds stress tensor
b	Span, m
C, c	Chord, m
C_{DES}	DES model coefficient
$C_{L,M,D}$	Lift, moment, and drag force coefficients
C_{d0}	Profile drag coefficient
C_f	Friction coefficient
C_{L_α}	$\partial C_L / \partial \alpha$
C_{M_α}	$\partial C_M / \partial \alpha$
C_p	Pressure coefficient $(p - p_\infty / q)$
$\overline{C_p}$	Time-averaged pressure coefficient
C_o	Courant (CFL) number $(u\Delta t / \Delta x)$
C_s	Smagorinsky constant
C_{b1}, C_{b2}, C_{b3}	Model constants for the Spalart-Allmaras model
C_{w1}, C_{w2}, C_{w3}	Model constants for the Spalart-Allmaras model
D	Spatial dimension
d	Width or Distance from wall
$\mathbf{d}$	Vector between P and N
e	Oswald's efficiency factor
$\tilde{d}$	Hybrid length scale for DES formulation
F_1, F_2	Blending functions for the k-ω SST model
f	Frequency, Hz
f_n	Simulation quantity of interest
f	Point in the centre through face

F	Mass flux through face
$G(x)$	Filter function
H	Total pressure, Pa
i, j, k	Unit vectors
k	Reduced frequency ($\omega c/2U$)
k	Turbulent kinetic energy
k	Largest characteristic length scales
k_r	Residual kinetic energy
L	Stream-wise separation distance, m
L	Lift, N
l	Characteristic turbulent eddy length scale, characteristic length
l	Characteristic length
l_o	Largest characteristic length scales
M	Mach number (u/a)
M	Moments, N m
N	Number of grid points
$\mathbf{n}$	Unit normal vector
P	Pressure, Pa
p	Static pressure, Pa
p	Order of convergence
P_k	Turbulence production limiter for the k-ω SST model
q	Dynamic pressure ($\frac{1}{2}\rho {U_\infty}^2$)
R	Autocorrelation coefficient
Re	Reynolds number ($\rho U c/\mu$)
r_e	Effective refinement ratio
S	Reference area, m^2
S	Invariant measure of strain rate for the k-ω SST model
S_{ij}	Strain-rate tensor
$\tilde{S}$	Local deformation rate
$\hat{S}$	Filtered strain-rate tensor
S_t	Strouhal number (fc/U)
$\mathbf{S}$	Outward-pointing face area vector
$\mathbf{S}_f$	Face area vector
S_u	Constant part of the source term
S_p	Linear part of the source term
S_ϕ	Source term
t	Time, s
t_c	Characteristic time (tU_∞/d)

Δt_c	Characteristic time-step ($\Delta t U_\infty / d$)
U, V	Velocity, ms^{-1}
$\mathbf{U}$	Velocity vector
$\mathbf{u}_b$	Mesh velocity
$\mathbf{u}_s$	Boundary surface velocity
V	Volume
V_p	Cell volume
$\overline{u}$	Time-averaged velocity, ms^{-1}
u'	Fluctuation around the mean velocity, ms^{-1}
u_τ	Friction velocity
u^+	Dimensionless velocity, (u/u_τ)
$\hat{u}$	Filtered velocity, ms^{-1}
V_H	Tail volume
u, v, w	Components of velocity in the x, y, z directions, ms^{-1}
y^+	Dimensionless first cell height, (yu_τ/ν)
$\overline{y}^+$	Time-averaged Dimensionless first cell height
x, y, z	Spatial (cartesian) coordinates
x_i	Position vector

Greek Symbols

α	Angle-of-Attack
α_0	Nominal Angle-of-Attack
$\alpha_{1,2}$	Model coefficients for the k-ω SST model
$\beta^*, \beta_{1,2}$	Model coefficients for the k-ω SST model
Δ	Filter width
Δ_{wake}	grid (cell) width in wake region
$\Delta_{x,y,z}$	Cell size in the relative directions
δ	Cell thickness
δ_{ij}	Kronecker delta function
ε	Downwash angle
ε	Dissipation per unit mass
Γ_ϕ	Diffusivity
γ	Blending coefficient
η	Kolmogorov length scale
η_t	Tail efficiency factor
κ	Non-dimensional wake number, von Kármán constant
λ	Wave length

λ_g	characteristic gust ($\pi c/k$)
μ, ν	dynamic and kinematic viscosity ($\nu = \mu/\rho$)
ν_t	Turbulent viscosity
ν_{sgs}	Subgrid scale eddy viscosity
$\tilde{\nu}$	Spalart variable
ρ	Density
$\sigma_{k1,2}, \sigma_{w1,2}$	Model coefficients for the k-ω SST model
τ	Lag time
τ_w	Wall shear stress
τ_{ij}	Viscous stress tensor
τ_{ij}^{sgs}	Subgrid scale stress tensor
$\phi(k)$	Theodorsen's function of reduced frequency
ϕ	General scalar quantity
ω	vorticity, s^{-1}
ω	Specific rate of dissipation

Acronyms & Abbreviations

AR	Aspect Ratio
AIAA	American Institute of Aeronautics and Astronautics
ASCII	American Standard Code for Information Interchange
AMSL	Above Mean Sea Level
BD	Blended Differencing or Backward Differencing
BWB	Blended-Wing-Body
CAD	Computer Aided Design
CD	Central Differencing
CFD	Computational Fluid Dynamics
CFL	Courant-Fredrich-Lewy number
CG	Centre-of-Gravity
CRM	Common Research Model
CPU	Central Processing Unit
CV	Control Volume
DES	Detached-Eddy Simulation
DDES	Delayed Detached-Eddy Simulation
DFT	Discrete Fourier Transform
DNS	Direct Numerical Simulation
DOF	Degrees of Freedom
DPW	Drag Prediction Workshop

FFT	Fast Fourier Transform
GTM	General Transport Model
FLOPS	Floating Point Operations Per Second
FVM	Finite Volume Method
HTP	Horizontal Tail-Plane
LDV	Laser Doppler Velocimetry
LE	Leading Edge
LEV	Leading Edge Vortex
LES	Large Eddy Simulation
LHS	Left Hand Side
LTS	Long Term Support
LRN	Low Reynolds Numbers
MAC	Mean Aerodynamic Chord
MPI	Message Passing Interface
MSL	Mean Sea Level
NACA	National Advisory Committee for Aeronautics
NASA	National Aeronautics and Space Agency
PIV	Particle Image Velocimetry
PISO	Pressure-Implicit with Splitting of Operators
PSD	Power Spectral Density
RANS	Reynolds-Averaged Navier-Stokes
RAM	Random Access Memory
RHS	Right Hand Side
RMS	Root Mean Square
SA	Spalart-Allmaras
SA-DES	Spalart-Allmaras Detached-Eddy Simulation
SACCON	Stability and Control Configuration
SGS	Sub-Grid Scale
SIMPLE	Semi-Implicit Method for Pressure Linked Equations
SST	Shear Stress Transport
TE	Trailing Edge
TEV	Trailing Edge Vortex
UAV	Unmanned Aerial Vehicle
UCAV	Unmanned Combat Aerial Vehicle
UD	Upwind Differencing
URANS	Unsteady Reynolds-Averaged Navier-Stokes

Sub- & Super-Scripts

∞	Freestream reference conditions
ac	Aerodynamic centre
c	Characteristic, convection, or chord
g	Gust
i, j, k	Index notation
$Lam.$	Laminar
max	Maximum
min	Minimum
N	Point in the centre of neighbouring control volume
ϕ^n	Current time-step
ϕ^o	Previous time-step
ϕ^{oo}	Second-previous time-step
P	Point in the centre of control volume
p	Pressure
r	Root
ref	Reference
rms	Root mean square
t, T	Tail or Turbulent
$Turb.$	Turbulent
w	Wing or Wake
$wall$	Wall
x, y, z	Components in the respective Cartesian directions

Publications

The work has resulted in the following Conferences and Presentations:

K. J. B. Tan, P. C. Wang, and S. Srigrarom, "Computational Modelling of Wing Downwash Profile with Reynolds-Averaged and Delayed Detached-Eddy Simulations," in 23rd AIAA Computational Fluid Dynamics Conference, p. 3960, 2017.

K. J. B. Tan, P. C. Wang, and S. Srigrarom, "Low-Speed Post-Stall Wing Wake Impingement on Horizontal Stabilizer of the Common Research Model," in 2018 Aviation Technology, Integration, and Operations Conference, p. 3898, 2018.

K. J. B. Tan, H. Hesse, and P. C. Wang, "Numerical Capture and Validation of a Massively Separated Bluff-Body Wake," in AIAA Aviation Forum 2020, p. 2713, 2020.

Declaration

With the exception of Chapters 1 and 2, which contain introductory material, all work in this thesis was carried out by the author unless otherwise explicitly stated.

Chapter 1

Wakes & Vortex Shedding Dynamics

The region of turbulent and recirculating flow generated as a result of a solid body moving through a fluid is known as its *wake*. Fluid flows in general can be catergorised as either free-shear flows or boundary layer flows. Wakes are classified as free-shear flows. Their characteristics can be described as the re-merger, or rearward extension of the boundary layer with a loss of momentum in the fluid, characterized as a deficit in dynamic pressure. As a fluid encounters an object, momentum is lost, resulting in a region of slower moving fluid surrounded by the faster moving freestream. Transition to turbulence then occurs a short distance downstream (Figure 1.1a), where mixing with the freestream, a recovery in momentum and widening of the wake can be observed. A typical visualisation of what is known as a von Kármán street is depicted in Figure 1.1b. A von Kármán street is identified as a pattern of swirling vortices induced through a process known as vortex shedding. This process is responsible for unsteady flow separation where fluids circumvent objects, especially for bluff-bodies. These flows are oscillating, and detach periodically from the surface of the geometry. This creates alternating low pressure vortices on either side which develop and convect farther downstream where the structure of the wake becomes less dependent of its source [1, 2]. The descriptors of wakes are its width, a drop in dynamic pressure, and a downward deflection along the wake center from asymmetrical geometry—such as a wing downwash [3].

Wake phenomena are also known to interact with secondary surfaces within the same flow field. This is critical, as flows over obstacles can produce wakes that convect downstream to become aerodynamically significant to other bodies in proximity. Fluctuating quantities from shear layer instabilities and vortex shedding coupled with a region of reduced dynamic pressure can alter aerodynamic behaviour, such as diminished surface forces from local Reynolds number changes, and induced unsteadiness from fluctuating quantities.

An aerodynamic design that accounts for wake effects is the horizontal stabilizer of a conventional fixed wing aircraft. The horizontal stabilizer is the dominant contributor to stability, and therefore the assessment of its pitch authority against local airflow properties is crucial to desirable flight characteristics. As the tail lies downstream of the wings, the interference of

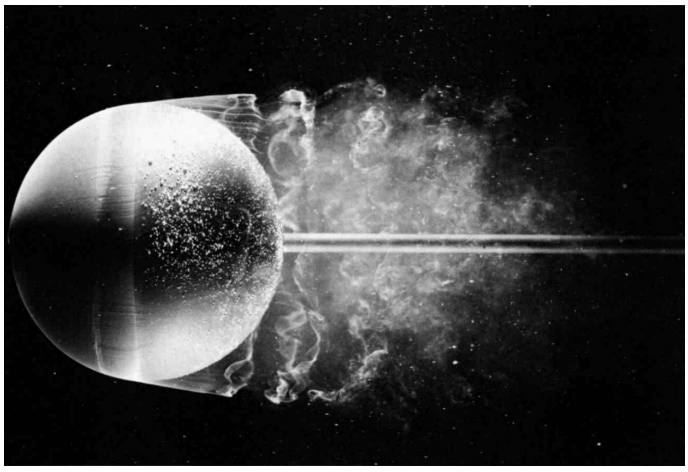

(a) Turbulent wake resulting from a flow over a sphere at $Re = 15\,000$.

(b) Kármán street behind a circular cylinder at $Re = 140$. Notice how the wake width grows as it progresses downstream.

Figure 1.1: Flow visualisation of wakes by Van Dyke [4].

airflow from the wing's wake alters its performance. To account for change in dynamic pressure, the resulting stabilizer effectiveness is often treated with an efficiency factor taken as a dynamic pressure ratio relative to the freestream [5]. In addition, the downward deflection of airflow from the wings as a result of lift also alters the stabilizers effective angle-of-attack. By extension, wake effects translate ultimately to aircraft pitch characteristics. Accounting for these effects are challenging, considering that the wake properties are dynamic as a function of attitude and trim.

The implications of a local wing wake of an aircraft on its tail have led to fatal accidents [6]. An example of this is the Lockheed P-38 (Figure 1.2) where it was forced into a nose-down dive. Recovery from this was difficult and pilots lost their lives. It was later discovered that the effects of the wing wake (due to induced flow separation from near critical Mach numbers) resulted in the loss of longitudinal control at the tail. It was determined that flow separation adversely affected wing lift, which caused downwash angles to be reduced drastically. This translated to a great increase in effective angle-of-attack at the tail, causing it to provide lift, inducing a pitching down moment for the aircraft. This is reportedly the first aircraft to have encountered this problem [7].

Figure 1.2: The Lockheed P-38, an aircraft that suffered from wing wake-tail interference in its early designs. Image by Lockheed Martin.

Wing tip vortices and aircraft wakes farther downstream are also known to cause accidents that have mandated separation distances between aircraft [8, 9]. This especially applies where larger aircraft precedes smaller ones due to the relative size of the wake they produce. Loss of lift together with control authority from the down-draft caused wing tip vortices and reduced dynamic pressure are common flight symptoms [10]. Wake turbulence have been known to last up to three minutes or longer, depending on the size and speed of the aircraft [11].

As aircraft begin to operate in proximity to urban or naval environments, it has been shown that the wakes emanated by buildings and even ships can have a considerable effect on aircraft operating in their proximity. This is known to affect helicopters and unmanned aerial vehicle aerodynamics, which results in loss of control and unpredictablility for pilots [12–16]. To sim-

ulate wake effects with pilot-in-the-loop tests, numerically modeled ship-wake data were used in the simulation of helicopter-ship flight deck landings. It was highlighted that the aerodynamic effects of the wake acting on the fuselage is key to simulating aircraft behavior at these flight regimes [17]. Similar emphasis on the importance of capturing wake effects acting on the fuselage is also made with studies on a rotor disk encountering a building represented as a bluff-body [18]. Neglecting these wake features contributed to operational difficulty for pilots, including tasks like hovering and approach for landing. Modelling the wake field around urban structures is also needed in the design of autonomous control logic for unmanned aerial vehicles, which were proven to impact their handling responses negatively should it be neglected [15, 16, 19].

It is evident that wake effects are a significant engineering consideration, occurring locally between surfaces like wings and tails [5, 7], to external interference, such as those from buildings [12], the handling qualities and flight simluation of rotorcraft encountering building or ships wakes [17, 18], to the controls for unmanned aerial vehicles under the influence of wind conditions induced by urban environments [16, 20, 21]. Bodies in tandem encountering a freestream flow therefore serve as stream-wise aerodynamic obstructions that generate turbulent and unsteady disturbances. This can affect aerodynamic and handling qualities of manoeuvring aircraft, and predicting these effects are critical for operational safety at these flight envelopes.

As wakes are turbulent flows, they are inherently unsteady and irregular. This naturally involves high levels of mixing and fluctuations in three dimensions across all length scales. Viscous effects are also present, contributing to stresses in the flow. Such complexity requires high-fidelity methods that accurately capture any physics of interest to predict induced behaviours. Accurate capture of wakes and vortex shedding dynamics is therefore a precursor that forms the foundation to modelling the physical loads as a result of these interactions.

1.1 The Study of Fluids & Their Capture

Classically, the foundation of fluid dynamics are studied through pure experimental observations and theoretical formulations. Experimental methods are namely in the form of flight experiments, drop tests, shock tubes, and more commonly, water and wind tunnels, among many more. These methods often require a model of the aerodynamic body in question, and a suitable method is chosen along with the appropriate measurement apparatus and visualisation technique for data collection [22]. Upon a deeper understanding of flow behaviour, this has gradually evolved into theoretical fluid dynamics [23]. This branched the study of physics into those concerning Newtonian fluids, and thus led to famous relations like the Euler's equation and viscous flow theories—like the Navier-Stokes equations [24]. As a result of these findings, fluid dynamics has historically always been based on the two polars of experiment and theory.

The advent of computers and development of accurate numerical algorithms revolutionised

how fluid dynamics problems are solved. Since its introduction, Computational Fluid Dynamics (CFD) have reduced wind tunnel usage by more than 50% between 1980 to 2010 [25]. CFD presents some advantages over pure experiment. Unlike wind tunnels which require physical hardware and infrastructure, CFD methods scale with the advancement of computing power and decreasing costs [26]. In addition, experiments only allow data extraction where physically possible. This subjects the experimental objectives to the limitations of the apparatus available, whereas CFD allows the sampling of any position in the flow field [27]. The ability to theoretically simulate and isolate specific phenomena for study also gives the user greater control over physical processes. However, these methods are supposed to work in synergy, and are not meant to replace each other. The need for validation and verification to ascertain and interpret results relies on support from experiment and theory, as its accuracy is still subjected to the understanding, implementation, and execution of numerical codes and algorithms [28].

1.1.1 Experimental Methods for Wake Capture

Experimental methods can be typically classified as visualisation or measurement methods. For wake survey systems, pressure data is primarily measured through the use of pitot-static tubes [29]. This collects static and total pressure information in the wake referencing freestream values. Due to the momentum loss in the flow, the total pressure deficit can then be attributed to the drag of the object upstream. The two typical measurement devices are known as the integrated wake rake (Figure 1.3) and a traversing wake probe. Integrating wake rakes are sometimes preferred because it eliminates the challenges that are introduced by the moving mechanisms on traversing wake probes. For the integrating wake rake, the array of pitot tubes lead into a single manifold which collects pressure data with a distribution as shown in Figure 1.4.

The integrated pitot array is a traditional example that is used to measure wake data, and its width has to span beyond the entire wake. This obtains the dynamic pressure profile perpendicular to the stream-wise flow direction behind an immersed object as seen in Figure 1.4. Based on this pressure distribution, the profile drag of the body can be expressed as a function of this dynamic pressure deficit [2]. The relationship between profile drag (d_0) and wake pressures is known as the Momentum Method [30, 31]:

$$d_0 = \int_{-\infty}^{\infty} \rho u (U_\infty - u)\, dz, \tag{1.1}$$

where ρ, u, and U_∞ are the reference density, stream-wise velocity, and freestream velocity respectively. This can be expressed to relate wake pressure quantities to the profile drag of a wing, which is accomplished by Betz [30] and the comparatively simpler Jones [31] method with the zero-lift drag coefficient:

$$C_{d_0} = \frac{2}{c} \int^{w} \frac{\sqrt{H_w - p_w}}{\sqrt{H_\infty - p_\infty}} \left(1 - \frac{\sqrt{H_w - p_\infty}}{\sqrt{H_\infty - p_\infty}} \right) dy, \tag{1.2}$$

Figure 1.3: An integrating wake rake and its mounting [29].

where c is the characteristic chord, while H and p are the total and static pressures relative to the wake and freestream, respectively. The limits of the wake width is usually defined where the momentum recovers to $0.99u_\infty$, as points of inflection in the measurements that can be seen in Figure 1.4. This is analogous to that of boundary layer thicknesses [32, 33]. The momentum method was validated experimentally using wakes at zero-lift for NACA 0012 and 0018 sections, and is shown to be accurate within 2% along $1.05 < x/c < 4.00$ compared to direct force measurements. The results obtained were also agreeable to theoretical estimations [34]. It was also highlighted that the results were more accurate when taken closer to the trailing edge. Both the Jones and Betz Methods were agreeable to within 0.5% of each other at $1.05 < x/c < 4.00$ [2, 33]. However, these methods are limited to zero-lift conditions due to the introduction of induced drag at higher angles-of-attack, although this can be theoretically accounted and corrected for [2].

While the wake momentum method has been demonstrated to be generally accurate, its limitations lie in the hardware as pitot tubes present some challenges that need to be considered [29]. Near the model, it is known for the probe to physically interfere with flow measurements, and the quality of results are also subjected to the probe geometry and its suitability for that particular flow regime [35]. This requires calibration against freestream flow conditions that have to be conducted beforehand [36]. The turbulent nature of wakes coupled with the sensitive nature of pitot tubes can introduce noise, which will require signal filtering that also has to be further validated with other means [29,37]. However, if these limitations can be overcome, wake survery methods can provide a level of accuracy that distinguishes itself from other experimental

techniques [38]. It has been demonstrated that a drag resolution of a 1-count precision can be obtained, and this can be useful for complementing the validation and verification of CFD results [36].

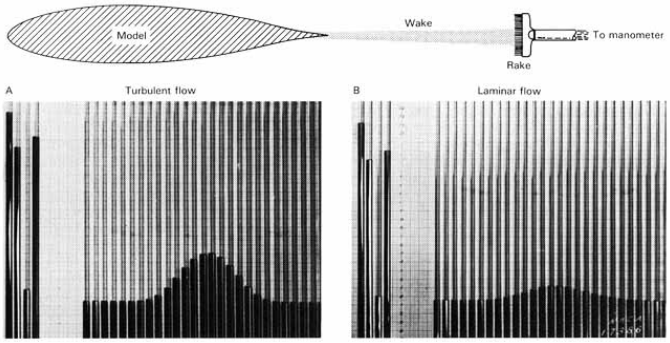

Figure 1.4: A wake survey rake measures dynamic pressure with a series of manometers. Here, the hump in the measurements represent the amount of drag, and is compared between turbulent (left) and laminar (right) flow [39].

1.1.2 Computational Modelling for Wake Capture

The CFD process constitutes of several components. A computational representation of the physical model has to first be developed. This geometry is then defined within a computational domain (for external aerodynamic flows) that is analogous to the test section of a wind tunnel. Numerical discretisation (Meshing) of the entire domain is done, assuming the flow conditions to be simulated. This accompanying mathematical solution is referred to as the governing equations, where the numerical schemes and turbulence models are implemented to appropriately simulate the flow in question. The numerical solution is then executed, and a computational representation of the flow variables are obtained in the results. Post-processing is done to interpret these results, where the choice of the above-mentioned practices are evaluated by validation and verifying the relevant quantities of interest.

The individual sub-fields within CFD encompasses more specialised areas of research that are continuously developing. Improved mesh generation methods and advancing turbulence models are among the goals for better CFD techniques, especially for practical applications [40]. As most flows significant to engineering are turbulent, high-fidelity models are required to accurately simulate and predict the nature of these flows. Figure 1.5 illustrates the hierarchy of turbulence modelling classes [41]. Current practices with Reynolds-Averaged Navier-Stokes (RANS) with one- or two-equation turbulence models are widespread [42]. However, there has been an increasing emergence toward hybrid RANS/LES for separated flows. This approach has been adopted while the demands of full-LES for entire aircraft geometries at flight Reynolds numbers remain unachievable [43]. Some of the differences that distinguishes these modelling techniques apart are discussed in greater detail in Section 2.2.1.

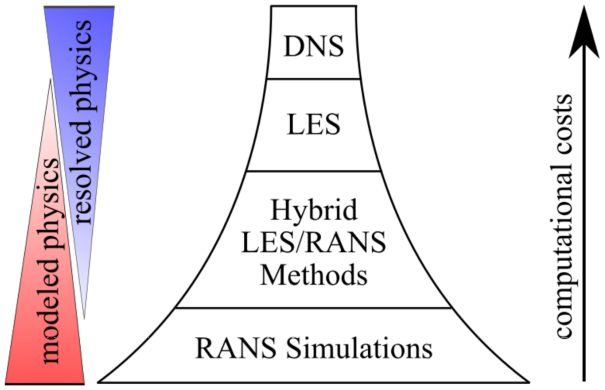

Figure 1.5: Representation of the hierarchy of turbulence modelling techniques, showing the trade-offs between computational costs and fidelity [41].

Computational analyses of wake characteristics and surface pressures for airfoils in ground effect ($Re = 4.6 \times 10^5$) compares the performance of six different Reynolds-Averaged Navier-Stokes (RANS) turbulence models across several metrics, including wake profiles [32]. These are evaluated and validated against experimental data captured with Doppler anemometry and Particle Image Velocitmetry, amongst other techniques [44, 45]. The performance for wake profile capture of the turbulence models were determined by their ability to predict key features accurately, such as the maximum wake deficit (u_{min}/U_∞), position of the points of inflection in the profile (y/c at u_{min}, $\delta_{top,bottom}$), and wake thickness (δ_{99}/c). The results demonstrated that all of the tested turbulence models performed equally well at capturing the wake profile along $x/c = 1.2$ at two ground clearance heights of $h/c = 0.224$ and 0.09. However, plotting of the complete velocity profile of the wake shows that the accuracy of the models begin to deviate from experimental data as the ride height narrows, likely attributed to larger flow gradients encountered near the ground. The models agreed better with the experiments at higher ground clearances. It is also noteworthy that as some models performed well in capturing the wake profile, they are relatively accurate for other parameters, as in the case for the Realizable k-ε model [46] (with enhanced wall treatment) which outperformed the k-ω SST model [47] in predicting the wake profile, but are less suitable for surface pressure predictions. The Realizable k-ε model predicted the velocity deficit (u_{min}/U_∞) accurate to 0.64%, and the vertical wake displacement ($(y/c)_{u_{min}}$) of 4.22%. These results have shown that the Realizable k-ε and k-ω SST are general models can be used to capture wake profiles and surface pressures for attached flows. However, the k-ε is not recommended for boundary layers flows or those with adverse pressure gradients [48].

Another 2D benchmark case advocated the use of the Spalart-Allmaras (SA) model over k-ω SST on near-wakes of the NACA 0012 [49]. Results solved with the CFL3D [50] and FUN3D [51] solvers demonstrated that the SA model predicts wake profiles of $\overline{U}/U_\infty$ and Reynolds shear stress of ($\overline{u'v'}/U_\infty^2$) with agreeing trends up to $3.00x/c$. However, it is worth highlighting that RANS models are subjected to inherent early dissipative behaviour farther downstream.

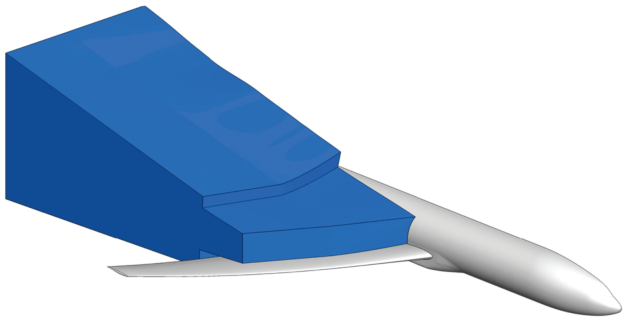

(a) Grid refinement region for a wing wake [54].

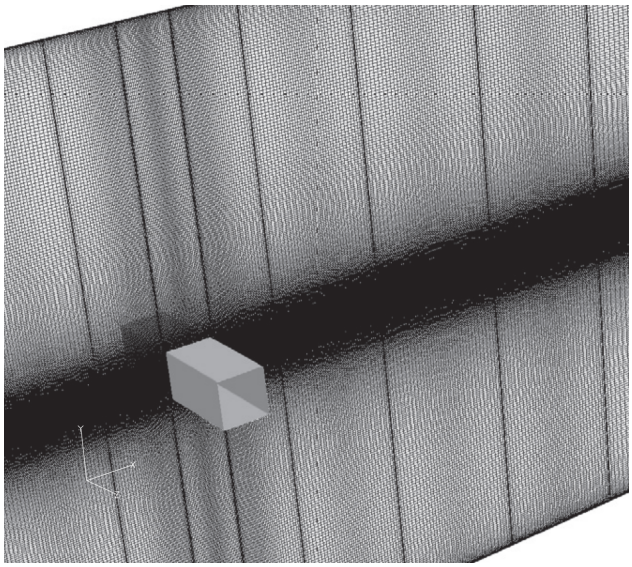

(b) Grid refinement for a flow over a bluff-body [55].

Figure 1.6: Examples of wake refinement regions defined by a grid block.

Regardless, the SA model used in the 2D benchmark case performed excellently for near-wake capture. For sensitivity to far-field boundary distances, it was expressed that results for a distance of $20c$ against $500c$ differed only by a negligible shift in lift coefficient, while the rest of the results remains unchanged.

Providing sufficient grid refinement for a wake region is computationally expensive, especially for a sufficiently large enclosure for stalled wake and a wall normal spacing of $y^+ \approx 1$ (Figure 1.6a). Notably, a domain discretized with spatial resolution in the order of 1% the reference chord is deemed adequate to capture relevant flow effects pertaining to the pressure coefficient spectra in the wake which depicts a well defined inertial subrange [52, 53]. The total amount of nodes in this mesh amounts to 51-million, of which 31-million are in the wake block. Due to the high cell count, the span-wise extent of the block for the work is limited to 60% wing semi-span. Other related work used a resolution of 3% the reference chord and demonstrated good accuracy for time-averaged wake profiles that were conforming to PIV-obtained data [54]. It is important to note that the number of grid points scales with n^3 [42]. Therefore, halving cell edge lengths increases the number of grid points considerably by a factor of 8.

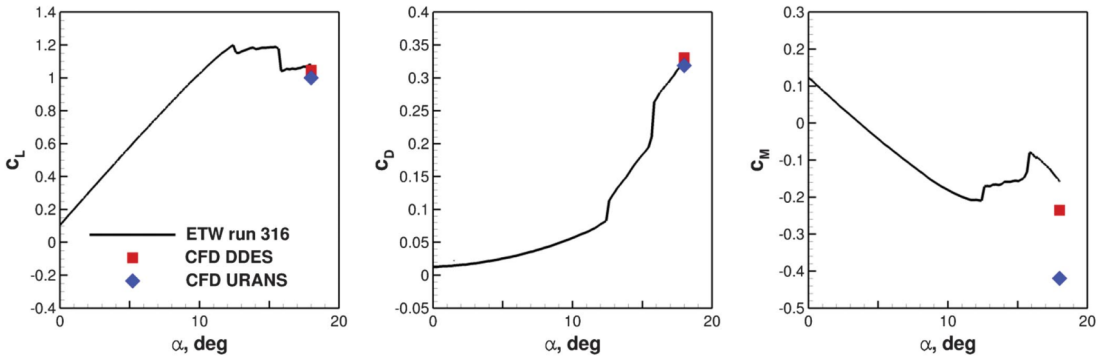

(a) Validation of longitudinal coefficients obtained with URANS and DDES methods compared with experiment at post-stall angle.

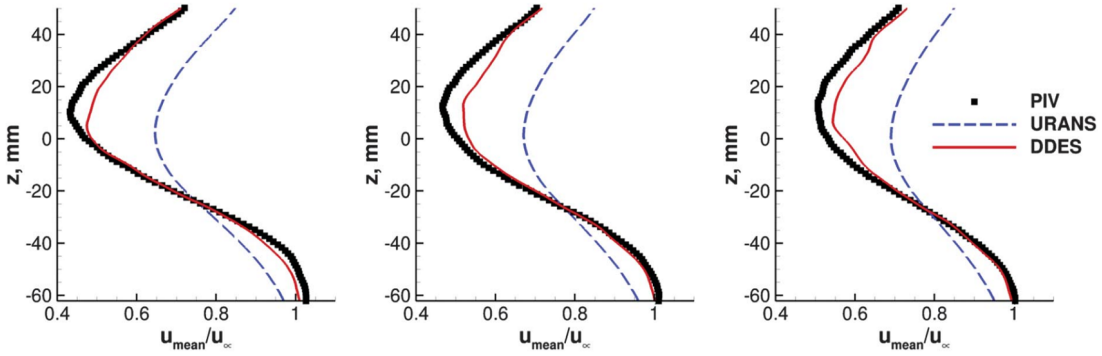

(b) Wake profiles at three downstream positions from the wing demonstrating good accuracy and agreement between DDES results and PIV methods.

Figure 1.7: Longitudinal coefficients of lift, drag, and pitching moments, and velocity wake profile along a PIV plane some distance downstream of the wing at low-speed stall ($M = 0.25, Re = 11.6 \times 10^6$) [52].

Overall, scale-resolving techniques are generally favoured for wake capture, especially for farther downstream distances with those involving flow separation. While URANS demonstrated lower accuracy as an under-prediction of the wake velocity deficit by up to 20%, it achieved comparable accuracy to wind tunnel force balance data for aerodynamic coefficients. Results for these longitudinal coefficients of lift, drag, and pitching moments, together with wake velocity profiles are extracted in Figure 1.7. It is evident that the performance of RANS-based techniques decreases with downstream distances on wake capture. Observations by Waldmann et al. for low-speed stall [52], concluded that DDES outperformed RANS methods when evaluated against experimental data for wake capture, especially for flow separated regimes. This is critical, as the assessment of aircraft stability will involve a tail-on geometry with a horizontal stabilizer located farther downstream than the distance considered here.

1.1.3 Computational Strategies for Unsteady Flows

Numerical assumptions must assume similar conditions to model unsteady and turbulent wake characteristics. The typical approach for unsteady flows involves a two-step process of refin-

ing a grid through spatial sensitivity studies, followed by an independent time-step study on the chosen grid(s). A Courant number of $Co \leq 1$ is attempted to capture large eddies, which establishes a relationship between time-step and local grid spacing [56,57]. It was also recommended by Spalart [57] that the ratio between the local cell size and the time-step for the LES region be $\Delta x_0/\Delta t = u_{max}$, where u_{max} is the local velocity which can be accelerated by up to $1.2u_\infty$. Also, Δx_0 needs to be at least five times smaller than that of the flow structure(s) to be resolved by LES. A characteristic time-step size of at least 0.025 is also necessary to accurately predict massively separated turbulent flows that are without boundary layer reattachment [58], and is similarly reported by others [59, 60].

Cummings et al. [61] optimised this segregated approach where the spatial and temporal scales are determined concurrently as these are correlated. This was demonstrated with a focus on near-wakes and localised flows using a range of geometries such as a NACA 6512 airfoil, a delta wing, and the F-16XL with different turbulence models [61]. This approach was also demonstrated by Frink [62] and Thompson et al. [63]. Beginning with recommendations for the boundary layer grid design for laminar and turbulent regimes, a newly formulated first-cell height at the wall is proposed [61]:

$$\Delta_{Lam.} = L\frac{1.3016y^+_{avg}}{Re^{0.75}}, \qquad \Delta_{Turb.} = L\frac{(13.1463y^+_{avg})^{0.875}}{Re^{0.90}}, \tag{1.3}$$

where L is the characteristic length of the flow. Equations 1.3 performed well for Reynolds numbers between $1.00 \times 10^5 < Re < 4.44 \times 10^7$ among the tested geometries. In contrast, the conventional method of determining the first cell height assumes a flat plate to estimate wall shear and friction velocity. The first cell height from the wall, y, is estimated with friction velocity, U_τ and wall shear stress, τ_w, where [64]:

$$y = \frac{y^+\mu}{\rho u_\tau}, \qquad u_\tau = \sqrt{\frac{\tau_w}{\rho}}, \qquad u^+ = \frac{u}{u_\tau}, \qquad \tau_w = \frac{1}{2}\rho U^2_\infty C_f, \tag{1.4}$$

with an initial assumption for the skin friction coefficient, C_f, can be taken: [65]:

$$C_f = [2\log_{10}(Re) - 0.65]^{-2.3}. \tag{1.5}$$

where y^+ is the dimensionless first cell height, μ is the reference dynamic viscosity, and u is the wall-parallel velocity. However, velocity gradients arising from acceleration around surface curvature increases the local y^+ resulting in these flat plate assumptions to be invalid. To ensure that the boundary layer resides within the near-wall grid, it is recommended for subsequent layers to grow at a rate of $< 1.25\delta$, with δ as the lower cell thickness, while 20 layers "should be adequate for a boundary layer". As a practice, Cummings et al. [61] used grids that are refined by a factor of $\sqrt{2}$. While both spatial and temporal scales are related, this heuristic strategy is proposed to optimise the total effort required for a set of computations.

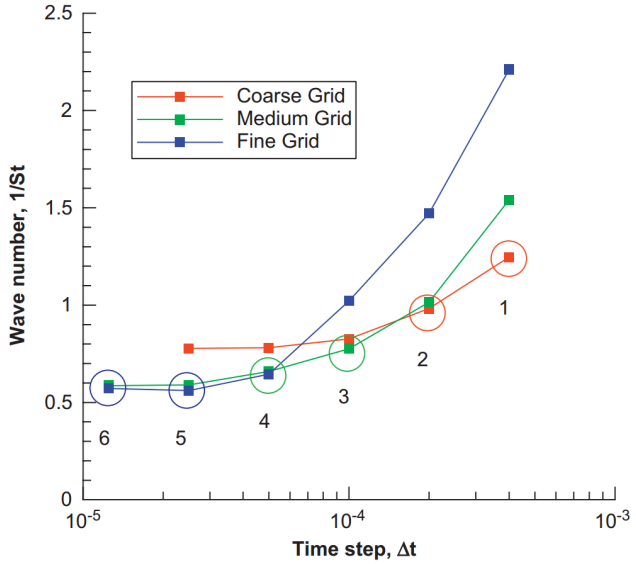

Figure 1.8: Proposed time-step and grid study showing asymptotic nature of time-step and grid combination with wave number as the result. [61].

Figure 1.8 shows the relationship between wave numbers ($1/S_t$) and time-steps (Δt), where the Strouhal number, $S_t = fL/U$. The coloured curves show results obtained with three different grids under multiple time-step sizes. It is argued that this approach of computing all combinations grids and time-step sizes can be time-consuming. Based on this heuristic approach, Cummings et al. [61] proposes that the results in Figure 1.8 are typical to that of unsteady cases, and only six of the circled cases need to be run, with two cases needed for each grid refinement. Each time-step is halved from the previous (i.e. $\Delta t_n = \Delta t_{n-1}/2$) and recommended starting $\Delta t_c = 0.01$, inspired by the Nyquist sampling rate [66]. In this example, points 1–6 are asymptotic and 4–6 are taken to be grid and time-step independent. Therefore the grid and time-step corresponding to point 4 is deemed most efficient and should be used. With this strategy, the effective number of simulations required to establish a grid and time step independent case is reduced significantly. Cummings et al. [61] concludes by emphasising that determining these conditions are driven primarily by the flow physics of interest, and that grid and time-step studies must be performed concurrently.

The above section(s) have discussed some methods for wake capture, with a focus on computational modelling. Key perspectives were provided in areas including grid requirements for wake capture, the limitations of turbulence modelling techniques, and strategies to approach the solution of unsteady flows. While the premise of the current work will be based on computational methods, the undertaken methodology will require references for validation and verification. This has led to the need for aerodynamic benchmark geometries for evaluation. One example for wakes is the canonical bluff-body flow.

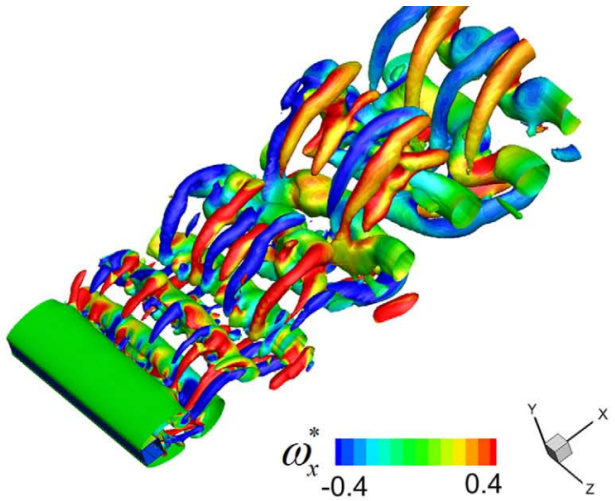

Figure 1.9: Identification of vortical structures shed by a bluff-body, contoured with stream-wise vorticity component [69].

1.2 Bluff-Body Wake Dynamics

As a myriad of possible geometry configurations can be responsible for a wake generator, the square beam bluff-body ("square cylinder") has been a long-standing benchmark geometry [67] for the validation of CFD methods with experiments [68]. Although the geometry may be relatively simple, complex flow phenomena can exist throughout flow regimes over the square beam (Figure 1.9). At lower, near laminar speeds ($Re \approx 100$), it has been observed that flow separation does not necessarily occur at the leading edges but remains attached on the surface of the geometry for half its width [69, 70]. At these slower and transitional regimes, several modes of flow invloving the transition from laminar flow to the alternating von Kármán street across $50 < Re < 160$ can also be observed. This mode occurs through the shedding of shear-layer instabilities over the leading edges and their transition to turbulence, where vortex shedding with wake dynamics become prevalent [71, 72]. The evolution of time-averaged drag and Strouhal number as the flow becomes transitional also behaves asymptotically at higher ($Re > 1 \times 10^4$) Reynolds numbers [69].

As highlighted in Section 1.1, numerical methods possess the flexibility for entire domains to be investigated freely without interference from physical apparatus. This allows the investigation of the wide range of flow phenomena the bluff-body presents, ranging from near-wall flow developments to vortex shedding and wake dynamics [68]. In addition, it favours the generation of highly orthogonal grids, preventing numerical diffusion [73]. However, as previously dicussed, general purpose RANS techniques based on the Boussinesq hypothesis for eddy-viscosity dampens convection begin to exhibit non-physical dissipating behaviours even for attached flow regimes. This is observed to occur as close as two characteristic lengths downstream [32, 49]. As bodies of interest can be located beyond this distance [17, 18], accurate capture of wake physics at these distances may be unsuitable for RANS-based techniques. This

inadequacy can be further exacerbated under massively separated conditions, despite good accuracy for surface force integrals. However, large-scale full- and half-loop vortex structures at transitional Reynolds numbers could still be distinguished in the wake of a finite ($AR = 7$) cuboid [74]. Key quadrupole and dipole wake structures were qualitatively identified in this transitional regime ($652 < Re < 13\,041$) with Reynolds Stress Models. In addition, findings on the asymptotic behaviour in the drag coefficient at Reynolds number range also agree with other studies [69].

At higher Reynolds numbers ($Re > 1.0 \times 10^4$), the wake shed by a bluff body can be described by several characteristic quantities. Benchmark conditions [55,68,75–79] at $Re = 21\,400$ showed that the time-averaged drag coefficient ranges approximately 2.1 to 2.4, with Strouhal numbers ranging 0.12 to 1.4. This shedding frequency is correlated to the vortex shedding pair that forms due to the roll-up of the shear-layer instabilities at the leading edges. A summary of these results both obtained from numerical and experimental methods can be found in Table 1.1. Moving along to the wake centre, a region of lower pressure and recirculation zone exists leeward of the geometry. As the momentum of the fluid recovers, a recirculation distance in the order of x/D where the local velocity at a point along this wake centre can be found to stagnate. Past this, the width of the wake grows, and the time-averaged (first-moment statistics) of wake centre velocity recovers towards the freestream. This process is illustrated in detail with time-averaged statistics in Figure 1.10 along multiple downstream stations obtained with DNS at $Re = 400$ [71]. Wake behaviour at such lower Reynolds exhibit similar characteristics. Close to the geometry ($x/D < 2$), the wake is clearly defined and shows the approximate size of the recirculation zone with the wake profile intersecting $\overline{u}_x/U = 0$. At these nearer stations, the acceleration of the flow past freestream values are apparent from the shear-layer instabilities. It is expected for fluctuating quantities to be larger in amplitude in these regions. Past this, the wake width widens and gradually recovers to the freestream from $x/D > 3$ onwards.

More importantly, fluctuating quantities become increasingly dominant at within turbulent wake regimes. They are aerodynamically responsible for buffeting loads, which are an important consideration in engineering. Unsteady-RANS (URANS) methods become unsuitable as these fluctuations can be lost through the process of Reynolds averaging and decomposition ($\phi_i = \overline{\Phi_i} + \phi_i'$). Wake behaviour can therefore become numerically damped, which is attributed to an excess of turbulent viscosity production [75]. LES techniques are among those that have been increasingly used for resolving the turbulent flows [76, 77]. Mean moment statistics along the wake centre have been captured using Scale Adaptive Simulations (SAS) [78], and one-equation dynamic models provided good agreement in terms of the root-mean-square velocities [76], evaluated against laser-Doppler measurements [68]. Near the walls, it is suggested that the capture of near-wall features are key as shear layer (Kelvin-Helmholtz) instabilities at the points of separation are propagated downstream into the von Kármán street [55]. However, turbulent length scales approach the order of the boundary layer thickness near the wall and LES depends

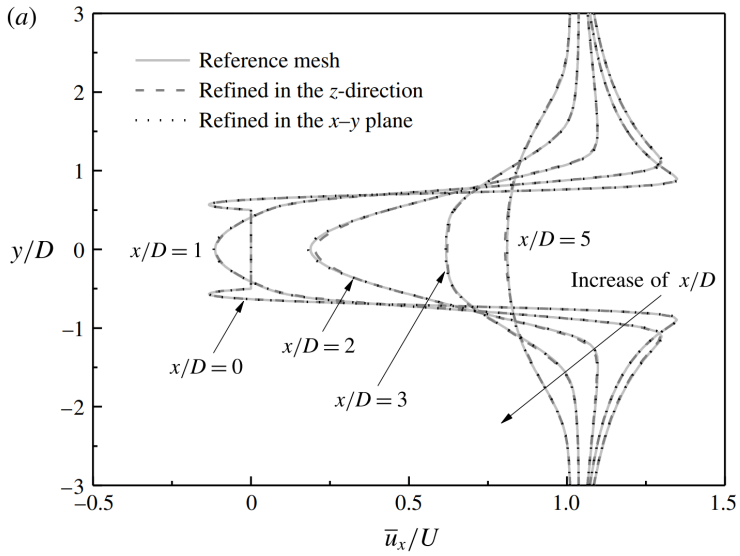

Figure 1.10: Time-averaged velocity profiles across the wake at multiple stream-wise stations aft of a square beam geometry, demonstrating the recovery in wake velocity [71].

Table 1.1: Summary of key vortex shedding parameters from numerical and experimental bluff-body benchmarks.

Case	Type	$Re \times 10^3$	AR	$\overline{C_D}$	S_t	λ	$C_D{}'$	$C_L{}'$
Numerical Cases								
Boudreau et al. [75]	URANS	21.4	7	2.11	0.133	0.97	0.14	1.56
	DDES	21.4	7	2.41	0.126	1.07	0.17	1.47
Barone and Roy [80]	DES	19.4	4	2.11	0.125	1.42	0.26	1.16
Fureby et al. [77]	LES	21.4	8	2.1	0.131	1.25	0.17	1.30
Sohankar et al. [76]	LES	22.0	4	2.09	0.128	1.07	0.27	1.40
Minguez et al. [55]	LES	21.4	-	2.2	0.141	1.28	-	-
Trias et al. [79]	DNS	22.0	4	2.18	0.132	1.04	0.205	1.71
Experimental Cases								
Lyn et al. [68]	Laser-Dopp.	21.4	9.75	2.1	0.132	1.38	-	-
Minguez et al. [55]	Laser-Dopp.	21.4	20	2.1	0.130	-	-	-
Luo et al. [81]	Water tunnel	34.0	9.2	2.21	0.13	-	0.18	1.21

on the filter width, with a sub-grid scale spacing ($\phi_i = \hat{\Phi}_i + \phi_i^{SGS}$) that can be limited towards DNS levels [79]. This can become unnecessarily computationally expensive in terms of wall grid resolution, especially for practical purposes.

However, advancements in turbulence modelling towards hybrid methods have alleviated some of these demands with a hybrid length scale definition where a RANS solution is confined to the boundary layer region, with an LES-like activation farther from the walls [82]. Hybrid RANS-LES methods therefore provide a good compromise between RANS and LES techniques [58, 83]. The evaluation of DDES capabilities determined that the accuracy of the wake statistics increases with refinement of the subgrid-scale definition [80]. The grid sensitivity study was performed on refinement sizes in the order of $\Delta y/D = [0.03, 0.05, 0.1]$ with agreeing results compared to pre-existing experimental data [68] were performed on a finer ($0.03\Delta y/D$) grid coupled with a modified Total Variation Diminishing scheme. However, the two coarser $\Delta y/D = [0.05, 0.1]$ refinement grids produced similar results, with an approximate $0.1\overline{U}/U_\infty$ over-prediction in wake velocity recovery. A similar $0.05\Delta/D$ grid resolution in the wake was also used with spatial (upwind-based) schemes that are second-order accurate, although with comparatively slightly better results [75]. Both examples successfully employed the hybrid method, by demonstrating reasonable accuracy in representing the time-averaged velocity recovery and its root-mean-square statistics for the wake centre.

1.3 Bluff-Body Wake Encounter Under Static Conditions

A series of canonical studies have been conducted to provide an insight on the effects of wake encounter on downstream geometries. An experimental investigation of an airfoil with an upstream cylinder as a wake generator (Figure 1.11) demonstrates that these conditions are capable of producing negative drag on the airfoil with a less distinct stall angle compared to wake-free conditions [84]. The work also investigates the effects of cylinder size with cylinder-airfoil separation distance. Findings were similarly reported in numerical studies, with stream-wise separation distance as the primary control variable [85]. Two modes were classified regarding the Kármán street behaviour. When the geometries are separated by two characteristic lengths ($L/d = 2$), counter-rotating vortices shed by the upstream body connect with the airfoil leading edge which slows the flow. As a result, the Kármán street is suppressed from this blockage and attenuates fluctuation intensities. At greater separation distances ($L/d \geq 4$), the instabilities are allowed to roll-up and develop further, which impinge onto the airfoil leading edge instead. However, the cylinder width used by Jiang et al. [85] as the wake generator is an order of magnitude smaller than the airfoil chord ($d/c = 0.1$) downstream. This affects the wake width relative to the downstream body. As the wake behaviour is characterised by the upstream characteristic length, a much narrower wake is emanated relative to the chord in the study done by Jiang et al. [85] compared to what is used by Lefebvre and Jones [84], where the respective charac-

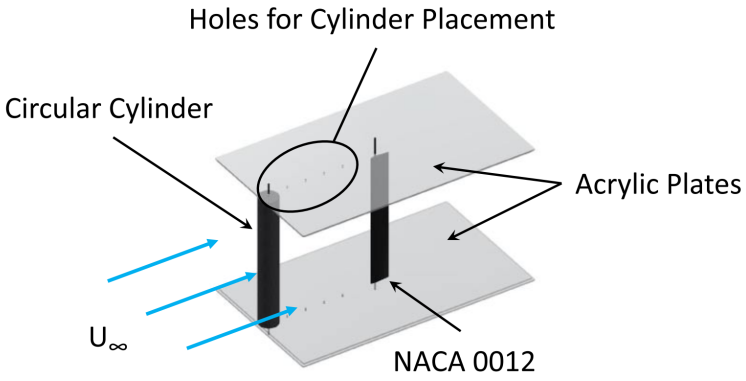

Figure 1.11: An example of an experimental platform of a tandem flow configuration with a cylinder as a wake generator [84].

teristic lengths of both geometries are similar. This leads to different wake characteristics and fluctuation intensities, and contributes to a greater magnitude in the aerodynamic response by the airfoil from the relatively larger sized wake generator. Additionally, Chirico et al. [18] used a cuboid of comparable characteristic length as opposed to a cylinder for the upstream geometry. This is arguably more suitable as a canonical shape representative of buildings—and by extension ships—as a generator for separated wakes. Ultimately, these work have illustrated that the effects by the downstream geometry can be affected by a myriad of control variables, but in a wake encounter, the geometry is engulfed by a region of reduced Reynolds number compared to the freestream. This is in addition to it being subjected to wake dynamics and turbulence from vortex shedding which further complicates analyses.

To evaluate the effects of wake interference on the downstream geometries, it is useful to compare results relative to wake-free conditions. Based on this, data for aerodynamic benchmarks like symmetrical airfoils provide a good reference. Evaluating symmetrical airfoil characteristics at Low Reynolds Numbers (LRN, $Re < 1 \times 10^6$) exhibit aerodynamic non-linearity for lift and drag coefficients against angle-of-attack [86]. This is further supported by numerically studying airfoil characteristics at $Re = 1 \times 10^4$ and 1×10^5 [87], showing that the drag coefficient at $\alpha = 0^\circ$ begins to become asymptotic beyond $Re \approx 4 \times 10^5$ for the NACA0012 [88]. However, as these investigations were conducted numerically, Reynolds-Averaged Navier-Stokes (RANS) models were reported to be less suitable at accurately predicting this LRN non-linearity, compared to Large Eddy Simulation (LES) methods relative to experiment data [86]. In the near-wall flow field, RANS predicts a separation point that is closer (aft) to the trailing edge than that obtained with the LES models. Furthermore, the separation bubble that forms over the leading edge for the LES and experimental results at higher angles-of-attack cannot be similarly captured with RANS [86]. At these critical conditions ($Re = 2.3 \times 10^4$), the flow over the leading edge undergoes a process of separation, transition, and finally reattachment on the upper surface of the airfoil, resulting in the generation of a laminar separation bubble [89]. This agrees with results based on Direct Numerical Simulations (DNS) of flow over a NACA0012 at low and

moderate Reynolds numbers ($Re = 5 \times 10^4$ and 1×10^6) at $\alpha = 5^\circ$ and 15°, respectively [90]. These highlight that the selection of the appropriate techniques is critical for accurately modelling wake physics.

As the aerodynamic response of the geometry subjected to the wake is dependent on the vortex shedding characteristics, a correlation in the behaviors between the bodies in tandem is expected. Coherent vortical structures reveal frequency content with Strouhal numbers in the order of 0.2 shed by canonical shapes such as cylinders [85, 91], and 0.13 for bluff-bodies [92]. Relative to the trailing geometry, this periodicity and coherence in the wake characterizes unsteady loads which could be represented by the Sear's function for gusts or Theodorsen's function for coupled pitch and heave [93, 94]. These functions are dependent on reduced frequency that is solely based on the dominant shedding frequency of the flow. However, modelling the response of an airfoil subjected to turbulence requires spectral analyses to evaluate the effects at each frequency in the wake spectra. The result of these empirical models is the attenuation and phase-lag of lift relative to a quasi-steady result, although these models have limitations where the approximated reponse deviates from measurements at higher angles-of-attack and gust amplitudes [94, 95].

1.4 Wing Wake Dynamics & Flow Behaviour at Flow Separation

Studies have also extended beyond the focus of bluff-bodies to compare vortex shedding behaviours with streamlined shapes. At flow separating attitudes without boundary layer reattachment, the shedding characteristics for symmetrical airfoils can resemble those typical of bluff-body wakes [96]. But as opposed to axisymmetric geometries, an airfoil emanates wakes that are more complicated, with multi-frequency systems shed at the leading and trailing edges [97, 98]. In addition, Strouhal numbers of streamlined bodies are more sensitive to changes in Reynolds numbers at lower ($\leq 10^\circ$) angles-of-attack [98]. At post-stall (15° to 90°), the Strouhal number tends to remain constant beyond $Re_c > 2.5 \times 10^4$, which is similar in magnitude observed for the square beam [69, 99]. The dominant frequencies in the wake spectra have Strouhal numbers ranging from 0.12 to 0.22, which coincides with those observable from bluff-bodies. However for streamlined bodies, a broader spectrum of frequencies can be observed within the wake spectra due to the shear-layers emanated from the asymmetry relative to the flow direction caused by the leading and trailing edges [99, 100].

Experimental investigations by Yarusevych and Boutilier [98] demonstrated that for lower Reynolds numbers without boundary layer reattachment, vortex shedding characteristics for three symmetrical airfoils resemble those typical of bluff-body wakes, but with a more substantial variation in Strouhal number with Reynolds number for bluff bodies. In this flow regime ($Re_c \approx 1 \times 10^5$, $\alpha = 10^\circ$), the Strouhal numbers for the three airfoils are observed to be within

$0.2 \leq S_t \leq 0.25$. The interpretation of these results are attempted in 2D (with the experimental model spanning the wind-tunnel test section width) and any physical features in the third dimension, like a swept wing or wing tip may introduce unobservable flow features or effects on shedding dynamics (See Appendix A).

The effects of a cantilever NACA 0012 wing root juncture and wing tip [99] show that they were able to reduce vortex shedding frequency. This is evident from span-wise frequency measurements, showing peak frequency towards its mid-span, furthest away from either the root of tip ends of the wing. Regardless, notable results on the vortex shedding dynamics demonstrate that the Strouhal number remains constant towards a sufficiently high Reynolds number ($Re_c > 25\,000$), measured at higher angles-of-attack from 15° to 90°. Furthermore, the measured Strouhal numbers at these angles range from 0.12 to 0.22, which agree with findings on shedding frequencies of 2D bluff bodies [101].

Huang and Lin [99] also classified the vortex shedding modes into four regions based on Reynolds number and angle-of-attack, which was originally described by Lienhard [100]. It is shown that these higher angles and Reynolds numbers (along with the present work) are likely to fall within the fourth “supercritical" region of classification for shear-layer instability waves. These modes are closely related to the boundary layer behaviour on the suction side surface of the wing. In addition, these wake behaviours are more complex at higher angles-of-attack and free stream velocities where a broader spectrum of frequencies are observed. This suggests a greater degree of unsteadiness that increases with angle-of-attack and freestream velocity.

The above sections (Section 1.2 to 1.4) have highlighted several points so far. Firstly, flow characteristics over bluff-bodies and their wakes are reproducible and is suitable for benchmarks. This includes comprehensive data contributed by a multitude of experimental and computational methods. The data available ranges from first- and second-moment statistics along the wake, together with body-forces that can be used for validation. Secondly, it is observed that the effects of flow separation over wings produces wakes that contain a broader spectra of frequencies and amplitudes (second-moment statistics). In addition, some wake characteristics observed at these higher angles are comparable to those shed from bluff-bodies. This implies that wakes induced by flow separation can be less dependent of their source. Ultimately, it is evident the effects of wakes are significant and has to be considered especially for tandem geometries. As a result, these insights can be extended to the investigation of aerodynamic interactions for such configurations. One example, as highlighted in the beginning of this chapter, is interaction that occurs between the wing and tail.

1.5 Wake Interactions in Tandem Configurations (Wing-Tail)

The literature reviewed on aircraft wing-tail interactions so far has been unsatisfactory. Those that have provided some insight on aircraft wing wakes were conducted under static conditions,

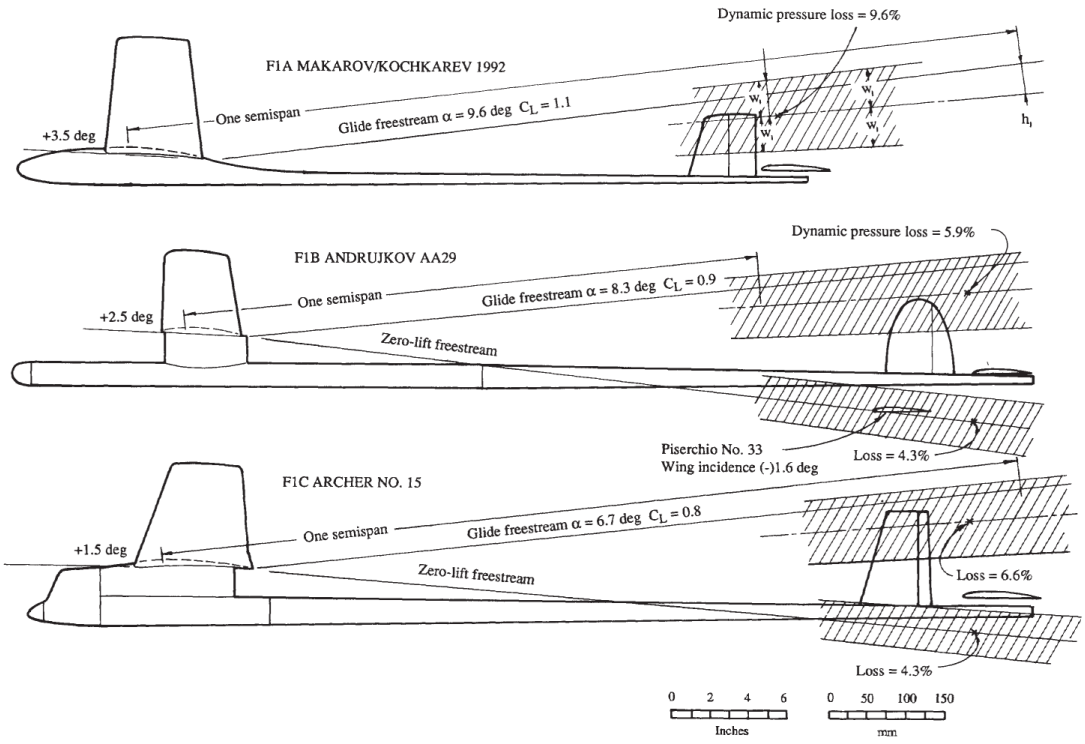

Figure 1.12: The impact of glider wing wakes on horizontal stabilizers with respect to local wing angle-of-attack and dynamic pressure loss [103].

and with little in-depth analyses on tail aerodynamics with regards to the wing wake [52,54,102]. While these reveal key information regarding their capture at stall, they do not provide adequate insight on its relevance and interaction with the tail. Therefore, the following sections serve to better understand these effects, beginning with the significance of the wing and tail and their contribution to longitudinal stability. Emphasis will be placed on the impact the wing wake on the overall configuration. Further efforts on computational aerodynamics for aircraft static *and* dynamic stability will be reviewed to discuss findings and the considerations involved for performing such investigations.

The drop in dynamic pressure and size of the wake's width is related to drag and distance behind the trailing edge [103]. This is significant especially if the wake impinges on another body—like from the wing wake of an aircraft onto its own tail for a conventional fixed wing configuration [104]. This interference can be detrimental to the tail's aerodynamic effectiveness, which is critical to its contribution to longitudinal stability, which is a primary flight attribute. At attitudes apart from direct blanketing of the wake over the tail, the proximity of wing downwash in relation to the tail can also induce a change in the effective tailplane angle-of-attack. The effects of dynamic pressure reduction and wake deflection are illustrated in Figure 1.12 where the position of the wake due to glide angle and lift coefficient is shown relative to horizontal stabilizers and zero-lift freestream direction. This example shows that the loss in dynamic pressure can be expected to drop by up to 9.6% in Figure 1.12 at the tail due to blanketing effects.

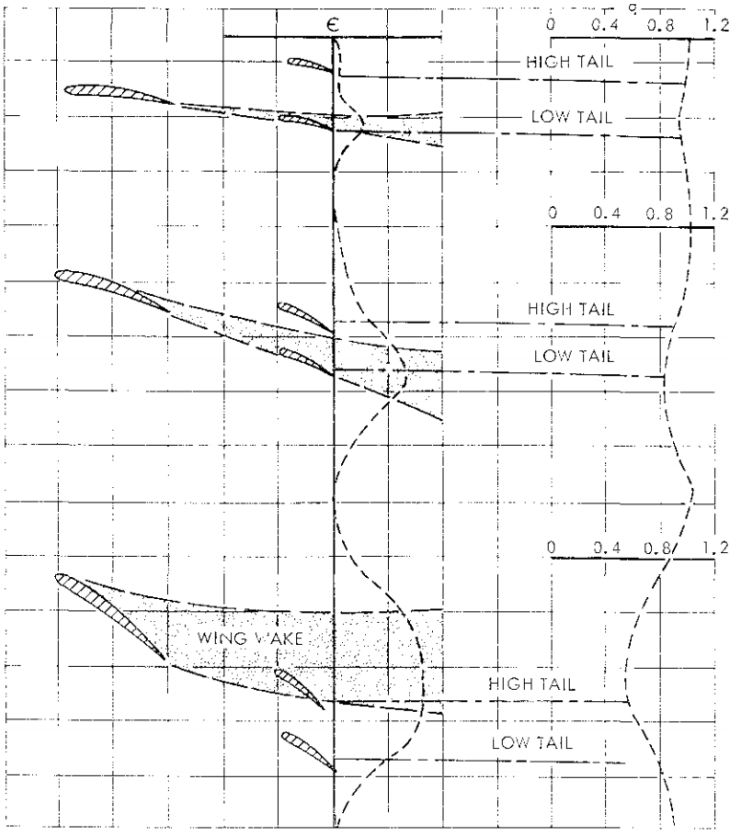

Figure 1.13: Three different instances of wing wake patterns, based on wake width due to angle-of-attack relative to the tail's position [105].

Along with this, the position change in the wake from downwash angle relative to the tail is also shown. This is significant, as the tail operates within the bounds of the wake and will encounter it during longitudinal manoeuvres. These effects are noteworthy despite the benign flight envelopes gliders are designed to operate within. Therefore, these conditions must be accounted for regarding general aircraft stability [5], and will be discussed in further detail in the coming sub-sections.

This aerodynamic interaction occurs due to several geometric and aerodynamic factors. The position of the Horizontal Tail-Plane (HTP) relative to the wing wake is also a determining factor towards the magnitude of which it has on the tail. In typical stream-wise wing wake patterns relative to tails [105], the physical height of the HTP on the empennage can alleviate some of the effects that the wing wake has on it, but with some considerations. A high-tail design, known as a T-tail, demonstrates both aerodynamic and structural benefits, such as a reduced tail footprint, resulting in lower induced drag and weight on the tail. However, the stall margin is compromised as the stabilizer can be engulfed by the wake at greater angles-of-attack, prohibiting the nose-down moments required for stall recovery (Figure 1.13). This can force the aircraft into what is known as a deep-stall condition.

Regardless of its position, the likelihood of the empennage interacting with the wing's wake increases as it widens downstream. Further widening occurs especially if the flow is separated

at the source. Wakes of low-speed post-stall conditions have been studied ($Re = 11.6 \times 10^6$, $M = 0.25$, $\alpha = 18°$) [52, 54] and it is demonstrated that at a flow separated (18°) angles-of-attack, the time-averaged stream-wise velocity profiles show a reduction of up to 60% in velocity relative to the freestream (Figure 1.7) in addition to a large wake width at the empennage (Figure 1.14). It is highlighted that the wake largely passes over the HTP, but its vertical extent (width) is still adequately large to suggest interactions with the HTP.

Based on wake positions depicted by Brynes et al. [105] in Figure 1.13, it is arguable that a low-tail design under identical stalling conditions may avoid this predicament as the wake will then be shed over the stabilizer instead. However, observations from low-speed stall [52] suggests that the vertical extent of the wake could still be adequately large enough to interact with even a low-tail design at stall. Contours of turbulent kinetic energy from the wing wake at relatively low-speed stall illustrates its position relative to the horizontal stabilizer in Figure 1.14. In addition, it is also highlighted that its influence even at lower, intermediate angles-of-attack may be still be significant as the HTP would be further immersed in the wake. Based on these observations, the wing's aerodynamic interaction with the HTP may be an unavoidable phenomenon throughout longitudinal attitudes and can be regardless of its position on the empennage.

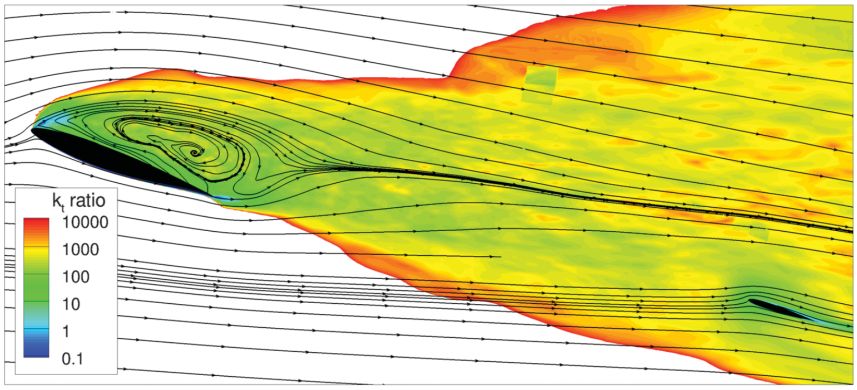

Figure 1.14: Contours of mean turbulent kinetic energy ratio and average velocity streamlines at 28.8% semi-span. Note the position of the wake relative to the horizontal stabilizer [52].

1.5.1 Significance of a Wing & Tail on Aircraft Stability

The total contribution of longitudinal stability of an aircraft is described as the synthesis of the aerodynamic forces and moments from physical components. These are primarily dominant from the wings and tail assembly, with more secondary contributions arising from the fuselage, nacelles, and propulsive system. For the contributions from a plain wing, its pitching moment about its CG due to lift and drag is given by the sum of its aerodynamic components [5]:

$$M_w = M_{ac_w} + (L_w \cos\alpha_w + D_w \sin\alpha_w)(h - h_{n_w})\bar{c} + (L_w \sin\alpha_w - D_w \cos\alpha_w)z. \tag{1.6}$$

where M_w and M_{ac_w} is the moment about the wing and its aerodynamic centre, while L_w, D_w, α_w, and $\bar{c}$, are the wing lift, drag, angle-of-attack, and mean chord, respectively. By assuming small angles and terms, and reducing to coefficient form with $\frac{1}{2}\rho V^2 S\bar{c}$, the equation reduces to:

$$C_{m_w} = C_{m_{ac_w}} + C_{L_w}(h - h_{n_w}), \tag{1.7}$$

where:

$$C_{L_w} = \alpha_w C_{L_{\alpha_w}}, \tag{1.8}$$

and the term $(h - h_{n_w})$ is known as the static margin with $C_{L_{\alpha_w}}$ as the wing lift curve slope.

The lift contribution by the tail alone and the synthesis of aircraft lift is taken as contribution from both the wing (with fuselage, denoted with $C_{L_{wb}}$) and tail:

$$C_{L_t} = \frac{2L_t}{\rho V^2 S_t}, \tag{1.9}$$

and:

$$C_L = C_{L_{wb}} + \frac{S_t}{S} C_{L_t}, \tag{1.10}$$

with S as the respective reference surface area. The forces for the tail are analogous to that of a wing and are analysed in a similar fashion. The key difference is that the tail is subjected to interference by the wing wake where its effective angle-of-attack is altered by wing downwash angles, ε. The moment contribution by the tail (denoted with a subscript t) is now given by:

$$\begin{aligned} M_t = &-l_t \left[L_t \cos(\alpha_{wb} - \varepsilon) + D_t \sin(\alpha_{wb} - \varepsilon)\right] \\ &- z_t \left[D_t \cos(\alpha_{wb} - \varepsilon) + L_t \sin(\alpha_{wb} - \varepsilon)\right] + M_{ac_t}. \end{aligned} \tag{1.11}$$

To empirically account for the drop in dynamic pressure as a result of wake interference, an efficiency factor defined by the ratio between the freestream and local tail dynamic pressures, $\eta_t = q_t/q$ is used, but can be challenging to determine [5]. However, it is suggested to be typically between 0.8 and 1.2 [106], but may decrease down to 0.5 for separated flows [105,107]. This must not be neglected, in addition to downwash angles, where are theoretically taken to be small [5]. Therefore, the equation is reduced to show in coefficient form:

$$C_{m_t} = \frac{2M_t}{\rho V^2 S\bar{c}} = -\frac{l_t}{\bar{c}} \frac{S_t}{S} C_{L_t} = -V_H C_{L_t}, \tag{1.12}$$

where V_H represents the tail volume, which is relative to the aircraft CG with the tail moment arm, l_t. Empirically, it is more convenient to use this moment arm with respect to a fixed reference point like the aerodynamic centre, as the aircraft CG is a function of flight time. Therefore,

the equation can be written as:

$$C_{m_t} = -\overline{V_H} C_{L_t} + C_{L_t} \frac{S_t}{S}(h - h_{n_{wb}}), \tag{1.13}$$

with:

$$\overline{V_H} = \frac{\overline{l_t}}{\overline{c}} \frac{S_t}{S}, \tag{1.14}$$

where $\overline{l_t}$ is the tail length taken with respect to the aircraft aerodynamic centre.

Based on the analyses, it is empirically convincing that the horizontal stabilizer's contribution to aircraft pitching moments and longitudinal stability is *significant*. The terms described in Equation 1.13 for the tail's contribution are major physical parameters, as compared to those described in Equation 1.7 for the wing's contribution towards pitching moments. This also emphasises that the tail is the dominant stabilising factor. This is evident in design data [108] where a tail-on/off condition chiefly determines the criterion for static stability ($C_{M_\alpha} < 0$)—and is a fundamental quality for flight.

1.5.2 Longitudinal Stability Characteristics

The static longitudinal stability of an aircraft based on the physical behaviour of the wing downwash ($d\varepsilon/d\alpha$) and relative tail location can be classified into three characteristics [105] shown in Figure 1.15. These are based on signs of $d\varepsilon/d\alpha$ and tail height where all of which are statically stable ($C_{M_\alpha} < 0$) before stall and generally contain regions of attached flows. However, their behaviour become distinct as pitch attitude increases, approaching stall regimes. This second region is known as the unstable pitch break and continuing breakdown of flow. At certain configurations (Figure 1.15c), a high and low tail (without an increase in tail volume ratio) establishes a nose-up moment representing an unstable flow after stall. Based on this behaviour, the change in attitude follows a progressive breakdown of flow and is observable as a result of its effects on pitch dynamics.

This correlation between breakdown of flow on pitch behaviour is also observed in the assessment of stability characteristics for a Blended Wing-Body (BWB) approaching stall [109–111]. This is shown in Figure 1.16 and highlights the progressive breakdown of flow on pitch behaviour into three regions. This three-part feasibility study was conducted to assess the BWB as a viable subsonic transport aircraft. Both computational [111] and experimental [110] studies were simultaneously carried out to cross-validate findings. Their objective was to assess the stability and control characteristics of the aircraft by focusing first on its longitudinal static stability. Although the results from both experimental and computational studies were inconclusive due to large discrepancies between experiment and numerical methods for pitching moments (Figure 1.16a) [111], the results exhibited similar trends. These trends can be observed to agree with the characteristics described by Byrnes et al. [105].

With reference to Figure 1.16b, Region I depicts longitudinal stability with generally attached flow. Region II shows a reversal of the pitch slope as an increase in C_{M_α} representing what is called an unstable pitch break with a breakdown of flow. This is caused by wing stall that results in a shift of aerodynamic centre [104]. This will be physically characterised as an abrupt pitch up in the aircraft. And finally, as the curve approaches post stall, Region III is described as stable flow and for this specific BWB case, can be described with a nose down slope, noting that the absolute values of C_M are not shown. Although this example uses a BWB geometry to demonstrate these effects, the same can be observed for a conventional fixed wing configuration as presented by Waldmann et al. [52] in Figure 1.7a for the NASA Common Research Model (CRM) geometry.

1.5.3 Computational Considerations for Tail Lengths

It has been highlighted in earlier sections that wake characteristics are a function of its distance from the source. As a result, the consequent effects of wake encounter are dependent on separation distance (Section 1.3). Under the context of wing-tail dynamics, this separation distance is the direct representation of an aircraft tail length. Considering this, an appropriate reference length for the present study of wing wake effects on its tail must be determined.

According to Silverstein and Bullivant [112], an aircraft tail typically lies 0.75 wing semi-spans downstream relative to physical wing and tail quarter chord points. For instance, the Lockheed C-130H has its tail located at approximately 0.63 wing semi-spans back [108], which corresponds to $3.18x/c$, and the tail quarter-span leading edge of the NASA CRM lies $3.24x/c$ aft of the wing with respect to local wing chord (10.181 m) at this aircraft butt-line station. Summary of these relative dimensions are summarised in Table 1.2. Based on these specifications, it is evident that the ratio provided by Silverstein [112] agrees with existing aircraft, which is found to be approximately 0.63 to 0.88 semi-spans downstream. However, this exact metric can sometimes be complicated to determine as the tail length needs to be defined explicitly. In contrast to Silverstein and Bullivant [112], who defines this as the distance between wing and tail quarter-chord points, Etkin and Reid references it as the CG to aerodynamic centre. These differences however, are assumed to be minor for the purpose of canonical studies.

It is important to consider the suitable turbulence modelling techniques as the use of RANS methods may exhibit dissipative behaviours at these relatively larger downstream distances. This dissipative behaviour is reported by Breuer et al. [113] where the modelling of effective eddy viscosity can be significantly over-predicted, especially for separated flows. This was conducted by comparing RANS, DES, and LES type modelling techniques for a flow over a flat plate at high angles of incidence. Their observations agree with those from the square beam wake cases (Section 1.2), as turbulent viscosity ratios (ν_t/ν) are modelled to be 40 times greater than in DDES solutions. This inflation in effective viscosity ($\nu + \nu_t$) affects the transport of momentum, which could be responsible for the increased rate at which the wake velocity recovers. This must

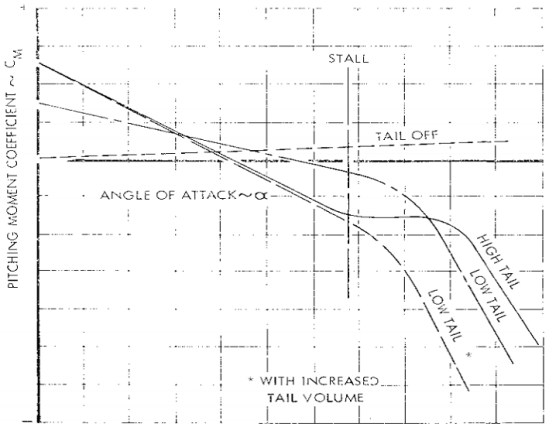

(a) Type 1: Straight wing ($d\varepsilon/d\alpha$ constant and < 1).

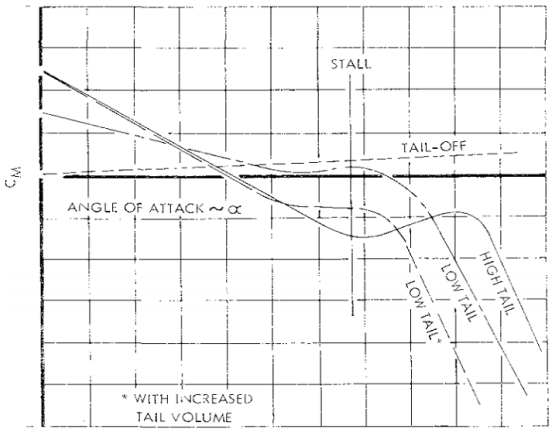

(b) Type 2: Swept wing with stable break at stall ($d\varepsilon/d\alpha$ increases with α and $(d\varepsilon/d\alpha)_{max}$ approaches 1).

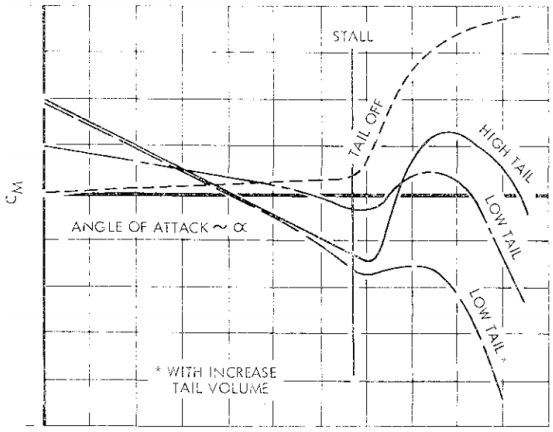

(c) Type 3: Swept wings with unstable break at stall ($d\varepsilon/d\alpha$ increases with α and $(d\varepsilon/d\alpha)_{max} > 1$).

Figure 1.15: Categories of pitch stiffness due to downwash angles and tail positions as a function of $d\varepsilon/d\alpha$ [105].

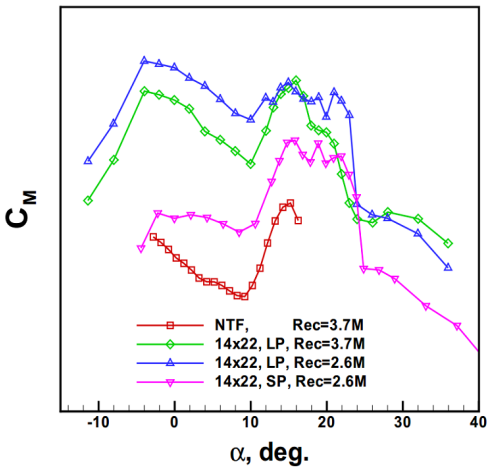

(a) Pitching moments of a BWB [110].

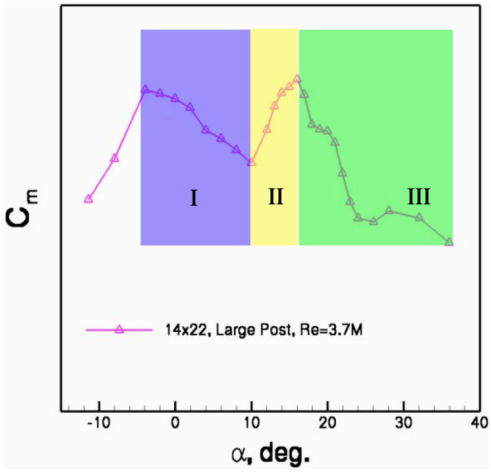

(b) Three key regions for stability and control [104].

Figure 1.16: The three key regions for stability and control observable on BWB and conventional configurations [111].

Table 1.2: Summary of aircraft tail moment arms relative to wing semi-span

Aircraft	l_t (m)	b (m)	$l_t b/2$	C_{MAC} (m)	l_t/C_{MAC}
Lockheed C130H	13.30	40.42	0.63	4.178	3.18
Fokker F-27	10.50	29.00	0.72	2.570	4.09
Airbus A320	25.63	60.30	0.88	4.194	6.11
UoG ATP/HS748*	11.00	30.63	0.71	2.786	3.95

* The ATP/HS 748 model is a 0.07-scale wing/fuselage combination here in full scale.

be considered for the relatively greater distances for typical aircraft tail lengths. In addition, a large tail length also requires the appropriate refinement region and resolution suitable for capturing any wake physics of interest. This has been discussed in Section 1.1.2.

1.5.4 Dynamic Stability Under Forced Harmonic Oscillations

Computational methods for stability can be extended to provide an insight on pitch damping—a combination of pitching moments due to pitch rate and angle-of-attack, which can be used as an indicator of dynamic stability. With oscillation about a nominal angle-of-attack, the hysteresis of pitching moments results in the computation of what quantifies as the pitch damping derivative. The distinction between damped and undamped pitch is indicated as a clockwise or counter-clockwise direction of the hysteresis loops, as a counter-clockwise pitch damping loop exhibits a damped configuration, and vice versa. Apart from the direction of the results, the magnitude of the pitching moments at nominal angle-of-attack also defines the magnitude of this derivative [104].

An earlier published case for the assessment of dynamic pitch stability with forced pitching of a BWB geometry ($Re = 7 \times 10^5$, $\Delta\alpha = \pm 5^\circ$, $k = 0.07$) [104] is extracted in Figure 1.17. These sub-figures illustrate solutions obtained with the SA and k-ω SST model, including additional results obtained with SA-DES in Figure 1.17d. The work highlighted challenges in establishing the balance between spatial and temporal resolution. As an attempt to determine the sensitivity of the URANS results to further grid refinements, an adapted and refinement mesh based on vorticity from the DES solution was used. Although more accurate results were obtained from this adapted and refined mesh for DES, the k-ω SST solution was re-attempted on this refined mesh with insignificant difference in results. Noting that the DES results are phase-averaged, the work reports that DES is better at reproducing the pitching moment hysteresis, although more time-steps for subsequent pitch cycles may be needed for averaging out the higher frequency/angle-of-attack content at $\alpha = 24^\circ$.

This example establishes the potential use of dynamic pitch simulations for assessing aircraft stability. However, as a BWB geometry does possess an empennage assembly, its wing wake characteristics are not a primary consideration. This is in contrast to a conventional wing-tail

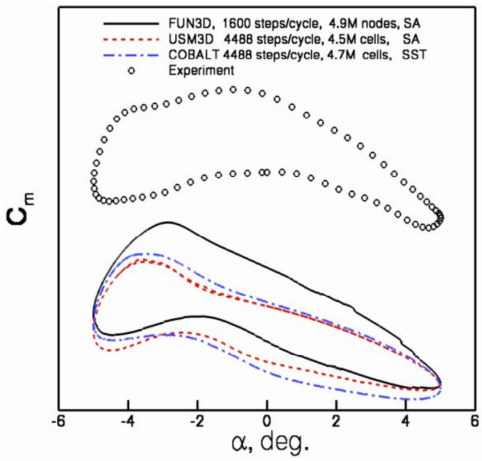

(a) $\alpha_0 = 0^\circ$ with URANS

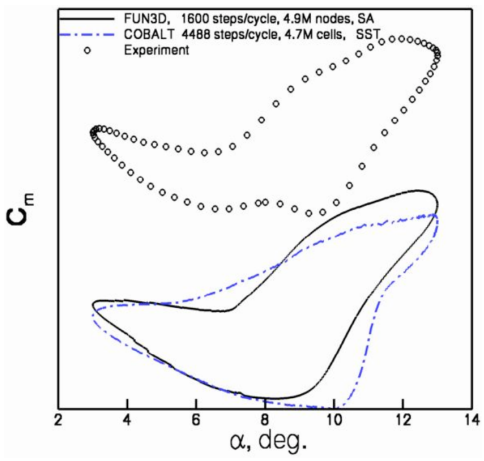

(b) $\alpha_0 = 8^\circ$ with URANS

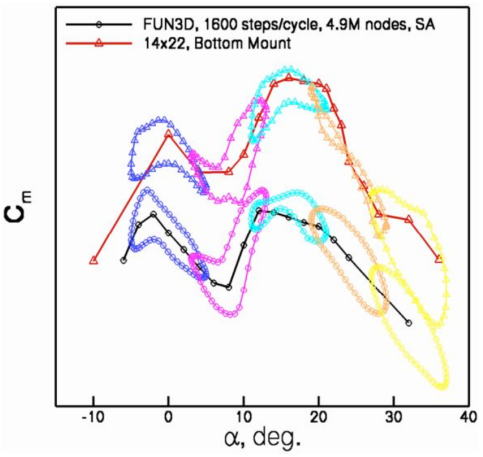

(c) Pitch hystereses with static results

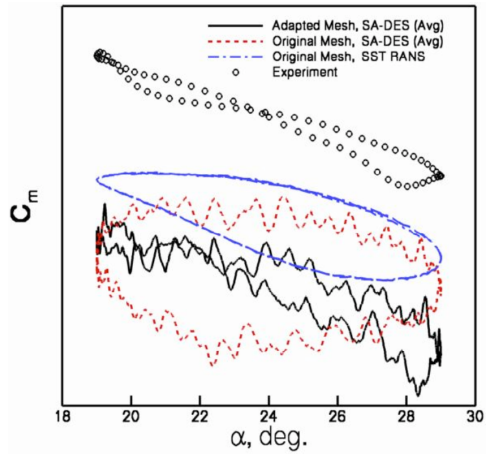

(d) $\alpha_0 = 24^\circ$ with URANS and DDES

Figure 1.17: Results for pitch hysteresis about multiple nominal angles-of-attack with different turbulence modelling techniques conducted on a blended wing-body at $Re = 7 \times 10^5$ [104].)

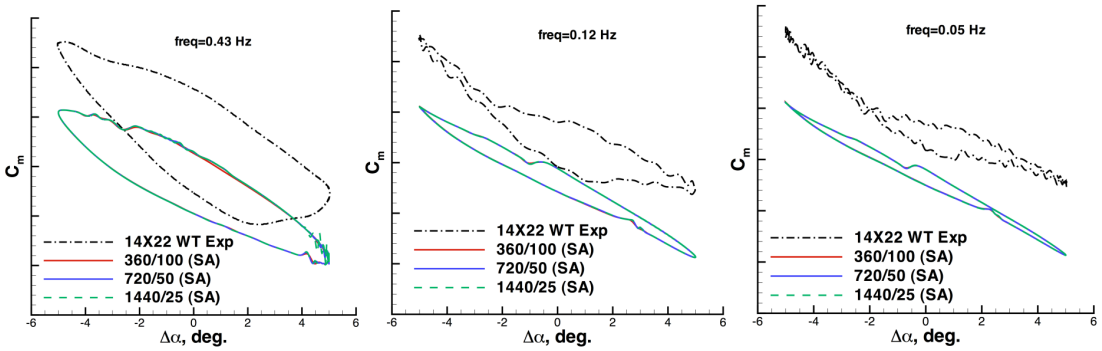

Figure 1.18: Convergence study by maintaining a constant product between the number of time-steps per cycle and sub-iterations (3600) across three different frequencies using the SA model ($Re = 5.4 \times 10^5, \alpha_0 = 24°$) [63].

configuration where the effects of wing downwash will be perceived by the tail. Therefore, capture of the wake region and its interaction with the horizontal stabilizer must be an added consideration. Regardless, the published results demonstrate typical lift and pitch hysteresis its indication of a dynamically stable aircraft.

1.5.5 Computational Strategies for Dynamic Pitch Simulations

Computation of longitudinal characteristics with dynamic pitch of a generic subsonic transport aircraft (Generic Transport Model) were conducted with URANS techniques (SA and k-ω SST) at $Re = 5.4 \times 10^5$, about a nominal angle-of-attack and amplitude of $\alpha_0 = 24°$ and $\Delta\alpha = \pm 5°$, respectively [63]. The work discusses a numerical strategy for quantifying numerical convergence in forced pitching cases. It is recommended that the total number of solution iterations per aircraft pitch cycle should be kept equal across cases. This is taken as the product of the number of time-steps per oscillation cycle and number of iterations per time-step. Results for three different combinations based on 36000 total solution iterations are extracted and presented in Figure 1.18, showing indiscernible differences in the results. In addition, a grid sensitivity study was conducted across three refinements demonstrating grid independence for lift and pitching moments, but details on the grid design and resolution, in particular the wake region, are ambiguous.

Considering that these are RANS-based models, the performance of SA and k-ω SST is commendable. The pitch damping hysteresis are effectively similar in overall size and shape compared to time-averaged wind tunnel data, although there was no discussion regarding the vertical phase shift in the results [63]. It is however reported that the choice of turbulence model has a greater impact than grid refinement levels at *post-stall* angles-of-attack, which should chosen first. At this angle ($\alpha_0 = 24°$), the inaccuracies are consistent with observations on the BWB case [104] where inadequacies in the RANS models are amplified with larger flow separation.

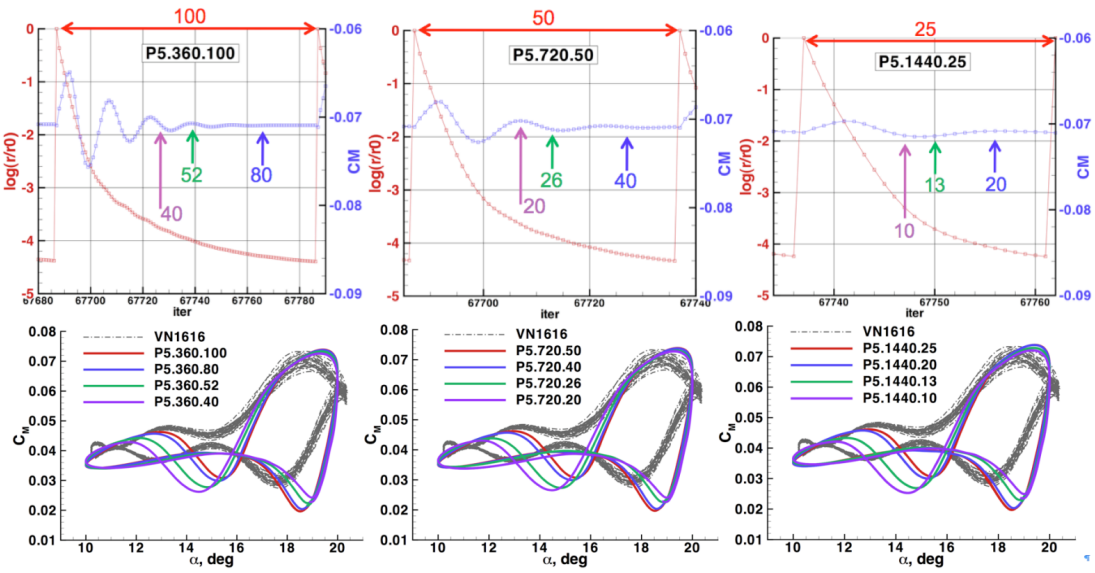

Figure 1.19: Correlation for sub-iterative convergence determined with pitching moment coefficient across decreasing number of sub-iterations [62].

The numerical approach for forced dynamic pitching is discussed in further detail on a flying wing geometry [62] similar to conventional fixed-wing configurations. The work proposes a strategy that begins by establishing well-converged reference solutions (by using more than necessary sub-iterations) on a reasonably coarse mesh paired with a second-order temporal discretisation scheme. Convergence at each time-step is accomplished by observing the solution residuals along with the pitching moment coefficient as seen in Figure 1.19. The plot compares sub-iterative residuals against the pitching moment coefficient within a single time-step. This is conducted across three different combinations of total iterations per pitch cycle and sub-iterations per time-step while the total number of iterations is kept constant. Upon determining the degree of numerical convergence, the solutions are then repeated with decreasing levels of *total* solution iterations. This determines the threshold for an “efficiently converged solution" illustrated in the pitch hysteresis in Figure 1.19. In this example, the results that deviate the most from the experiment are between 28 800 and 18 720 total iterations. This indicates the threshold for a balanced combination of solution settings.

It is reported that quantifying the degree of numerical convergence can be challenging due to the many variables involved in a solution. Determining this might require user judgement to balance computational efficiency and numerical accuracy [62]. Nevertheless, it is recommended for the overall approach to begin with the most non-linear and unsteady case such that the numerical approach chosen can then be applicable to other, more benign cases.

Among the forced pitch oscillation cases that are reviewed, only one utilized DES which proved to be advantageous for higher angles-of-attack [104]. By comparison, this revealed the relatively poorer performance of URANS, especially when massive flow separation is involved. Unfortunately, the reported computational approach that was undertaken is ambiguous. How-

ever, Frink [62] comments that the proposed strategies are unlikely to be applicable for such turbulence modelling techniques like DES. One potential reason is the requirement for sufficiently refined temporal and spatial scales in addition to a physically meaningful total solution time frame. This might require increasingly large wake refinement regions coupled with minuscule time-steps, and could therefore cause the proposed approach to be computationally prohibitive.

A summary of the reviewed cases for forced pitching of aircraft-related geometries are listed in Table 1.3. The reviewed literature for dynamic pitch simulations have not discussed the significant effects of any wing-tail interaction or wake block grid details, especially for conventional aircraft geometry used by Thompson et al. [63]. This is a significant discussion point, as aerodynamic interactions will definitely be present as the tail passes through the wing take during the pitching motion of the aircraft. This is in contrast to work by Waldmann et al. [52], Lutz et al. [54], and Gansel et al. [114] where adequate treatment of the near-wake is conducted, although for a static case at high angles-of-attack. This lack of attention on the tail's aerodynamic interactions with the wing wake is also highlighted by Gansel et al. [53] citing concerns for the computational modelling of transport aircraft configurations dealing with turbulent fluctuations in the wake with regards to the tail [115, 116].

Table 1.3: Comparison of reviewed forced pitching oscillation cases, comparing flow parameters and case set-up

Case Geometry	Flow conditions Re, M	Pitch break α	Amplitudes & Frequencies	Characteristic time-step	Total iter. /cycle	Reduced freqs.	Turb. models	Cells (million) y^+ at $0.5C_{ref}$
Hall et al. BWB [104]	7×10^5, 0.1	9°	$\Delta\alpha=\pm5°$ at 0°, 8°, 16° 24°, 32°	-	-	0.07	SA k-ω SST SA-DDES	0.7, 4.7, 4.9
Thompson et al. GTM [63]	5.4×10^5, 0.077	10°	$\Delta\alpha=\pm5°$ at 24° $f=0.43$ Hz 0.12 Hz 0.05 Hz	$\Delta t_c=0.02$ 1500 time-steps	36000	0.01483 0.00401 0.00167	SA k-ω SST	6, 12, 24 $y^+=0.75$
Frink SACCON [62]	1.61×10^6, 0.0144	17.89°	$\Delta\alpha=\pm5°$ at 0°, 10°, 15°, 20° $f=1$ Hz 2 Hz 3 Hz	$\Delta t_c=0.006$ to 0.290	36000	0.06 0.12 0.18	SA k-ω SST	3, 6, 9, 12 $y^+=0.5$

Key information regarding aircraft stability in terms of its wing-tail effects have been reviewed. This was firstly based on general wake phenomena and its impact on downstream aerodynamics. This concept has been extended to aircraft wing wake-tail dynamics where the separation distance (i.e. tail length) is taken as the region for interest with regards to wing-tail aerodynamic interactions. Important aspects are the significance of the tandem configuration to aircraft stability, aircraft longitudinal static stability characteristics, and the current state of computational studies for evaluating (dynamic) pitch through forced harmonic motion. The existing work reveals some challenges and best practices for assessing aircraft dynamic stability while a lack of focus in the aerodynamic phenomena in the downwash region is identified. Contrary to what is recommended for wake capture, the turbulence modelling techniques employed in these studies may arguably be unsuitable for wing wakes, which is a significant consideration for the tail. By extension, this would affect the modelling tail effects and therefore any stability characteristics. This presents the opportunity to provide insights on wake interactions, especially under oscillating conditions. The present work therefore develops a computational framework for unsteady wake capture and its effects on downstream aerodynamics.

1.6 Closing Statements

In summary, the literature review emphasises that the effects of wake phenomena on downstream bodies are significant which cannot be neglected. Any relevant wake physics must be accurately captured prior to the consequential effects of a wake encounter. An initial overview of the concepts involving wake capture and the study of vortex shedding dynamics are given where both streamlined and bluff-body geometries were generally considered first. This provided a foundation to understand the expected wake physics and computational methodologies involved. Such benchmark flows also allow data reproducibility, which is essential for validation and verification of results. For computational approaches on wake capture and unsteady flows, the literature review has revealed and recommended the following best practices and considerations:

1. The highly turbulent and unsteady nature of wakes, especially with flow separation, can be challenging to model. Capturing these physics successfully are therefore heavily reliant on the type of turbulence modelling technique, which favours scale-resolving techniques such as DES for resolving the turbulent scales in the wake (See Section 1.1.2).

2. Canonical geometries are useful for benchmarking purposes. This ensures that the obtained results are physically meaningful and reproducible. These geometries could subsequently be used as wake generators for studies after successful validation and verification, which ascertains the computational results (See Section 1.2).

3. The resolution for highly unsteady and separated flows depends on spatial and temporal scales that are physically coupled. This must be determined concurrently. This extends

to the selection of the appropriate numerical schemes in addition to a suitable turbulence modelling technique. An adequate solution is defined by its ability to capture the relevant spatial and temporal scales of interest. This is driven by a sufficiently fine grid point spacing, coupled with a suitable time-step size to satisfy the Courant number criterion (See Section 1.1.3).

The conditions for wake encounters may not be necessarily static. This branched the literature review into more specialised cases involving computational methods for aircraft stability. Therefore, aircraft static stability characteristics are subsequently reviewed, revealing some distinct behaviours in the pitching moment coefficients especially at higher angles-of-attack. These behaviours were distinguished into different types that were governed by pre- and post-stall regimes over the aircraft. Methods for static stability criteria subsequently evolved into those for dynamic stability with recommended practices. However, upon deeper investigation, more focus on the wing wake region bounded by the tail length was desired, especially for conventional fixed wing configurations. As it is shown under static conditions that the tail is the chief contributor to pitch stability, adequate numerical treatment must be given to the its local flow field or physically meaningful data would be lost. This would lead to misrepresentation of tail loads, and consequently its contribution to total aircraft stability. The main gaps in the literature under this context can be summarised with the following:

1. Aircraft tail lengths are a direct analogy for separation distances in tandem flows (See Section 1.5.3). As a result, this affects mesh sizes as an adequately large refinement area is needed to capture the wake including the tail. This is also an added consideration of turbulence modelling technique selection, which based on findings in the benchmark cases, have shown that RANS-based models are unsuitable due to the formulation of Reynolds stress and eddy-viscosity for convective acceleration (More details in Chapter 2).

2. The techniques presented for computational studies on dynamic pitch through forced harmonic oscillations are mostly limited to RANS turbulence modelling (Section 1.5.5). This is key, while in view of the point above, work on wake capture has demonstrated that RANS-type modelling may not be suitable, especially if flow separation is present.

3. Flow separation needs to be considered, as confidence on computational methods for aircraft stability and control well-within the flight envelope is high. To advance this boundary more studies are needed to be conducted for regimes at the edge of flight envelopes, which reinforces the idea of modelling for flow separation with higher-fidelity turbulence modelling techniques (See Section 1.5.2).

In summary, the work will explore the effects of wake encounters and its influence on downstream aerodynamics. This will be accomplished first based on static conditions for simple wake capture, followed by engaging a dynamic case for in-depth analyses with regards to wing-tail interactions for dynamic stability.

1.6.1 Overall Research Milestones: Aims & Objectives

To advance the understanding of wake encounters and its effects on downstream aerodynamics, the scope of the work will be narrowed into two wake encounter regimes:

- Under ***Static*** conditions, where a canonical geometry is used as a wake generator located upstream of a geometry of interest. This tandem flow configuration is analogous to aerodynamic obstructions, where vortex shedding dynamics of a body upstream interferes with freestream conditions.
- Under ***Dynamic*** conditions, where a forced (harmonic) motion induces a wake encounter between a wing-tail tandem configuration. This represents an environment analogous to a pitching manoeuvre, where the wing wake is amplified with stall and flow separation which is shed onto the horizontal stabilizer downstream.

The overarching strategy to fulfil these conditions will be the development of a three-part approach that forms the basis of validation, application, and extension of the numerical framework for wake encounter on downstream aerodynamics. Ultimately, this framework addresses the requirement for accurate modelling of wakes supplemented with high-fidelity turbulence modelling techniques. Referencing the conditions above, this framework can be established through the course of the following aims and objectives for this thesis.

1. A process to validate and verify the computational approach must be established. To address this, a high-resolution wake capture will be conducted through an aerodynamic benchmark. Results will consider the potential implications the captured wake has on a downstream geometry of interest.

    (a) In view of the library of benchmark data provided by Lyn et. al [68] and subsequent works (See Table 1.1), the modelled wake definition should be supported by validation of vortex shedding parameters, including the first- and second-moment statistics of the wake profile. This will be captured with a DES approach, where findings will be evaluated with RANS-based models (More details on the selected turbulence models in Chapter 2).

2. Upon successful validation of the bluff-body wake capture, its effects on a downstream geometry will be investigated. To address this, the impact of the wake on a NACA wing-section separated by a pre-determined distance downstream will be conducted. To better understand the consequential effects of large amplitude wakes on downstream aerodynamic effects [84], a validated wake-free condition will be used as control reference. The resulting influence of the wake can then be quantified, and its unsteady response can be better represented.

(a) While wakes are unsteady, it can be expected for the resulting aerodynamic response downstream to follow. This would result in an aerodynamic correlation between the two geometries. As vortex shedding behaviour is oscillatory, the resulting response may exhibit corresponding harmonic behaviour. This could be used as a basis for approximation methods like the Sear's and Theodorsen's functions [94] to predict downstream behaviour due to wake influence. Such approximations are unable to account for the frequency content in the wake which can only be captured with computational or experimental methods [85].

3. To achieve dynamic conditions, the techniques validated so far will be expanded to include grid motion. To accomplish this, an overset grid method will be explored to generate mesh movement, demonstrated on an isolated wing-tail tandem configuration. The analyses will be conducted under forced harmonic pitch. This approach forms the basis of the investigation of tail loads and its dynamic encounter with the wing wake.

   (a) The key region of focus will be on tail aerodynamics as a result of wing wake interaction. As the system is oscillatory, it is expected for it to exhibit harmonic characteristics. Focus will be on identifying key aerodynamic behaviour as a result of pitch oscillations between the wing wake and tail. This addresses a gap in the literature where aircraft wing wakes are investigated only under static conditions accomplished by Waldmann et al. [52, 102], with those under dynamic conditions performed by Thompson et al. [63], Frink [62], and outlined by Hall et al. [104], where more focus on the wing wake region is desired (See Table 1.3).

The successful completion of the above aims and objectives constitutes the overall contribution of the research.

1.6.2 Original Research Contributions

A novel insight on the effects of wake encounters on downstream aerodynamics by studying tandem flow configurations under a computational framework for both static and dynamic conditions will be accomplished. Under static conditions, this is achieved with a high-fidelity DES technique. The validity of the results supported with experimental and numerical data from existing literature ensures that a resolution capable of capturing wake physics up to its second-moment statistics (fluctuations) and turbulent characteristics is imposed.

- The vortex shedding and wake statistics collected expands the library of available benchmark data for such flows. The results also evaluate and develop the extent of numerical treatment for turbulence through an auto-correlation function of wake velocity probe data.

- By applying this model to study its effects on a downstream wing-section, results should reveal that the response exhibited by this wing-section is indeed harmonic in nature, and is correlated to the wake shed upstream. A proposition can then be made to predict this unsteady response empirically as a function of its reduced frequency through the Sear's and Theodorsen's functions.

For the dynamic case, the computational framework surrounding the DES turbulence model can be expanded to include overset grid methods for mesh movement. This enables forced harmonic motion to be introduced into the tandem system, providing insights onto wing wake-tail dynamics rarely discussed in the landscape of forced harmonic pitching simulations. The pitching motion will induce high angle-of-attack dynamics for stall and flow separation, inducing wake features that can only be captured through DES (or higher fidelity methods).

- Results should successfully capture the pitch hysteresis including stall dynamics for the wings. This is identifiable through characteristic LEV/TEVs that are observed to interact with the tail. Tail aerodynamics will then be shown to correlate to the wing wake-induced local flow fields, which will be evident with instantaneous tail surface pressure distributions.

- Identifying the distinct features in the total response of the system can be attributed to wing stall with its flow separated wake effects at the tail. The wake-tail effects will be observed to occur after a phase lag due to its convection across the tail moment arm. Breaking down of the results individually and evaluating it with the total response of the system should reveal that wing wake-tail effects are evident in the total system.

- The wing and tail lift response can both be empirically approximated as a sinusoidal function excluding wake effects at the tail. This develops a postulate that tail loads inclusive of wake effects can be predicted with an additional factor to account for the gust introduced by the wing wake.

1.6.3 Outline of Thesis Chapters

This thesis constitutes a total of six chapters, with the literature review and methodology highlighting the various principles behind the research presented in the first two. The subsequent three chapters present findings that address the objectives, while the final chapter concludes with recommendations for future work.

1. Chapter 1 reviews the existing literature, providing an overview of wakes and their significance. This review focuses on wing wakes and their interaction with the horizontal stabilizer located downstream, especially for those experiencing dynamic conditions. The existing work surveyed also highlights the relevant computational methodologies involved,

such as solution strategies for modelling of unsteady flows, and the key turbulence modelling considerations for RANS and DES, among other methods. This gives insights and recommendations for the best practices to approach the discussed problems. The chapter then concludes by highlighting the motivation and original contribution for the current work with its aims and objectives.

2. Chapter 2 presents the underlying governing equations and their constitutional relations for fluids. While wakes are the underlying flow phenomenon in question, the development of the DDES turbulence modelling approach for its capture together with the various numerical methods for the spatial and temporal schemes involved in the discretisation of governing equations are highlighted. Some of the tools and resources responsible for implementing and executing the chosen methods are also outlined here. This includes the open-sourced solver, OpenFOAM, and other pre- and post-processing utilities for accomplishing the targeted aims and objectives.

3. Chapter 3 presents results that are based on the validation and verification processes outlined so far. The purpose of this chapter affirms that the use of the chosen tools and resources for the wake capture are valid. This is conducted with a flow over a bluff-body geometry, where surface-force integrals and the first and second moment statistics in the wake are evaluated with other existing results from the literature surveyed. This ensures that the wake data collected is physically meaningful and the methodology is suitable for the context of research. It also contributes by expanding the available pool of computational results for benchmarking.

4. Chapter 4 expands on the validated bluff-body wake results to investigate its impact on a downstream (NACA0012) wing-section. Results from this chapter advances the understanding of a wake encounter under *static* conditions, where the geometries are uncoupled with no physical relation to each other. The results reveal massive flow separation as a consequence of the highly unsteady wake encounter, where the response by the wing-section depicts local flow fields and pressure contours akin to large heave dynamics. In addition, an empirical approximation is proposed for the resulting harmonic response as a function its reduced frequency. This explores the use of the Sear's and Theodorsen's function for approximating the unsteady loads involved, by treating the wake encounter as a harmonic gust or a relative pitch/heave by the wing-section.

5. Chapter 5 compounds the DDES turbulence modelling method that has been successfully applied so far with an overset grid. The overset method enables *dynamic* grid motion, which allows the physical motion of a forced harmonic pitch for a wing-tail tandem configuration. In contrast to Chapter 4, the rotational motion of these bodies is now coupled, with a centre about a point on the wing chord. The amplitude of dynamic motion is also designed to induce flow separation over the wings, which creates identifiable

LEV/TEVs. Unsteady loads by the moving wing and tail is empirically approximated with the Theodorsen's function but with distinct features caused by flow separation and wake interaction by the tail which are highlighted. The synthesis of force contribution by this entire system also portrays these features, which can be correlated and attributed to the individual components of wing stall and wake interaction at the tail.

6. Chapter 6 finally concludes the theme of the thesis and highlights key contributions. It also recommends any potential future work, like the further application and expansion of the numerical framework accomplished in Chapters 3 and 5 to the prediction of downstream aerodynamic loads due to wake encounter.

Chapter 2

Computational Methodology & Approach

2.1 Introduction

The following chapter details the computational framework and approach taken that serves as a foundation to the results in the coming chapters. These are the appropriate governing equations and constitutional relationships for the medium of Newtonian fluids. As viscosity and turbulent flow is a major theme for wakes, the characterisation of turbulence is discussed, which will be used to introduce the formulations and principles behind RANS, LES, and finally the DES turbulence modelling technique that is applied for wake capture. The discretisation of the governing equations through the Finite Volume Method (FVM) is then briefly described along with the various numerical schemes and processes that are used to transform the partial differential equations into a corresponding system of algebraic equations. Finally, an overview of the tools and resources that are utilised to implement and execute the work is outlined.

2.2 Governing Equations & Relations for Newtonian Fluids

The governing equations of continuum mechanics can be written in the form of conservation laws. For a fluid flow in three dimensions, this can be described by a system of five partial differential equations—one for conservation of mass, three for momentum, and one for energy. Based on this, the numerical procedure adopted hereafter assumes that the flows are incompressible and isothermal. Therefore, the incompressible Navier-Stokes equations in conservation form are given by:

$$\frac{\partial u_i}{\partial x_i} = 0, \tag{2.1}$$

$$\frac{\partial u_i}{\partial t} + u_j \frac{\partial u_i}{\partial x_j} = -\frac{1}{\rho}\frac{\partial p}{\partial x_i} + \nu \frac{\partial^2 u_i}{\partial x_j \partial x_j}. \tag{2.2}$$

where the last term in Equation 2.2 contains the viscous stress tensor, which for a Newtonian fluid, is proportional to the strain-rate tensor through:

$$\tau_{ij} = 2\mu S_{ij}, \tag{2.3}$$

with the viscous strain-rate tensor,

$$S_{ij} = \frac{1}{2}\left(\frac{\partial u_i}{\partial x_j} + \frac{\partial u_j}{\partial x_i}\right). \tag{2.4}$$

As an incompressible assumption is taken, the scalar properties in the governing equations are made kinematic with the MSL reference density of air at $1.225\,\mathrm{kg\,m^{-3}}$, and a dynamic viscosity of $1.789 \times 10^{-5}\,\mathrm{Pa\,s}$. Therefore, flow conditions are based on Reynolds numbers that are velocity driven, determined by Lyn et al. [68] and Lefebvre and Jones [84] for the static cases, and Thompson et al. [63] for the dynamic case, which describe the fluid flow conditions considered in this thesis. This allows a direct evaluation of the solver performance and its results with existing numerical and experimental cases in the literature.

2.2.1 Characterising Turbulence

Most fluid flows of engineering importance that occur above a certain Reynolds number are turbulent. At higher Reynolds numbers, flows become dominant with inertial effects and the viscosity of the flow can no longer maintain laminar behaviour. This leads to instabilities in the flow, making it irregular and 3-dimensional as this transition from laminar to turbulence occurs. Turbulence is described as a state of continuous instability, characterised by irregularity of the properties in the flow, with an increase in diffusivity and energy dissipation. Turbulent flows are always 3-dimensional and exhibit strong time dependence (fluctuations) regardless if the initial and boundary conditions are constant [117].

Turbulent flow scales range from the smallest turbulent eddies to larger features with size in order of magnitude as the geometry. The larger scales act on the smaller eddies through kinetic energy where they are passed from the larger to smaller scales progressively. This is termed as the energy cascade. The flows to be considered in this work are considered large, where inertial forces dominate in the order of $Re > 1 \times 10^4$. At the smallest scales, viscous effects begin to dominate and the energy is dissipated. The local characteristic Reynolds numbers at this scale are in the order of unity, such that the inertial and viscous forces are of equal strength [1]. The energy associated to this cascade that occurs through turbulent motion is therefore known as turbulent kinetic energy, k, and the rate at which this energy is transferred is the rate of dissipation, where:

$$\varepsilon = -\frac{dk}{dt}. \tag{2.5}$$

This rate is determined by the largest eddies and the range of characteristic length scales from the

largest (l_o) to the smallest (η) eddies depends on the Reynolds number (based on the turbulent characteristics) of the flow:

$$\frac{\eta}{l_o} \sim Re_T^{-3/4}. \tag{2.6}$$

In a similar fashion, the respective velocity and time scales also have Reynolds number dependence as:

$$\frac{u_\eta}{u_o} \sim Re_T^{-1/4}, \qquad \frac{\tau_\eta}{\tau_o} \sim Re_T^{-1/2}. \tag{2.7}$$

Based on these it is clear that the Reynolds number of the flow increases with the range of scales existent in the flow and the smallest and largest scales differ in orders of magnitude apart. The smallest spatial and temporal scales, which are known as the Kolmogorov micro-scales are determined based on the rate of dissipation and kinematic viscosity, ν, where:

$$\eta = (\nu^3/\varepsilon)^{1/4}, \qquad u_\eta = (\varepsilon\nu)^{1/4}, \qquad \tau_\eta = (\nu/\varepsilon)^{1/2}. \tag{2.8}$$

Therefore the Kolmogorov micro-scales are in the order of:

$$Re = \frac{\eta u_\eta}{\nu} = 1. \tag{2.9}$$

In contrast, the largest scales are in the same order of magnitude as the characteristic length of the flow, such as vortex shedding and boundary layer thickness. These hypotheses [118] claim that the small scales are independent of the flow geometry and statistically isotropic whereas anisotropic turbulence only exist for the larger length scales. This leads to distinct regions in the energy cascade where the largest scales in the flow are therefore known as the energy containing range and the isotropic turbulence range is known as the dissipative or viscous range. The remainder of which, that lies in between these scales, is called the inertial sub-range. Scales in the inertial sub-range can be defined by the rate of dissipation, ε alone.

As the time and length scales are generally represented by frequencies and wavelengths, this entire energy spectrum can be represented by turbulent kinetic energy and wave numbers where:

$$k = \int^{\infty} E(\kappa)\, d\kappa. \tag{2.10}$$

where $E(\kappa)$ is the energy spectral density taken as a Fourier analysis of the turbulent kinetic energy, k. From here, the energy spectrum $E(\kappa)$ can be taken as a relation to k, where:

$$E(\kappa) = C_K \varepsilon^{2/3} \kappa^{-5/3}. \tag{2.11}$$

As such, the decay of the function $E(\kappa)$ with respect to the wave number, κ can be defined by a $-5/3$ slope which also can be used as a measure if the cascade is in equilibrium.

To solve for all flow length scales, the governing equations have to be numerically integrated over the entire range of turbulent scales. This is known as a Direct Numerical Solution

(DNS) [119]. To achieve this, grid and time-step sizes require prohibitive levels of computational resources as the smallest scales of motion for turbulent flows may be in the order of 0.1 to 0.01 mm with frequencies around 10 kHz. Such spatial and temporal resolution are unattainable for engineering applications [1] and as such, a wide range of simulation techniques for turbulent flows exist [120]. A brief overview of the RANS and DES (which is a hybrid RANS/LES method) techniques used in this thesis will be described.

2.2.2 Reynolds-Averaging

A statistical and economical approach to the modelling of turbulent flows separates the local value of a variable into its mean and fluctuation parts. This process is known as Reynolds decomposition. Reynolds-Averaging the Navier-Stokes equations first takes the decomposition of an instantaneous variable, such as a velocity signal, decomposed into its mean (U_i) and instantaneous fluctuating parts (u_i') as illustrated in Figure 2.1. This decomposition assumes the form:

$$u_i = U_i + u_i'. \tag{2.12}$$

For statistically stationary turbulence, the mean flow does not change with time and therefore the time-average is calculated from the instantaneous variable by:

$$\overline{u_i} = \lim_{T\to\infty} \frac{1}{T} \int_t^{t+T} u_i \, dt. \tag{2.13}$$

Limiting the time-history, T, towards a sufficiently large instance compared to the period of random fluctuations ensures that the statistical average is sufficiently sampled to be insensitive to the total amount of time samples taken. A result of averaging the instantaneous component decomposes it to the time-average of the mean flow, U_i and is equivalent to the mean where $U_i = \langle U_i \rangle$, and the fluctuations therefore become zero, $u_i' = 0$. However, wakes are physically unsteady where even the modelling of the mean flow in the system will have time dependence. Applying this procedure on all the flow variables and substituted into the incompressible Navier-Stokes equations provides what is known as the Reynolds-Averaged Navier-Stokes (RANS) equation:

$$\rho \frac{\partial \overline{U}_i}{\partial t} + \rho \frac{\partial (\overline{U_j U_j} + \overline{u_i u_j})}{\partial x_j} = -\frac{\partial \overline{P}}{\partial x_i} + \frac{\partial \tau_{ij}}{\partial x_j}. \tag{2.14}$$

This process produces a remaining term on the right known as the Reynolds stress tensor as a result of Reynolds-Averaging, compromising of three normal and six symmetrical shear stresses. In order to close this systems of equations, a turbulence modelling technique is required, where the Reynolds stress tensor is expressed in terms of the known quantities. This approach describes a relationship between the Reynolds stress tensor and the mean velocity gradient, known as the

Boussinesq approximation [121] for eddy-viscosity:

$$\tau_{ij} = -\rho\overline{u_i' u_j'} = 2\mu_t \overline{S}_{ij} - \frac{2}{3}\rho k \delta_{ij}, \tag{2.15}$$

where δ_{ij} is the Kronecker delta function where:

$$\delta_{ij} = \begin{cases} 1, & i = j \\ 0, & i \neq j \end{cases} \tag{2.16}$$

and the specific turbulent kinetic energy of the fluctuations is defined as:

$$k = \frac{1}{2}\overline{u_i u_i}. \tag{2.17}$$

This leaves the turbulent viscosity for closure of the equations. There are many different formulations to approach this problem of modelling eddy viscosity [49]. In the present work, two existing eddy-viscosity models are considered, which have been thoroughly tested and are highly regarded [49].

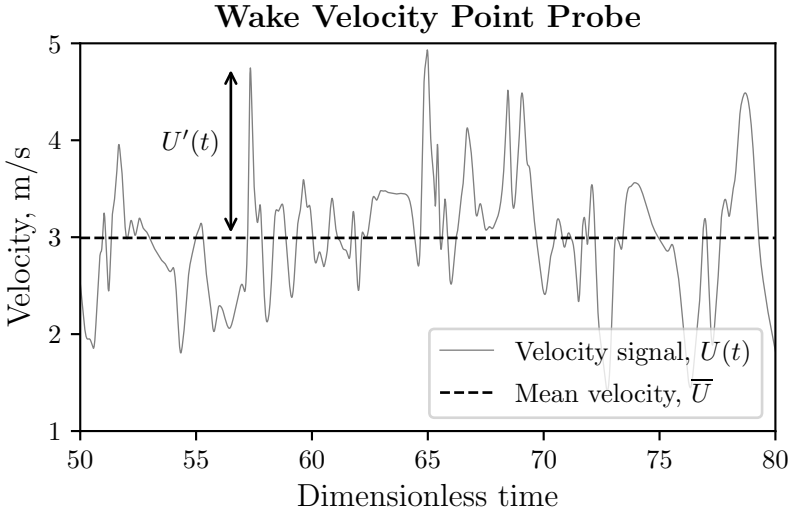

Figure 2.1: Reynolds decomposition of a velocity signal from wake results in a later chapter into its mean and instantaneous parts.

The Spalart-Allmaras One Equation Model

Many popular approaches exist for evaluating the eddy viscosity term, ν_t, with some of the most popular being the k-ε two-equation models and its variants [46, 122–124], the k-ω two-equation model [125, 126] and its variants such as the SST [47] which is blend of the two. However, the most popular turbulence modelling equation developed for aerodynamic applications is the

Table 2.1: Default model coefficients for the Spalart-Allmaras turbulence model.

$\sigma_{\nu t}$	C_{b1}	C_{b2}	C_{w1}	C_{w2}	C_{w3}	$C_{\upsilon 1}$	C_s
2/3	0.1355	0.622	$\frac{C_{b1}}{k^2}+\frac{1+C_{b2}}{\sigma_{\nu t}}$	0.3	2	7.1	0.3

one-equation Spalart Allmaras (SA) turbulence modelling equation [127]. It is a popular choice for benchmarking, including drag prediction [128], and solver validation [49].

The SA model is also an eddy-viscosity-based turbulence model but solves for a single equation for a working variable $\tilde{\nu}$, which is related to the turbulent eddy-viscosity through:

$$\nu_t = \tilde{\nu} f_{\upsilon 1}, \tag{2.18}$$

with the function $f_{\upsilon 1}$ given by:

$$f_{\upsilon 1} = \frac{X^3}{X^3 + C_{\upsilon 1}^3}. \tag{2.19}$$

The transport equation is given by :

$$\underbrace{\frac{\partial \tilde{\nu}}{\partial t} + \frac{\partial (\tilde{\nu} u_j)}{\partial x_j}}_{\text{Convection}} = \underbrace{c_{b1}\tilde{\nu}\tilde{S}}_{\text{Production}} - \underbrace{c_{w1} f_w \left(\frac{\tilde{\nu}}{d}\right)^2}_{\text{Destruction}} + \underbrace{\frac{1}{\sigma}\frac{\partial}{\partial x_k}\left[(\nu+\tilde{\nu})\frac{\tilde{\nu}}{\partial x_k}\right] + \frac{c_{b2}}{\sigma}\frac{\partial \tilde{\nu}}{\partial x_k}\frac{\partial \tilde{\nu}}{\partial x_k}}_{\text{Diffusion}}, \tag{2.20}$$

implemented *without* the f_{t2} trip term [129], with the default model coefficients as given in Table 2.1. The turbulent eddy-viscosity is then calculated using the transport equation, and the Boussinesq approximation is then used to determine the Reynolds stresses to provide closure to the Navier-Stokes equations.

Although RANS methods may be an economical present-day approach to modelling of turbulent flows, the process of Reynolds-Averaging yields the non-linear Reynolds stress tensor that arises due to convective acceleration from the governing equations. This effect on the behaviour on the mean flow acts as a viscous-like stress term, which is a non-physical representation of convective acceleration.

The k-ω SST Model

The two-equation k-ω SST model is used to predict the transport of turbulent kinetic energy and specific dissipation rate. The motivation behind the development of this model was driven by the need for accurate prediction of flows with strong adverse pressure gradients and separation. It is based on a zonal formulation that ensures a proper selection of k-ω and k-ε zones without user interaction [130]. This introduces an additional computation where the distance from the wall is required in the function. This allows the model to blend between the standard k-ω and k-ε models [46, 48].

Table 2.2: Default model coefficients for the k-ω SST turbulence model.

β^*	α_1	β_1	σ_{k1}	$\sigma_{\omega1}$	α_2	β_2	σ_{k2}	$\sigma_{\omega2}$
0.09	5/9	3/40	0.85	0.5	0.44	0.0828	1	0.856

In contrast to the SA one-equation model, the additional transport equation in this two-equation model obtains turbulence intensity, which addresses the turbulent kinetic energy term in the Boussinesq hypothesis (Equation 2.15). The transport equations for turbulence kinetic energy and specific dissipation rate are given by:

$$\frac{\partial k}{\partial t} + u_j \frac{\partial k}{\partial x_j} = P_k - \beta^* k\omega + \frac{\partial}{x_j}\left[(\nu + \sigma_k \nu_t)\frac{\partial k}{\partial x_j}\right], \tag{2.21}$$

$$\frac{\partial \omega}{\partial t} + u_j \frac{\partial \omega}{\partial x_j} = \alpha S^2 - \beta \omega^2 + \frac{\partial}{\partial x_j}\left[(\nu + \sigma_\omega \nu_t)\frac{\partial \omega}{\partial x_j}\right] + 2(1 - F_1)\sigma_{\omega^2}\frac{1}{\omega}\frac{\partial k}{\partial x_i}\frac{\partial \omega}{\partial x_i}, \tag{2.22}$$

where F_1 is the blending function that distinguishes the definition between the boundary layer and the freestream. This is defined by:

$$F_1 = \tanh\left\{\left\{\min\left[\max\left(\frac{\sqrt{k}}{\beta^*\omega y}, \frac{500\nu}{y^2\omega}\right), \frac{4\rho\sigma_{\omega2}k}{CD_{k\omega}y^2}\right]\right\}^4\right\}, \tag{2.23}$$

where:

$$CD_{k\omega} = \max\left(2\rho\sigma_{\omega2}\frac{1}{\omega}\frac{\partial k}{\partial x_i}\frac{\partial \omega}{\partial x_i}, 10^{-10}\right), \tag{2.24}$$

with y as the distance to the nearest wall boundary condition. Based on this, $F_1 = 0$ away from the surface which provides the k-ε model and $F_1 = 1$ within the boundary layer. The above formulation is now related to back to close for eddy-viscosity through:

$$\nu_t = \frac{a_1 k}{\max(a_1\omega, SF_2)}, \tag{2.25}$$

where:

$$F_2 = \tanh\left[\left[\max\left(\frac{2\sqrt{k}}{\beta^*\omega y}, \frac{500\nu}{y^2\omega}\right)\right]^2\right], \tag{2.26}$$

and S here is the invariant measure of strain rate and F_2 is the second blending function. In the current usage, all model constants and further sub-functions are taken as recommended by the source [130]. Table 2.2 summarises the constants used for the present formulation.

2.2.3 Large Eddy Simulations

The second approach (DES, Section 2.2.4) is a hybrid method that is partly based on RANS and LES, where a spatial filter is used. Larger scale structures are resolved on a given mesh

defined by the sub-grid scales, where features in order smaller than the sub-grid is modelled. The rationale behind this principle lies in the fact that the small scales of turbulence are more homogeneous and isotropic and therefore easier to model. As the mesh gets finer, the number of scales that require modelling becomes smaller, thus approaching Direct Numerical Simulation. Examples of LES-based approaches can be found in Deardorfi [131], Givi [132], and Moin and Kim [133]. For LES, the flow variables are split into two parts, analogous to RANS methods. But instead of decomposition of the flow variable into a mean and fluctuating part, LES applies a spatial filtering (denoted with a circumflex) distinguishing a resolvable and subgrid-scale (*sgs*) component.

$$u_i = \hat{u}_i + u_i^{sgs}. \tag{2.27}$$

These two components of the subgrid-scale decomposition are separated through filtering techniques. This is applied through the maximum cell dimensions of the given grid known as the filter width where:

$$\Delta = max(\Delta_x, \Delta_y, \Delta_z). \tag{2.28}$$

The filtering function takes the form of a convolution integral:

$$\overline{u_i}(x) = \int G(x-x')u(x')\,dx', \tag{2.29}$$

where G is the filter function, which for a computational grid takes the form of a box filter where:

$$G(x) = \begin{cases} 1/\Delta, & |x| \leq \Delta/2 \\ 0, & \text{Otherwise.} \end{cases} \tag{2.30}$$

Based on this, the Navier-Stokes equations can be obtained for the filtered component of the flow, taking the form:

$$\frac{\partial \hat{\rho}\hat{u}_i}{\partial t} + \frac{\partial \hat{\rho}\widehat{u_i u_j}}{\partial x_j} = -\frac{\partial \hat{P}}{\partial x_i} + \frac{\partial \tau_{ij}}{\partial x_j}. \tag{2.31}$$

In a similar fashion to Reynolds-Averaging, non-linear convective terms are present, and the difference between the filtered product and product of two filtered variables is the subgrid-scale stress tensor, τ_{ij}^{sgs}:

$$\widehat{u_i u_j} = \hat{u}_i \hat{u}_j + \tau_{ij}^{sgs}. \tag{2.32}$$

These subgrid-scale stresses describe the resolved and subgrid scale turbulent interactions [134] and as such can be decomposed into its anisotropic and isotropic parts:

$$\tau_{ij}^{sgs} = a_{ij}^{sgs} + \frac{2}{3}k_r\delta_{ij}, \tag{2.33}$$

where the residual turbulent kinetic energy is given by:

$$k_r = \frac{1}{2}\tau_{ij}^{sgs}. \tag{2.34}$$

As such the filtered Navier-Stokes equations now assume the form:

$$\frac{\partial \hat{\rho}\hat{u}_i}{\partial t} + \frac{\partial \hat{\rho}\hat{u}_i\hat{u}_j}{\partial x_j} = -\frac{\partial \hat{P}}{\partial x_i} + \frac{\partial}{\partial x_j}(\tau_{ij} + \tau_{ij}^{sgs}). \tag{2.35}$$

Analogous to RANS formulations, the Smagorinsky method is the simplest and most widely used approach for subgrid scale modelling. Here, an anisotropic stress tensor is introduced with an eddy viscosity associated to this relationship, called the Smagorinsky eddy viscosity, μ^{sgs} where:

$$a_{ij}^{sgs} = -2\mu^{sgs}\hat{S_{ij}}, \tag{2.36}$$

and the Smagorinsky eddy viscosity is taken as a scalar quantity where:

$$\mu^{sgs} = \hat{\rho}(C_S\Delta)^2\sqrt{\hat{S_{ij}}\hat{S_{ij}}}, \tag{2.37}$$

with C_S as the Smagorinsky constant taken as 0.18. Finally with these, the relation for the subgrid-scale stress tensor can be defined:

$$\tau_{ij}^{sgs} = 2\mu^{sgs}\hat{S_{ij}} - \frac{2}{3}\hat{\rho}k_r\delta_{ij}. \tag{2.38}$$

This formulation therefore suggests that the energy contained in the subgrid-scales is a much smaller proportion if the total flow energy than the RANS turbulent energy, meaning that only the smallest, isotropic scales need to be modelled [119]. However, the limitations of LES exist towards the near-wall regions. Approaching the wall, turbulent length scales decrease to that of the same order of the boundary layer thickness. To prevent non-physical modelling at such small length scales close to the walls, computational requirements for grid refinement in these regions have to be inflated to prohibitive (DNS) levels.

2.2.4 Detached Eddy Simulation

While the LES formulation is proposed as a means to overcome the prohibitive costs of DNS, the challenge of turbulent length scales being in the order of the boundary layer thickness near the walls still exists. To alleviate these requirements, a hybrid RANS/LES approach was developed by Spalart et al. [57,82,83]. This approach compromises by having RANS modelling techniques applied at the boundary layer region with LES for larger eddies in the remainder of the domain.

The DES formulation lies conceptually between the relationship of the production and de-

struction terms in the SA model (Equation 2.20). Their balancing give the relationship,

$$\tilde{\nu} \propto \tilde{S} d^2, \tag{2.39}$$

with d as the distance to the wall. Comparing this with Equation 2.37 for the Smagorinsky eddy-viscosity shows that a similar proportionality exists between the two terms, with the exception of a grid spacing, Δ. This is such that,

$$\nu^{sgs} \propto \hat{S} \Delta^2. \tag{2.40}$$

It is suggested that if d is replaced with Δ in the wall destruction term (Equation 2.39 and 2.20), the SA model will now exhibit Smagorinsky LES model-like behaviour. This hybrid formulation allows a RANS-like behaviour and a Smagorinsky-like LES model that switches depending on the proportions between the distance to the wall and local grid spacing. Therefore, this new hybrid length scale is replaced by,

$$\tilde{d} \equiv \min(d, C_{DES}\Delta). \tag{2.41}$$

However, the definition of the hybrid length scale used here is based on a further develoepd variant known as the Delayed-DES (DDES) model which provides an adjustment to the definition of the hybrid length scale that . This improved variant narrows the region of uncertainty between RANS and LES modes and has been demonstrated to perform more accurately for massively separated flows [83]. The hybrid distance is therefore:

$$\tilde{d} \equiv d - f_d \max(0, d - C_{DES}\Delta), \tag{2.42}$$

with:

$$f_d \equiv 1 - \tanh([8r_d]^3), \qquad r_d \equiv \frac{\nu_t + \nu}{\sqrt{U_{ij}U_{ij}}k^2 d^2}, \tag{2.43}$$

as $f_d = 0$ yields RANS and LES modes for the hybrid length scale, with the constant $C_{DES} = 0.65$ calibrated for homogeneous turbulence [135]. The quantity r_d is a marker of the wall region equal to 1 in a log layer and 0 in a free shear flow. Based on this formulation, the model is now restricted to RANS near to the walls where $D < \Delta$, and has a subgrid-scale model for $d > \Delta$. This is useful for wake capture as it allows LES levels of resolution in these regions, while maintaining a reasonable compromise on wall grid requirements. Nevertheless, the grid should still be adequately refined in wake regions such that the majority of the flow length scales are resolved.

2.3 Numerical Solver: The OpenFOAM CFD Toolkit

OpenFOAM (Open-source Field Operation and Manipulation) is a free and open-sourced C++ toolkit of customisable numerical solvers, with pre- and post-processing utilities for solving computational fluid dynamics problems [136, 137]. It is shipped with approximately 250 (and growing) pre-built applications that fall into two categories: *solvers*, that are each designed to solve a specific problem in fluid (or continuum) mechanics; and *utilities*, that are designed to perform tasks that involve data manipulation [138]. The structural layout of OpenFOAM is illustrated in Figure 2.2.

There are several advtangaes to OpenFOAM over other CFD software, and is increasingly gaining popularity in various communities [139, 140]. It is free, governed under the GNU General Public Licence [141], and is independent of the number of users, jobs, and processing cores. It uses a partial differential equation-friendly syntax and is highly customisable through plain text input files [142]. Built-in utilities for mesh conversion are also available that convert and generate meshes from popular third-party meshing tools such as ANSYS (`.msh`), I-DEAS (`.ans`), Star-CD (`STAR-CD/PROSTAR`), GAMBIT (`.neu`), and CFX (`.geo`) extensions.

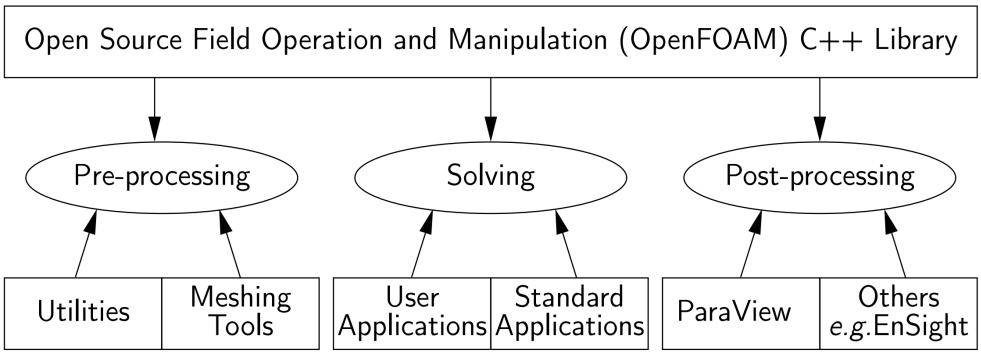

Figure 2.2: Overview of the OpenFOAM structure [138].

Parallel processing utilities are also supported by public domain OpenMPI [143] of the standard Message Passing Interface [144] by default. This allows the case decomposition, reconstruction, and redistribution to perform parallel computations. This is known to scale well up to approximately 1000 CPU cores for both simple tutorial and complex industrial cases, with suitable hardware [145]. The resulting data output can be post-processed with other complementary open-sourced software scientific data visualisation software (Paraview, Mayavi), or even converted to be compatible with proprietary kits such as ANSYS EnSight and Tecplot. Raw data output are in the form of `.dat` and `.csv` extensions.

OpenFOAM uses the FVM that is a co-located methodology on an unstructured polyhedral grid with arbitrary grid elements. The primitive variables are cell-centred at the control volume centroids. A variety of available interpolation, discretisation, and matrix solution schemes can be selected at runtime and those that are used will be briefly covered in the coming sections.

2.3.1 Finite Volume Method

The FVM is developed by applying the integral form of the Navier-Stokes equations to a control volume in the computational domain. The transport of variable control volumes are governed by the standard form of the transport equation. For a general scalar property, ϕ, this is:

$$\underbrace{\frac{\partial \rho\phi}{\partial t}}_{\text{Temporal derivative}} + \underbrace{\nabla\cdot(\rho\mathbf{U}\phi)}_{\text{Convection term}} - \underbrace{\nabla\cdot(\rho\Gamma_\phi\nabla\phi)}_{\text{Diffusion term}} = \underbrace{S_\phi(\phi)}_{\text{Source term}} . \tag{2.44}$$

This equation is second-order due to the second derivative in the diffusion term. Discretisation of the transport equation is treated individually, by applying the FVM on this equation for the control volume, V_P around the its point, P, (Figure 2.3) gives the integral form of the transport equation:

$$\int_t^{t+\Delta t}\left[\frac{\partial}{\partial t}\int_{V_P}\rho\phi\,dV + \int_{V_P}\nabla\cdot(\rho\mathbf{U}\phi)\,dV - \int_{V_P}\nabla\cdot(\rho\Gamma_\phi\nabla\phi)\,dV\right]dt = \int_t^{t+\Delta t}\left(\int_{V_P}S_\phi(\phi)\,dV\right)dt. \tag{2.45}$$

The coming sections will briefly highlight the key points in the discretisation approach for the terms in the above equation. Refer to Versteeg [1], Patankar [146], Hirsch [147], and Jasak [148], for more complete and detailed derivations and analyses.

2.3.2 Discretisation Schemes

This section discusses the spatial numerical schemes that are used for the solutions in the coming chapters. The discretisation of spatial terms is based on the Gauss' theorem with it in second-order accurate discretised form:

$$(\nabla\cdot\mathbf{a})V_P = \sum_f \mathbf{S}\cdot\mathbf{a}_f. \tag{2.46}$$

Here, the subscript f implies that the general vector property, $\mathbf{a}$, is in the middle of the face with $\mathbf{S}$ as the outward pointing face area vector, and V_P is the cell volume. This has to account for owner-neighbour cell relationship summed over the faces which therefore gives:

$$\sum_f \mathbf{S}\cdot\mathbf{a}_f = \sum_{owner}\mathbf{S}\cdot\mathbf{a}_f - \sum_{neighbour}\mathbf{S}\cdot\mathbf{a}_f. \tag{2.47}$$

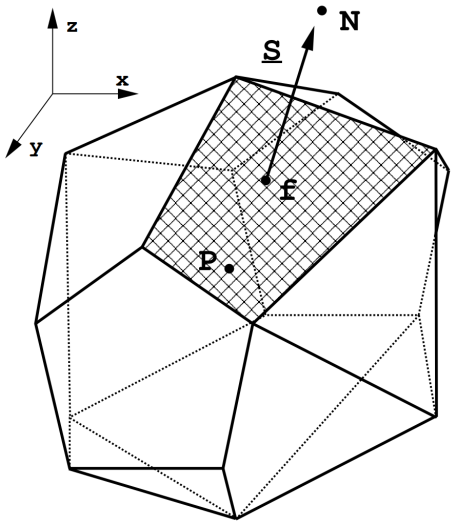

Figure 2.3: A control volume, illustrated by Jasak [148].

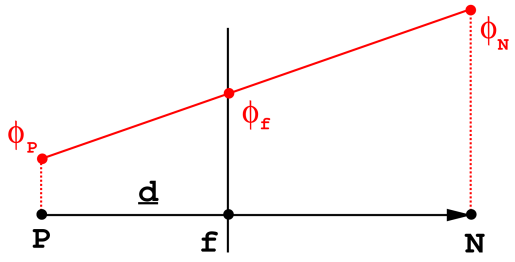

Figure 2.4: Face interpolation, illustrated by Jasak [148].

Spatial Schemes

The discretisation of the convection term is done by (using Eqn 2.46):

$$\begin{aligned}\int_{V_P} \nabla \cdot (\rho \mathbf{U} \phi)\, dV &= \sum_f \mathbf{S} \cdot (\rho \mathbf{U} \phi)_f, \\ &= \sum_f \mathbf{S} \cdot (\rho \mathbf{U})_f \phi_f, \\ &= \sum_f F \phi_f,\end{aligned} \tag{2.48}$$

where $F = \mathbf{S} \cdot (\rho \mathbf{U})_f$, which is the mass flux through the particular face. A Blended Central-Upwind differencing scheme is used for the convection terms in the solutions. This preserves boundedness and accuracy, that is result of a linear combination between the two schemes [149]. Central Differencing assumes a linear variation of ϕ between P and N in Figure 2.4. The face values here are calculated based on:

$$\phi_f = f_x \phi_P + (1 - f_x)\phi_N, \tag{2.49}$$

where f_x is the interpolation factor taken as the ratio of distance between $\overline{fN}$ and $\overline{PN}$:

$$f_x = \frac{\overline{fN}}{\overline{PN}}, \tag{2.50}$$

and has been demonstrated to be second-order accurate on non-uniform meshes [150], but may exhibit non-physical oscillations in convection-dominated problems affecting its boundedness [146, 147]. On the other hand, the Upwind Differencing (UD) scheme determines the face value based on the flow direction:

$$\phi_f = \begin{cases} \phi_f = \phi_P, & F \geq 0 \\ \phi_f = \phi_N, & F < 0. \end{cases} \tag{2.51}$$

With this scheme, boundedness is guaranteed at the expense of accuracy, and therefore UD should not be used exclusively as it can distort the solution beyond acceptable levels of accuracy.

In an attempt to preserve both boundedness and accuracy, the Blended Differencing (BD) scheme is used. This is linear combination of CD (2.49) and UD (Equation 2.51), where the face value is now calculated by:

$$\phi_f = (1 - \gamma)(\phi_f)_{UD} + \gamma(\phi_f)_{CD}, \tag{2.52}$$

where the blending factor, γ, $0 \leq \gamma \leq 1$. A blending factor of 0.75 is used, which as a result of Equation 2.52 gives CD a 75% weight for face values.

Similarly for diffusion, it can be discretised such that:

$$\begin{aligned}\int_{V_P} \nabla \cdot (\rho \Gamma_\phi \nabla \phi)\, dV &= \sum_f \mathbf{S} \cdot (\rho \Gamma_\phi \nabla \phi)_f, \\ &= \sum_f (\rho \Gamma_\phi)_f S \cdot (\nabla \phi)_f.\end{aligned} \tag{2.53}$$

where Γ_ϕ is the diffusivity. Because of non-orthogonality in practical meshes, i.e. the face area vector is not parallel to the vector connecting cell centres, the discretisation of the diffusion terms uses an orthogonal correction approach outlined by Jasak [148].

Temporal Scheme

Using Equations 2.48 and 2.53, the integral form of the scalar transport (Equation 2.45) can be written in its *semi*-discretised form [148]:

$$\begin{aligned}\int_t^{t+\Delta t} \left[\left(\frac{\partial \rho \phi}{\partial t} \right)_P V_P + \sum_f F \phi_f - \sum_f (\rho \Gamma_\phi)_f \mathbf{S} \cdot (\nabla \phi)_f \right] dt \\ = \int_t^{t+\Delta t} (S_u V_P + S_p V_P \phi_P)\, dt.\end{aligned} \tag{2.54}$$

where S_u and S_p are the constant and linear parts of the source term, respectively. The RHS of this equation is the result of the discretisation of the source terms in the transport equation, which is not covered here. The time-marching solutions use what is known as Backward Differencing and is second-order accurate. To achieve this, the Taylor series expansion of ϕ with respect to time around $\phi(t+\Delta t) = \phi^n$ gives:

$$\phi(t) = \phi^o = \phi^n - \frac{\partial \phi}{\partial t}\Delta t + \frac{1}{2}\frac{\partial^2 \phi}{\partial t^2}\Delta t^2 + O(\Delta t^3). \tag{2.55}$$

Knowing this, the temporal derivative in Equation 2.54 can be expressed as:

$$\frac{\partial \phi}{\partial t} = \frac{\phi^n - \phi^o}{\Delta t} + \frac{1}{2}\frac{\partial^2 \phi}{\partial t^2}\Delta t + O(\Delta t^2). \tag{2.56}$$

To maintain second-order accuracy, Backward Differencing considers three time levels. For the second old time level:

$$\phi(t-\Delta t) = \phi^{oo} = \phi^n - 2\frac{\partial \phi}{\partial t}\Delta t + 2\frac{\partial^2 \phi}{\partial t^2}\Delta t^2 + O(\Delta t^3). \tag{2.57}$$

To eliminate the truncation error, the second-order accurate approximation of the temporal derivative for Backward Differencing can be made by combining Equations 2.55 and 2.57 to

give:

$$\frac{\partial \phi}{\partial t} = \frac{\frac{3}{2}\phi^n - 2\phi^o + \frac{1}{2}\phi^{oo}}{\Delta t}. \tag{2.58}$$

This can be substituted into Equation 2.54 together with the other spatial schemes presented above to complete the discretised form of the transport equation. This produces a system of algebraic equations that will be solved for iteratively.

2.3.3 FVM on Moving (Overset) Meshes

This section will briefly introduce moving mesh (overset) implementation for OpenFOAM [151] that is used in Chapter 5 for conducting forced harmonic motion. The overset method is based on multiple grids that are superimposed over each other. In order to achieve this dynamic motion, a suitable technique that allows mesh movement has to be employed. For such a case, the FVM can be extended to moving meshes. The definition of conservation laws will involve a moving volume, represented by a mesh velocity, $\mathbf{u}_s$ accounting for the Space Conservation Law [152]. This is based on the integral form of the governing equation (Equation 2.45) for a *moving* volume, V, bounded by a closed surface, S. The FVM is then modified to include cell volume and mesh motion fluxes:

$$\frac{\partial}{\partial t}\int_V \rho\phi\,\partial V + \oint_S \rho\mathbf{n}\cdot(u-\mathbf{u}_s)\phi\,\partial S - \oint_S \rho\Gamma_\phi\mathbf{n}\cdot\nabla\phi\,\partial S = \int_V s_\phi\,\partial V, \tag{2.59}$$

where $\mathbf{n}$ is the unit normal vector, $\mathbf{u}_s$ is the boundary surface velocity, and s_ϕ as the volumetric source, with the Space Conservation Law defined by [152]:

$$\frac{\partial}{\partial t}\int_V dV - \oint_S \mathbf{n}\cdot\mathbf{u}_s\,\partial S = 0. \tag{2.60}$$

To achieve connectivity between all the grids, the governing partial differential equations on both the background mesh and the overset mesh have to be computed [153]. Within the background domain, the elements that are bounded by the walls of the sub-meshes have to be marked as "holes" to be removed from the computational domain. The boundaries of the overset domain are then responsible for interpolating the transport variables to the background mesh [154]. At each time-step, all cells in the domain are designated as either as a calculated, an interpolation fringe, or an empty type of cell as shown in Figure 2.5 for an example of a three-part overset mesh. This process occurs over a few key steps. Firstly, the empty cells are located in the background grid. These cells are identified and removed from the solution at each time-step. A disadvantage to overset methods is its increase in computation time primarily due to this step of the solution process [155]. Subsequently, cells adjacent to these empty cells are allocated as fringe cells where their boundaries are used for solution interpolation. In addition, cells at the boundary of the sub-meshes are also allocated as fringes. These cells are responsible for interpolating to the background grid. Thirdly, neighbouring cells between the grids are identified

and coupled as interpolation partners, which are also known as donor cells. After these cell types are allocated and identified, the solution interpolation occurs. The quality of the overset simulation is directly impacted by these key steps, which are depending on the interpolation scheme in addition to the quality of the grids [156].

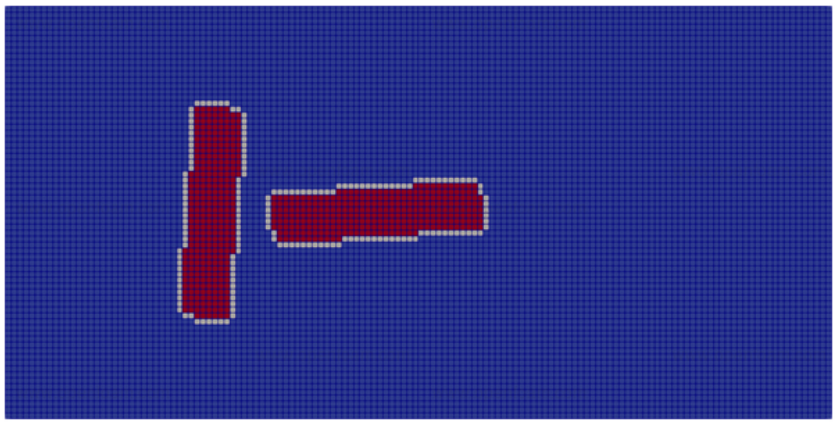

Figure 2.5: Different types of cells in a three-component overset mesh (One background mesh with two rotors geometries). Blue: calculated, white: interpolated, red: empty [157].

Overset Interpolation Scheme

Fringe interpolation uses the Inverse Distance scheme, where the weighted average is based on the distance between the interpolation and donor cell centres. The general form of the interpolation function for obtaining an interpolated value $\tilde{\phi}$ at a given point x is defined with:

$$\tilde{\phi}(x) = \frac{\sum_{i=1}^{N} w_i \phi(x_i)}{\sum_{i=1}^{N} w_i}, \tag{2.61}$$

where the weight corresponding to the i-th donor cell,

$$w_i = \frac{1}{|x - x_i|^P}, \tag{2.62}$$

with x_i as the known point to distance to x. This is summed up over N, which is the total number of points used in the interpolation with P as the power parameter constant [158]. As the weight in Equation 2.62 is inversely proportional to the distance between the interpolated points, the discrete time-step size affects the arbitrary distance between cells at each time-step. Thus, the mesh motion introduces an additional simulation control parameter known as a *mesh* Courant number. Analogous to the *flow* Courant number, this defines the motion of the sub-zone meshes relative to each other. This criteria ensures that an adequately refined time-step size satisfies the desired temporal resolution with regards to mesh movement to support interpolation at the fringes. This has to be considered in addition to the flow field on the static grid. Ideally, the

ratio between the mesh and flow Courant numbers should be maintained at unity throughout the range of motion conducted in the simulation.

2.3.4 Discretisation Procedure for Navier-Stokes

This section briefly describes the discretisation procedure for the Navier-Stokes equations in its incompressible form (Equations 2.1 and 2.2). Two challenges arise from the equations, which are the non-linearity of the momentum equation (Equation 2.2) and the pressure-velocity coupling.

Derivation of the Pressure Equation

For the pressure equation, a *semi*-discretised form of the momentum equation is used [159]:

$$a_P \mathbf{U}_p = \mathbf{H}(\mathbf{U}) - \nabla p. \tag{2.63}$$

This is obtained from the integral form of the momentum equation [159], where a_P and $\mathbf{H}(\mathbf{U})$ are the diagonal and the off-diagonal coefficient matrices, respectively. $\mathbf{H}(\mathbf{U})$ consists of the matrix coefficients for all neighbours that are multiplied by the corresponding velocities and a transient term as shown below. For external flows such as in the coming cases, there are no additional source terms, giving:

$$\mathbf{H}(\mathbf{U}) = -\sum_N a_N \mathbf{U}_N + \frac{\mathbf{U}^o}{\Delta t}, \tag{2.64}$$

where a_N is the matrix coefficient corresponding to the neighbour N.

The continuity equation (Equation 2.1) in its discretised form is:

$$\nabla \cdot = \sum_f \mathbf{S} \cdot \mathbf{U}_f = 0. \tag{2.65}$$

Rearranging Equation 2.63 in terms of $\mathbf{U}$ gives;

$$\mathbf{U}_P = \frac{\mathbf{H}(\mathbf{U})}{a_P} - \frac{1}{a_P} \nabla p. \tag{2.66}$$

This is known as the explicit velocity correction. Velocities on the cell faces are expressed at the interpolate of the above to give:

$$\mathbf{U}_f = \left(\frac{\mathbf{H}(\mathbf{U})}{a_P} \right)_f - \left(\frac{1}{a_P} \right)_f (\nabla p)_f. \tag{2.67}$$

Substituting this into the discretised form of the continuity equation (Equation 2.65) gives the

pressure equation:

$$\begin{aligned} \nabla \cdot \left(\frac{1}{a_P} \nabla p \right) &= \nabla \cdot \left(\frac{\mathbf{H}(\mathbf{U})}{a_P} \right) \\ &= \sum_f \mathbf{S} \cdot \left(\frac{\mathbf{H}(\mathbf{U})}{a_P} \right)_f . \end{aligned} \tag{2.68}$$

Finally, the discretised form of the incompressible Navier-Stokes system is:

$$a_P \mathbf{U}_P = \mathbf{H}(\mathbf{U}) - \sum_f \mathbf{S}(p)_f, \tag{2.69}$$

$$\sum_f \mathbf{S} \cdot \left[\left(\frac{1}{a_P} \right)_f (\nabla p)_f \right] = \sum_f \mathbf{S} \cdot \left(\frac{\mathbf{H}(\mathbf{U})}{a_P} \right)_f . \tag{2.70}$$

Where the face flux F is obtained by rearranging Equation 2.70:

$$F = \mathbf{S} \cdot \mathbf{U}_f = \mathbf{S} \cdot \left[\left(\frac{\mathbf{H}(\mathbf{U})}{a_P} \right)_f - \left(\frac{1}{a_P} \right)_f (\nabla p)_f \right] . \tag{2.71}$$

When the condition imposed by Equation 2.68 is satisfied, the face fluxes are guaranteed to be conservative [148].

2.3.5 Pressure-Velocity Coupling

The discretised forms of the Navier-Stokes equations (Equation 2.69 and 2.70) show a linear inter-dependence between velocity and pressure. A segregated approach is taken for this coupling by solving the system of equations in sequence. These are namely the PISO [160] and SIMPLE [146] methods for modelling of unsteady and steady-state flows, respectively.

The SIMPLE Algorithm

The SIMPLE algorithm is primarily used for solving towards a steady-state solution. However, in the coming chapters, it is primarily used for the solution initialisation of the internal fields before beginning transient cases. It is often observed that this reduces total computation time by allowing a theoretical flow development period with a steady-state solution of the internal fields. With SIMPLE, the approximation of the velocity field is obtained by solving the momentum equation. The pressure gradient term is calculated using the pressure distribution from the previous iteration or an initial guess, which in most cases is initiated with a uniform field. The solutions are under-relaxed in an implicit manner using an under-relaxation factor. The original

system of equations for every control volume in the system is given by [148]:

$$a_P \phi_P^n + \sum_N a_N \phi_N^n = R_P. \tag{2.72}$$

where R_P is the right hand side of the algebraic equation. Because of the lack of the temporal derivative in steady-state calculations, the diagonal dominance needs to be numerically enhanced through under-relaxation on both LHS and RHS of the equation:

$$a_P \phi_P^n + \frac{1-\alpha}{\alpha} a_P \phi_P^n + \sum_N a_N \phi_N^n = R_P + \frac{1-\alpha}{\alpha} a_P \phi_P^o. \tag{2.73}$$

Here, $0 < \alpha \leq 1$ is the under-relaxation factor. The recommended values are $\alpha_p = 0.2$ for pressure and $\alpha_U = 0.8$ for momentum, respectively [149]. The pressure equation is then formulated and solved to obtain the new pressure distribution. With this pressure, a new set of conservative fluxes are gotten with Equation 2.71.

$$p^{new} = p^{old} + \alpha_p (p^p - p^{old}). \tag{2.74}$$

The approach to using the SIMPLE algorithm [146] for steady-state, incompressible and turbulent flows is summarised by Jasak [148] as follows:

1. Set all field values to some initial guess.
2. Assemble and solve the under-relaxed momentum predictor equation.
3. Solve the pressure equation and calculate the conservative fluxes. Update the pressure field with an appropriate under-relaxation. Perform the explicit velocity correction (Equation 2.66).
4. Solve the other equations in the system using the available fluxes, pressure and velocity fields. In order to improve convergence, under-relax the other equations in an implicit manner, as shown in Equation 2.73.

The PISO Algorithm

The PISO algorithm is used for computing time-marching solutions, which is essentially for all the results in the present work. This pressure-velocity treatment for transient flow calclations has been originally proposed by Issa [160]. Again, with reference to the discretised form of the incompressible Naver-Stokes equations (Equation 2.69 and 2.70), the momentum equation is solved first (Equation 2.70) by using the pressure field from the previous (or initial) time-step. This is known as the momentum predictor, which gives an approximation of the new velocity field. This prediction of new velocities assembles the $\mathbf{H}(\mathbf{U})$ operator that formulates a new pressure equation, which gives the pressure solution for an updated pressure field. Equation 2.71

dictates the conservative fluxes that will be consistent with this new pressure field, which can then be used to correct the velocity field. This step is achieved explicitly using Equation 2.66 for velocity correction. This internal loop between the implicit momentum predictor with pressure solutions for explicit velocity corrections repeat until the pre-determined solution tolerance setting is reached. Best practices recommend three to four orders of magnitude decrease in the residuals in the primitive variables [161].

A summary provided by Jasak [148] of the solution procedure for transient simulations using the PISO algorithm [160] for incompressible and turbulent flows is as follows:

1. Setting initial conditions for all field values.
2. Start the calculation of the new time-step values.
3. Assemble and solve the momentum predictor equation with the available face fluxes.
4. Go through the PISO loop until the tolerance for pressure-velocity system is reached. At this stage, pressure and velocity fields for the current time-step are obtained, as well as the new set of conservative fluxes.
5. Using the conservative fluxes, solve all other equations in the system. If the flow is turbulent, calculate the effective viscosity from the turbulence variables.
6. If the final time is not reached, return to step 2.

2.4 Strategies for Solution Discretisation & Convergence

All of the solutions detailed in this thesis will employ structured grids. This provides higher orthogonality and nodal edge control through refinement along block edges and node grading towards key flow regions. Structured grids are also preferable as it allows for grid points to be aligned with the dominant flow direction that results in less numerical diffusion from Upwind-based schemes compared to unstructured grids [1]. The finer edge control also allows better near-wall grid design for capturing boundary layers. The grid design prioritises non-orthogonality, skewness, and aspect ratio. For detailed mesh reports on the respective grids in the current work, see Appendix B.

Examining grid convergence determines the ordered discretisation error of the simulation [161]. This involves conducting the simulation on successively finer grids. The approach to grid convergence studies is based on Richardson's extrapolate [162]. As the grid is refined, discretisation errors should asymptotically approach zero. A minimum of three grids of increasing refinement ratios are recommended for determining the index of convergence across these grids.

The order of convergence, p, based on the set of grids is determined by:

$$p = \ln\left(\frac{f_3 - f_2}{f_2 - f_1}\right) / \ln(r), \tag{2.75}$$

where f_n is the simulation quantity of interest, which are the force coefficients in most cases seen in the coming chapters. The effective refinement ratio is determined with:

$$r_e = \left(\frac{N_1}{N_2}\right)^{\frac{1}{D}}, \tag{2.76}$$

where N is the number of points between grids and D is the spatial dimension. This is based on the total number of grid points instead of grid spacing ($r = h_2/h_1$) as the edge spacing may be kept inconsistent across grids to satisfy the desired resolution. For example in the case of Chapter 4, refinements of $\Delta_{wake} = [0.1, 0.07, 0.05]d$ is used. The Richardson's extrapolate is then used to define the p^{th}-order of the grid:

$$f_{h=0} \cong f_1 + \frac{f_1 - f_2}{r^p - 1}. \tag{2.77}$$

The selection of a suitable time-step size is one of the most important factors in unsteady calculations. This directly affects temporal resolution in terms of the finest available sampling rate, where too large of time-step results in loss of higher frequency flow details, whereas unnecessarily small time-step increases the computational resources needed for the solution. To achieve a balance, the sensitivity of the simulation output has to be studied with respect to time-step size. This often requires some preliminary studies to establish the best practices suitable for the simulation objectives to resolve for appropriate scales of the problem. In this case, a dimensionless time-step and frequency is used to as a guideline for relating time-step sizes to the flow and geometry characteristics. This is achieved through the Strouhal number and convective time:

$$S_t = \frac{fl}{u_\infty}, \qquad t_c = \frac{u_\infty t}{l}, \tag{2.78}$$

where f is the frequency of the system, l is the characteristic length, and t is the solution time. Relative to the spatial grid, the strategy for approaching the inter-dependence between space and time for the numerical domain is as previously discussed in Section 1.1.3. This is governed by the ratio between spatial and temporal coordinates known as the Courant number. For a 1-Dimensional case in the x-direction, this is defined as,

$$Co = \frac{u\Delta t}{\Delta x}, \tag{2.79}$$

which can be extended for n-dimensions as:

$$Co = \Delta t \left(\sum_{i=1}^{n} \frac{u_{xi}}{\Delta x_i} \right) \leq Co_{max}. \tag{2.80}$$

This condition ensures that the transport of any variable over the duration of a single time-step must be at least within the spatial distance of discrete points in the grid. This mandates that the information from a given cell can propagate to *only* its immediate neighbours.

2.5 Resources

A summary of the resources used for the work are as follows:

- Workstation:
  - Duo Intel Xeon E5-2695 v4 Processors (2×18 cores) at 2.1 GHz (without Intel Turbo boost) and 256GB of RAM. The processor has a *maximum* theoretical peak performance of approximately 700 GFLOPS [163]. The cases presented in this thesis are run exclusively off the CPU, but it is worth highlighting that OpenFOAM demonstrates a potential speed-up with GPU processing and parallelisation [164].
  - The system operates on Ubuntu (v16.04 LTS and v18.04 LTS).
- Pre-Processing:
  - ANSYS ICEM CFD [165] is used for the generation of the respective meshes. The grids are exported as a `.msh` (ASCII) extension and then converted into the OpenFOAM `polyMesh` format using the `fluent3DMeshToFoam` utility.
  - SALOME [166], FreeCAD [167], and SolidWorks [168] are used primarily for geometry preparation, in particular the NASA CRM for the work seen in Appendix A. OpenVSP [169] is used for the geometries in the primary chapters.
- Processing:
  - OpenFOAM v6.0 and v1906 [170, 171]
- Post-processing:
  - ParaView v5.4 [172] for illustrations and data visualisation.
  - Python 3.6 with numerous libraries including Matplotlib, NumPy, SciPy, and pandas [173–177] for data manipulation and plotting.

Chapter 3

Bluff-Body Vortex Shedding and Wake Dynamics

3.1 Introduction

As mentioned in Chapter 1 (Section 1.6.1), a process for validation and verification must be achieved to ascertain results from the chosen methodology. To accomplish this, this chapter focuses on the applied numerical methodologies for a canonical study of a wake generator represented with a flow encountering a square beam bluff-body. Vortex shedding dynamics and wake physics are simulated using the OpenFOAM CFD C++ toolkit, where the solvers validity and accuracy of the wake simulated is evaluated against pre-existing experimental benchmark data. The extent of wake capture is first validated at the source, where the suitability of the near-wall grid design is assessed to ensure adequate boundary layer and wall surface treatment. This translates to the time-averaged and fluctuating first- and second-moment statistics of lift and drag surface-force coefficients. The frequency spectra of these forces also detail characteristics between their shedding behaviours. Moving downstream, the wake centre and cross-stream profiles are measured up to $6D$ in the stream-wise direction, where coherent vortex structures are identified as part of the von Kármán street. The formation of these structures are emanated from the leading edges as shear-layer instabilities which roll-up and stretch into these larger, coherent vortex structures.

The work further distinguishes itself by establishing the extent of turbulent wake treatment with both DES and RANS methods where the former agrees well to published results performed with LES and DNS methods [55, 76, 79]. Here, the expected inherent dissipating characteristics of the RANS solutions also become evident, and are demonstrated through eddy viscosity ratios in the wake. The robustness of the solution is further examined with an auto-correlation (time-lag) function of velocity probe data, revealing the extent of captured turbulent statistics through the definition of an integral time scale. Insight to the fluctuating quantities are also further given with spectral analyses and validation of turbulent shear stresses due to wake fluctuations. Given

these, a recommended practice for capturing bluff-body wakes can be made which will form the foundation of modelling subsequent simulations with wake encounters.

3.2 Simulation Methodology for Wake Capture

The wall mounted Square Beam of characteristic length, D, with infinite span is placed adjacent to the horizontal oncoming flow. The side boundaries of the domain spans $7D$ ($AR = 7$) across, with the inlet and outlet spaced $40D$ apart. The top and bottom boundaries are spaced at $14D$ with the geometry located at the centroid of this domain. These are based on a Cartesian coordinate system where the positive x direction is aligned with the flow, as illustrated in Figure 3.1. For validation, this geometry is identical to most of the numerical and experimental literature listed in Table 3.4.

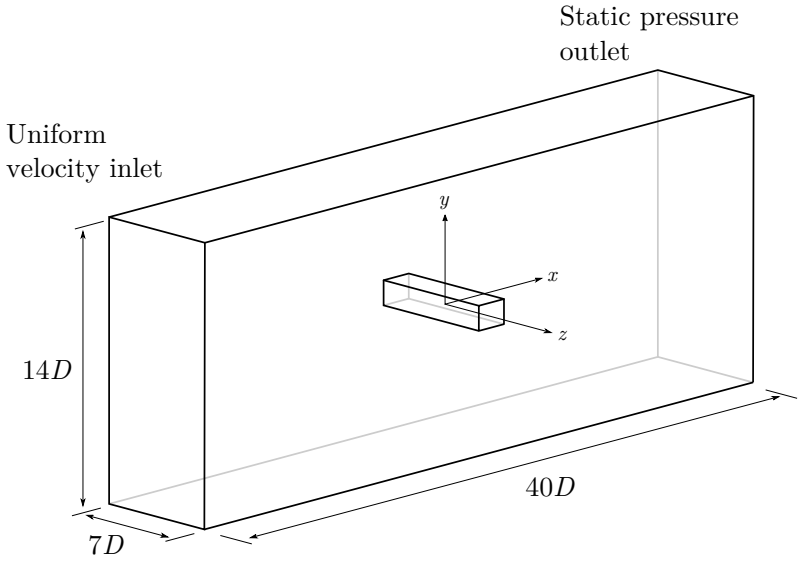

Figure 3.1: The square beam simulation domain.

3.2.1 Summary of Numerical Settings

Flow conditions are at $Re = 2.14 \times 10^4$, with reference to standard sea-level conditions, assuming fully turbulent, incompressible, isothermal conditions of the Navier-Stokes equations (See Section 2.2). The equations are discretised with schemes that are nominally second-order accurate. Spatially, the divergence terms are discretised with a blended central-upwind differencing scheme (CD-UD) [178] with a blending coefficient weighted at 0.75. Time discretisation is achieved with a second-order implicit, backward-differencing scheme [179]. For more details on the discretisation schemes, see Section 2.3.1).

A segregated approach is taken for pressure-velocity coupling with the time-marching solution achieved with the PISO (Pressure-Implicit with Splitting Operators) algorithm [160]. A

constant time-step selection that is adequately fine ensures that the algorithm is conditionally stable with diagonal dominance. This is based on the maximum Courant number in the domain, by referencing the smallest cell sizes with highest relative local velocities due to the shear layer instabilities that are located over the leading edges of the geometry. Under these conditions, the wake $C_o \approx 0.2$, and translates to $\Delta t_c = 6.25 \times 10^{-3}$ which satisfies the Courant–Friedrichs–Lewy condition [56].

For time-averaging, the solution time-history is limited towards a sufficiently large instance relative to fluctuations to ensure that the statistical average (mean) is sufficiently sampled to be insensitive to the amount of time samples taken. After allowing a flow development phase of approximately 50 characteristic lengths, a subsequent sample size of 250 is sampled for the URANS case. Due to the turbulent extent of the DDES solution, this sample size is further increased to 950. Table 3.2 summarises and compares the case parameters alongside existing studies that were previously discussed in Section 1.2.

Turbulence Modelling

A total of three turbulence modelling techniques are used in this chapter. The first is the Spalart-Allmaras one-equation turbulence model solves for a single transport quantity. The variant used here excludes the f_{t2} trip term, calibrated with the model coefficients that are as recommended by the source [127, 129]. Being a one-equation model, it neglects turbulent kinetic energy in the Boussinesq hypothesis for Reynolds stresses. Because of this its performance can therefore be impeded especially for the modelling of massively separated flows or those with adverse pressure gradients as seen in this case.

The second RANS model that is considered is the k-ω SST model that based on two-equations for the transport of turbulent kinetic energy and specific dissipation rate. It is also highly regarded [49] which offers a blend between the standard k-ω and k-ε models [46,48]. The additional equation obtains turbulence intensity, which in contrast to the one-equation model, addresses turbulent kinetic energy in the Boussinesq hypothesis. All model constants and sub-functions are taken as given by the source [48] (See Section 2.2.2).

The DES formulation is built upon the SA model that is based on the correlation of its production ($c_{b1}\tilde{\nu}\tilde{S}$) and destruction ($c_{w1}f_w(\tilde{\nu}/d)$) terms in its transport equation [83]. Balancing these terms gives a relationship that scales the eddy-viscosity with the local deformation rate and distance to the wall. This is analogous to the Smagorinsky model where it scales with its sub-grid scale eddy-viscosity and grid spacing instead. With this, the distance to the wall in the original SA model can be replaced with a hybrid length scale that yields between RANS and LES modes. This hybrid formulation allows a RANS-like behaviour and a Smagorinsky-like LES model that switches depending on the proportions between the distance to the wall and local grid spacing. The sub-variant used here is the Delayed-DES (DDES) model which provides an adjustment to the definition of the hybrid length scale that narrows the region of

uncertainty between RANS and LES modes. This improved variant has been demonstrated to perform more accurately for massively separated flows [83].

3.2.2 Grid Description

A structured grid is used as it supports upwind-based schemes with grid points that are dominantly aligned to the general flow direction, reducing numerical diffusion [180]. An O-H-grid topology composed of 15 hexagonal blocks discretizes the fluid domain for the geometry as illustrated in Figure 3.2. The O-grid surrounds the beam at a distance of $0.3D$ from the surface for the boundary layer grid, where the first cell height resides within the viscous sub-layer at $y^+ < 1$. This first cell stretches at a cell growth rate of 1.1 over 25 layers. The $\Delta x, z$ cell widths are also maintained at $0.05D$, which transfers along parallel block edges for cell isotropy in the wake block located downstream. The highest aspect ratio among cells which are at the wall are in the order of 100. Downstream, a single block is used for wake refinement, and extends up to $7D$ in the stream-wise direction from the geometry origin at its centroid. The grid then expands to the far field regions of the domain boundaries. With this grid design, the entire computational domain comprises of approximately 4.1×10^6 elements. In terms of quality, the grid has a maximum non-orthogonality of 47°, which occurs along the four leading and trailing edges of the geometry. Because of the high orthogonality among all other cells, mostly in the volume of the wake block, the overall non-orthogonality quality of the grid is strong which averages to 7°.

Table 3.1: Summary of grid statistics.

Topology	Blocks	y^+	Layers	Growth, δ	Δ_{wake}
Hex, Structured, O-H	15	< 1	25	1.10	0.05D

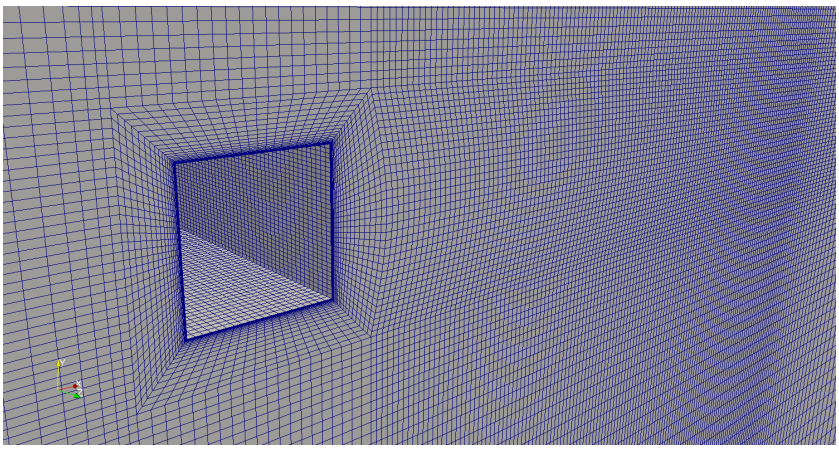

(a) Computational domain with wake refinement block

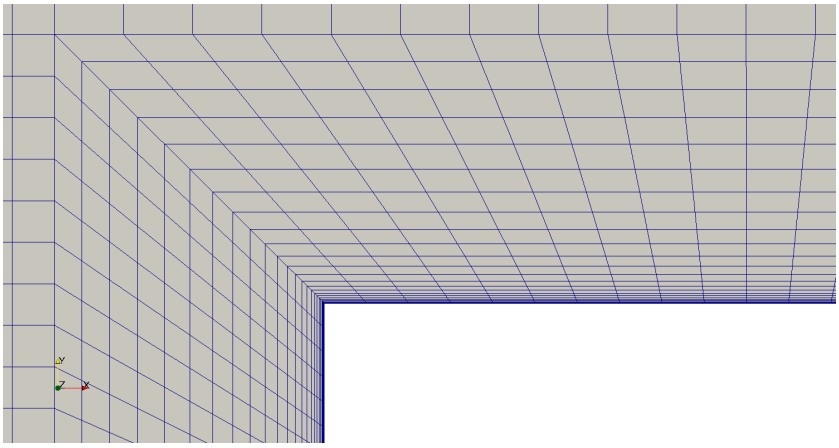

(b) Wall grid design, $y^+ < 1$

Figure 3.2: A structured O-H-grid topology with a block (H-grid) downstream used for cell refinement in the wake region.

Table 3.2: Case comparisons of similar Reynolds numbers for wake block grid cell size, characteristic time step, Courant number, and time-history sample size with the current bluff-body case.

Cases	Sim. Type	$Re \times 10^3$	Δ_{wake}, D	$\Delta t_c \times 10^{-3}$	Co	T
Current case	URANS (DDES)	21.4	0.05	6.25 (3.125)	0.2	250 (950)
Boudreau et al. [75]	URANS (DDES)	21.4	0.05	10	0.2	209.5 (1507.5)
Barone and Roy [80]	DES	19.4	0.095-0.032	3.2	-	250.8
Sohankar et al. [76]	LES	22.0	0.1-0.16	12.5	-	-
Fureby et al. [77]	LES	21.4	-	-	0.5	-
Trias et al. [79]	DNS	22.0	-	0.97 & 1.71	-	605

3.2.3 Boundary and Initial Conditions

The solution domain is velocity-driven, with a freestream inlet and a static pressure outlet. No-slip boundary conditions are imposed on the walls with all remaining far field boundaries taken to be of zero flux and normal components. Computation of turbulent viscosity, ν_t, is constrained with a turbulent viscosity ratio of $\nu_{t_\infty}/\nu_\infty = 0.01$. The turbulent viscosity for the inlet is determined using kinematic viscosity, $\nu = \mu/\rho$. For the SA model, the modified eddy-viscosity term, $\tilde{\nu}$, where $\tilde{\nu}_\infty = 5\nu_\infty$ for fully turbulent flows, and at the walls, $\nu_{t_{wall}} = \nu_{wall} = 0$ is used. The k-ω SST model introduces two additional terms, which are the turbulent kinetic energy, k, and specific dissipation, ω. The inlet values reference the freestream based on turbulent intensity where $k_{inlet} = 3/2(U_\infty I)^2$, taking $I = 0.01$, and specific dissipation, $\nu_t = k/\omega$. To impose no-slip conditions at the walls, the turbulent kinetic energy, $k_{wall} = 0$.

The grid is initially calibrated for grid independence with the SA model assuming steady flow conditions. The internal fields from this steady solution is then subsequently used for the initialisation of the time-marching transient calculations. The URANS solution is used for the initialisation of the DDES case where a development time of 50 convective time-steps is used for the solution to adjust to the updated turbulence model. These numerical solutions are achieved through pisoFoam solver in the OpenFOAM library [136, 181].

Table 3.3: Summary of boundary conditions for the computational domain.

Boundary	Type	Velocity	Kinematic pressure
Inlet	Inflow	$u_i = U_\infty$	$\partial p/\partial n = 0$
Outlet	Outflow	$\partial u_i/\partial n = 0$	p = 0
Far fields	-	$\partial u_i/\partial n = u_i \cdot \hat{n} = 0$	$\partial p/\partial n = p \cdot \hat{n} = 0$
Walls	No-slip	$u_i = 0$	$\partial p/\partial n = 0$

3.3 Turbulent Wake Capture Shed by a Bluff Body

3.3.1 Evaluation of Boundary Layer Grid

The near-wall grid is assessed independently as an extract of the top surface grid settings described in Table 3.1 under identical flow conditions. A fully developed boundary layer over this distance is achieved with a cyclic inlet-outlet interface where evaluation with the Law of the Wall is valid [64]. The dimensionless velocity is obtained as:

$$y^+ = \frac{yu_\tau}{\nu}, \qquad u^+ = \frac{u}{u_\tau}, \tag{3.1}$$

where:

$$u_\tau = \sqrt{\frac{\tau_w}{\rho}}, \qquad \tau_w = \mu \left(\frac{\partial u}{\partial y} \right)_{y=0}, \tag{3.2}$$

with u_τ and τ_w as the friction velocity and wall shear stress, respectively.

Discrete points in Figure 3.3 represent cell-centred values. Based on this boundary layer grid design, six cell centres reside well within the viscous sub-layer at $y^+ < 5$ [182]. The same grid is run with the k-ω SST model and compares well against the SA results, and other numerical studies [127] with comparable flow conditions ($Re = 1.0 \times 10^4$). The cyclic flow conditions for the present grid assumes attached flow but the formation of a separation zone over the leading edges of the geometry would induce much lower local velocities over the upper and lower surfaces of the square beam. This is expected to result in a $y^+ < 1$ for the full case due to boundary layer recirculation with lower local velocities. This result demonstrates adequate grid design for capturing boundary layer effects.

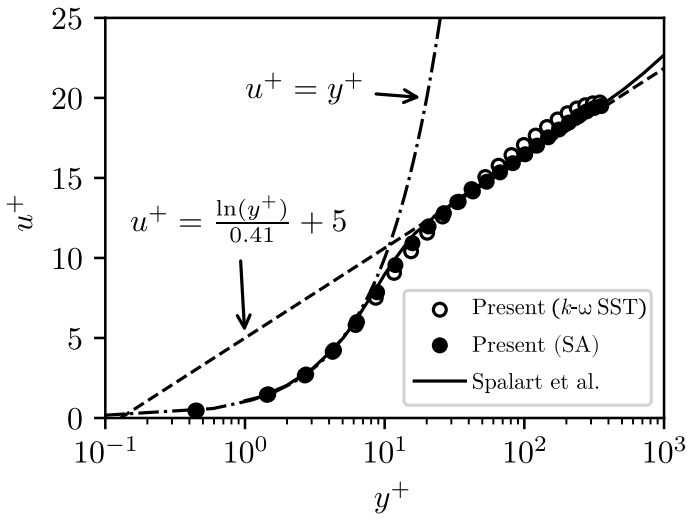

Figure 3.3: Evaluation of wall grid design with Law of the Wall in the present case (k-ω SST and SA) with data from Spalart et al. [127].

Although a desired boundary layer grid density is achieved, the performance of DDES is inherently subjected to its RANS-LES transition behaviour especially with the “Modelled-Stress Depletion" of free shear layers near the wall [83]. The local shear-layer instabilities shed from the leading edge of the geometry (Figure 3.4) falls within this region and category of flows, but should only be further investigated through shear-layer studies, like a flow over a forward-facing step [183]. This reproduces flow phenomena comparable to those shed over the square beam leading edge. However, it is noteworthy that the depiction of Kelvin-Helmholtz structures by Minguez et al. [55] in Figure 3.4b demonstrates comparable leading edge flow patterns to those in the present case. This includes leading edge separation bubbles (Figure 3.4a) created by the Kelvin-Helmholtz shear-layer instabilities that are continuously shed over the leading

edge. Throughout this process, the boundary layer periodically reattaches onto the surface of the square beam, which are then convected past the characteristic length of the geometry which rolls up into vortices behind the geometry. Farther downstream features past this are detailed as part of wake validation and is discussed in the following sections.

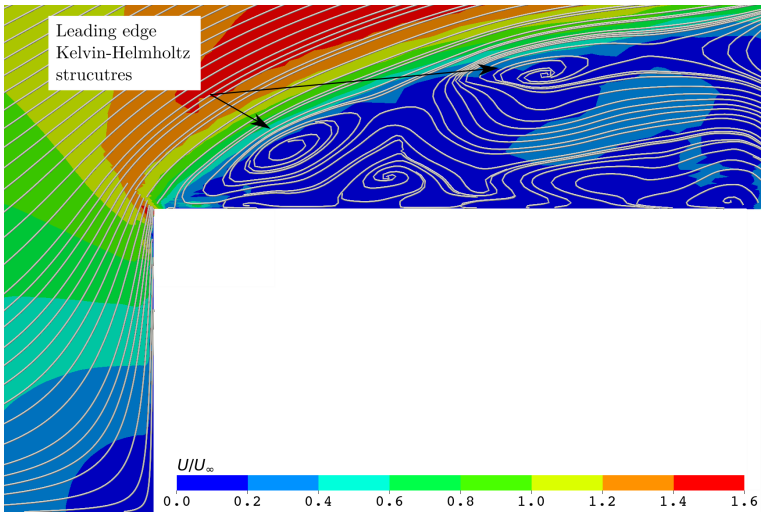

(a) Streamlines of Kelvin-Helmholtz structures over the leading edge from the present study.

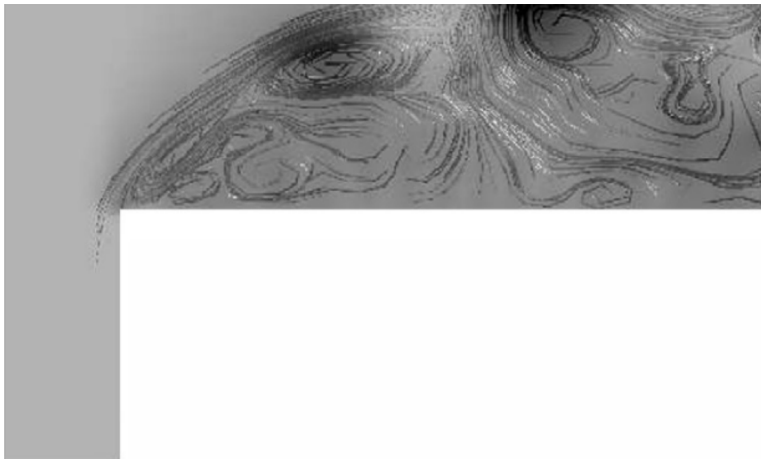

(b) Streamlines of Kelvin-Helmholtz structures over the leading edge by Minguez et al. [55].

Figure 3.4: Visualisaton of Kelvin-Helmholtz (shear-layer) instability structures over the leading edge of the square cylinder for the present case and that depicted by Minguez et al. [55].

3.3.2 Vortex Shedding Dynamics and Surface Integral Statistics

Vortex shedding dynamics is made apparent through instantaneous contours of the von Kármán street as illustrated for the three cases in Figure 3.5. Coherent 3-dimensional flow structures are identified with iso-surfaces of wake vortices identified with the λ_2-criterion [184] contoured with instantaneous velocity. Based on the contours, the DDES solution is capable of capturing and identifying a greater resolution of smaller-scale vortex structures in comparison to the URANS cases. The shear-layers emanated from the leading edges are convected downstream

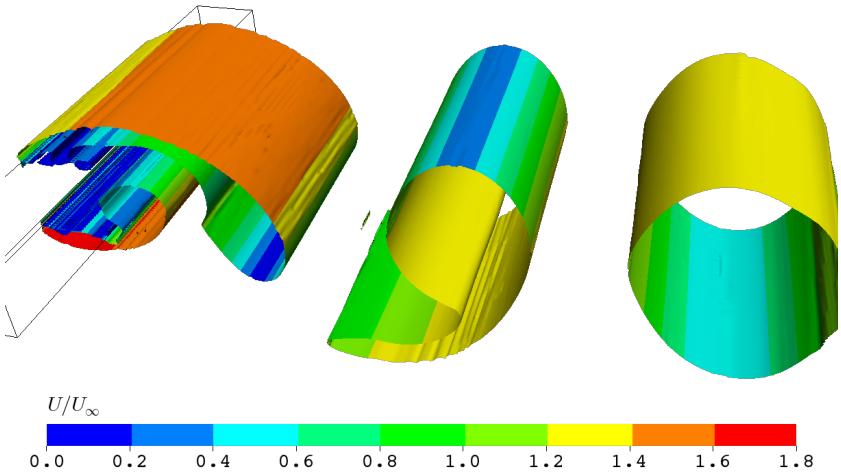

(a) SA

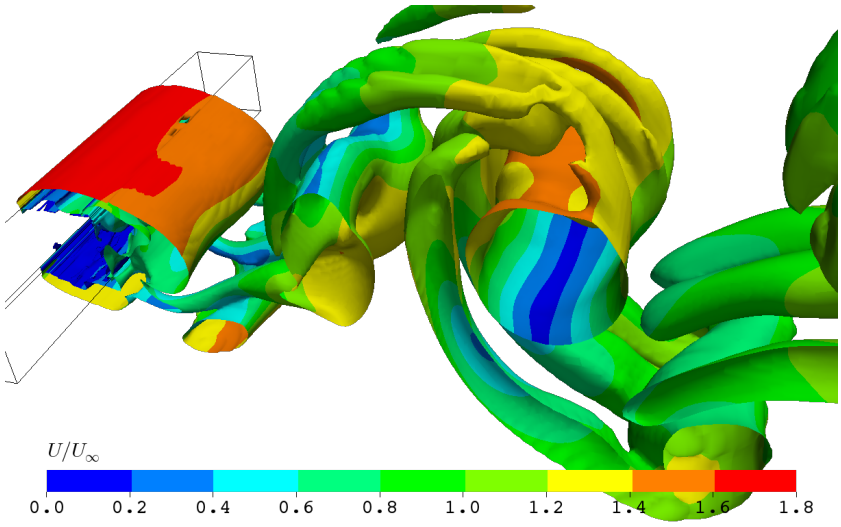

(b) k-ω SST

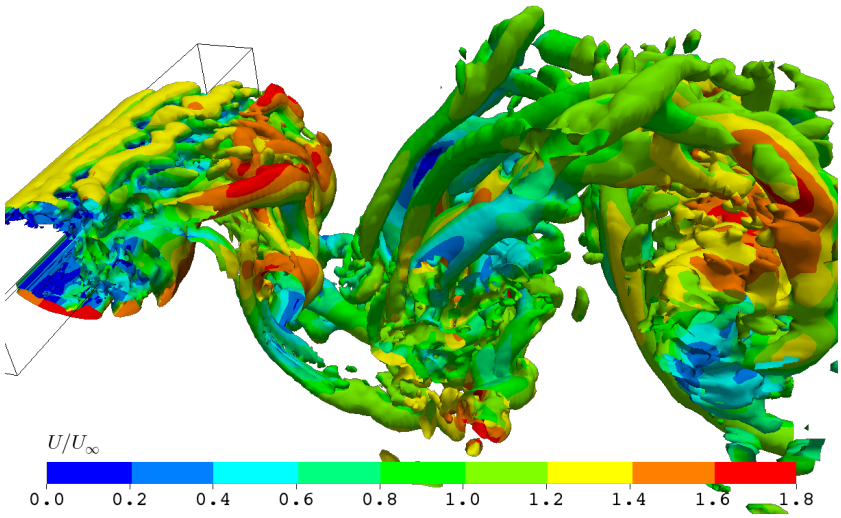

(c) DDES

Figure 3.5: Instantaneous vortical structures identified with λ_2-criterion iso-surfaces (cut-off value $= 50$) contoured with freestream-normalised velocity magnitude (U/U_∞).

that eventually roll-up and stretch into a larger coherent span-wise vortex structures trailing the geometry. This is observable for all cases but the DDES solution distinguishes itself with much greater flow details.

The drag coefficient frequency oscillates at approximately *twice* that of lift based on Discrete Fourier Transform with the analyses as shown in Figure 3.6. These are at 4.37 and 8.91 Hz for the SA results (Figure 3.6a) and overall observations for all three cases agree with the von Kármán street dynamics as these parallel and perpendicular forces persist in cross-flow directions [64]. This relationship is easily distinguishable for the SA and k-ω SST cases in their frequency domains (Figures 3.6a and 3.6b) but not as apparent for the DDES case, which is only revealed in its power spectra (Figure 3.6c). Both peak dominant frequencies for the URANS cases agree at approximately 4.3 Hz, whereas results from the DDES are relatively higher by approximately 2 %. Using this frequency, a period of 0.225 s for the DDES case can be obtained and reveals a resolution of 1126 time-steps per wave period, which satisfies the Nyquist sampling criteria [66]. Despite the significant similarities between the models in the frequency domain, their differences become apparent in the (log-log) power spectra, which shows that the hybrid solution can capture more information compared against the eddy-viscosity solutions.

The results for dominant frequencies in Figure 3.6 corresponds to a Strouhal number of 0.140 and 0.142 for the SA and DDES solutions, respectively. This amounts to a difference of 1.43 % between the two techniques, but is over-predicted by 7.58 % with respect to the experimental data [68]. Table 3.4 summarises these surface-integral statistics against other comparable benchmarks of the same square beam geometry. Metrics are mainly based on the time-averaged lift and drag coefficients alongside root-mean-square statistics of their respective signals. The obtained drag coefficient has a good agreement with the benchmarks, accurate to a 100-count precision.

Comparing the general flow field around the square beam shows relevant similarities to that of Minguez et al. [55] as marked in the Figure 3.7. This includes boundary layer recirculation zones (points (a) and (b)) and two counter-rotating vortices in the wake that forms a recirculation length, where the velocity along this centre stagnates at a distance away from the leeward side of the geometry. The major separation zones (point (a)) along the top and bottom surface of the geometry are comparable, along with smaller bubbles located above the trailing edge (point (b)). However, there are some minor dissimilarities between the two cases near the leading edge, which brings the discussion back to the possibility of inherent DES behaviour in the RANS-LES transition region and the shedding of shear-layer instabilities (Section 3.3.1). As for the wake, its mean recirculation length is captured with a 5% error relative to the experiment [68] and 3% to LES results (Figure 3.7b) by taking the closest stagnation point along the time-averaged wake centre. This difference also accounts for the precision of the discrete measurement to the closest cell-centre. In comparison, the present results under-predict this length by less than 5 % relative to the experiment and other numerical work in Table 3.4.

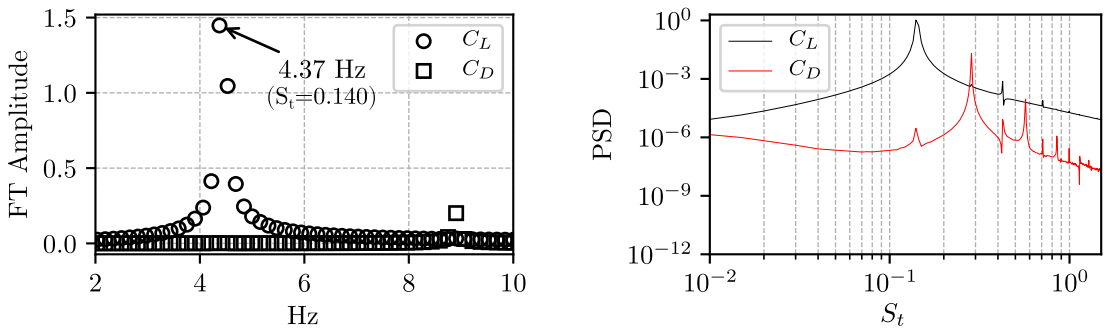

(a) SA

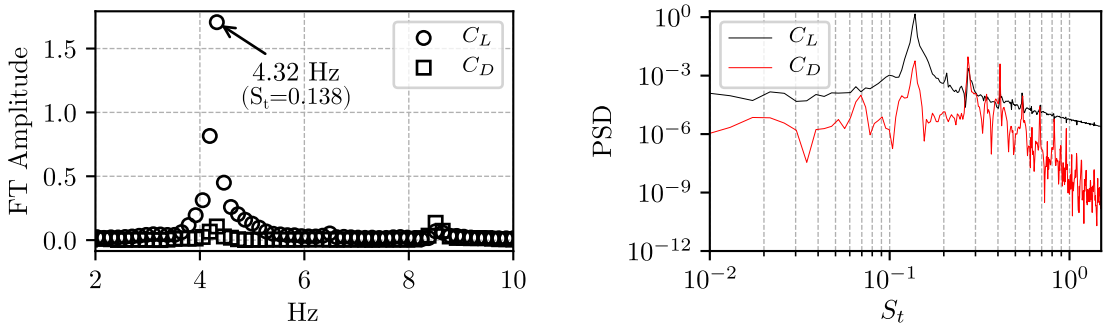

(b) k-ω SST

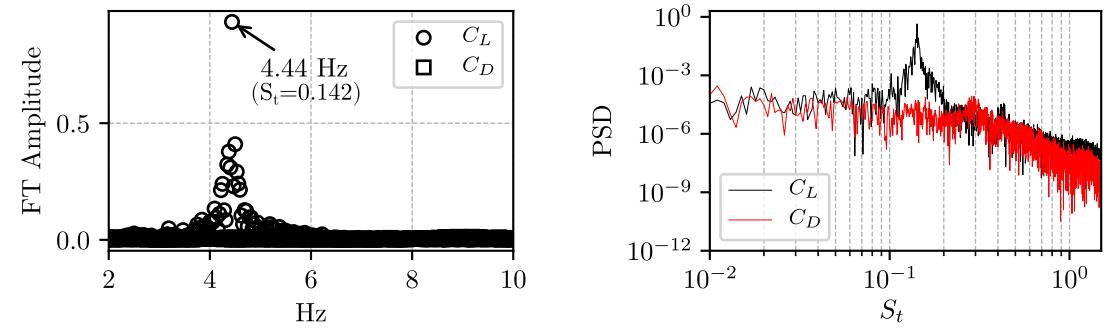

(c) DDES

Figure 3.6: Time-history of force coefficients from all three solutions in the frequency and log-log power spectra ($S_t = fD/U$) domains.

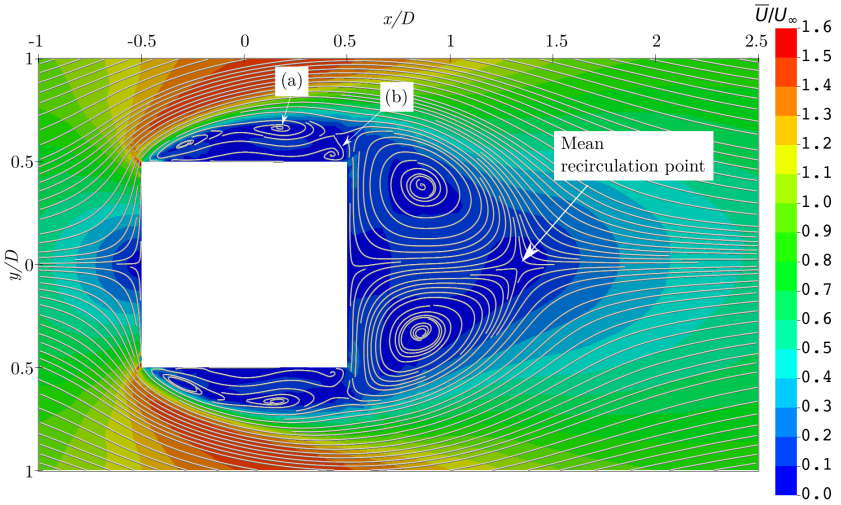

(a) Streamlines of time-averaged velocity ($\overline{U}/U_\infty$) from the present case.

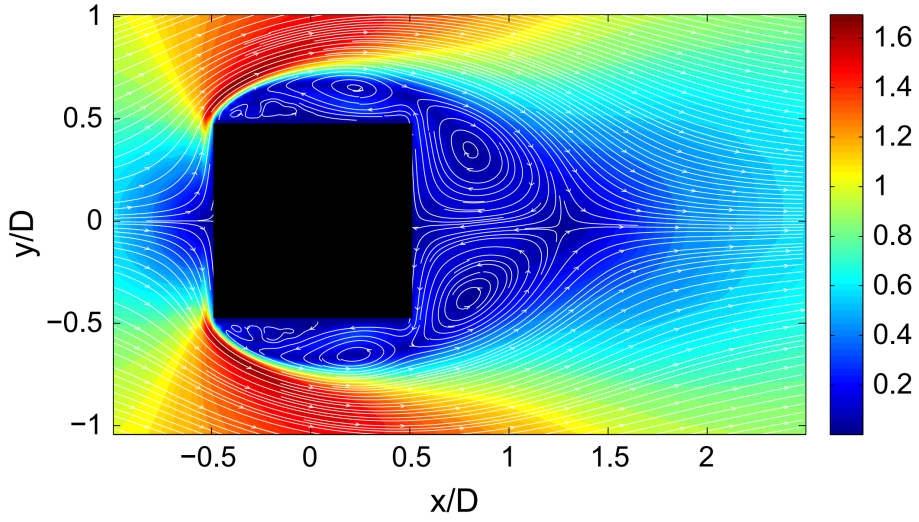

(b) Mean streamlines and mean stream-wise velocity ($\overline{u}/U_\infty$) by Minguez et al. [55].

Figure 3.7: Time-averaged flow visualisation of the flow field around the bluff-body. The mean recirculation zone downstream can be clearly identified in both cases.

Table 3.4: Comparison of key vortex shedding parameters for the bluff-body benchmark case, including results from the present case.

Case	Type	$Re \times 10^3$	AR	$\overline{C_D}$	S_t	λ	$C_D{}'$	$C_L{}'$
Numerical Case								
Present studies	SA-noft2	21.4	7	2.15	0.140	0.93	0.15	1.39
with OpenFOAM	k-ω SST	21.4	7	2.26	0.138	0.93	0.16	1.44
	DDES	21.4	7	2.19	0.142	1.31	0.12	0.95
	DDES-2	21.4	7	2.22	0.142	-	0.08	0.99
Numerical Cases								
Boudreau et al. [75]	URANS	21.4	7	2.11	0.133	0.97	0.14	1.56
	DDES	21.4	7	2.41	0.126	1.07	0.17	1.47
Barone and Roy [80]	DES	19.4	4	2.11	0.125	1.42	0.26	1.16
Fureby et al. [77]	LES	21.4	8	2.1	0.131	1.25	0.17	1.30
Sohankar et al. [76]	LES	22.0	4	2.09	0.128	1.07	0.27	1.40
Minguez et al. [55]	LES	21.4	-	2.2	0.141	1.28	-	-
Trias et al. [79]	DNS	22.0	4	2.18	0.132	1.04	0.205	1.71
Experimental Cases								
Lyn et al. [68]	Laser-Dopp.	21.4	9.75	2.1	0.132	1.38	-	-
Minguez et al. [55]	Laser-Dopp.	21.4	20	2.1	0.130	-	-	-
Luo et al. [81]	Water tunnel	34.0	9.2	2.21	0.13	-	0.18	1.21

To investigate the difference in Strouhal numbers, it was reported that a two-component Laser-Doppler Velocimetry along the wake is used for monitoring velocity fluctuations [68]. Identical locations along this centre ($x/D = [1,2,3,6]$) are similarly probed for their point vertical velocity component and the dominant frequencies at these locations coincides with lift at approximately 4.44 Hz. Further investigation for sensitivity with regards to time discretisation by halving the time-step size (DDES-2 in Table 3.4) also reveals no appreciable difference in the Strouhal number. Other work (Table 3.4) also lists numerical cases that are corrected for blockage effects. This correction factor is applied to confined (ducted) spaces and non-slip far field boundary conditions [76, 80]. However, blockage corrections should not apply considering the far field boundary conditions for the present case as this does not lead to an increase in dynamic pressure across the domain. Despite the over-prediction in Strouhal number relative to the experimental cases, the key results obtained are consistent with other numerical cases for time-averaged drag prediction, Strouhal number, and mean recirculation length [55, 77, 79].

3.3.3 First- and Second-Moment Wake Statistics

The DDES solution provides a significantly greater amount of flow details by comparing the instantaneous velocity magnitude and span-wise vorticity component contours in Figures 3.8 and 3.9. The results from both the SA and k-ω SST solutions appear to convey the same degree of

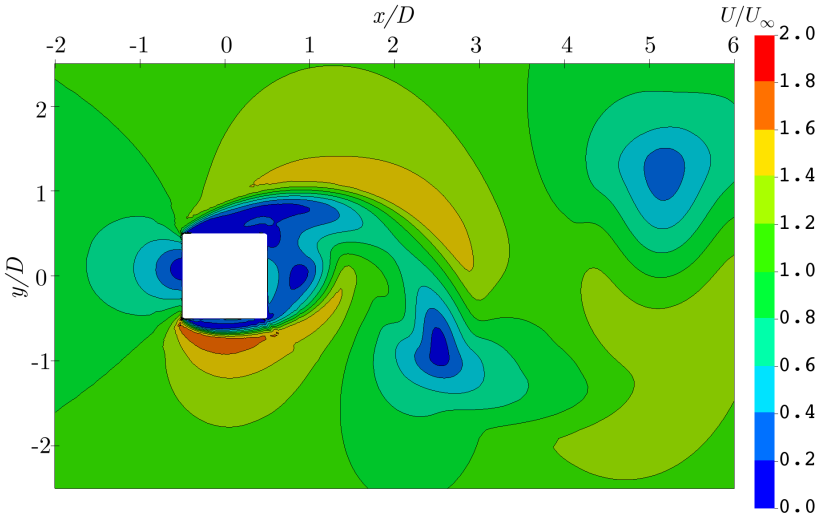

(a) URANS (SA)

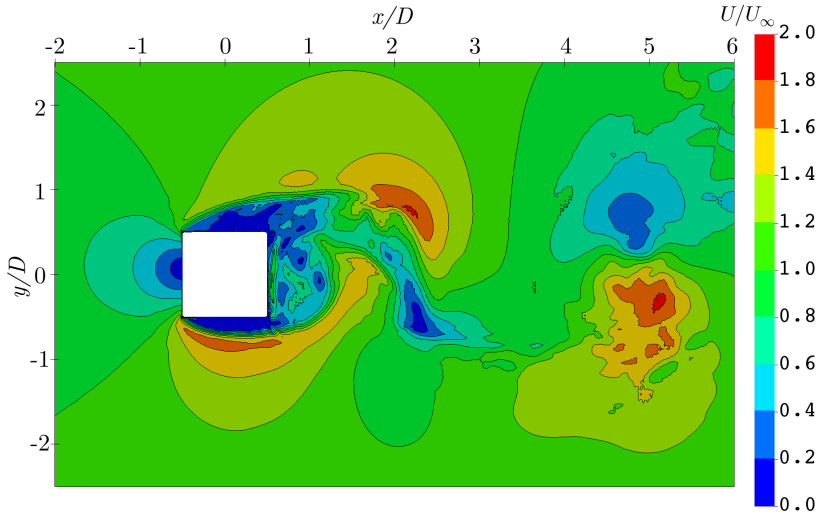

(b) DDES

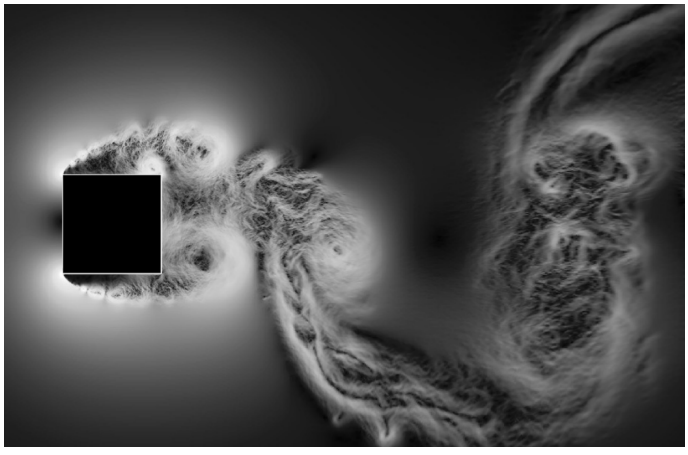

(c) DNS flow visualisation by Trias et al. [79].

Figure 3.8: Instantaneous freestream-normalised velocity (U/U_∞) contours at a comparable vortex shedding phase.

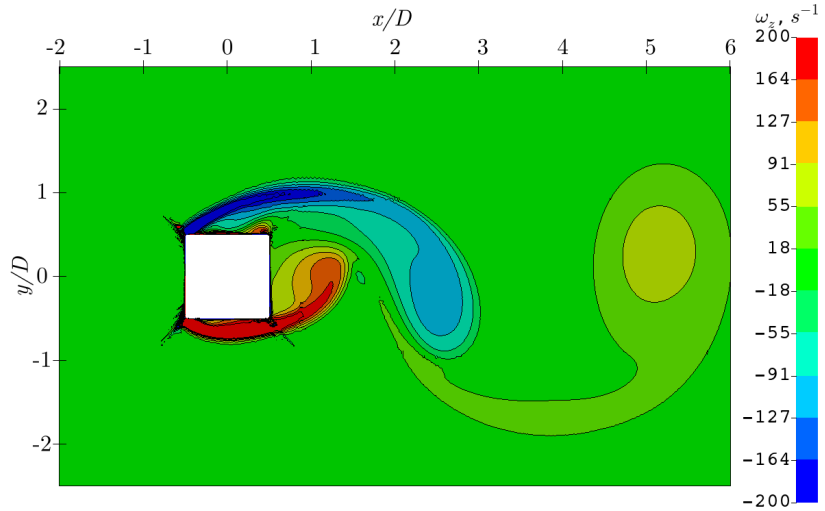

(a) URANS (SA)

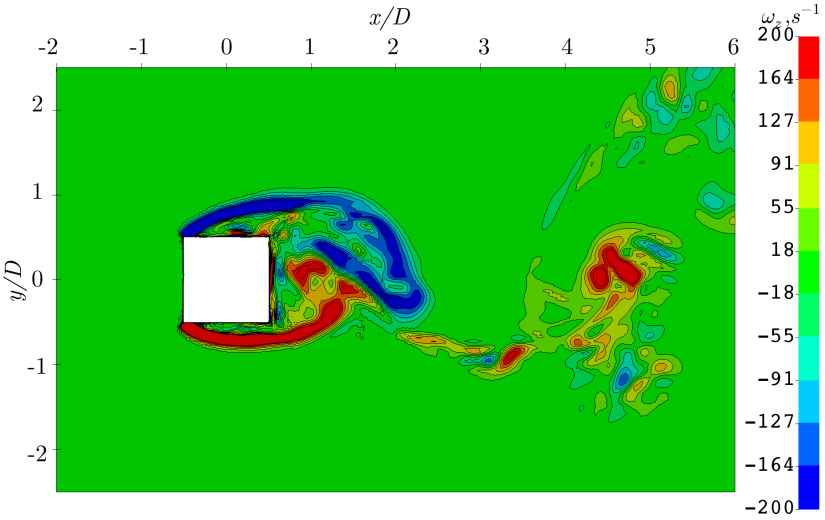

(b) DDES

Figure 3.9: Instantaneous span-wise vorticity (ω_z) contours at a comparable vortex shedding phase.

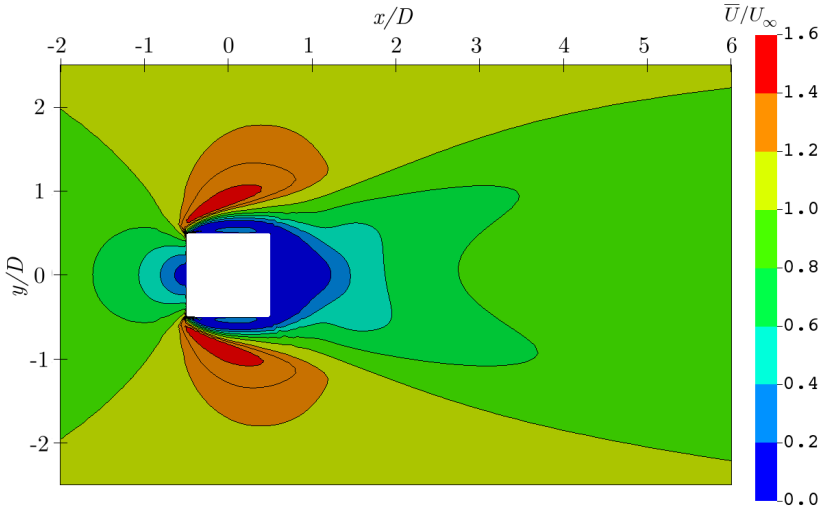

(a) URANS (SA)

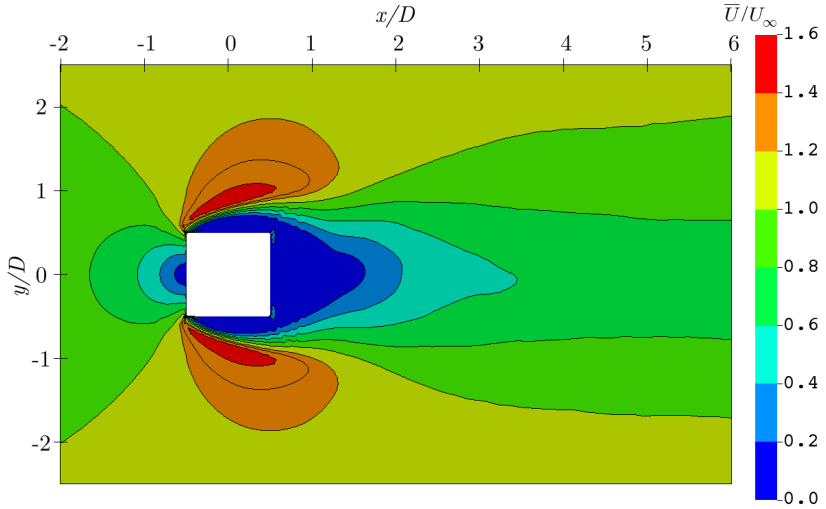

(b) DDES

Figure 3.10: Time-averaged freestream-normalised velocity contours ($\overline{U}/U_\infty$).

information in the instantaneous contours and therefore only that from the SA solution is presented. Finer flow details are easily observable through the velocity contours (Figure 3.8) and the amount of mixing downstream, convected from the upper and lower shear-layers over the leading edges of the bluff-body is evident in Figure 3.9b. This vortex roll-up for the URANS and DDES cases correlate well with depictions by Trias et al. [79] in Figure 3.8c. In this DNS solution, both span- and stream-wise vortices are reported, which are also observable in the present DDES results using vorticity contours (Figure 3.9b). For the URANS solution, the significant loss of information through the process of Reynolds decomposition reduces the entire turbulence spectrum such that only the mean flow statistics remain is therefore very apparent (Figures 3.8a and 3.9a). Furthermore, time-averaging the velocity fields—which also appear identical for the two URANS models—also reveal a larger, diffused wake (Figure 3.10). However, the vertical extent of the shear layer emanated from the leading edges are similar between both the URANS and DDES solutions, which extends to a width of approximately $2y/D$. The time-averaged velocity fields also reveal an earlier recovery in the SA solution (Figure 3.10a) by almost $0.3\overline{U}/U_\infty$.

The accuracy for the first-moments of the wake capture is evaluated in terms of its wake velocity recovery along the centre, and wake profiles evaluated across 4 downstream stations. The normalised time-averaged stream-wise velocity profile is presented in Figure 3.11 and evaluated against experimental data [68] up to $x/D = 6$. The URANS models over-predict this velocity profile, characterised as an early recovery. On the other hand, the DDES model provides excellent accuracy although marginally over-predicting beyond $x/D = 3$. The second-moment statistics of velocity fluctuation is evaluated along this same centre. Figure 3.12 illustrates the freestream-normalised root-mean-square of stream-wise, $RMS(u')/U_\infty$, and transversal $RMS(v')/U_\infty$ velocities, up to the same downstream distance of $x/D = 6$.

The results obtained from the URANS models generally under-predict fluctuations. However, the horizontal location of the fluctuation peak is predicted with reasonable accuracy, positioned at $x/D \approx 1.5$. Thereafter, the fluctuations depict severely damped results in the RMS of the velocity farther downstream, that plateau along $u'/U_\infty \approx 0.03$ at distances beyond $x/D = 4$ especially for the SA case. This is non-physical compared to the experimental results [68], and that observed from the DDES case. In contrast, DDES only models the turbulence spectrum partially, which are filtered based on the smallest grid scales. Investigating the total effective viscosity $(\nu + \nu_t)$ of the instantaneous field reveals a significant over-prediction in turbulent viscosity ratio, by approximately 50 times of that for the URANS cases compared to DDES which showed only a time-averaged maximum of $\nu_t/\nu = 8$ compared to 200 shown in Figure 3.13. The same order of magnitude in this over-prediction of total effective viscosities is also reported [75]. In contrast to the experimental data, the DDES results predicts the fluctuation peak slightly farther downstream. This disagrees with that reported by [79], where the peak is depicted to be farther upstream instead. The fluctuations are slightly over-predicted in the near wake ($x/D = 2$) while

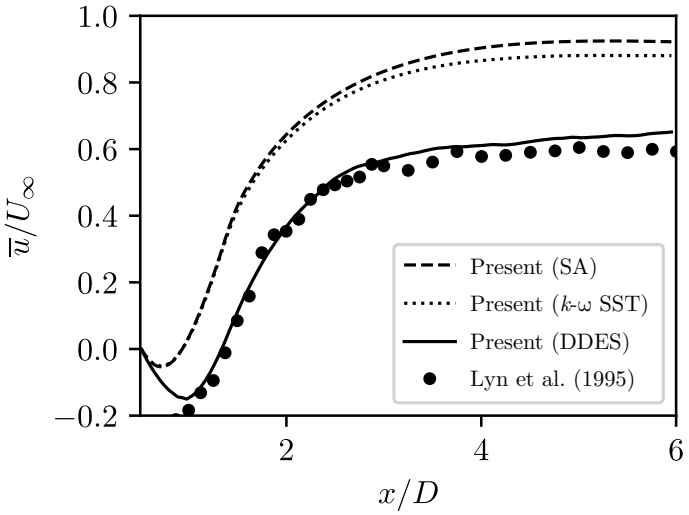

Figure 3.11: Comparison of first-moment (time-averaged) statistics of u-velocity component with experimental data [68].

it is expected for results to fall short due to damping from sub-grid scale viscosity. This observation is also highlighted by other numerical work listed in Table 3.4. Regardless, excellent agreement is obtained farther downstream, especially within $3 < x/D < 6$ which predicts the range of $rms(u')/U_\infty \approx 0.3$ against the experimental data [68]. The transversal fluctuations (Figure 3.12b) yield similar results among the numerical cases within the $x/D < 3$ range, but begin to deviate past this distance as the URANS results begin to over-predict relative to the experimental data while the DDES solution maintains some degree of accuracy ($rms(u')/U_\infty \approx 0.1$) for the remainder of the results.

Velocity deficit profiles for the normalised stream-wise velocity component are illustrated in Figure 3.14 for $x/D = [1,2,3,6]$. DDES results show excellent agreement with the experimental data at x/D, especially for the limits of the wake width at approximately $\overline{u}/U_\infty$. However, results for comparison at the farther downstream stations are unreported. Nevertheless, the wake centre velocities in Figure 3.11 correspond to those along the wake centre in Figure 3.14, and therefore confidence for the accuracy in the maximum wake momentum deficit is high. As expected for the URANS results, the wake velocity profiles model early wake recovery farther downstream and prove to be inadequate at capturing even the first-moment statistics along this location.

The results obtained so far has demonstrated good correlation in terms of the wake descriptors and also quantitatively for vortex shedding parameters against the cited sources. Key vortex structures were also identified, illustrating different orders of fidelty across the two tested turbulence modelling methods. These have good accuracy and are comparable even to that of LES and DNS methods [76, 79] among others, despite being conducted on an identical grid with the RANS models.

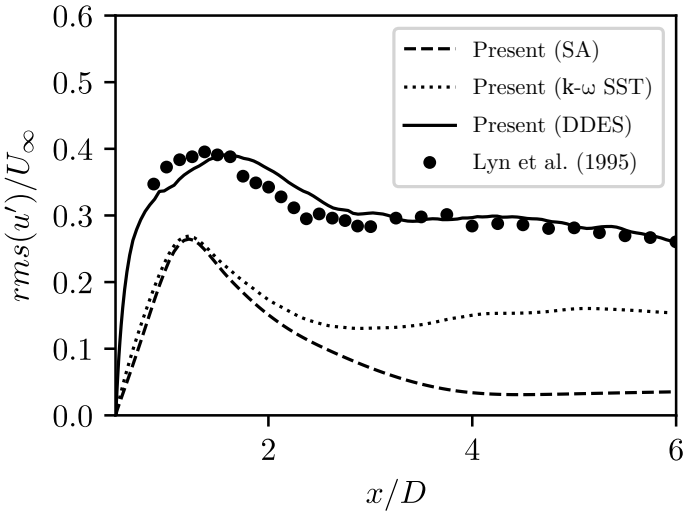

(a) *u*-component fluctuation.

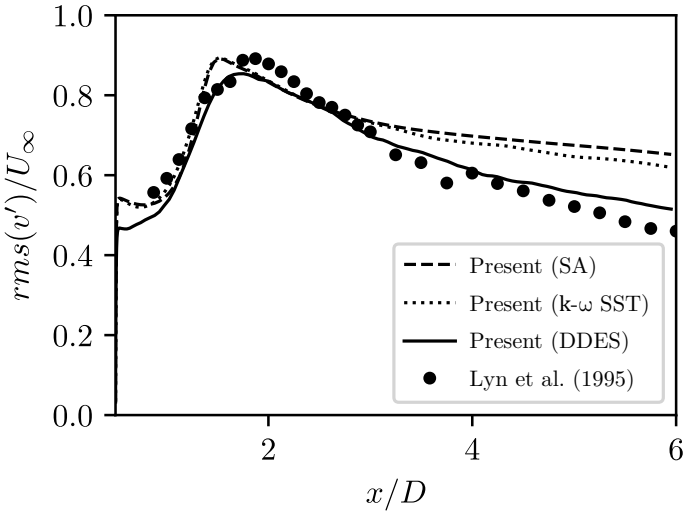

(b) *v*-component fluctuation.

Figure 3.12: Comparison of second-moment (root-mean-square) statistics of *u* and *v* velocity component fluctuations with experimental data [68].

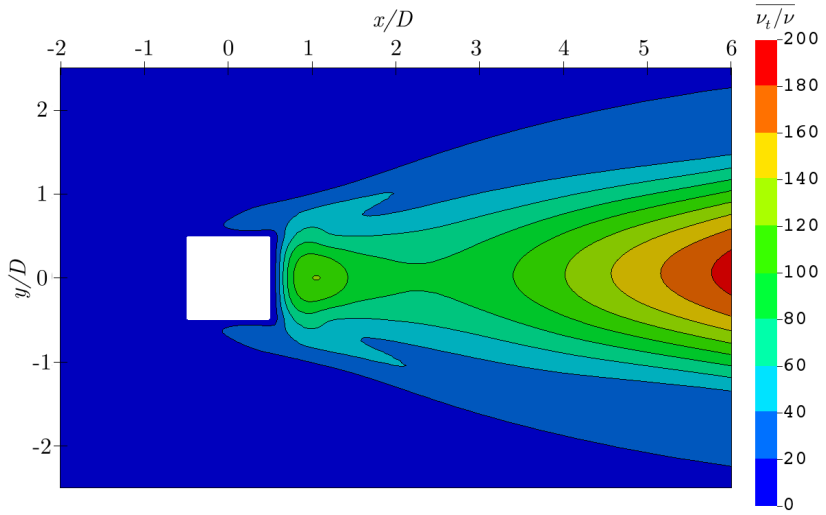

(a) URANS (SA)

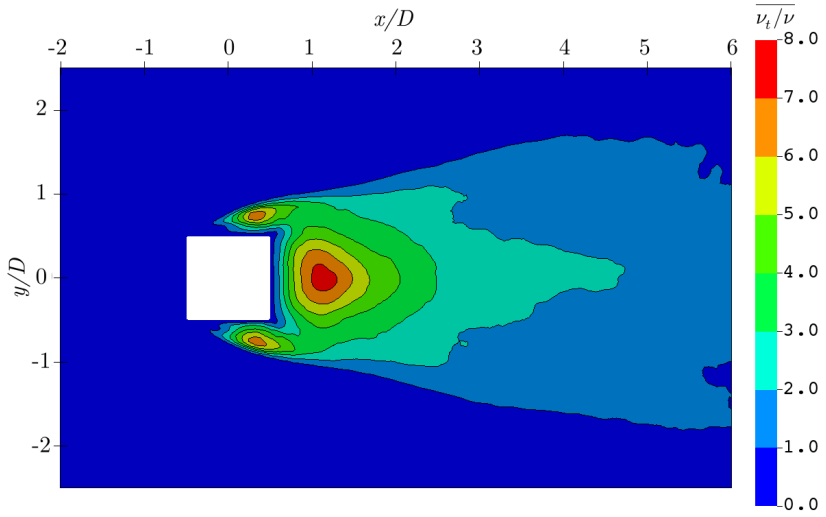

(b) DDES

Figure 3.13: A significant inflation in the time-averaged turbulent viscosity ratios ($\overline{\nu_t/\nu}$) between the URANS and DDES solutions. Note the difference in scale.

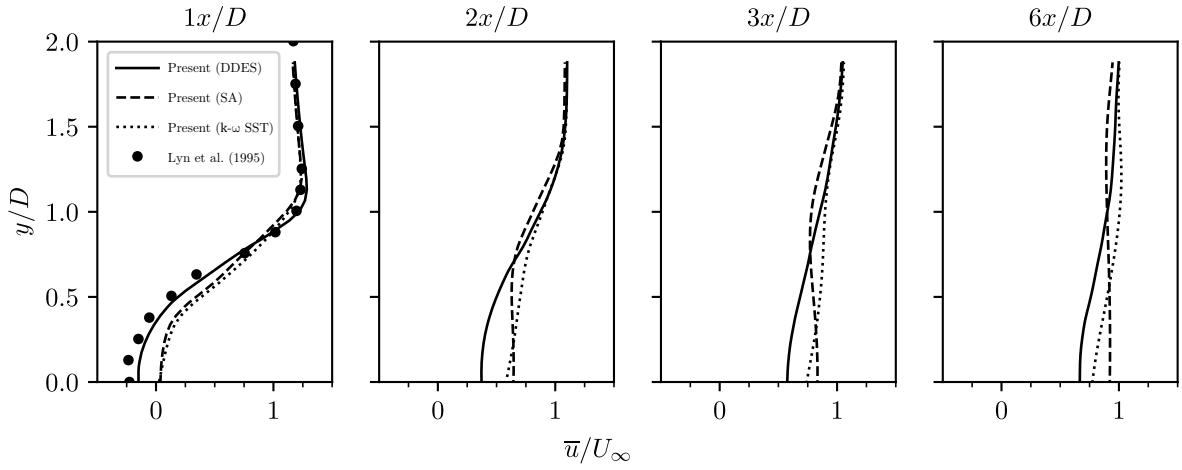

Figure 3.14: Time-averaged wake velocity profiles across subsequent downstream stations for the present studies with experiment data by Lyn et al. [68].

3.3.4 Wake Stresses, Auto-correlation, and Power Spectra

Figure 3.15 illustrates the captured turbulent normal and shear stresses compared against the experimental data at x/D [68]. This is based on the product of time-averaged fluctuating components across the wake subtracted from the mean of their product where $\overline{u_i' u_j'} = \overline{u_i u_j} - \overline{u_i} \cdot \overline{u_j}$. The normal stress depicted in Figure 3.15a peaks at approximately $0.4\overline{u'u'}/{U_\infty}^2$ due to the shear-layers being shed before rolling-up and diminishing towards the wake centre into the recirculation zone. Here, the transverse $\overline{v'v'}$ normal stress begin to dominate, peaking at approximately $0.25\overline{v'v'}/{U_\infty}^2$. This exchange due to the roll-up of the shear-layer instabilities is captured through the $\overline{u'v'}$ shear-stresses that correspond well to the experimental data [68]. As the shear-layers roll-up and develop slightly farther downstream at $x/D = 2$ (Figure 3.15b), $\overline{v'v'}$ begins to dominate in the wake, reflective of the trend that is observed in the second-moment statistics along the wake centre (Figure 3.12b). These stresses that exist in the cross-stream directions exceed ($> 0.6\overline{v'v'}/{U_\infty}^2$) even that of what was previously observed in the stream-wise direction at x/D. In terms of shear-stress at this location, the result depicts that it grows in width but sustains its intensity at approximately $-0.15\overline{u'v'}/{U_\infty}^2$. While experimental data for the stresses is unavailable at the subsequent downstream ($x/D = [2,3,6]$) distances, insights on the extent of turbulent wake treatment is assessed using power spectra and correlation techniques.

It has been demonstrated that correlation functions are a useful tool for the statistical analyses of turbulent flows, demonstrated in the case of a similar benchmark DNS simulation [79]. This is characterised as the auto-correlation function of velocity time-history with a wake probe. Examining the two locations in Figure 3.17 with spatial two-point (one-time) correlation where $R(x) = U(x)U(x+\Delta x)$ reveals that they are strongly correlated at $|R(x)| \approx 0.75$ among their vertical velocity components. The same strong correlations (approx. 0.7) are also observed with the lift (and moment) coefficients, that is evident in the peak Strouhal number in the wake

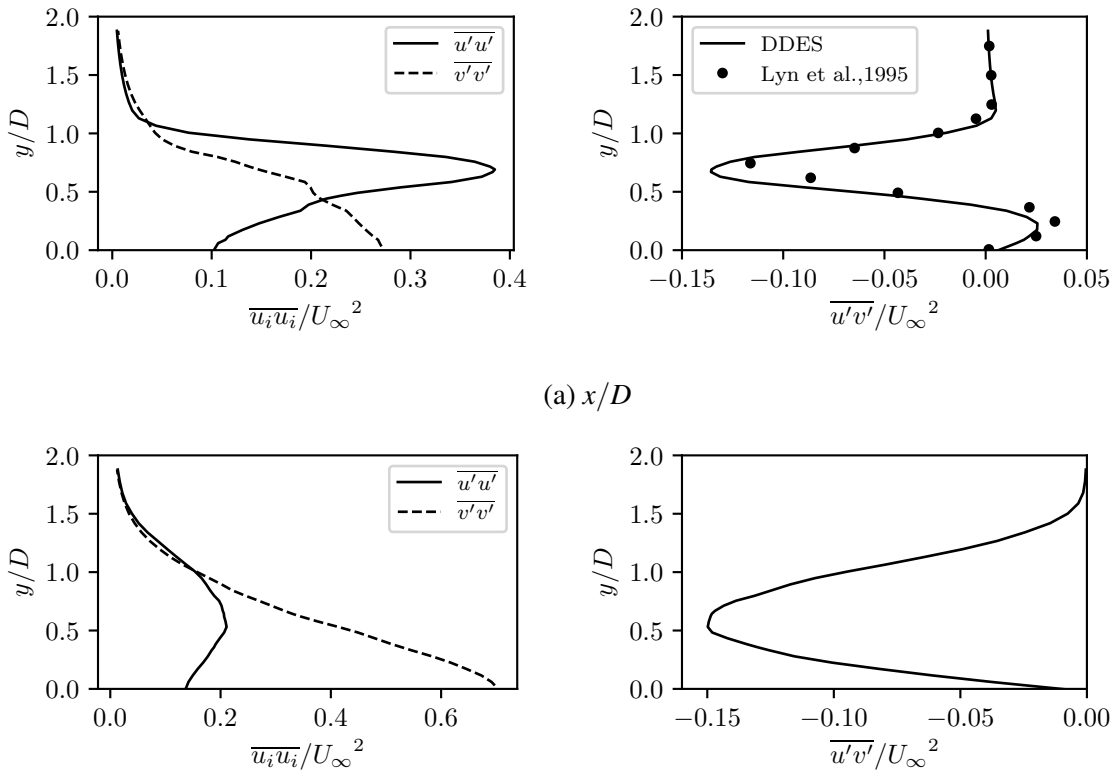

(a) x/D

(b) $x/D = 2$

Figure 3.15: Wake normal and shear wake profile stresses compared with experimental data [68].

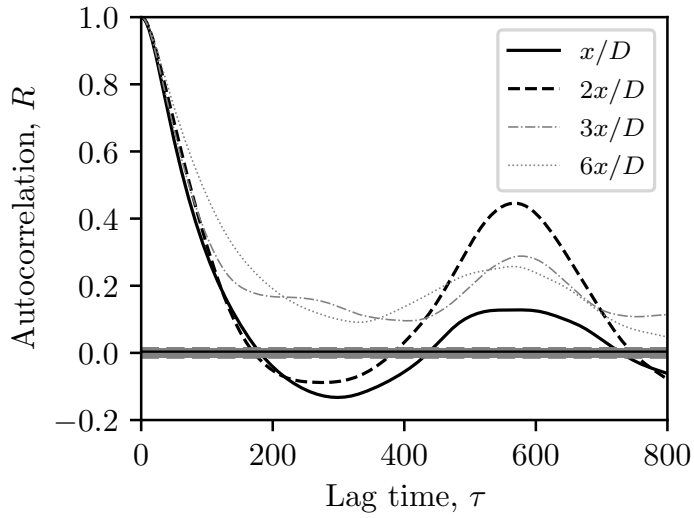

Figure 3.16: Auto-correlation coefficient of wake point probe velocity as a function of lag time.

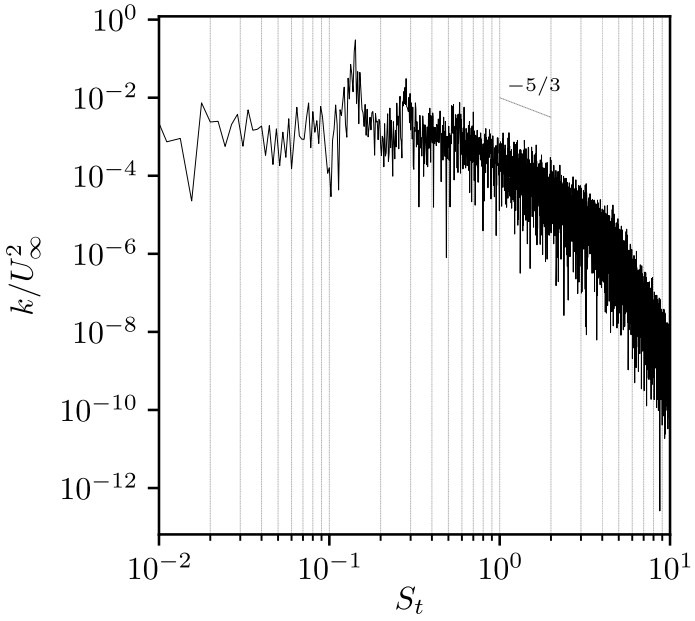

(a) $x/D = 2$

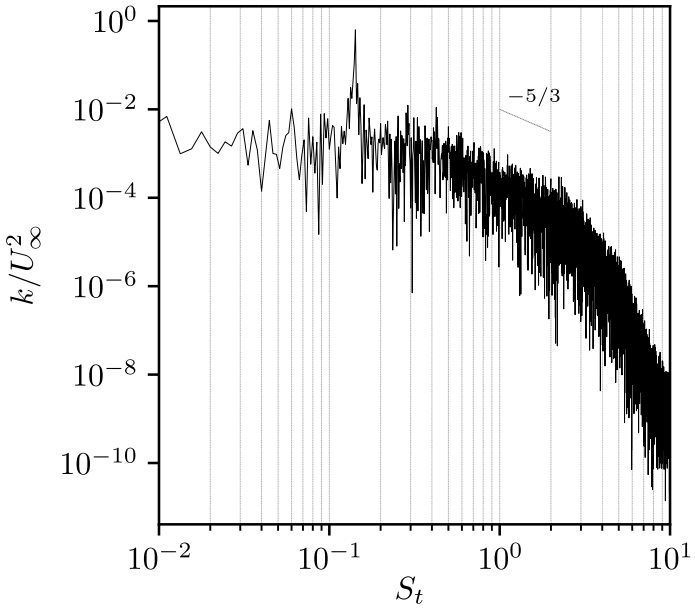

(b) $x/D = 6$

Figure 3.17: Log-log distribution of velocity power spectral densities probed at two different stations along wake centre.

power spectra which coincides with the surface force Strouhal number (Figures 3.6). An auto-correlation as a function of lag time is illustrated in Figure 3.16 for the four probed locations as well. This is achieved through the individual velocity signals as a correlation with themselves. This normalised auto-correlation coefficient is obtained with:

$$R(\tau) = \frac{U(t)U(t+\tau)}{U(t)^2}, \tag{3.3}$$

with τ as the lag time. The result of this function begins at unity ($R(0) = 1$) for all probed locations and decays with increasing time lag where $R(\tau) < 1$ for all $\tau > 0$, which converges to zero for locations up to $x/D = 2$. Successive peaks can also be observed as the shedding cycles repeat, typical for a periodic signal that is characteristic of vortex shedding cycles. Adequate resolution at these locations allows for the clear definition of an integral length scale of turbulence. Despite good accuracy for the time-averaged moment statistics, the integral scale for probed locations at $x/D = [3,6]$ are not as clearly defined, although close ($< 0.2R(\tau)$). At these farther downstream distances, the results in Figure 3.11 show an over-prediction (approx. $0.05\overline{u}/U_\infty$) that deviates beyond $4x/D$ that is attributed to turbulence decay and dissipation. As the grid remains isotropic throughout the wake refinement region up to $6x/D$, it is expected for the subgrid-scale viscosities to dominate as the length scales dissipate downstream. Velocities are subsequently probed at locations corresponding to those in Figure 3.14. Turbulent wake spectra at $x/D = [2,6]$ presented in Figure 3.17 shows frequency peaks coinciding with the Strouhal number of the flow indicates wake coherence throughout these distances, demonstrating inhomogeneity expected for vortex shedding. The sum of values in the power spectra is checked by validating it against the variance of the velocity signal equal to $1.55U_\infty^2$ for $x/D = 2$.

3.4 Chapter Closure

Statistical and instantaneous results of vortex shedding and wake capture for a massively separated flow generated by a bluff-body are provided with URANS and DDES methods obtained on identical grids. The solutions presented are nominally second-order accurate using an implicit constant backward time-stepping scheme coupled with a blended upwind-central differencing spatial discretisation scheme. Shedding dynamics, including the Strouhal number, statistics of lift and drag coefficients, along with time-averaged moment statistics of the wake profiles and stresses are among the results presented. Although the Strouhal number is slightly over-predicted compared to experimental values, the effects of blockage and the application of correction factors need to be considered when imposing the appropriate far-field boundary conditions as this will influence the resulting shedding frequencies. Additionally, this dominant frequency was insensitive to time-discretisation studies with half a time-step size. Key vortex structures were also identified among the models tested, and the von Kármán street was identified of vary-

ing resolution based on the turbulence model used. The amount of detail in the flow were also reflected in the respective force coefficient spectra, which showed good correlation with existing sources for the dominant wake shedding frequencies.

For wake capture, the errors for URANS are attributed to inherent damping, evident as as inflation in total effective viscosity that affects even the mean flow. The DDES results in comparison, demonstrate excellent accuracy that is even comparable to that of LES [55, 76] and DNS [79] methods for wake recovery and RMS statistics up to the measured distance of $x/D = 6$ compared against experimental data [68]. This supersedes RANS in terms of accuracy on the given (RANS-calibrated) grid resolution ($\Delta = 0.05D$), and the significant improvement in accuracy is achieved with just a marginal trade-off in computational effort that is still much lower than that required of LES. Other benchmarks [75, 80] used comparable spatial resolution for wake definition but the extent of turbulent treatment is expanded and assessed in this work. The analyses illustrated the definition of an integral time scale utilising an auto-correlation function along downstream points in the wake. This is clearly defined up to a distance of $x/D = 2$ under the given grid design, where the resulting signal indicates periodicity and coherence that is also evident in its power spectra. Although this definition is slightly diminished farther downstream, the time-averaged and fluctuating (root-mean-square) statistics along the wake centre which are of practical importance are captured accurately, and this is further supported through validation of turbulent wake stresses.

Chapter 4

Wing-Section in Bluff-Body Wake Interference

4.1 Introduction

To study the aerodynamic effects of wake interaction, a square beam bluff-body is chosen as the wake generator to be placed ahead of a NACA0012 wing-section. This configuration is a canonical example that is representative of an aerodynamic body encountering the wake emanated by a bluff-body, like a building or ship wake. The current study expands on this by focusing on the aerodynamic response of the airfoil and its surrounding flow field. As aerodynamic behavior differs in- and out-of-wake interference, this difference can be quantified by referencing conventional wake-free conditions. This serves as a baseline reference for the results obtained. The accuracy of the wake capture has been validated previously [185], and the data is developed further here to provide an insight on its downstream wake interactions on an airfoil. The resulting wake-induced response of the airfoil will be approximated using the Sear's and Theodorsen's functions, where the wake shed by the bluff-body is treated as a harmonic gust field, and the relative sinusoidal behaviour of the von Kármán vortex street is treated relatively as a harmonic pitch/heave motion with respect to the airfoil. The result therefore presents the bluff-body wake as a mechanism for inducing unsteady loads, and subsequently allows the approximation of the aerodynamic response by its wake encounter.

4.2 Simulation Details for the Reference NACA0012 & Beam-Airfoil Configurations

The bluff-body geometry is based on the ERCOFTAC UFR2-02 "square cylinder" case as illustrated in Figure 4.1 [67]. This is a benchmark case where a square beam is placed adjacent to an oncoming flow that spans the entire width of the test domain, effectively of infinite span

achieved with slip conditions on both ends of the domain walls. The bluff-body used as a wake generator in this work and is modelled after this benchmark case, and was validated as part of prior work to this study. Here, the same geometry is used, with its span limited to $4c$ instead of $7c$ as pictured in Figure 4.1.

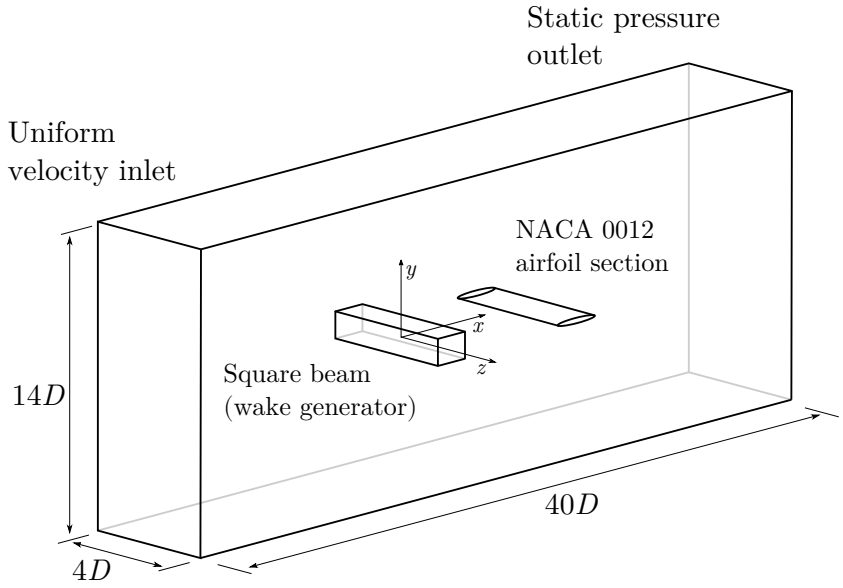

Figure 4.1: The ERCOFTAC "square cylinder" benchmark case [67] that is adopted as a wake generator for a NACA0012 wing-section located downstream.

4.2.1 Summary of Numerical Settings

Flow conditions are set at $Re_d = 2.14 \times 10^4$ for all cases, with reference to standard sea-level conditions, assuming fully turbulent, incompressible, isothermal conditions of the Navier-Stokes equations (See Section 2.2). These conditions are based on the validated wake data established in Chapter 3. The equations in the general form are discretised with schemes that are nominally second-order accurate. Spatially, the divergence terms are discretised with a blended Central-Upwind differencing scheme where the blending coefficient, γ, weighted at 0.75. Time discretisation is achieved with a second-order implicit, Backward-Differencing scheme [179]. For more details on the discretisation schemes, see Section 2.3.1).

A segregated approach is taken where the pressure-velocity coupling for the time-marching solution is achieved with the PISO (Pressure-Implicit with Splitting Operators) algorithm [160]. A constant time-step selection that is adequately fine ensures that the algorithm is conditionally stable with diagonal dominance. This is based on the maximum Courant number in the domain, by referencing the smallest cell sizes with highest relative local velocities due to the shear layer instabilities that are located over the leading edges of the bluff-body, and at the trailing edge of the NACA0012 [56].

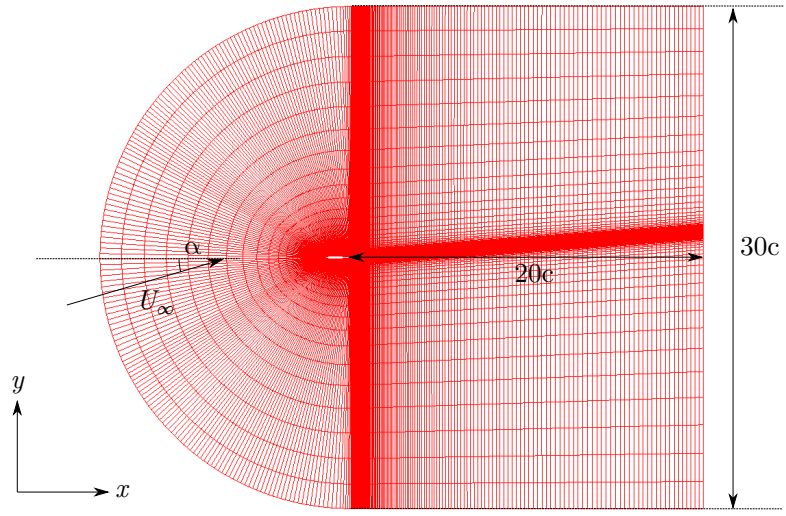

(a) C-grid domain overview

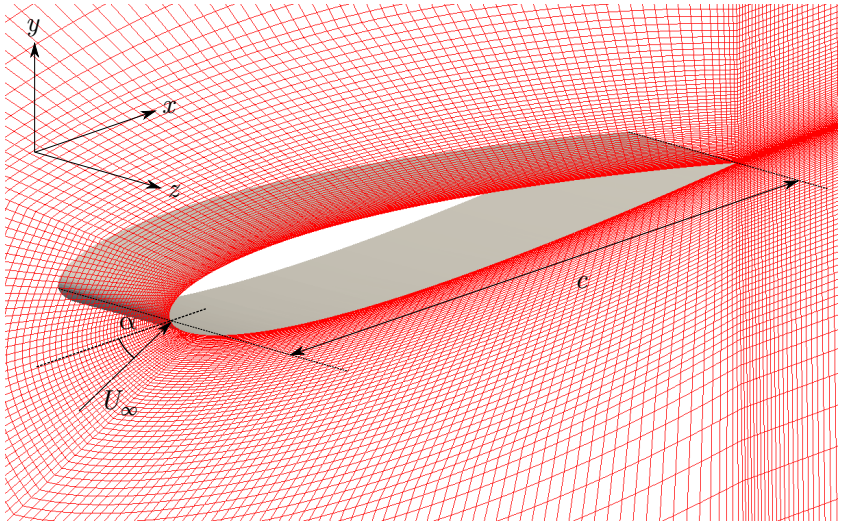

(b) Local grid around the NACA0012

Figure 4.2: Structured grid topology for the wake-free baseline case.

Turbulence Modelling and Solution Statistics

Closure for the governing equations for turbulence are modelled with DDES based on the SA one-equation turbulence model.

As the solutions are unsteady, the solution time-history is limited towards a sufficiently large instance relative to fluctuations to ensure that the statistical average (mean) is sufficiently sampled to be insensitive to the amount of time samples taken. This is after allowing a flow development period of 15-30 characteristic time-lengths for time-averaged results.

Apart from the bluff-body, a wake-free condition of a standalone NACA0012 airfoil is used as a baseline reference for comparison to study its effects under the influence of a bluff-body wake. The surface-force coefficients are the quantities of interest for validation. In addition, the accuracy of its wake profile will be tested with the momentum method to validate the capture of its wake against its zero-lift profile drag [2]. The simulations are conducted in the body frame of

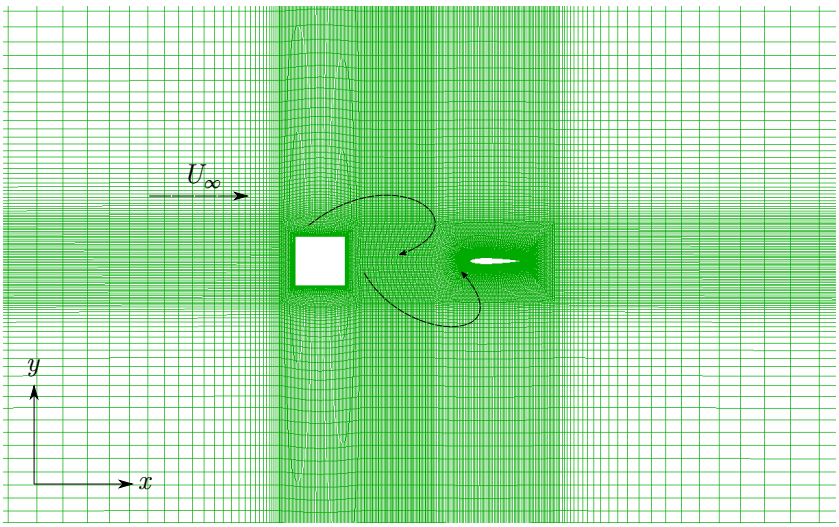

(a) H-grid domain overview

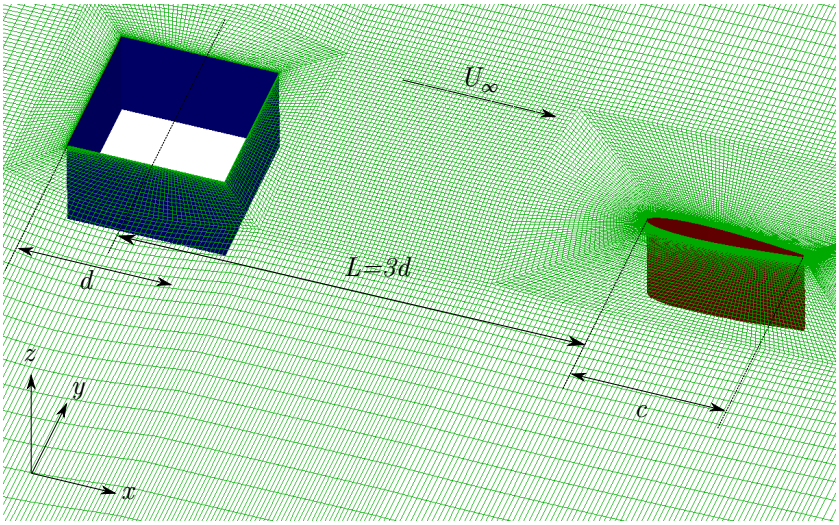

(b) Local grid around the Beam-Airfoil configuration

Figure 4.3: Structured grid topology for beam-airfoil computations.

reference (Figure 4.2a), with the freestream angle of incidence determining the angle-of-attack with the airfoil, which is conducted at $\alpha = 0^\circ$ (Figure 4.2b).

To study the effects of the airfoil *with* wake interference, the NACA0012 is placed aft of the bluff-body at $L/d = 3$, where the origin is at the bluff-body center, with the separation distance measured to the airfoil leading edge (Figure 4.3a). The square beam bluff-body adjacent to the freestream serves as a wake generator in tandem to the NACA0012 airfoil trailing behind at $\alpha = 0^\circ$ relative to this freestream direction (Figure 4.3b). Both geometries share identical characteristic lengths where $d = c$.

In terms of the exact geometries for the NACA0012, it should be noted that the trailing edge for the airfoil used for the Beam-Airfoil case features a cropped trailing edge cusp by 0.75% its reference chord. However, the shortened chord due to the crop has been extended to its intended absolute length to compensate. This modification is made to assist in the generation and overall

grid quality at the trailing edge of the airfoil for the structured H-grid topology used for the Beam-Airfoil case. The wake-free case however, does not feature this cropped cusp because of the C-grid topology that is used.

4.2.2 Boundary Conditions and Grid Calibration

The solution domains are velocity-driven, with a freestream velocity inlet coupled with a reference static pressure outlet. No-slip boundary conditions are imposed on the walls of the bluff-body and airfoil, with all remaining boundaries taken to be smooth as slip-walls of zero flux and normal components (symmetry). Grid convergence for the wake-free case is done, and is based on the approach outlined in Section 2.4.

The internal fields of the DDES solution are initialized after calibration with the Spalart-Allmaras Reynolds Averaged Navier-Stokes (RANS) one-equation turbulence model. These are conducted under steady flow assumptions with this grid convergence approach. In previous work for bluff-body wake capture, it was validated that a wake refinement resolution of $\Delta_{wake} = 0.05d$ is adequately fine to capture both the first- and second-moment statistics along the wake center (time-averaged velocity and root-mean-square of the fluctuations) up to a distance of $x/d = 6$. Based on this experience, the same grid requirements are imposed for the current Beam-Airfoil case, especially in the wake region bounded by the two geometries in tandem where $\Delta_{wake} \approx 0.03d$. Table 4.1 summarizes the case statistics for the following work.

Table 4.1: Case summary (Re=21,400).

Case	Method	α (°)	d/c	L/d	$\overline{y^+}_{avg}$	Δ_{wake} (d)	Δt_c	t_c
NACA0012	DDES	0	–	–	0.56	–	3.125×10^{-3}	156.25
Beam-Airfoil	DDES	0	1.0	3.0	–	0.03	3.125×10^{-4}	187.5

4.3 The Reference NACA0012 Case

Assessment of the near-wall grid resolution is based on the dimensionless wall distribution over the chord of the airfoil, illustrated in Figure 4.4. The resulting grid resolution shows a distribution of $\overline{y^+} < 1$ over a majority of the chord and Figure 4.5 illustrates the chord-wise pressure coefficient distribution. At $\alpha = 0°$, the symmetrical flow condition poses an identical distribution over both its upper and lower surface with a suction peak approaching $\overline{C_p} = -0.5$ around $0.1x/c$. At this attitude, the flow is still relatively attached, with an adverse pressure gradient over its remaining chord aft of the suction peak. These results agree well with other numerical benchmark data [186, 187] that are extracted and also presented in Figure 4.5.

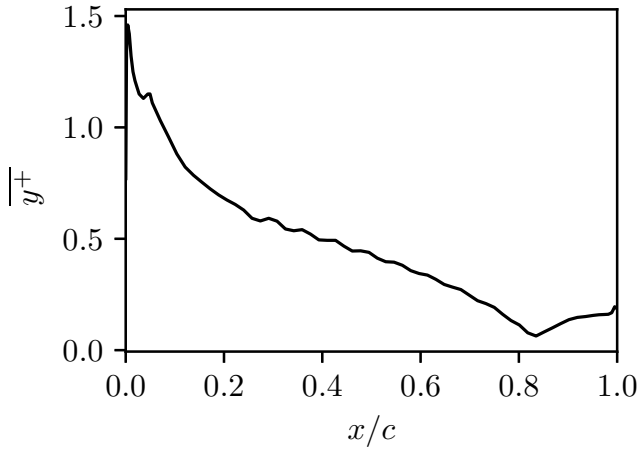

Figure 4.4: y^+ distribution of over the NACA0012 at 0 degree angle-of-attack.

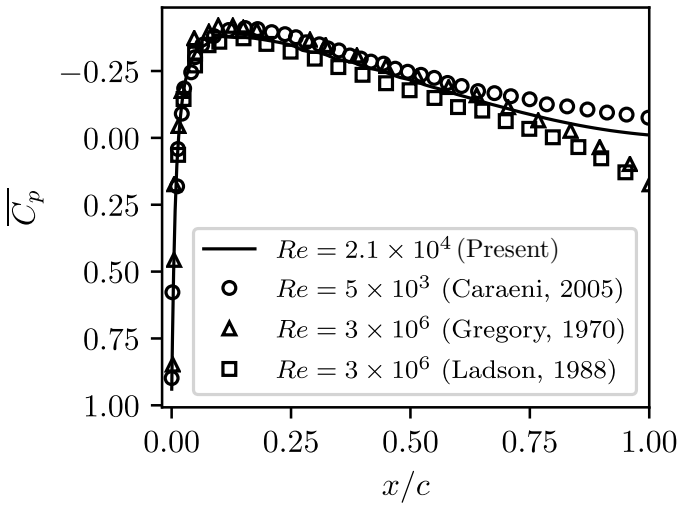

Figure 4.5: Evaluation of pressure coefficient distribution over the NACA0012 at zero degree angle-of-attack (present study: $Re = 2.1 \times 10^4$) against pre-existing data [186, 187].

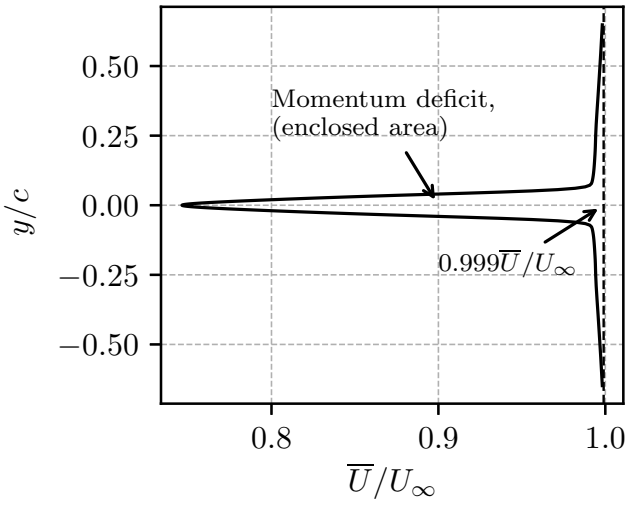

Figure 4.6: Wake velocity deficit for the wake-free NACA0012 at $\alpha = 0^\circ$ measured downstream at $x/c = 2$. Limits for integration are bounded at 99.9% of the freestream velocity.

4.3.1 NACA0012 Near-Wake Validation with the Momentum Method

Wake characteristics can be described as the re-merger, or rearward extension of the boundary layer with a loss of momentum in the fluid, characterized as a deficit in dynamic pressure due to profile drag. As the fluid encounters an object, momentum is lost, resulting in a region of slower moving fluid surrounded by the faster moving freestream. Transition to turbulence then occurs a short distance downstream, where mixing with the freestream, a recovery in momentum and widening of the wake can be observed [27].

The zero-lift wake shed by the airfoil is then validated using the Jones wake momentum method [2] where the deficit in dynamic pressure across the wake profile is taken due to its profile drag. This velocity deficit across the wake profile characterizes the airfoil profile drag defined by:

$$C_{d_0} = \frac{2}{c}\int^{w} \frac{\sqrt{H_w - p_w}}{\sqrt{H_\infty - p_\infty}}\left(1 - \frac{\sqrt{H_w - p_\infty}}{\sqrt{H_\infty - p_\infty}}\right) dy, \tag{4.1}$$

where the limits of integration are bounded within the velocity deficit curve as in Figure 4.6. Results for the respective pressures and velocities are obtained along $x/d = 2$ and numerically integrated to obtain the total momentum deficit based on Equation 4.1. The result obtained at $x/c = 2$ is plotted in Figure 4.6. Values on this profile are based on cell-centres and are numerically integrated with the Simpson's rule where,

$$\int_a^b f(x)dx \approx \frac{\Delta x}{3}(y_o + 4y_1 + 2y_2 + 4y_3 + 2y_4 + \cdots + 2y_{n-2} + 4y_{n-1} + y_n). \tag{4.2}$$

The resulting area under the curve amounts to a $C_{d0} = 0.0255$, with a difference of 8.3% compared to the measured surface drag integral over the airfoil at 0.0278. These results are evaluated

against experimental data [188,189], and as shown in Figure 4.7, where the non-linearity of drag coefficients against Reynolds numbers is presented. Here, the obtained drag coefficient taken as a surface-integral compares well with the data [188, 189], while the result from the momentum method slightly under-predicts this. This validates the results obtained for the NACA0012 under conventional wake-free conditions and will also serve as a baseline reference for comparison with the main case under the effects of a wake encounter.

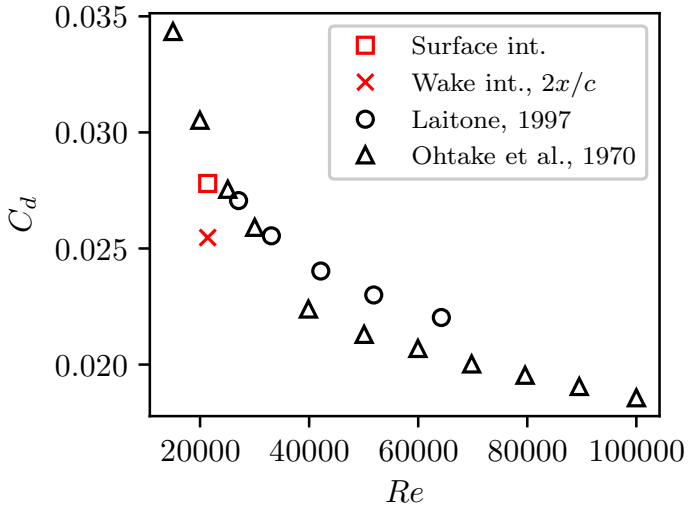

Figure 4.7: Drag coefficient of the NACA0012 measured as a surface integral and with the wake momentum method at $2x/c$ (present study in red), compared with pre-existing experimental data against Reynolds number [188, 189]. Obtained data are at $Re = 21\,400$.

4.4 Bluff-Body Wake Definition and Validation

Before evaluating the effects of the airfoil in wake interference, the validity of the bluff-body wake was evaluated [185]. Its vortex shedding dynamics and wake profile were validated against pre-existing experimental data [68]. These DDES results (Figure 4.8) in comparison to those from selected URANS models like the SA and k-ω SST models (URANS results not reproduced here) demonstrate excellent accuracy that is comparable even to that of LES [76] against experiments on the given grid resolution ($\Delta_{wake} = 0.05d$). Measurements for the wakes first- and second-moment statistics along its centre (Figure 4.9) are obtained up to 6 downstream characteristic lengths, where results are shown to agree excellently with experimental benchmark data [68]. The spectral content in the wake also reveals coherence in the shedding dynamics, evident with a peak frequency of the Fast Fourier Transform and Power Spectral Density of lift and drag time-histories (Figure 3.6). Based on this, the von Kármán wake emanated from the bluff-body can be characterized as a periodic gust experienced by a body located downstream. This

will consequently affect the aerodynamic behavior of the airfoil that will be located downstream as part of this study.

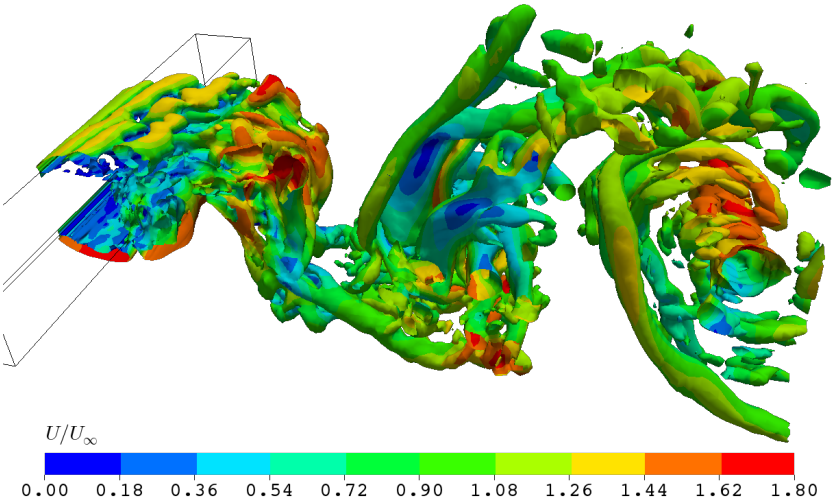

Figure 4.8: Bluff-body wake visualised with λ_2-criterion iso-surfaces (cut-off value $= 50$) contoured by instantaneous freestream-normalised velocity magnitude (U/U_∞).

4.5 The Bluff-Body and NACA0012 Tandem Configuration

Results for the tandem configuration (Figures 4.10 and 4.11) are analysed with both time-averaged and instantaneous fields, detailing the salient flow features as a result of the vortex shedding from the bluff-body and onto the airfoil. The turbulent nature of the flow as illustrated is depicted with iso-surfaces contoured with velocity magnitude where the vortical structures are identified with the λ_2-criterion. These features are as expected of a von Kármán street emanated from the bluff-body, however, due to the presence of the airfoil, the formation of the vortex roll-up emanated from the shear-layer instabilities shed from the leading edges of the bluff-body are interrupted, which subsequently alters the aerodynamic behavior of the airfoil. The following sections detail these results.

4.5.1 Vortex Shedding and Time-Averaged Results

The respective time-histories of the force coefficients for both geometries are illustrated in Figure 4.12. As the airfoil follows the bluff-body in its wake, respective force coefficient time-histories indicate that the signals exhibit an aerodynamic correlation. Their similarities highlight the aerodynamic influence the wake has on the airfoil, which can be similarly inferred with downstream load oscillations that are attributed to wake fluctuations [102]. Further analyses of these force coefficient time-histories for both geometries (Figure 4.12) demonstrates a strong statistical dependence between them as a result of vortex shedding. At this given separation

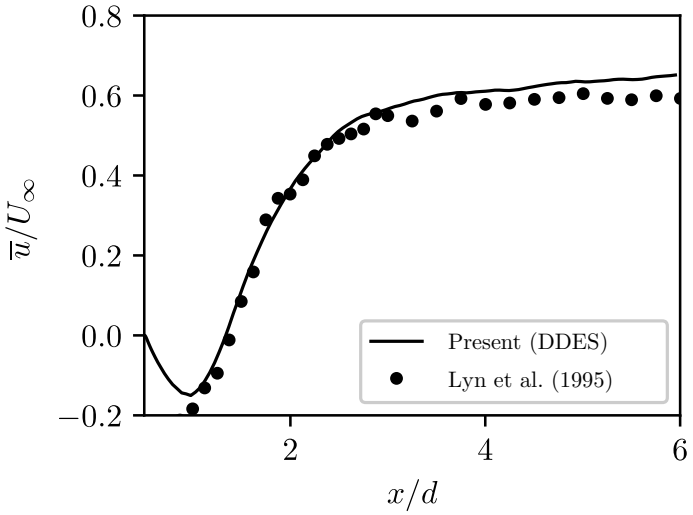

(a) Velocity recovery

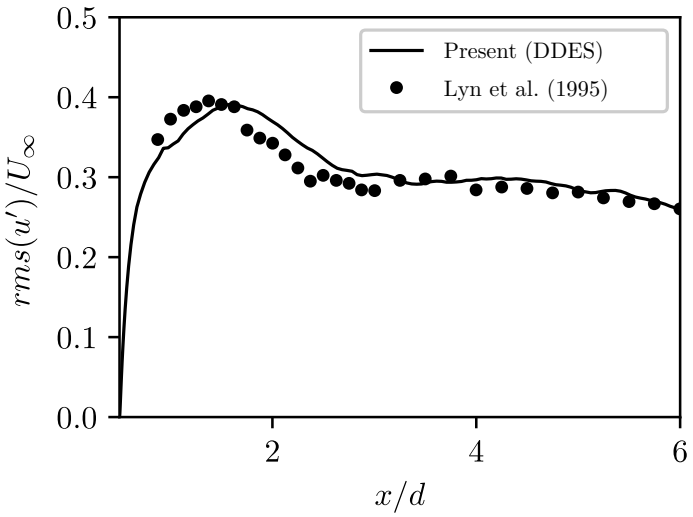

(b) Velocity fluctuation (root-mean-square)

Figure 4.9: Validation of bluff-body wake centre velocity from the present study up to $x/d = 6$ against the ERCOFTAC benchmark by Lyn et al. [68].

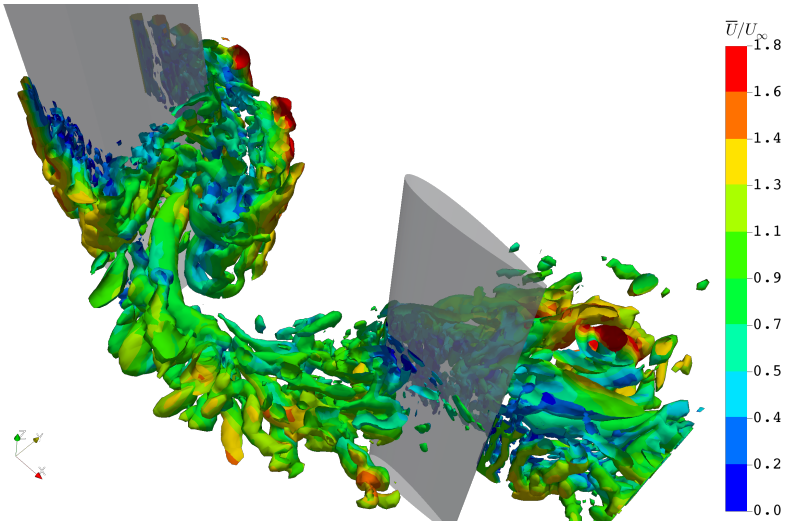

Figure 4.10: Iso-surfaces of λ_2-criterion (cut-off value $= 50$) contoured by instantaneous velocity (U/U_∞).

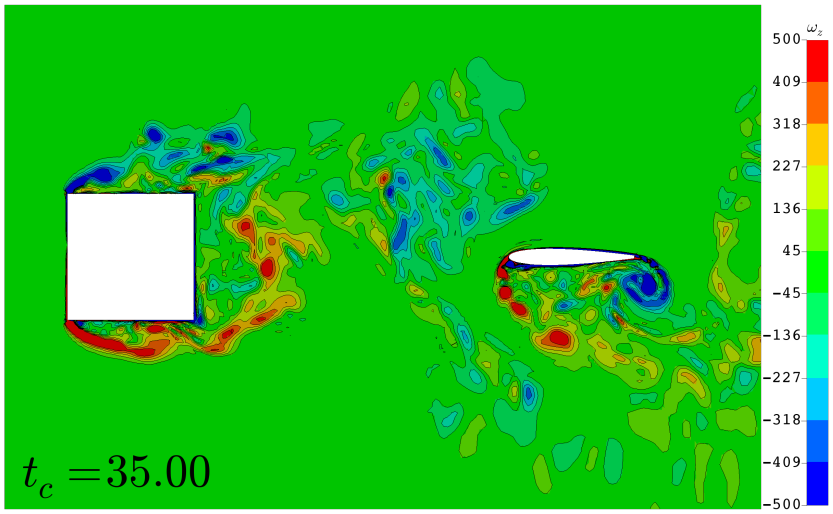

Figure 4.11: Instantaneous contours of span-wise vorticity (ω_z) magnitude.

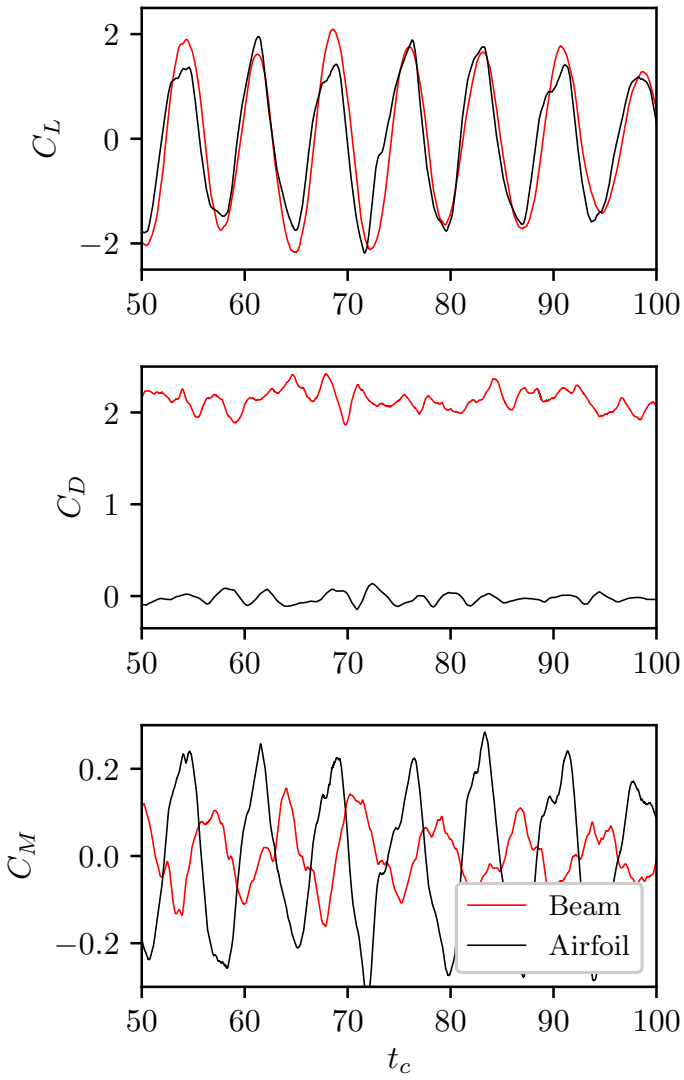

Figure 4.12: Force coefficient history of the tandem configuration for lift, drag, and (pitching) moment coefficients across 50 convective time-steps.

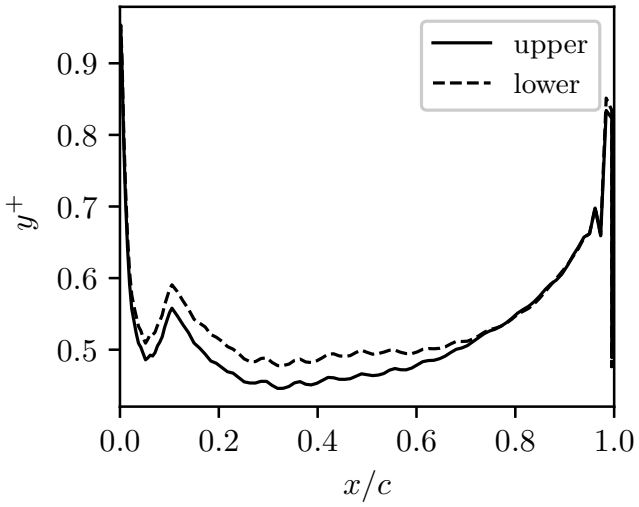

Figure 4.13: y^+ distribution over the NACA0012 in-wake.

distance, the lift coefficients of both the bluff-body and airfoil are strongly correlated with a pairwise correlation coefficient of 0.90, whereas their moments share this similarity but are inversely correlated at -0.75. However, the drag coefficients for the tandem pair do not exhibit any strong correlation at only -0.11.

To ensure that adequate treatment is provided at the walls of the airfoil for capturing surface-forces, the extent of the near-wall grid resolution on the airfoil with wake interaction is illustrated in Figure 4.13. The resulting overall y^+ distribution around the airfoil is seen to be $y^+ < 1$ across the entire chord. Under these conditions, the resulting time-averaged surface-force integral of lift with wake interaction is effectively zero, while the airfoil located at this distance ($L/d = 3$) in the wake responds with negative drag at -0.0221. This behaviour is similarly reported by Lefebvre and Jones [84]. Furthermore, due to the highly turbulent content in the wake, the resulting aerodynamic effects acting on the airfoil are revealed in their respective frequency spectra illustrated with the Fourier series and Power Spectral Density in Figure 4.14. In these results, a distinct frequency of 4 Hz for lift and approximately 8 Hz for drag is clearly indicated. This relationship between the frequencies for the freestream-parallel and cross-stream directions are approximately double, and is typical of von Kármán dynamics [185]. This dominant shedding frequency is also reflected in the wake bounded by the two geometries at the probed $L/d = 2$ location (Figure 4.15). Notably, a slight reduction in the dominant shedding frequency (from 4.44 Hz to 4 Hz) is noted between the airfoil and benchmark validation cases. This difference could be attributed to changes in circulation of the flow field from the presence of the airfoil, acting as detached splitter plate despite the separation distance [190]. This is known to affect circulation, depending on configuration and the airfoils relative length and strength of secondary vortices. Similarly, time-averaged velocity contours illustrated in Figure 4.16 reveal a blanketing of the NACA0012 in a region of lower velocity and dynamic pressure (from constant

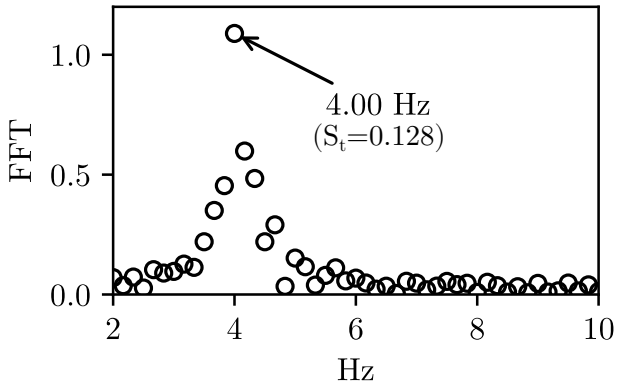

(a) Fourier transform (C_L only)

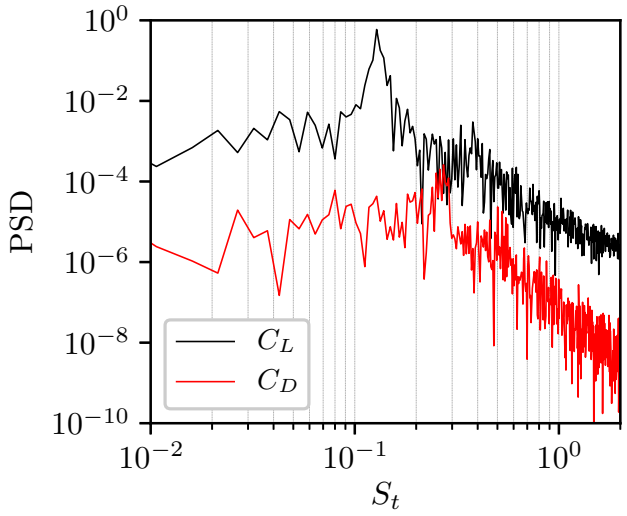

(b) Power spectral density

Figure 4.14: Frequency and power spectra of lift and drag coefficients for the NACA0012 from wake interference.

density) surrounding the airfoil. In terms of the time-averaged forces, the tandem configuration has a negligible impact on the bluff-body when compared to those obtained in the past work for its drag coefficient and Strouhal number. As such, apart from the apparent reduction in lift frequency, further upstream effects the airfoil has on the bluff-body are neglected.

Due to the blanketing of the wake shed by the bluff-body, it is expected for the NACA0012 to exhibit pressure coefficient characteristics comparable to that of the reference wake-free case but with a diminished pressure profile as a consequence of the lower dynamic pressure in the bluff-body wake. However, the time-averaged result reveals separated flow over the airfoil as it is engulfed by the wake. In terms of pressure, this is defined as a suction over both upper and lower surfaces denoted by a negative $\overline{C_p}$ across its entire chord. The pressure distribution (C_p) is used to quantify the effects of the wake on the airfoil surface. At an effective zero degree

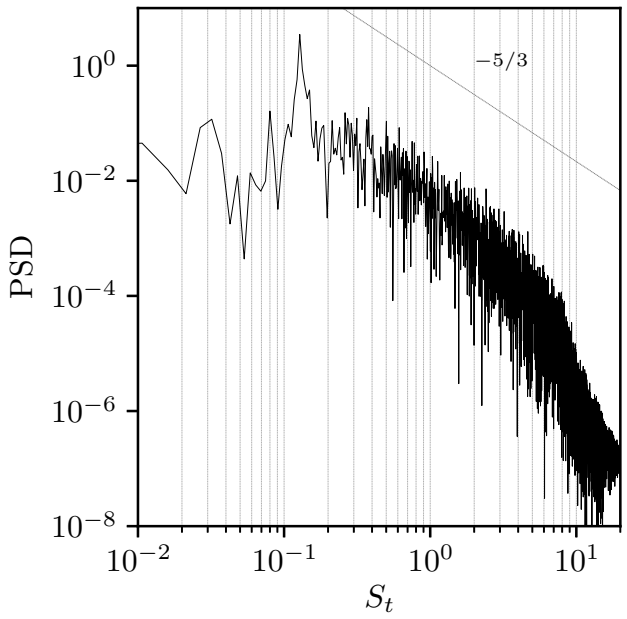

Figure 4.15: Power spectral density of wake velocity magnitude at $L/d = 2$.

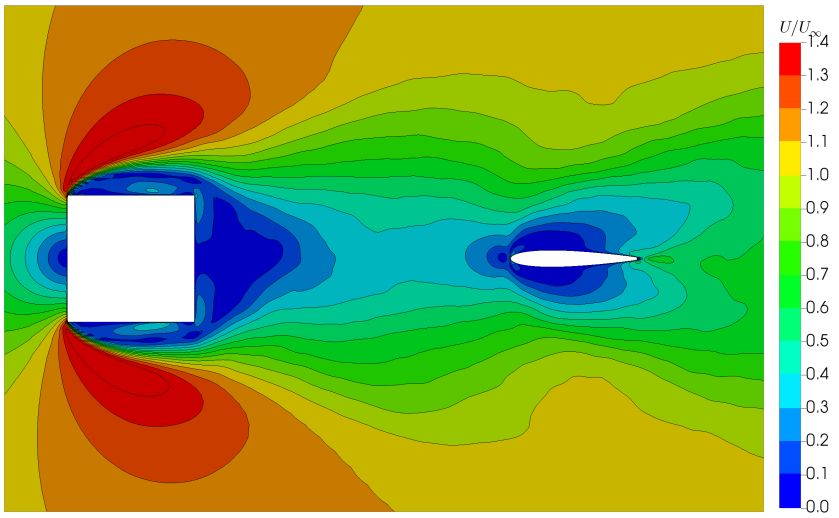

Figure 4.16: Time-averaged freestream-normalised velocity magnitude ($\overline{U}/U_\infty$) results at $L = 3d$.

angle-of-attack, this pressure distribution can be used to obtain its lift bounded by these profiles across the upper and lower surfaces, where,

$$C_l = \frac{1}{x_{TE} - x_{LE}} \int_{x_{LE}}^{x_{TE}} \left(C_{p_{lower}}(x) - C_{p_{upper}}(x) \right) dx. \tag{4.3}$$

Here, $x_{TE} - x_{LE}$ is the chord length, with C_p as the pressure coefficient over the upper and lower surfaces of the airfoil section. The chord-wise distribution of time-averaged pressure coefficient over the NACA0012 is shown in Figure 4.17. For these statistics, the time sample size is taken to be adequately large to ensure that the result does not differ significantly in the span-wise direction, and the symmetry between the upper and lower surfaces cannot be obtained without significantly increasing the time-history of the solution. The result compares the pressure coefficient distribution for both in- and out-of-wake effects acting on the airfoil.

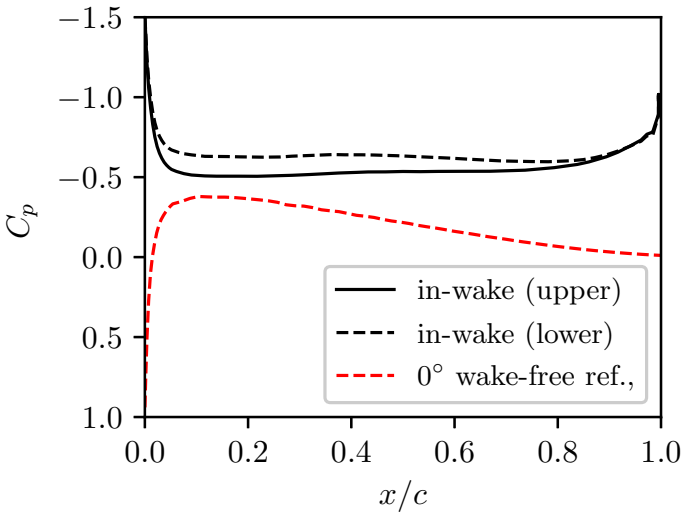

Figure 4.17: Pressure coefficient distribution over the NACA0012 with both in- and out-of-wake interference as reference.

4.5.2 Breakdown of Instantaneous Flow Features

As the resulting flow is unsteady, instantaneous results will provide valuable information on flow behavior, especially regarding the transient interactions between the wake and airfoil. Freestream-normalized instantaneous velocity contours are shown in Figure 4.18 with their respective pressure coefficient counterparts in Figure 4.19. The time-steps have been selected to best portray the dominant flow features as the wake emanates from the bluff-body and interacts with the NACA0012. The instantaneous results reveal the interaction of vortex shedding pairs emanated from the leading edges of the bluff-body as shear-layers that subsequently roll up into vortices. This affects the flow characteristics around the NACA0012 located $x/d = 3$

downstream, which creates its own LEV/TEV pairs. These vortices shed throughout the tandem bluff-body and airfoil system can be easily distinguishable through the low pressure coefficient cores in Figure 4.19.

The instantaneous time-series begins at $t_c = 35.00$ (Figure 4.18a) to allow the flow to develop, and shows the formation of a vortex roll-up that has detached from the upper leading edge of the bluff-body geometry. Simultaneously, the velocity contours around the NACA0012 exhibits a significant downwash forming both LEV/TEV from the airfoil (Figure 4.20c).

Subsequently at $t_c = 36.56$, as the vortices shed from the bluff-body convect downstream, this region of higher velocity induces a lower pressure region above the airfoil (Figures 4.18b and 4.19b). At this instant, an early formation of a leading edge (separation) vortex is evident over the airfoil leading edge.

At $t_c = 38.44$, as the flow convects past the upper surface of the airfoil exiting the frame, the LEV detaches from the airfoil leading edge with another at its trailing edge clearly visible in Figure 4.19c. This exhibits contours that can be expected from that of heaving or plunging motions, and is similarly mirrored to the beginning time-step (Figure 4.18a and 4.18c). At this instance (4.19c), up to seven low pressure vortex cores are distinguishable, where five vortices are shed originating from the bluff-body shear-layer instabilities (three at bluff-body shear-layer, two between the geometries), and a LEV/TEV pair shed from the airfoil.

Approximately half the shedding cycle is completed at $t_c = 40.00$, as the flow is now effectively a mirrored instance of that captured in $t_c = 36.56$, where a low pressure region exists above (now under) the airfoil. However, the formation of the airfoil LEV is not visible here. The remaining instances ($t_c = 42.50$ and 44.06) complete the flow cycle, alternating between low and high pressure regions above and below the airfoil again.

Transient effects on the airfoil can be better appreciated through the instantaneous profiles of pressure coefficient (Figure 4.21) at the same selected convective time-steps. Overall, the instantaneous pressure on the airfoil resides on the suction side ($C_p < 0$), agreeing with the time-averaged results based on the in-wake results (Figure 4.17).

At $t_c = 35.00$ (Figure 4.21a), a region of positive C_p exists between $0.2 < x/c < 0.6$ indicating a downwash which agrees with the corresponding velocity and pressure contours shown in Figures 4.18 and 4.19. On the lower surface, the relatively flat C_p distribution indicates an effect of massive separation without reattachment throughout the entire chord. The same observations can conversely be made when shedding cycles alternate at the bluff-body upper and lower surfaces at $t_c = 38.44$ and $t_c = 42.50$ (Figures 4.21c and 4.21e). These three instances indicate a suction of approximately $C_p = -1.5$ over the respective surfaces, which is significantly higher than the suction peak in the reference wake-free case at approximately $\overline{C_p} = -0.5$, despite the airfoil being located at the wake center.

The remaining time instances at $t_c = 36.56$, 40.00, and 44.06 exhibit the transition effects between shedding cycles. At $t_c = 36.56$ (Figure 4.21b), The initial formation of a leading edge

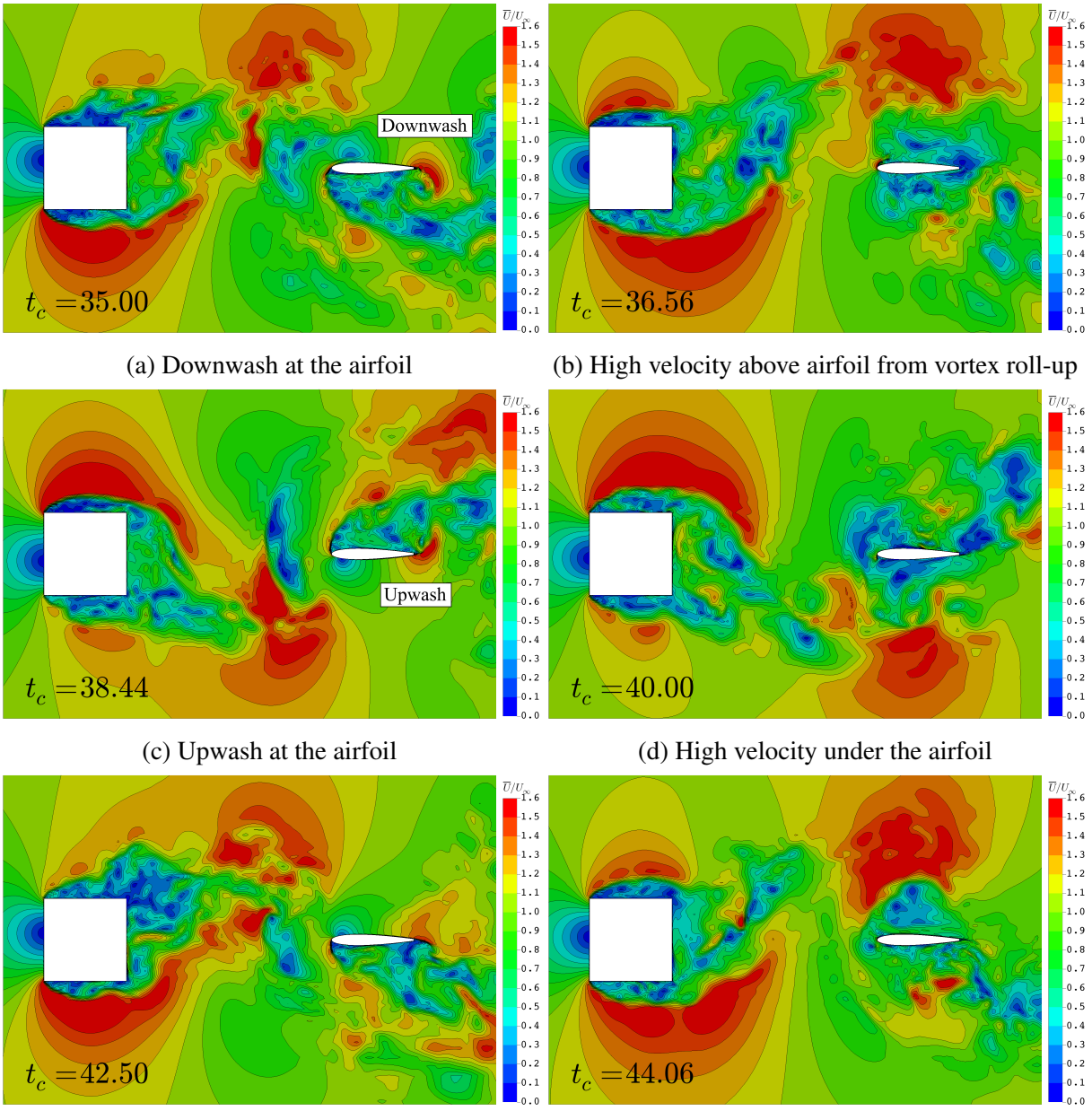

(a) Downwash at the airfoil

(b) High velocity above airfoil from vortex roll-up

(c) Upwash at the airfoil

(d) High velocity under the airfoil

(e) Downwash at the airfoil

(f) Flow cycle repeats

Figure 4.18: Consecutive freestream-normalised velocity contours (U/U_∞) at a separation distance of $L/d = 3$ demonstrating wake interference inducing massive flow separation over the NACA0012.

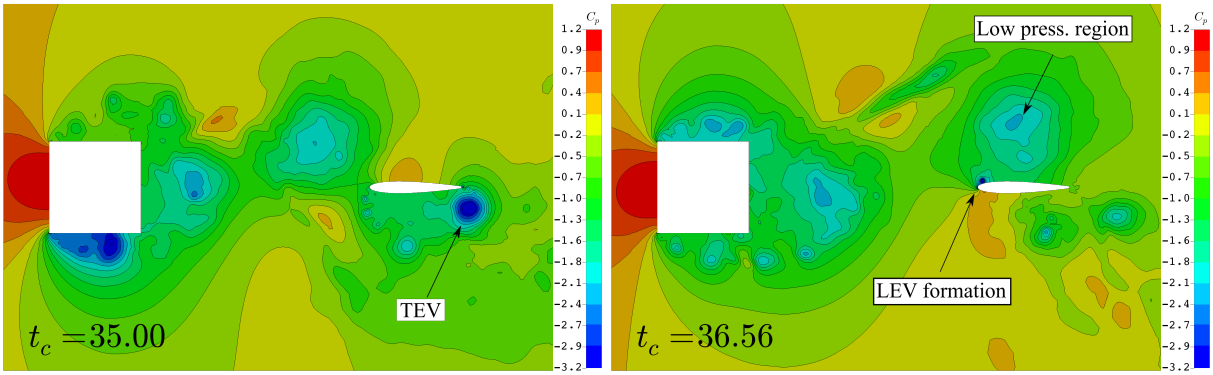

(a) Airfoil TEV clearly visible

(b) Low pressure above airfoil with LEV formation

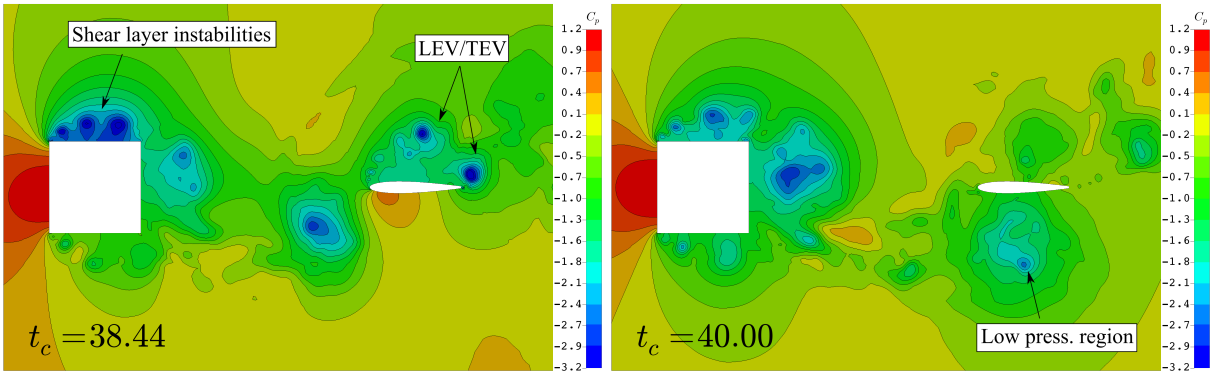

(c) Bluff-body instabilities with LEV and TEVs

(d) Low pressure region under the airfoil

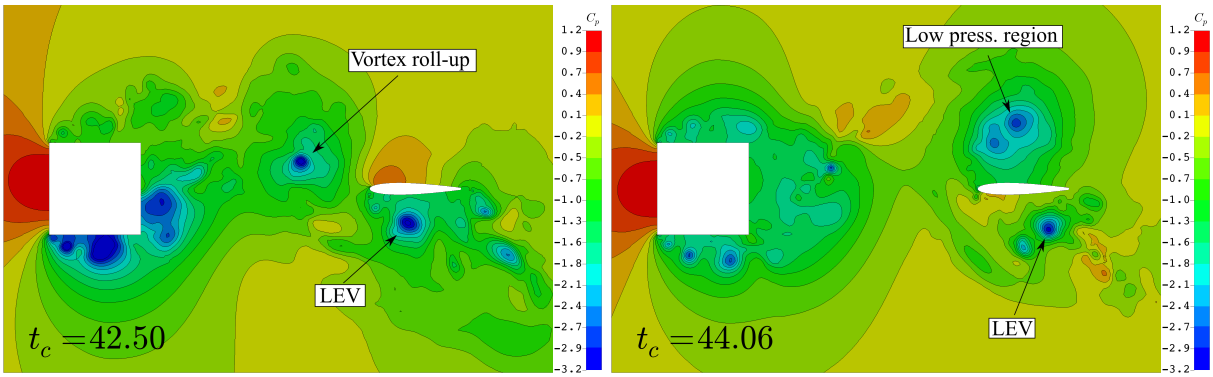

(e) Several LEVs and TEVs visible again

(f) Flow cycle repeats

Figure 4.19: Consecutive pressure coefficient contours (C_p) at a separation distance of $L/d = 3$. Low pressure vortex core regions (in blue) are clearly distinguishable.

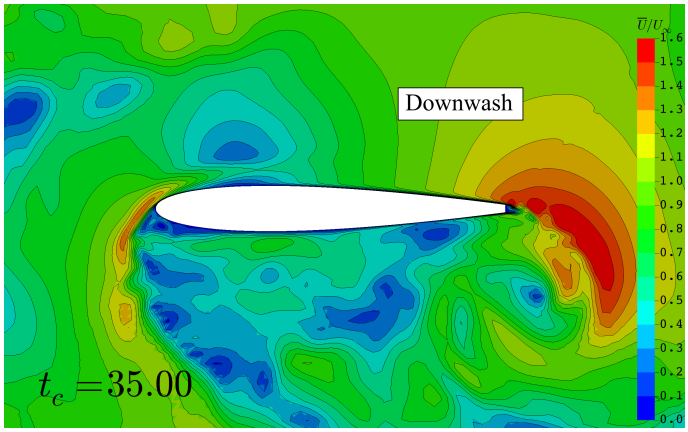

(a) Velocity magnitude (U/U_∞)

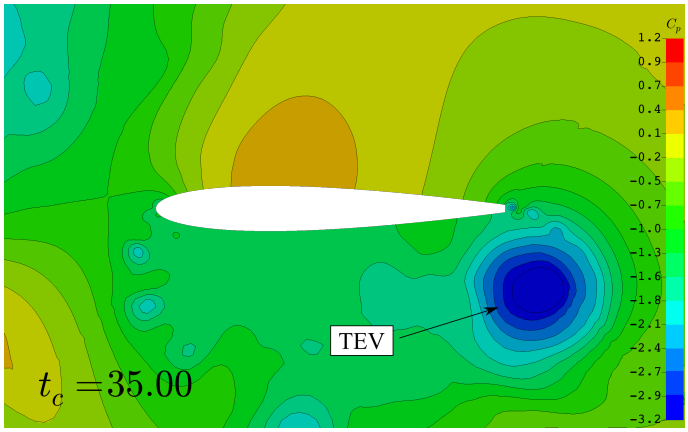

(b) Pressure coefficient (C_p)

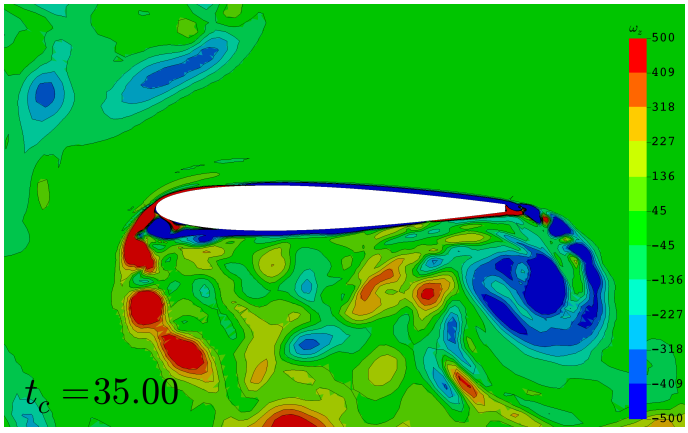

(c) Span-wise vorticity (ω_z)

Figure 4.20: Instantaneous contours around the NACA0012 at $L/d = 3$, at a characteristic time of 35.00.

separation vortex is denoted with a corresponding spike in C_p just forward of $0.1x/c$, up to a peak of almost $C_p = -3.0$, and transitions with some reattachment for the remainder of the chord. The general C_p profile at this instant exhibits similarities to that of an airfoil at high angle-of-attack [90], whereas this effect here is wake-induced. This formation of the leading edge separation vortex (visible in Figure 4.19b) corresponds with its own higher pressure peak (positive C_p) as a stagnation point on the lower surface just aft of the leading edge at approximately $x/c = 0.1$. The remaining two time instances (Figures 4.21d and 4.21f) feature a relatively reduced bounded areas defined by their C_p curves. At these time-steps, the overall lift is reduced by way of Equation 4.3 as the airfoil is obscured from the freestream by the bluff-body.

4.5.3 Wake Interference as a Harmonic Relative Motion

The results around the trailing airfoil so far are based on flow field contours and surface pressure coefficients that exhibit behaviors expected from oscillatory heave dynamics. As the data reveals sinusoidal characteristics with a distinct frequency in the spectra presented in Figure 4.14, the characteristic frequency from the raw signal is used to obtain an attenuated sinusoidal response reconstructed with this dominant frequency ($f = 4.00\,\text{Hz}$, $k = 0.402$) and the standard deviation of the signal ($\sigma = 1.13$). An extract of the loads on the airfoil in terms of its lift coefficient is plotted in Figure 4.22 across 50 convective time-steps.

The aerodynamic response related to an unsteady sinusoidal gust field can be approximated with the Sear's function [94]. This provides an alternative assessment of the wake-induced unsteady aerodynamic loads at the airfoil. In addition to verifying the response from the wake encounter, applying the function reveals its potential to approximate the airfoils response due to wake encounter. In this function, an airfoil moving through a sinusoidal gust field with a vertical velocity expressed as a function of time can be defined by $w_g = w_{g0}e^{j\omega t}$. Here, the gust amplitude, w_{g0} is taken as the time-average vertical velocity component that corresponds to the gust direction along the wake center at the chosen separation distance ($x/d = 3$) that was previously validated (Figure 4.9). The lift response acting at the quarter-chord point of an airfoil can then be described as a function of reduced frequency k, where,

$$L = \frac{1}{2}\rho U_\infty c a_1 w_{g0} e^{j\omega t}\phi(k), \tag{4.4}$$

with a_1 as the airfoil lift curve slope, and $\phi(k)$ is the Sear's function with its magnitude estimated with [191]:

$$|\phi(k)|^2 = \frac{d+k}{d+(\pi d+1)k+2\pi k^2}. \tag{4.5}$$

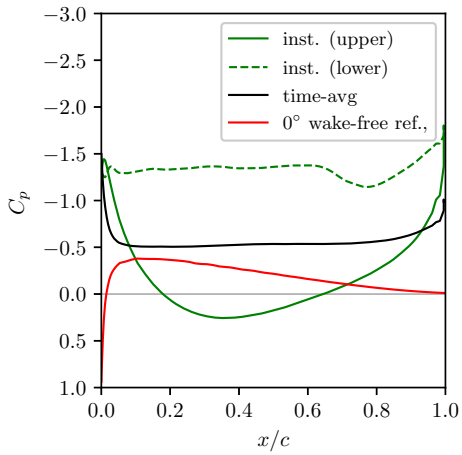

(a) 35.00

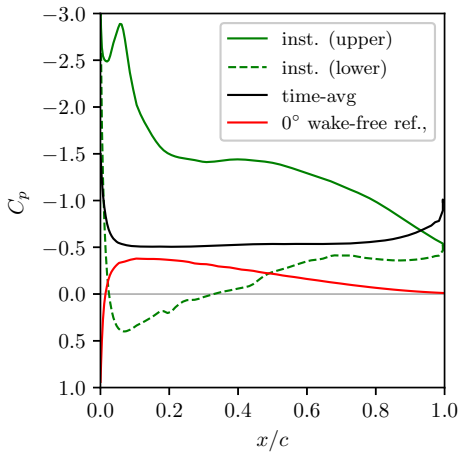

(b) 36.56

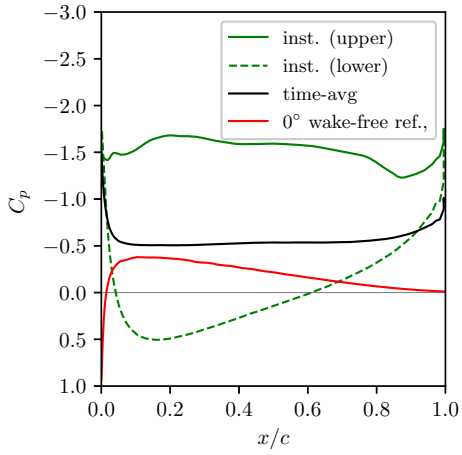

(c) 38.44

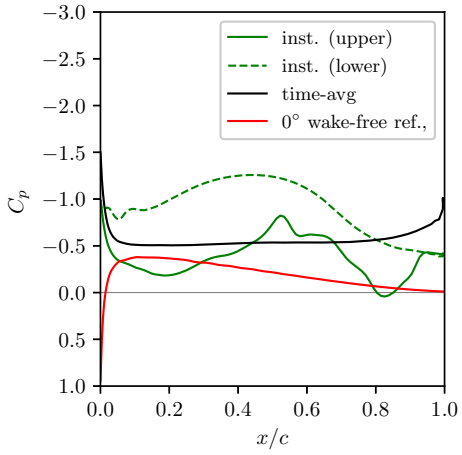

(d) 40.00

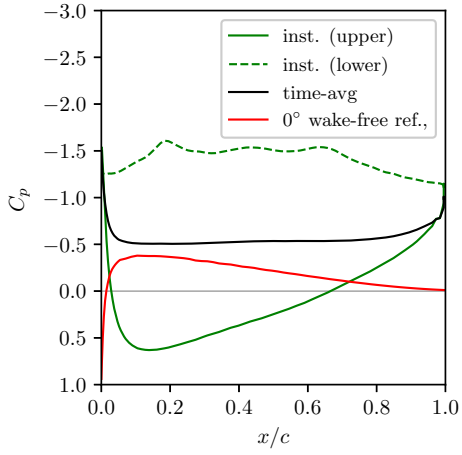

(e) 42.50

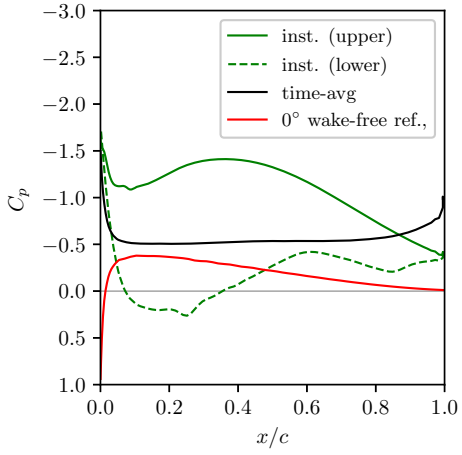

(f) 44.06

Figure 4.21: Instantaneous pressure distributions over the NACA0012 with wake encounter. Reference to time-averaged results for both in- and out-of-wake interference are also illustrated.

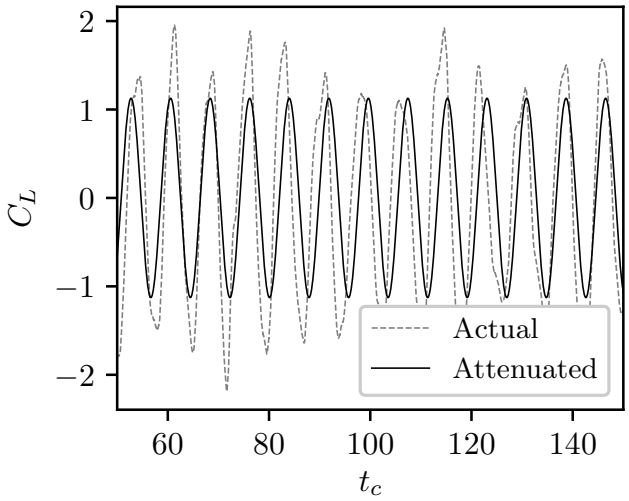

Figure 4.22: Lift coefficient time-history of the NACA0012 in-wake (raw data) with its attenuated counterpart.

The constant $d = 0.1811$ and the phase of $\phi(k)$ is approximated as a piecewise function with:

$$\angle\phi(k) = \begin{cases} -48.095k^2 + 87.297k^4 - 61.471k^3 + 21.917k^2 - 3.664k, & k \leq 0.61, \\ 0.982k - 0.597, & k > 0.61. \end{cases} \tag{4.6}$$

Similar to the Sear's function, the Theodorsen's function $C(k) = F(k) + jG(k)$ is also based on reduced frequency where the approximate expression for $C(k)$ can be obtained with [94]:

$$C(k) = \begin{cases} 1 - \dfrac{0.165}{1 - \dfrac{0.045}{k}j} - \dfrac{0.355}{1 - \dfrac{0.30}{k}j}, & k \leq 0.5, \\ 1 - \dfrac{0.165}{1 - \dfrac{0.041}{k}j} - \dfrac{0.355}{1 - \dfrac{0.32}{k}j}, & k > 0.5. \end{cases} \tag{4.7}$$

with the lift response:

$$L = \pi\rho b^2 \left[\ddot{z} + U_\infty\dot{\theta} - ba\ddot{\theta}\right] + 2\pi\rho U_\infty bC(k)\left[\dot{z} + U_\infty\theta + b(\tfrac{1}{2} - a)\dot{\theta}\right], \tag{4.8}$$

where $z = z_0 e^{i\omega t}$ and $\theta = \theta_0 e^{i\omega t}$ for oscillatory heave and pitch displacements, respectively. Due to the nature of the velocity contours and pressure coefficient distribution acting on the airfoil, a heave-only assumption is taken for the relative motion, reducing the lift response to

$$L = \pi\rho b^2\ddot{z} + 2\pi\rho U_\infty bC(k)\dot{z}. \tag{4.9}$$

The resulting reduced frequency for the airfoil under wake effects is represented on the corre-

sponding Sear's and Theodorsen's function complex planes in Figure 4.23. The approximations of $\phi(k)$ and $C(k)$ based on Eqs. (4.6) and (4.7) are $\phi(k) = 0.42 + 0.08j$ and $C(k) = 0.62 - 0.18j$, respectively. Subsequently, the resulting lift coefficients are obtained through the Eqs. (4.4) and (4.9) to provide the response of the airfoil given in Figure 4.24.

From these results, the chord-normalized wavelength of the sinusoidal gust is then obtained to be $7.81\lambda_g/c$ based on a gust assumption. For the airfoil taken as a relative heave motion, it is discovered that a chord-normalized heave amplitude of $3.6z_0/c$ approximates the attenuated lift signal well. Both functions here have shown to be good estimates of the airfoil's response under the influence of the bluff-body wake with respect to the attenuated lift signal, noting that it is based on the standard deviation. Under the conditions of the study, the proposed approach could be useful as an initial insight to the potential aerodynamic loads the downstream geometry experiences from wake encounter. Represented as a relative harmonic motion with the Sear's or Theodorsen's functions, this approach can be utilized as an empirical approximation prior to in-depth analyses for a wake encounter.

4.6 Chapter Closure

A high-fidelity simulation framework evaluating the effects of a wake encounter on a symmetrical airfoil is conducted at $Re = 2.14 \times 10^4$. This is based on a canonical example of a bluff-body and NACA0012 airfoil in tandem separated by $3d$. The bluff-body acts as a wake generator, comparable to an aerodynamic obstacle such as a building to an aircraft in its wake. The numerical solution is based on a Delayed Detached-Eddy Simulation technique, performed on a structured grid using the OpenFOAM solver with discretisation schemes that are nominally second-order accurate. As validity of the response by the airfoil is dependent on the accuracy of wake capture, the vortex shedding characteristics and wake profile of the bluff-body have been verified based on a experimental benchmark case. In addition, the evaluations for the airfoil under wake effects are performed with reference to a baseline (wake-free) case that is further verified at zero degree angle-of-attack.

At this separation distance, the respective geometries exhibit a strong positive correlation in lift and moment behaviour. While weakly correlated for drag coefficient, the wake induces a negative-drag effect on the airfoil. Time-averaging also reveals flow separation occurring over the entire chord, denoted by a negative pressure coefficient acting away (suction) from its surface. Combined with this, the unsteadiness of the wake field induces the shedding of airfoil LEV/TEV with pressure distribution resembling heave motion or large-amplitude gust. As it is revealed that as the resultant lifting behavior by the airfoil is oscillatory, an attempt at approximating this response is performed using the Sear's and Theodorsen's functions. Although both functions are dependent on reduced frequency, the airfoil's response can be approximated with the Sear's function by using the wake information at the given separation distance as the gust

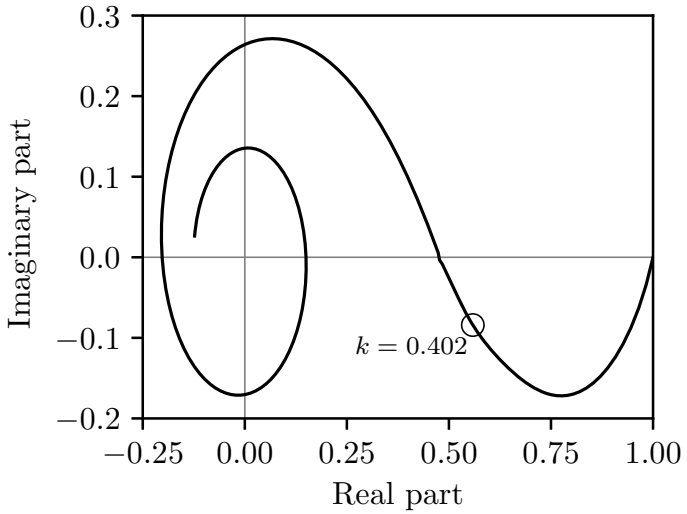

(a) Sear's function

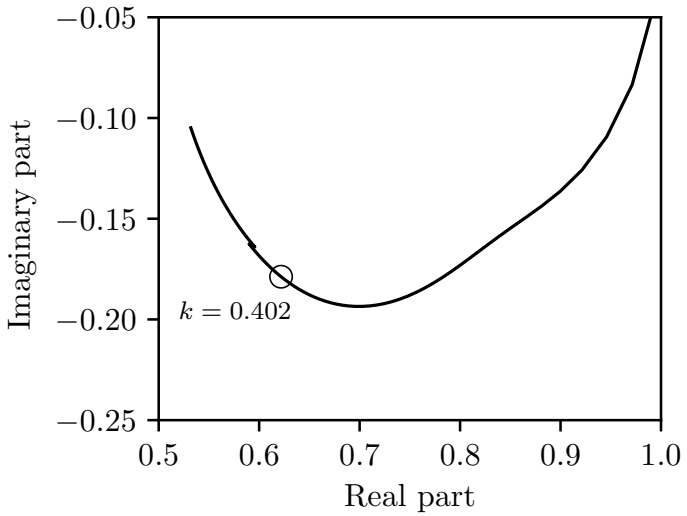

(b) Theodorsen's function

Figure 4.23: Reduced frequency of the NACA0012 in wake encounter with respect to the complex plane representation of the Sear's and Theodorsen's functions.

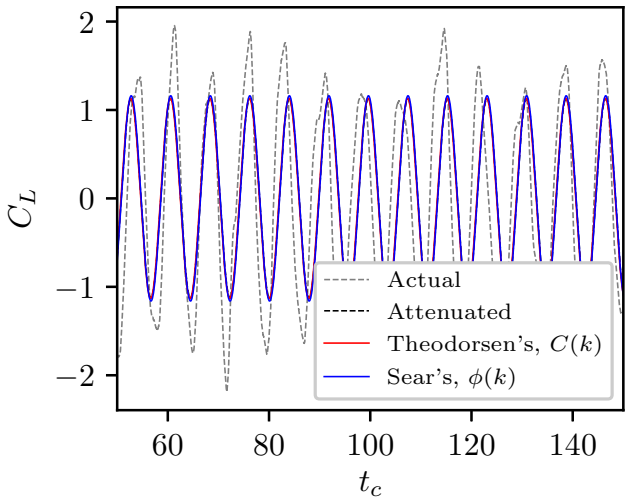

(a) Overview of lift response

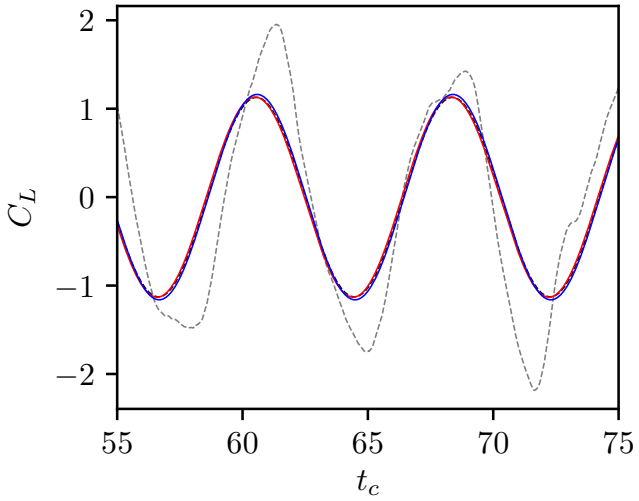

(b) Close-up across 20 convective time-steps

Figure 4.24: Comparison of lift response due to wake data modeled as a gust encounter (Sear's function), and as a heave (Theodorsen's function) in comparison to the attenuated and actual lift time-histories.

field. On the other hand, the Theodorsen's function approximates this airfoil lift response with a chord-normalized heave amplitude that is obtained heuristically under the given conditions of this study. This suggests that the effects of a wake encounter can be reduced to the relative effects of heave oscillation and gust loads at the airfoil.

However, the resulting response can be attenuated based on these simplifications, as the effects of the entire frequency content in the turbulent flow field should ultimately be considered. Furthermore, these conclusions are limited to the respective longitudinal directions as any spanwise effects are neglected. An infinite span was used for the geometries as part of the work focused on validating the wake results. Although this can be extended to geometries of finite aspect ratios (e.g. cuboids), such analyses would complicate the validation of wake dynamics, and is therefore unconsidered in the present work. Additionally, the sensitivity of the results could be further tested to include separation distance and Reynolds number as control variables. This is particularly useful for testing the approximations made by the unsteady response functions under the proposed simulation framework. While it would be expected for some results to differ, the underlying mechanisms for a wake encounter that are demonstrated here should still be relevant.

In view of the above, the results highlight the impact of a bluff-body wake encounter on the aerodynamics of a downstream geometry modelled as an airfoil. The resultant behaviour induced by the wake is oscillatory, exhibiting characteristics similarly expected to those of forced harmonic pitch and heave motions. The work subsequently proposes an approach to approximate this behaviour, which can be convenient for preliminary assessment prior to in-depth analyses for aircraft operating at such regimes. This can be especially useful at flight envelopes in proximity to obstacles such as buildings or ships that emanate wakes considerable to aircraft aerodynamics.

Chapter 5

Wing-Tail Under Forced Harmonic Pitch

5.1 Introduction

While the stability of an aircraft is driven by its tail [5], the adverse effects of the wing wake become more apparent and dominant at higher angles-of-attack. At these attitudes, the size of the wake width grows as the flow separates over the wing, resulting in a region of reduced dynamic pressure. This wake width then develops into what is larger than the characteristic length of the wing, which can blanket the tail [52], reducing its effectiveness and pitch authority. Although these effects can be generally avoided with different tail heights and configurations, it has been found that the effects of the wing wake are generally present and experienced by the tail throughout an aircraft flight regime [102].

So far, the effects of a wake encounter using the present computational framework have been demonstrated exclusively under static conditions (Chapter 4). This led to a better understanding of wake physics and its aerodynamic impact on a wing-section downstream. However, wake encounter regimes can often be compounded with dynamic conditions, with the motion of the bodies in tandem. Aircraft wing-tail aerodynamics are taken as an example of this. Furthermore, wake characteristics develop dynamically as the attitude of the geometries change, resulting in complicated and challenging physics to predict. The transition between attached and separated flow emanates unsteadiness in wake characteristics which will impact the downstream aerodynamics differently. As mentioned in Chapter 1 (Section 1.6.1), a gap exists in the literature where aircraft wing wakes are investigated mostly under static conditions [52, 102], while those under dynamic conditions require more focus on the wing wake region [62, 63]. This chapter therefore aims to advance the understanding of wake interactions occurring under forced harmonic motion, inducing dynamics that cannot be accomplished by exclusively investigating static cases that have already been established in the literature.

To achieve this, the geometry in this chapter focuses on a wing-tail configuration in tandem experiencing dynamic pitch. The motion of the bodies are relative to a single rotation centre, representative of an aircraft undergoing pitch oscillations. This reveals any dormant interactions

between wing wake-tail dynamics. The harmonics of the problem also enables dynamic flow phenomena to be studied where an oscillating wing wake transitioning between attached and separated flow from pitch is expected. The wake is expected to interact with a tail geometry downstream which experiences a coupled pitch/heave motion as a result of its tail moment arm.

The resulting aerodynamics at the tail due to the wake is a function of several components in a dynamic system. Namely, its physical motion relative to the rotational centre with its tail length, the freestream flow conditions affecting wing wake properties, together with the reduced frequency of the harmonic system. These ultimately affect the timing and position of the tail relative to the wake throughout the pitch motion. The interaction between the wing and tail is therefore complicated, and revealing the underlying tail aerodynamics as a result this will be challenging. Considering the many variables involved, these conditions of study will have to be pre-determined. An isolated geometry that only considers the wing and tail will be used, taking that the wing is the major contributor to aerodynamic interference at the tail. Focus will be on capturing tail aerodynamics as a consequence of the described pitch oscillations. Along with the insight provided on wing wake-tail interference, a recommendation for using the Theodorsen's function to simplify and predict tail loads will be made.

5.2 Simulation Methodology for Dynamic Pitching

The flow conditions are set at $Re_c = 2.14 \times 10^4$ relative to the wing chord, referencing standard sea-level conditions, assuming fully turbulent, incompressible, isothermal conditions of the Navier-Stokes equations. These flow conditions are identical to what is used in the previous chapters for consistency, following the validation of flow separated wakes conducted in Chapter 3. While these freestream conditions may not be representative of flight conditions [102], it translates to a reduced frequency that is comparable to the dynamic cases in the literature [62, 63]. For turbulence modelling, the previous chapters have also demonstrated that the DDES hybrid RANS/LES modelling method is highly suitable for capturing wake behaviour and is therefore used here again. Likewise from the previous two chapters, the variant used is based on the SA formulation [83]. The DES method is also suitable in this context as flow separation is expected to be induced during the pitch cycle. While viscous wake effects will be dominant, a suitable turbulence modelling method—such as DES, will be needed to capture the relevant wake physics.

To achieve dynamic grid motion, the overset method is used to translate the respective subgrids for the wing and tail geometries in time. The pitch oscillations for angular displacement, $\Delta\alpha(t)$, are described using simple harmonic motion, where,

$$\Delta\alpha(t) = \alpha\cos(\omega t - \phi), \tag{5.1}$$

with the output with respect to convective time illustrated in Figure 5.1. The complete mesh motion for the total simulation time is then provided as a look-up table, which allows up to 6-DOF to be described at each time-step for the complete harmonic motion of the overset grids. In the present case only pitch is considered. Prior to the motion, an initial angle-of-attack is set to $\alpha = 5^\circ$ in the meshing stage, and a time of $\phi = 6.25t_c$ is given for the flow to develop, with uniform initial conditions. Velocity and pressure contours for this developed flow after $6.25t_c$ is shown in Figure 5.2. Following this instant, forced harmonic pitching begins at a frequency of 1 Hz resulting in a reduced frequency of 0.1 and is allowed to undergo a total of three cycles.

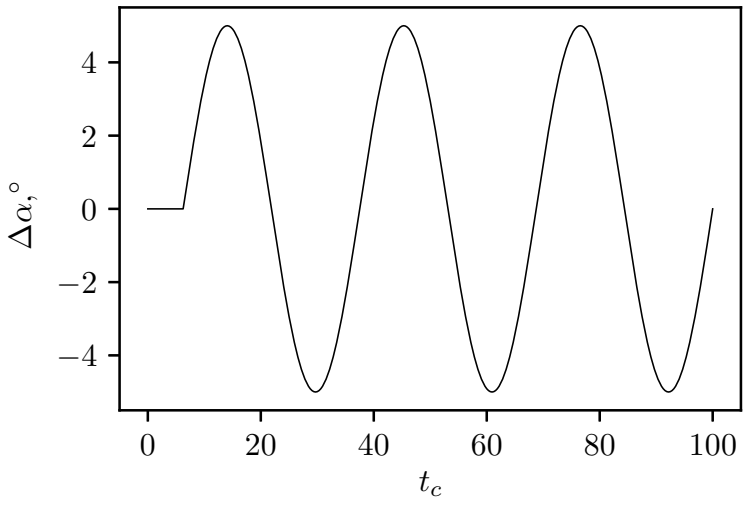

Figure 5.1: Three-cycle forced harmonic pitching motion induced to the wing-tail configuration of 5° in addition to its nominal angle-of-attack, at 1 Hz. A flow development time of $6.25t_c$ is allowed before mesh motion occurs.

Due to the large gradients induced from the mesh motion, a wider range of flow Courant numbers are expected compared to static conditions as seen in $t_c \leq 6.25$. The PIMPLE algorithm is used [192], coupled with a *Co*-based adjustable time-stepping method that is limited to a $Co_{max} < 4$. This is calibrated for computational efficiency accounting for the minute cells along the trailing edges of the wing and tail boundary layer grids. In spite of this, the average $Co \leq 1$ throughout the solution domain. The strategy proposed by Frink [62] and Thompson et al. [63] suggests tracking the number of solution iterations per harmonic cycle to establish numerical convergence is only valid for constant time-stepping solutions. As an adaptive time-stepping technique is used here, the strategy outlined in Section 1.5.5 by them cannot be applied on the present case. Adopting such an approach would be computationally inefficient from the large range of cell sizes present in the domain, and a too large of a time-step size would cause temporal resolution to decrease to unacceptable levels. To overcome this, the first pitch cycle is closely monitored and the numerical tolerances are calibrated to allow an adequate amount of iterations for convergence across this initial phase. This results in a total number of iterations that ensures

numerical convergence, with a slight trade off in computational efficiency.

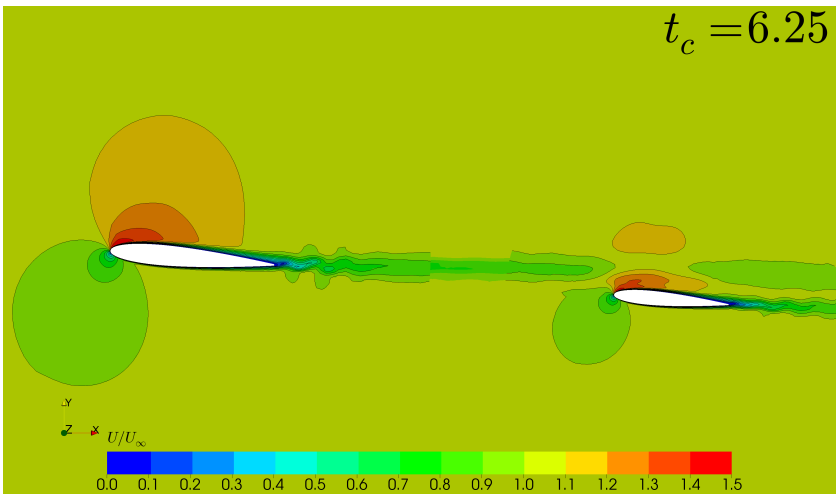

(a) Freestream-normalised velocity magnitude (U/U_∞)

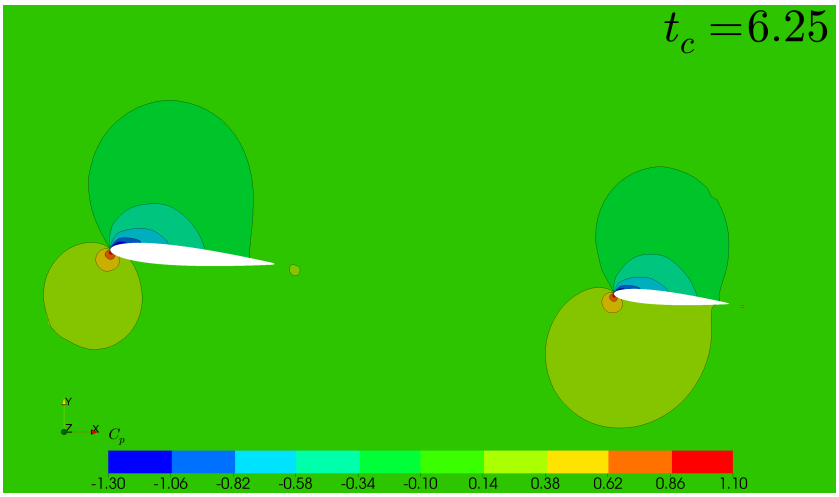

(b) Pressure coefficient contours (C_p)

Figure 5.2: The initial flow condition after a flow development time of $6.25t_c$ with a nominal angle-of-attack of 5°.

5.2.1 Overset Grid Methodology for Forced Harmonic Motion

The wing-tail geometry consists of two NACA0012 rectangular wing-sections in tandem. To represent a conventional wing-tail configuration, the chord of the NACA0012 tail located downstream at the rear is reduced to 70% of the front (main) wing chord ($C_{tail} = 0.7C_{wing}$), with a separation distance of $x/C_{MAC} = 4.28$. This separation distance is based on typical tail lengths suggested by Silverstein and Bullivant [112] and an average of those aircraft tail lengths and mean aerodynamic chords surveyed in Table 1.2 (Section 1.5.3). There is no vertical displacement of the tail relative to the wing chord line, and both wing and tail are at 0° incidence to the freestream when level.

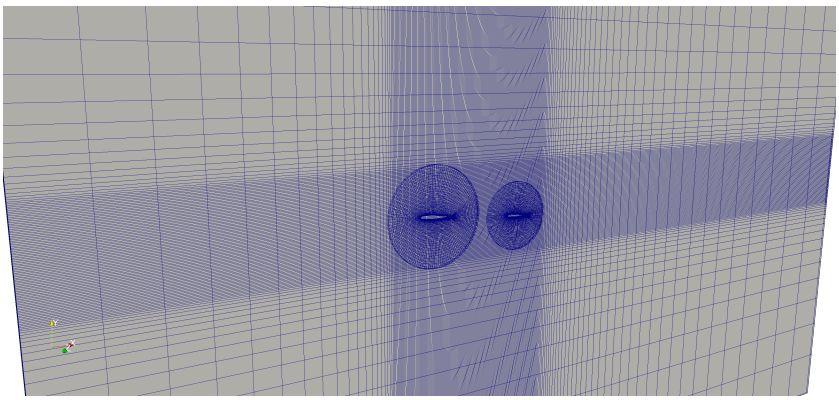

(a) Domain overview

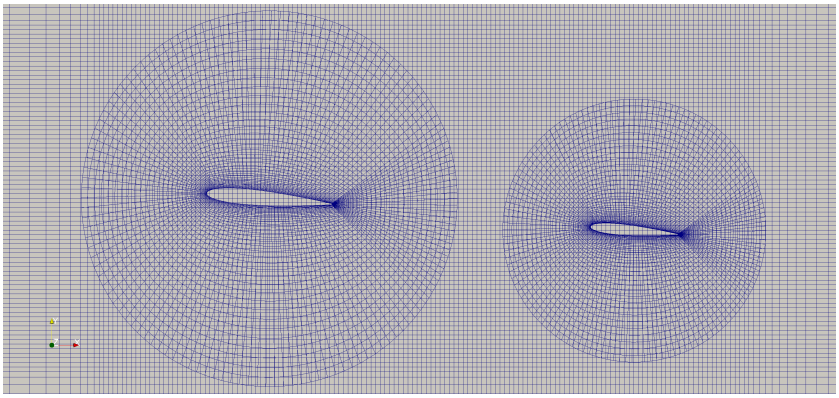

(b) Close-up view of the wing-tail configuration

Figure 5.3: Overset grid overview of the wing-tail configuration onto a background grid with localised grading concentrated towards the wake region. Centre of rotation occurs about $0.25C_{MAC}$.

The individual overset grids for the wing and tail are superimposed over a background grid that defines the overall computational domain, making this a 3-part mesh (Figure 5.3). Cell clusters that provide the wing wake refinement region is accomplished with the background mesh as illustrated in Figure 5.3a. The local cells in this refinement region are set to $\Delta_{wake} \approx 0.05C_{MAC}$. This domain is adjacent to the oncoming freestream, but the relative position of the tandem configuration is rotated at a $\alpha_0 = +5^\circ$ pitch up clearly seen in Figure 5.3b. The forced harmonic motion then amounts to a nominal angle-of-attack of $\alpha = 5^\circ$ with a $\Delta\alpha(t) = \pm 5^\circ$ pitch amplitude about the wing quarter chord point. This results in the wing undergoing pitch oscillations about $0.25C_{MAC}$ exclusively, while the tail experiences a coupled pitch-heave motion due to its moment arm. This condition is designed to be relatable to pre-existing cases, summarised in Table 5.1.

For the overset grid, the definition of different cell zones have to be defined to allow the continuous transport of variables through the domain. The distinction in these zones is illustrated in Figure 5.4 and 5.5, highlighting the different allocated cell types. These are regions containing empty/blocked cells that represent the geometries (red), the interpolation fringes (green), and the background mesh (blue). The wing and tail sub-mesh zones bounded by their respective inter-

polation fringes are sized at a radius of $1.5C$ from their respective mid-chords. The interpolation fringes do not overlap with this sizing and separation distance for the two sub-meshes. The status of these cells types (empty, background, interpolation fringe) ensures domain connectivity and their coupling [193].

A visualisation of the wing and tail sub-zone meshes relative to the background mesh is depicted in Figure 5.5. Here, the wing and tail sub-zone grids are overlaid on to the background mesh highlighted with different cell types. The background grid is designed to account for approximately four to six empty cells (red) along the thickness of the geometries, with the interpolation fringe (green) for the walls. This ensures that an appropriate background grid definition is given for the geometries, especially for the tail (Figure 5.5b), where the largest movements are expected.

Based on the initial flow development time, the boundary layer grid of both geometries result in a dimensionless first cell height of $y^+ = 1$. For this described grid design, the total grid points in the domain amount to approximately 650k cells for all elements in this 3-part mesh. This is kept economical while uncompromising on the solution integrity in terms of wake refinement ($\Delta_{wake} \approx 0.05C_{MAC}$) as mesh motion can be computationally expensive. This is in contrast to the literature, where entire the aircraft geometries including the fuselage and nacelles are discretised resulting in higher total cell counts.

Similar problem scales are also observed in other work as summarised in Table 5.1, which includes settings for the present case. As highlighted in the literature review, only one of these considers the use of a DDES for dynamic pitch. However, the case by Hall et al. [104] is performed on a BWB geometry which lacks an empennage assembly and is therefore slightly beyond the scope of focus in this work, which emphasises on tail aerodynamics. Most of the simulation parameters are comparable although Mach number is likely to have been determined by wind tunnel test specifications for the other cases. The present results are based only on the DDES turbulence modelling technique coupled with an adaptive time-step based on the instantaneous Courant number during solution run-time. This is in contrast to what is used by Frink [62] and Thompson et al. [63] for reasons discussed in Section 1.5.5. The use of DDES also complements these other two work as it is required for capturing meaningful wake physics that cannot be achieved by RANS that are beyond the scope of their work.

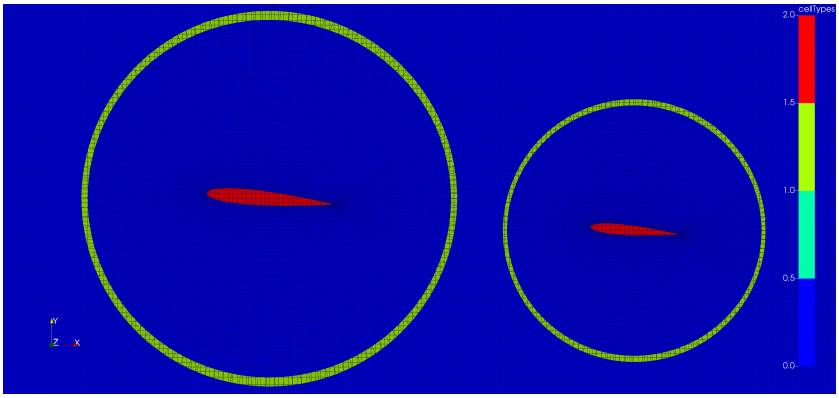

(a) Wing tail sub-zones with outer interpolation fringes

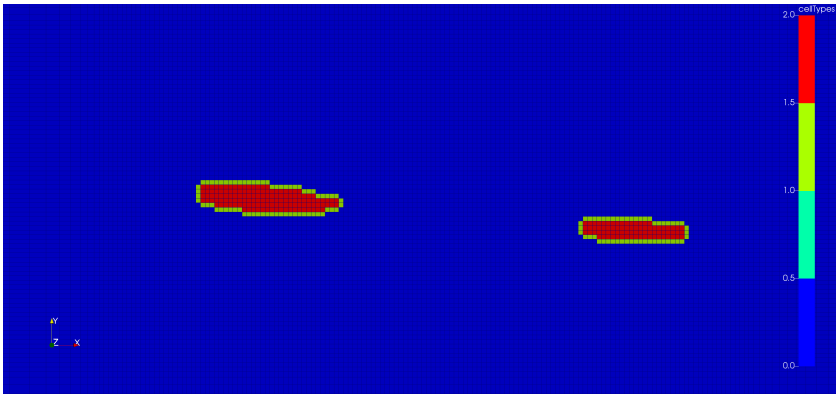

(b) Wing tail grid with wall fringes

Figure 5.4: Overset grid of the wing-tail configuration with the background mesh (blue) highlighting the boundaries of overset cell types (red: empty cells, green: interpolation fringe, blue: background mesh).

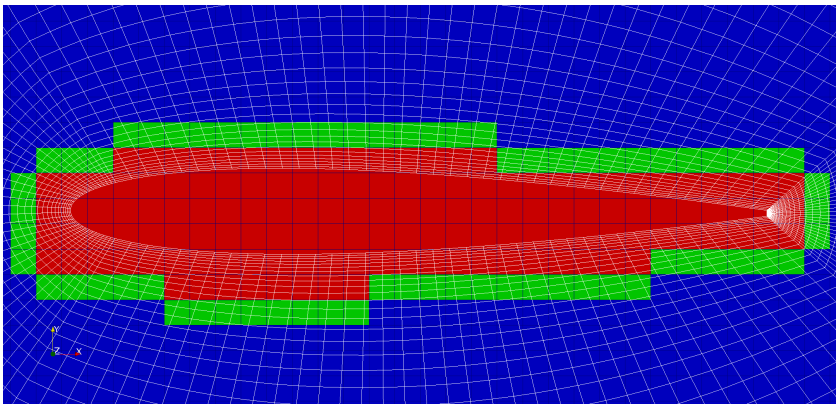

(a) Wing boundary layer grid

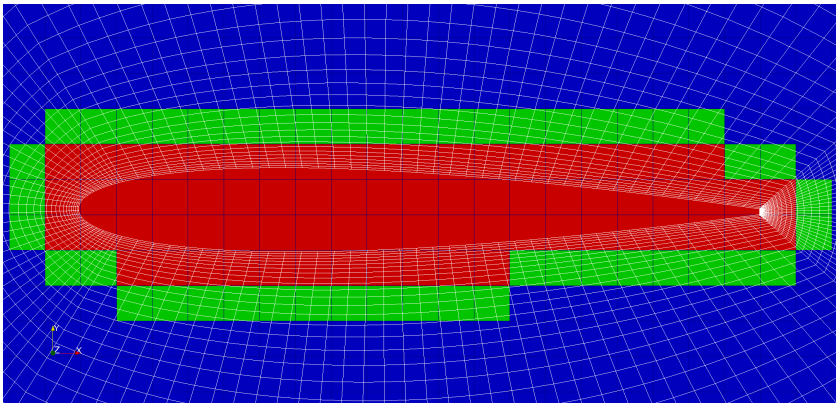

(b) Tail boundary layer grid

Figure 5.5: Both wing and tail boundary layer grids superimposed over the background grid illustrating the contrast in different cell zone sizes (red: empty cells, green: interpolation fringe, blue: background mesh). Note the number of cells that define each region.

Table 5.1: Comparison of reviewed forced pitching oscillation cases, including the present case, comparing flow parameters and case set-up.

Case Geometry	Flow conditions Re, M	Pitch break α	Amplitudes & Frequencies	Characteristic time-step	Total iter. /cycle	Reduced freqs.	Turb. models	Cells (million) y^+ at $0.5C_{ref}$
Present case: Tandem NACA0012	2.1×10^4, 0.01	-	$\Delta\alpha = \pm 5°$ at 5° $f = 1$ Hz	Adaptive Co-based	-	0.1	SA-DDES	0.65 $y^+ = 1$
Hall et al. BWB [104]	7×10^5, 0.1	9°	$\Delta\alpha = \pm 5°$ at 0°, 8°, 16° 24°, 32°	-	-	0.07	SA k-ω SST SA-DDES	0.7, 4.7, 4.9
Thompson et al. GTM [63]	5.4×10^5, 0.077	10°	$\Delta\alpha = \pm 5°$ at 24° $f = 0.43$ Hz 0.12 Hz 0.05 Hz	$\Delta t_c = 0.02$ 1500 time-steps	36000	0.01483 0.00401 0.00167	SA k-ω SST	6, 12, 24 $y^+ = 0.75$
Frink SACCON [62]	1.61×10^6, 0.0144	17.89°	$\Delta\alpha = \pm 5°$ at 0°, 10°, 15°, 20° $f = 1$ Hz 2 Hz 3 Hz	$\Delta t_c = 0.006$ to 0.290	36000	0.06 0.12 0.18	SA k-ω SST	3, 6, 9, 12 $y^+ = 0.5$

5.3 Wing-Tail Behaviour in Forced Harmonic Pitch

The following analyses presents results for the flow over the wing-tail geometry in forced harmonic pitch oscillation. This is conducted at the described motion of $\alpha(t) = 5 \pm 5^\circ$ at $k = 0.1$ that is comparable to the other cases listed in Table 5.1 with the exception of the Reynolds number while still within an incompressible regime. The general observation in the resulting solution shows that as the tandem configuration oscillates, the tail pitches and heaves in and out of the wing wake. This induces a periodic interaction that is evident in the force coefficient time-histories. With the wing as the wake generator, the results can be analysed as two separate parts, by focusing firstly on the wing in harmonic pitch motion that is independently assessed from the tail downstream. This approach is adopted from Etkin and Reid [5] where the aircraft behaviour lies in the synthesis of individual aerodynamic components. The conditions of forced pitching also induces flow separation as the wing stalls at the higher, peak angles-of-attack. This sheds a flow separated wake that will convect downstream to interact with the tail.

Subsequently, the results focus on the tail relative to the wing wake, where the primary contribution lies in advancing the understanding of the tail interaction with its wing wake under these conditions. Key flow features such as its interaction with the wing LEV/TEVs are captured, and presented relative to tail surface pressure distribution as a result of this interaction. As the tail exhibits sinusoidal lift characteristics resulting from heave due to the moment arm, the Theodorsen's function is proposed as a suitable approximation method. However, this neglects the underlying response due to wake encounter, which is observed as distinct variances that deviate along the harmonic response.

Finally, distinct features in the *total* response of the system can be attributed to the wing stall and wake interference with the tail that was previously analysed separately. The total contribution by the system can therefore be described as the synthesis of both wing and wake-tail dynamics. This is revealed in the lifting response of the tandem configuration while undergoes this forced pitching manoeuvre.

5.3.1 Wing Behaviour in Dynamic Pitch

The characteristic waveform of the force coefficients by the wing undergoing the harmonic pitch cycle are illustrated in Figure 5.6. The results are shown across 100 convective time-steps, demonstrating its longitudinal forces and pitching moment response. The section of the solution that is allowed to develop at the initial $t_c \leq 6.25$ is reflected in the output, and plateaus to a quasi-steady state before the pitch oscillations begin. This initial phase begins with a pitch up where the effective angle-of-attack gradually increases up to a peak of $\alpha(t) = 10^\circ$. This characteristic spike in lift coefficient is periodic and can be attributed to the hysteresis of the problem, as $dC_L/d\alpha$ decreases toward the maximum angle-of-attack. A stall indicated with a sharp drop in lift follows the decrease in pitch back down to its nominal value and then its trough at $\alpha(t) = 0^\circ$.

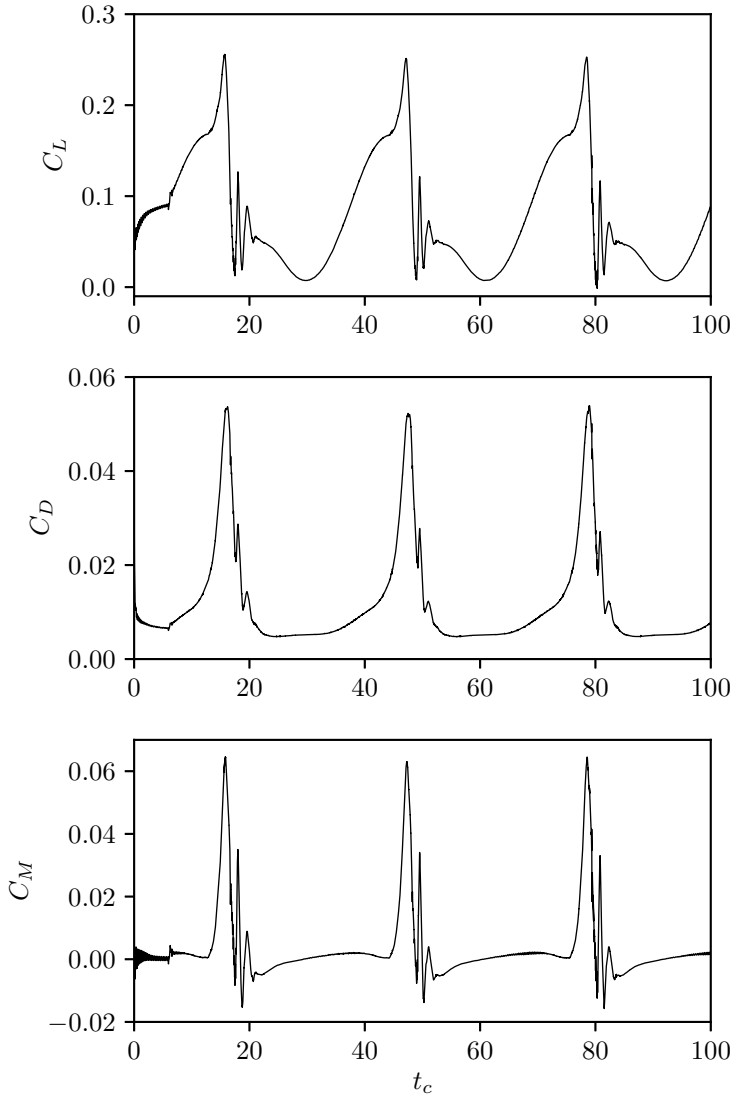

Figure 5.6: Wing-only force coefficient time-history resulting from forced harmonic pitching about $0.25C_{MAC}$ at $\alpha = 5 \pm 5^\circ$.

This is observed to occur for total three pitch cycles.

The hysteresis in the lifting response by the wing is illustrated in Figure 5.7. Here, the initialisation portion of the solution becomes more apparent and the stall behaviour relative to angle-of-attack is better represented. The lift curve is clearly defined up to the maximum $\alpha(t) = 10^\circ$ before the flow separates with a corresponding sharp decline in lift. It is apparent that the wing undergoes a complete stall as indicated by its loss in lift coefficient at approximately $\alpha(t) < 9^\circ$ on the downstroke (point b). Throughout this phase, large oscillations in the lift coefficient occur before it begins to settle at approximately 6° (point c). The reattachment of the flow can be better visualised in terms of its flow field, which are depicted in Figures 5.8. These are taken across $46.88 \leq t_c \leq 50.00$ with contours of velocity magnitude and pressure coefficient, showing the upper surface flow separation that occurs in this phase. The shedding of

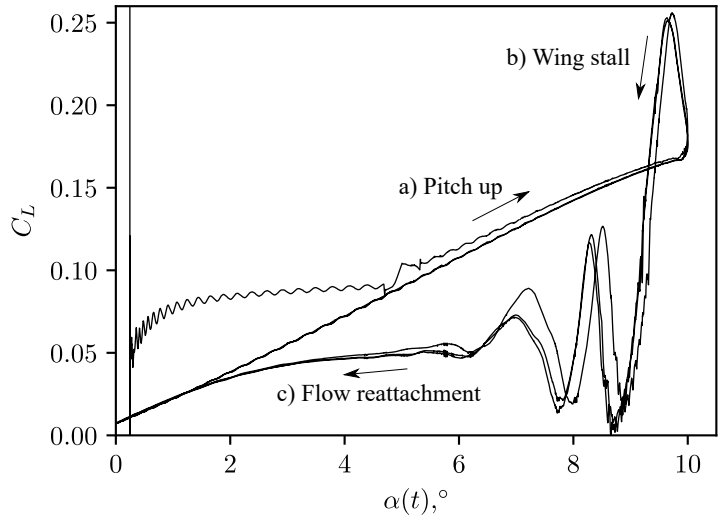

Figure 5.7: Hysteresis of wing lift coefficient against angle-of-attack undergoing forced pitch oscillations (three cycles) about $0.25C_{MAC}$ at $\alpha = 5 \pm 5^\circ$, $k = 0.1$.

the wing LEV/TEV are captured clearly, identified with low-pressure vortex cores that emanate from the leading and trailing edges of the wing.

Two of the corresponding convective time-steps ($t_c = [46.88, 48.44]$, at $\alpha(t) = [9.75, 9.04]^\circ$) in Figures 5.9 show a negative C_p across the entire upper surface of the wing. This is characteristic of a complete wing stall, with the effects of the LEV convecting over the upper surface of the wing captured with a suction peak in negative C_p at approximately $x/c = 0.75$ (Figure 5.9a). This same effect is repeated at $t_c = 48.44$ (Figure 5.9b) as the LEV detaches from the top surface of the wing. However, the LEV and TEV in this instant nearly coalesce toward the trailing edge as depicted in Figure 5.8d. The influence of this larger low pressure vortex core is evident in Figure 5.9b as a large suction magnitude of up $C_p = -3$ can be seen.

As the wing undergoes this harmonic pitch oscillation, its response due to this motion can be approximated with the Theodorsen's function [94] for the estimation of unsteady loads. The results obtained in this section can therefore be partially verified knowing the harmonic pitch characteristics of this predetermined wing motion. Figure 5.10 shows the Theodorsens's approximation in comparison with the wing lift response as a result of forced harmonic pitch oscillation. Note that the sinusoidal function has been corrected to account for flow development time and nominal lift coefficient at ($\alpha_0 = 5^\circ$). The result and the empirical approximation compares well, where both amplitude and phase correspond to the computational results, especially during the pitch-up phases (positive $dC_L/d\alpha$). However, this is with the exception that the function is unable to capture the stall characteristics of the wing. This limitation in the Theodorsen's function agrees with what is reported by Cordes et al. [93] and Amiralaei et al. [194], where it is only limited to moderate angles-of-attack without flow separation. It is worth mentioning that the application of the function here is in contrast to what is demonstrated in Chapter 4, as

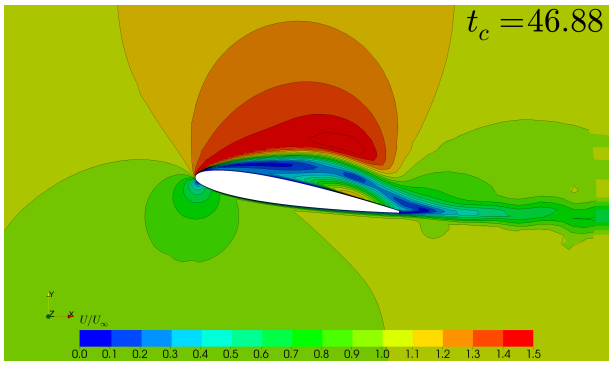

(a) Velocity magnitude, $t_c = 46.88$, $\alpha(t) = 9.75°$

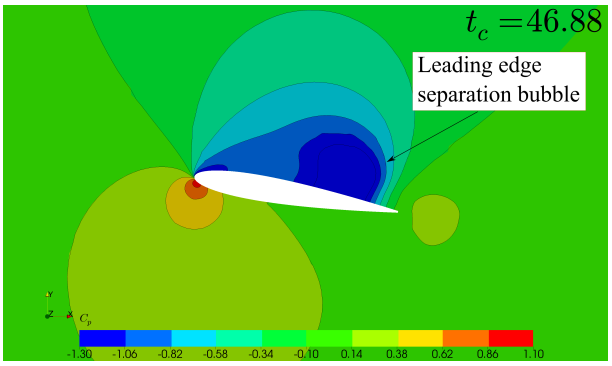

(b) Pressure coefficient, $t_c = 46.88$, $\alpha(t) = 9.75°$

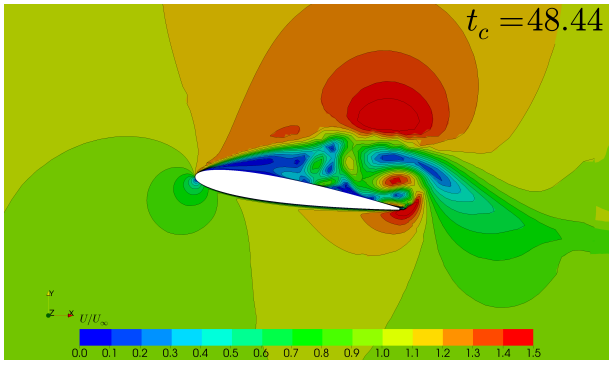

(c) Velocity magnitude, $t_c = 48.44$, $\alpha(t) = 9.04°$

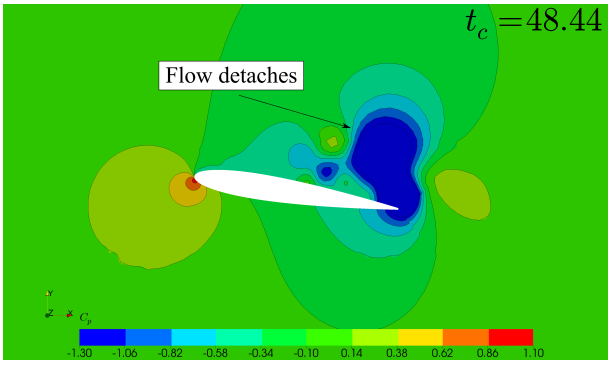

(d) Pressure coefficient, $t_c = 48.44$, $\alpha(t) = 9.04°$

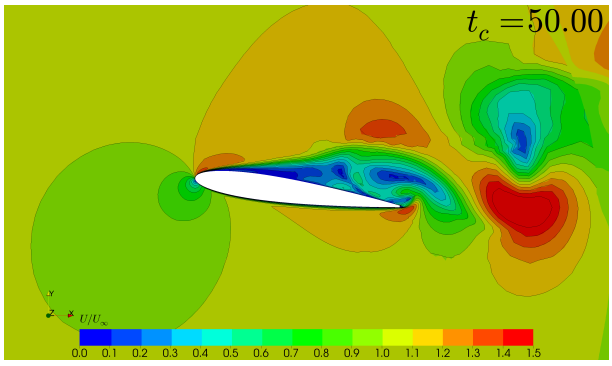

(e) Velocity magnitude, $t_c = 50.00$, $\alpha(t) = 7.93°$

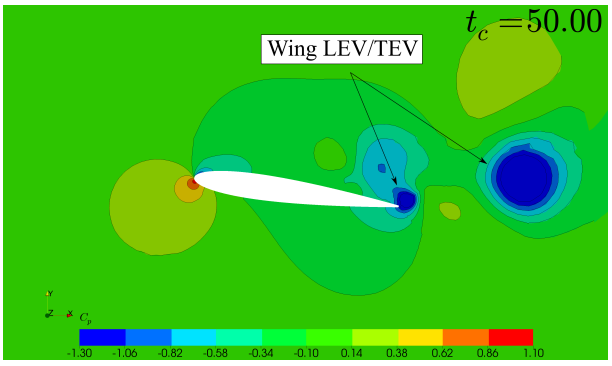

(f) Pressure coefficient, $t_c = 50.00$, $\alpha(t) = 7.93°$

Figure 5.8: Freestream-normalised velocity contours (U/U_∞) and its corresponding pressure coefficient (C_p) around the wing at $t_c = [46.88, 48.44, 50.00]$.

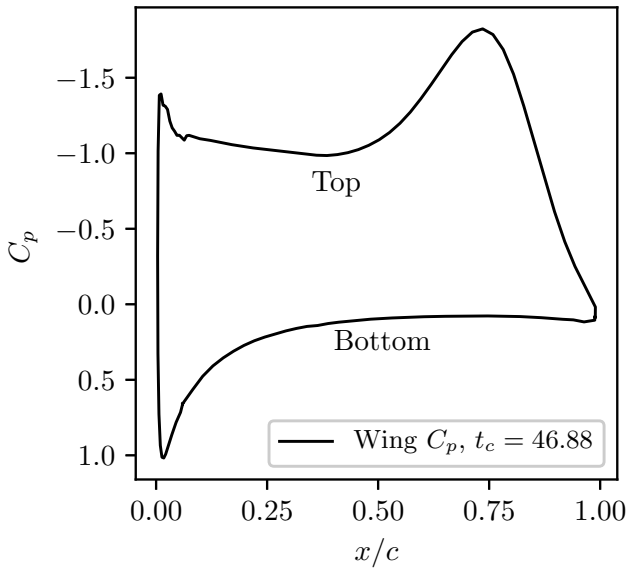

(a) $t_c = 46.88$, $\alpha(t) = 9.75°$

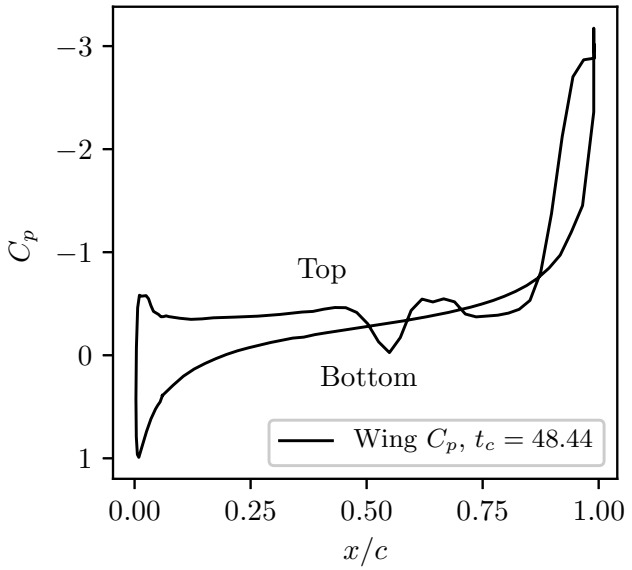

(b) $t_c = 48.44$, $\alpha(t) = 9.04°$

Figure 5.9: Instantaneous pressure coefficient across the wing at $t_c = [46.88, 48.44]$.

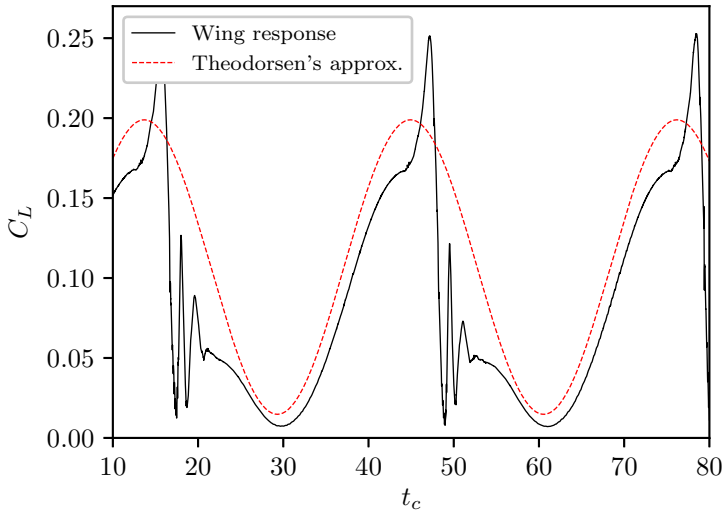

Figure 5.10: Comparison of the wing lift response to the Theodorsen's approximation [94] for symmetric airfoils undergoing harmonic pitch.

a difference in the accuracy between the two modes of application can be seen. Here, the flow is attached especially during the pitch-up phases, whereas what was observed in Chapter 4 provided a flow condition that is massively separated resembling heave dynamics, resulting in flow separation throughout the regime. In comparison, the wing in the present case experiences attached flow throughout its pitch up motion. This further supports the claims made by Amiralaei et al. [194], where the effectiveness of the Theodorsen's function yields reasonable results when the effects of viscosity are minimal.

Apart from the wing response, the additional key feature for verification is in its wake. While the wing undergoes a harmonic motion, its wake characteristics change with angle-of-attack. Instantaneous data will not be physically meaningful, while time-averaging is invalid as a large range of spectral content is present in addition to constantly changing grid points. As a result, conducting statistical analyses for the present wake data is challenging. For these reasons, analyses for the wing response is only measured against the Theodorsen's function as a validation metric, and the outcome supports the reported wing behaviour as shown in Figure 5.10.

5.3.2 Tail Behaviour Subjected to Wing Wake

The tail response in terms of its force coefficient time-histories is illustrated in Figure 5.11. The tail undergoes a motion that is similar to its wing, with the exception of the tail moment arm that contributes to a heave. As the motion of both wing and tail are coupled with identical angle-of-attack relative to the freestream, the tail lift response exhibits similar sinusoidal waveform characteristics including the large variances evident during the negative $dC_L/d\alpha$ sections in the

force history. Similarly to the wing, flow separation may be responsible for such a behaviour but the variances in the tail moments also reveal the influence of the wing wake.

The magnitude of these variances exceed the sinusoidal peaks of the tail response which are presented in terms of $\alpha(t)$ in Figure 5.12. It becomes more apparent that as the geometry pitches up, the tail plunges out of wing wake influence, providing a relatively distinct lift curve up to the maximum of $\alpha(t) = 10^\circ$. The stall characteristics decreases the lift coefficient slightly as the configuration pitches back down. At this instant, the effects of the wing wake begin to manifest as large variances in the tail lift response (point b). The occurrence of this phenomenon depends on the convective time of the wake relative to the tail length, but at present these large amplitudes reveal themselves at $4^\circ \leq \alpha(t) \leq 7^\circ$. The oscillations begin to settle as the configuration approaches its trough at $\alpha(t) = 0^\circ$ and the tail resides in the attached wing wake. These phases of the pitch cycle showing the effects of wake interaction are important to distinguish wake interactions at the tail.

As a result of the configuration pitching down, the tail heaves into the currently separated wing wake. The sequence of flow events that captures this interaction that occurs between $4^\circ \leq \alpha(t) \leq 7^\circ$ can be better visualised using Figures 5.13 to 5.16. Figure 5.13 illustrates the flow in terms of pressure coefficient. With this contour, the wing LEV and TEV low pressure vortex cores are clearly identifiable. However, distinguishing the source of these vortices requires the aid of vorticity contours where the span-wise component (ω_z) is shown in Figure 5.14. Knowing its sign and therefore the rotational direction reveals the source of the individual vortices. This shows that the wing trailing edge sheds a dominant vortex compared to the leading edge, which convects over the system. This is expected as the pitch centre of the geometry is farther from the trailing edge ($0.25C_{MAC}$).

Details of this flow sequence are revealed between $51.25 \leq t_c \leq 51.88$ (Figures 5.13c to 5.13e) as the wing TEV coincides with the tail while it heaves into the wake. The wing TEV convects downstream, which almost coalesces with the tail LEV pictured in Figure 5.13d. However, their counter-rotation prevents this from occurring based on the sign of the vorticity component shown in Figure 5.14d). As this wing TEV now convects farther downstream and over the tail, its low pressure core is observed to affect tail loads. This effect can be inferred from results showing instantaneous pressure coefficient distribution in Figure 5.15 manifested as low pressure suction peaks. These peaks convect across $0.25C_t$ over the top surface within approximately $0.32t_c$. This corresponds to the large variances in tail loads as shown previously in Figure 5.11. While this observation for the wing TEV relative to the tail may be unique to this reduced frequency, the contours presented so far provide some insight to the understanding of this wake interaction, which also encompasses some extent of flow separation at the wing.

The extent of numerical dissipation in the solution is demonstrated through the effects of turbulent viscosity ratio in Figure 5.16. Peak viscosity ratios at approximately $15\nu_t/\nu$ that lie within the low pressure vortex cores are depicted. This provides an indication of the rise in

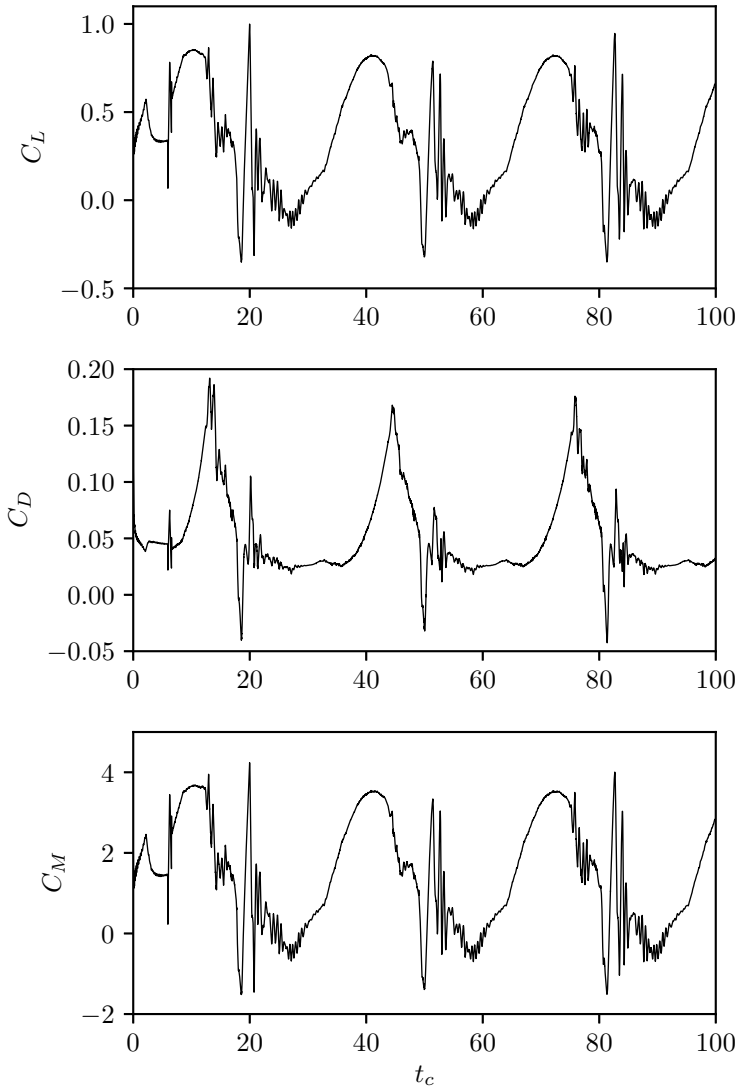

Figure 5.11: Tail-only force coefficient time-history resulting from forced harmonic pitching about $0.25C_{MAC}$

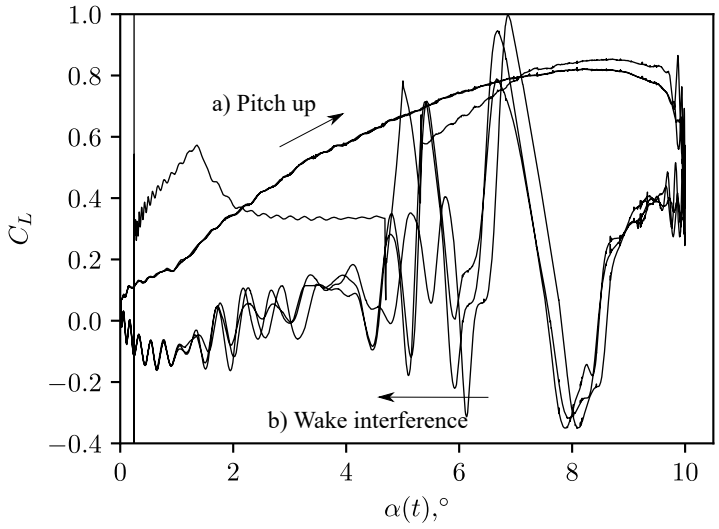

Figure 5.12: Hysteresis of tail lift coefficient against angle-of-attack. Total of three forced harmonic oscillations about $0.25C_{MAC}$ at its wing ($\alpha(t) = 5 \pm 5^\circ$, $k = 0.1$).

turbulent transfer of energy as a result of the moving eddies in the wake, which relates to higher stresses in the flow. However, the dynamic grid makes analyses beyond the instantaneous results challenging, especially for averaging statistics. Averaging a dynamic overset grid does not provide physically meaningful results as the discrete location of grid points are time-dependent. Statistical analyses in the wake like turbulent length scales and its stresses with regards to the tail would allow these effects to be better quantified. Nevertheless, comparing the results between the wing and tail hints toward some degree of correlation between their individual responses. Because of the wake, a correlation between their respective lift coefficients can be inferred. This is supported with a pairwise correlation coefficient of 0.92, which is a strong indicator of the inter-dependence between the two geometries. While the coupled motion of the configuration contributes heavily to this correlation, the slight phase lag can be attributed to the tail moment arm with heave at the tail, inducing an even greater degree of unsteadiness in the system. These observations support the inferrences made by Waldmann et al. [102] under static conditions for wing-tail correlations regarding the phase lag by the tail moment arm.

Similar to the wing, the tail response is verified with the Theodorsen's function shown in Figure 5.17. In contrast to the wing pitch-exclusive dynamics, the tail experiences heave as a result of its moment arm from the rotational centre. Knowing the total pitch angle (10°) with its tail length gives an estimation for its heave amplitude. The result of this is also a sinusoidal function that is corrected for its nominal $C_L(\alpha)$. Ignoring the large variances due to the wake interference, the Theodorsen's approximation fits the tail response very well. In addition, the tail does not appear to exhibit the same stall characteristics compared to the wing. Other irregularities in terms of smaller variances are also present in the negative $dC_L/d\alpha$ regions but this is indistinguishable between wing wake interference or tail stall. However, examining

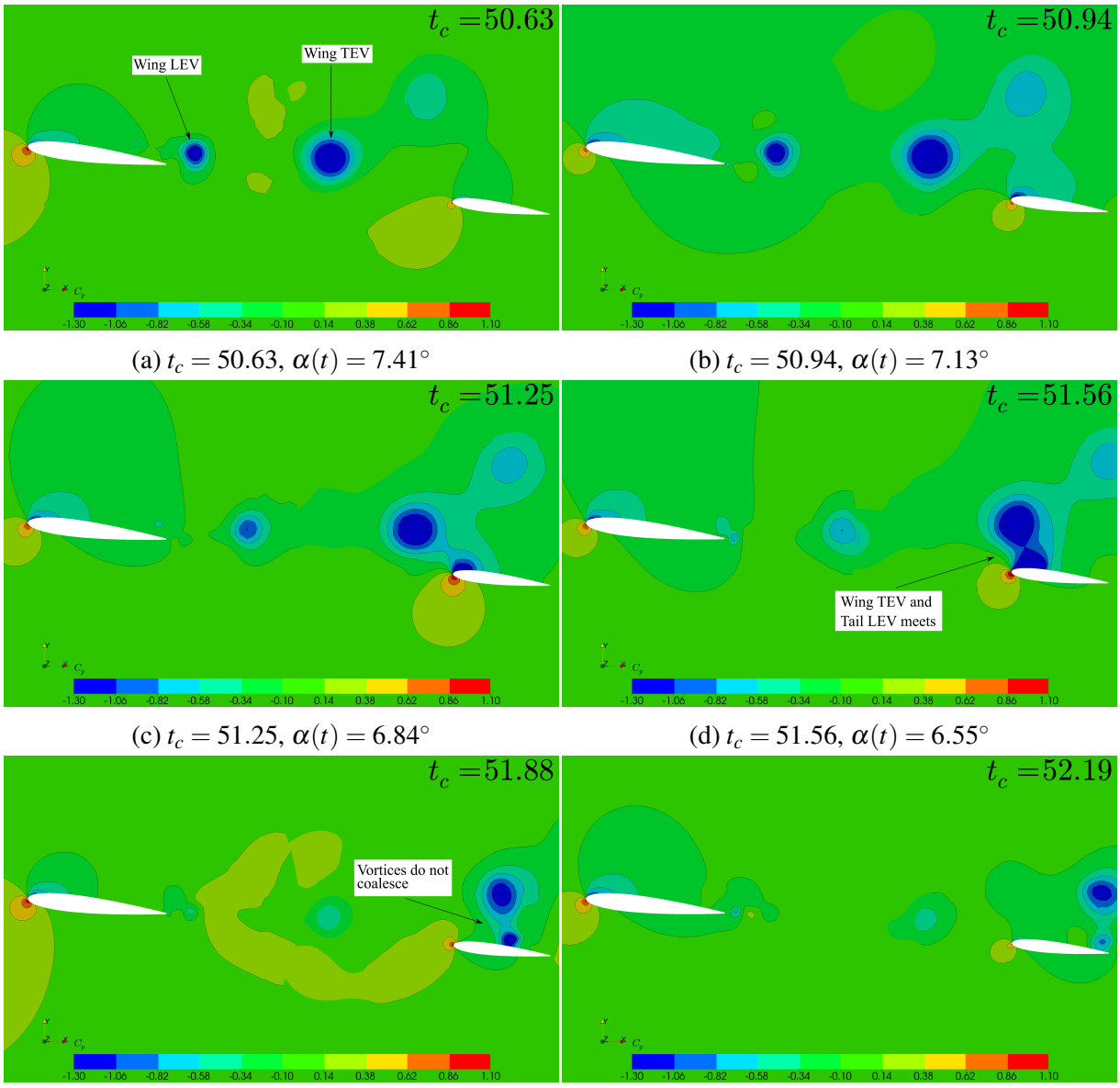

(a) $t_c = 50.63$, $\alpha(t) = 7.41°$

(b) $t_c = 50.94$, $\alpha(t) = 7.13°$

(c) $t_c = 51.25$, $\alpha(t) = 6.84°$

(d) $t_c = 51.56$, $\alpha(t) = 6.55°$

(e) $t_c = 51.88$, $\alpha(t) = 6.24°$

(f) $t_c = 52.19$, $\alpha(t) = 5.94°$

Figure 5.13: Pressure coefficient (C_p) contours showing the convection of wing LEV and TEV relative to the tail across $1.56t_c$. LEV and TEV low pressure zones (in blue) are clearly identifiable (Configuration pitching down).

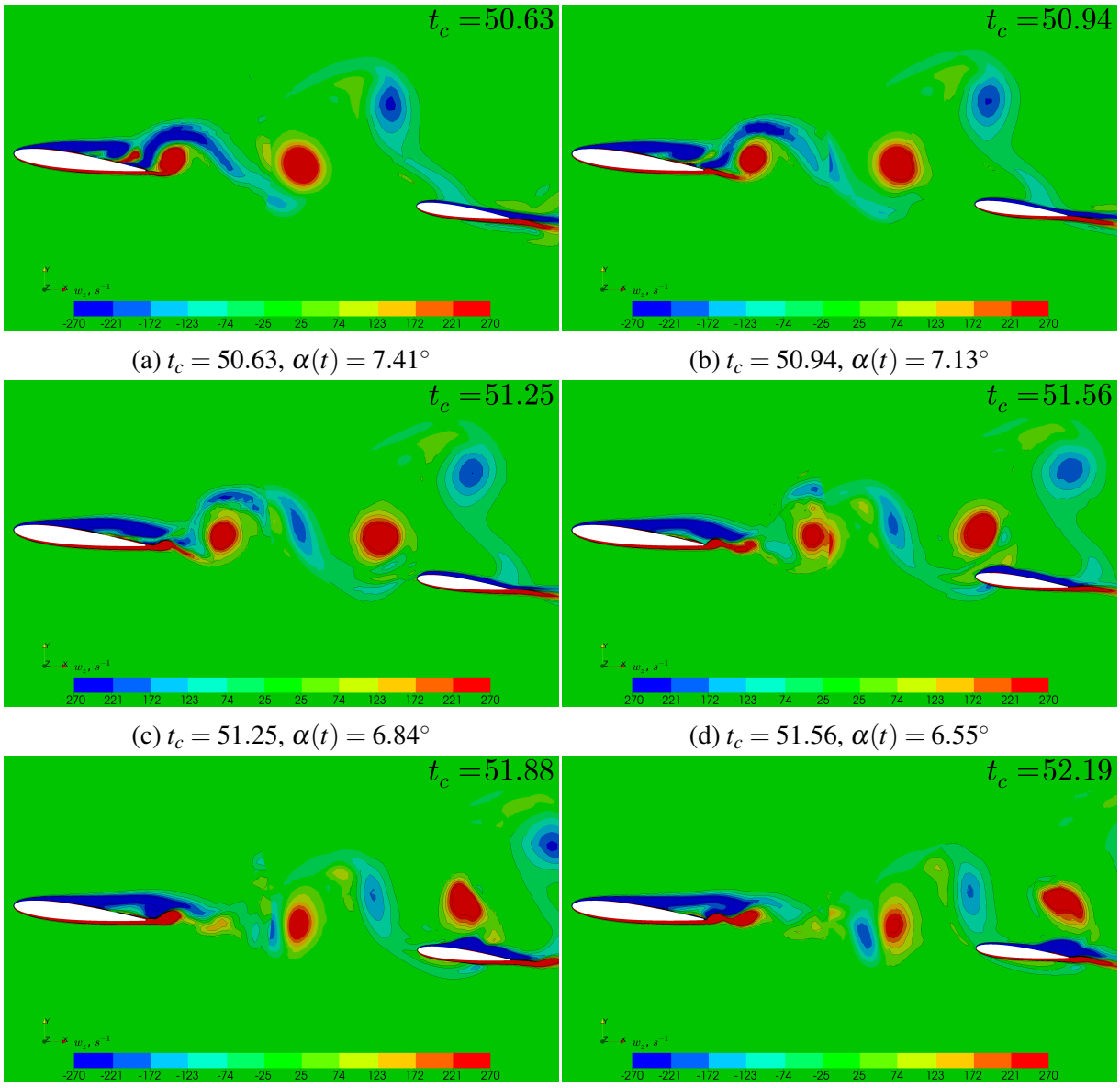

(a) $t_c = 50.63$, $\alpha(t) = 7.41°$ (b) $t_c = 50.94$, $\alpha(t) = 7.13°$

(c) $t_c = 51.25$, $\alpha(t) = 6.84°$ (d) $t_c = 51.56$, $\alpha(t) = 6.55°$

(e) $t_c = 51.88$, $\alpha(t) = 6.24°$ (f) $t_c = 52.19$, $\alpha(t) = 5.94°$

Figure 5.14: Span-wise vorticity contours (ω_z) showing the convection of wing LEV and TEV (Red; counter-clockwise, Blue; clockwise) relative to the tail across $1.56t_c$ (Configuration pitching down).

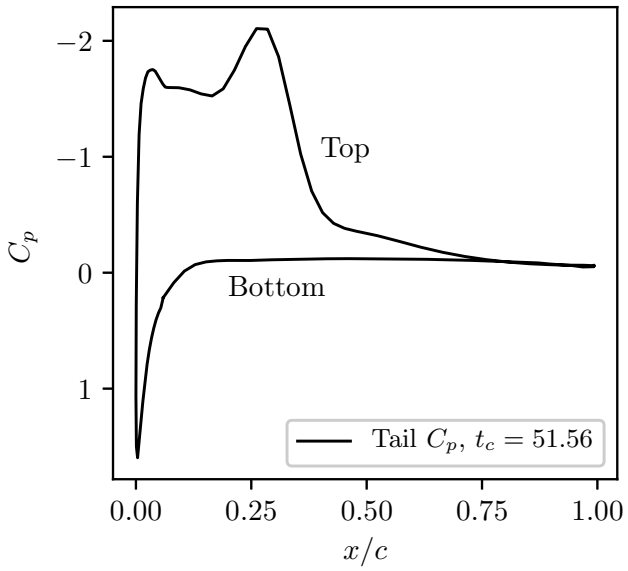

(a) $t_c = 51.56$, $\alpha(t) = 6.55^\circ$

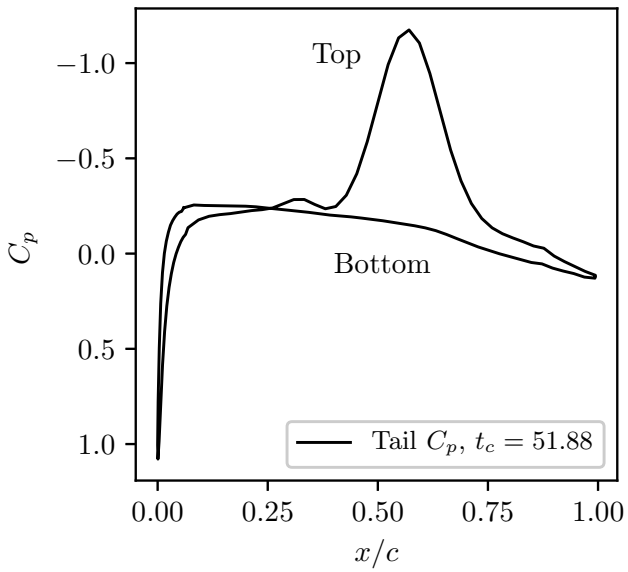

(b) $t_c = 51.88$, $\alpha(t) = 6.24^\circ$

Figure 5.15: Instantaneous pressure coefficient across the tail with the wing wake passing over its top surface as a low pressure suction peak.

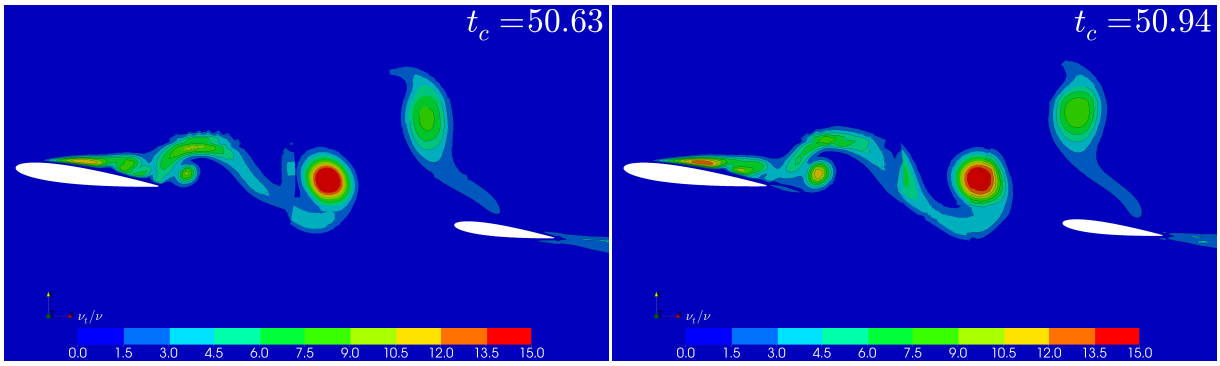

(a) $t_c = 50.63$, $\alpha(t) = 7.41°$ (b) $t_c = 50.94$, $\alpha(t) = 7.13°$

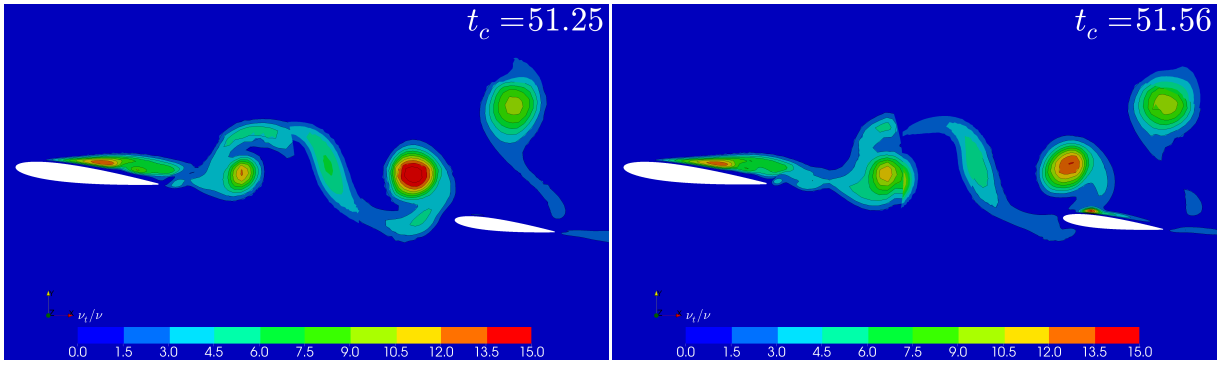

(c) $t_c = 51.25$, $\alpha(t) = 6.84°$ (d) $t_c = 51.56$, $\alpha(t) = 6.55°$

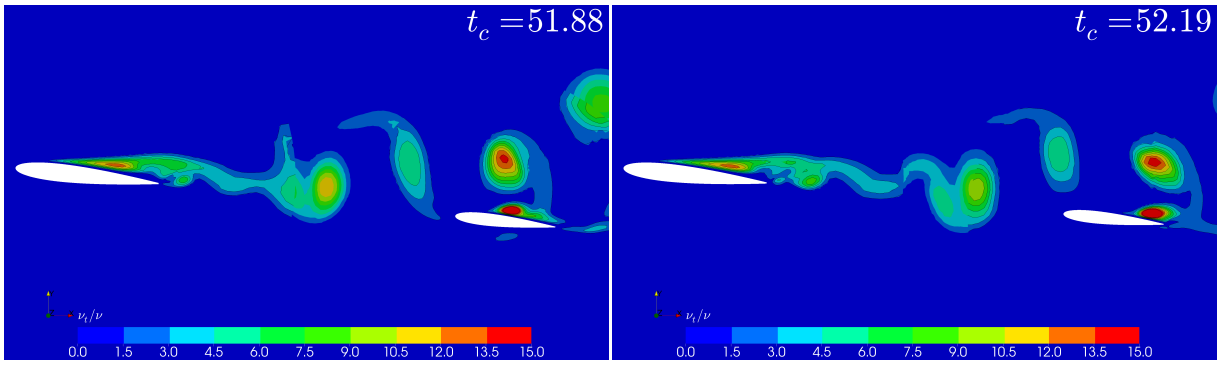

(e) $t_c = 51.88$, $\alpha(t) = 6.24°$ (f) $t_c = 52.19$, $\alpha(t) = 5.94°$

Figure 5.16: Turbulent viscosity ratio (ν_t/ν) showing the convection of wing LEV/TEV relative to the tail across $1.56t_c$ (Configuration pitching down).

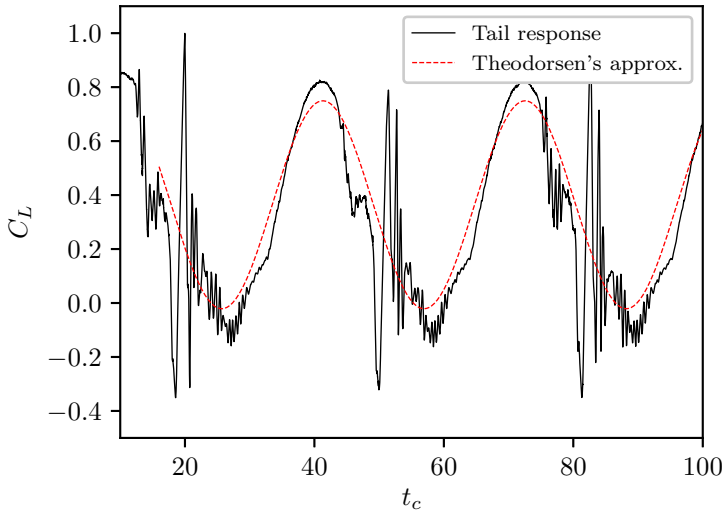

Figure 5.17: Comparison of the tail lift response subjected to wing wake interference to the Theodorsen's approximation [94] for symmetric airfoils undergoing coupled pitch and heave.

the tail pressure coefficient distribution also do not reveal the involvement of significant tail stall dynamics. Based on these, the dissimilar tail stall characteristics despite sharing an identical angle-of-attack with the wing is likely due to the effects of local Reynolds numbers. As the tail is sized to 70% the wing chord, it perceives different local flow conditions, in addition to a region of reduced velocities induced by the wake. This causes different local flow conditions which may alter stall characteristics. The hysteresis caused by the heave motion may also have contributed to this, but this is a function of reduced frequency and can only be determined with differing dynamic conditions of the study.

5.3.3 Synthesis of Force Contribution by Both Wing and Tail

Results so far have treated the wing and tail individually. As this is a coupled system, their significance therefore lies in the synthesis of all components (wing and tail) for the total response of the tandem configuration. Figure 5.18 shows this in terms of its force coefficients, with the system taken as a coupled whole. Here, the lift characteristics encompasses distinct features that can be explained considering the aforementioned discussions for the wing and tail.

Figure 5.19 singles out a pitch cycle for the lift coefficient of the entire system. Following what was discussed, two distinct features can be highlighted from this response. Assuming that the wing contributes to the majority of the lift, the characteristic “pinch" in the lift coefficient due to hysteresis can be identified. This was apparent before in Figure 5.6, and was attributed to wing pitching and stall dynamics. In addition, the decrease in angle-of-attack leads to an interaction between the wing wake and tail. This leads to the second response highlighted in Figure 5.19 where the wake affects the tail. Although the phase and amplitude of this inter-

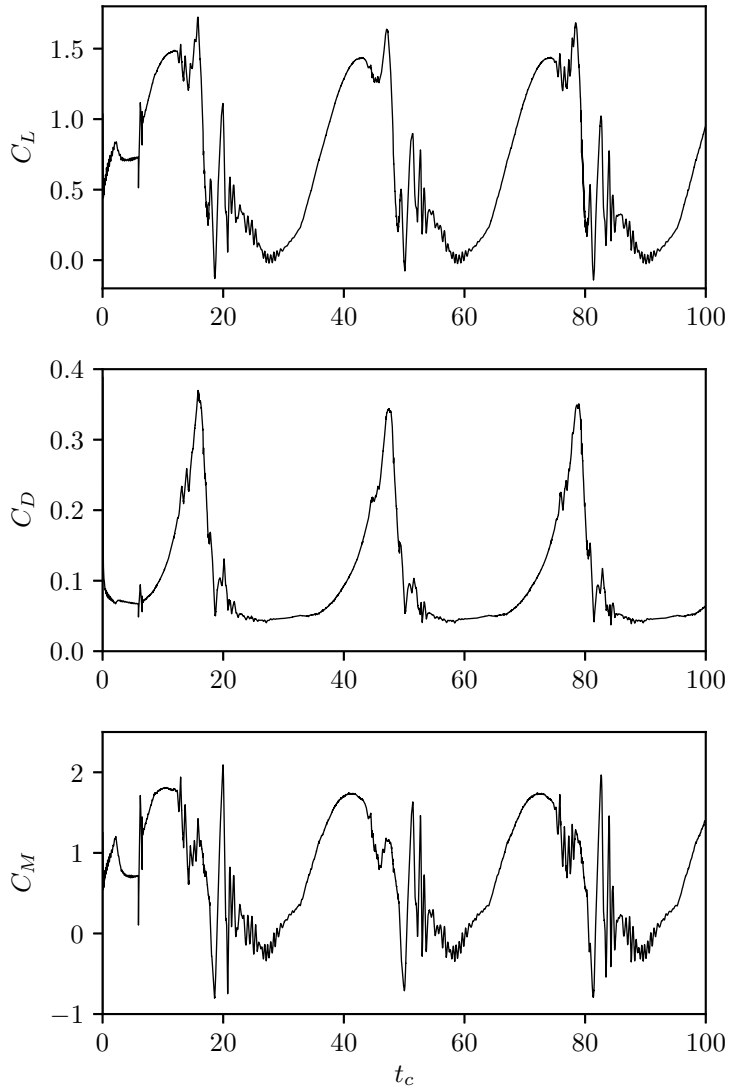

Figure 5.18: Total force coefficients for the wing-tail configuration undergoing forced harmonic pitch oscillation.

action are highly dependent on reduced frequency, the present conditions allow these features to be distinguishable, and demonstrate the aerodynamic coupling that occurs between the two geometries.

So far, the breakdown of components have been captured and analysed as part of this chapter. The results and observations agree with the mechanics outlined by Etkin and Reid [5] where the total behaviour of the system lies in the contribution of individual systems. In the present case, this is limited to the dominant contributors of lift—and therefore moments—which are the wing and tail. Furthermore, their correlations are successfully identified and presented through physical phenomena. This advances the observations made by Waldmann et al. [52, 102] where the tail is engulfed by the wing wake only under *static* conditions. Aircraft stability characteristics with dynamic pitch were also studied by Frink [62] and Thompson et al. [63] but local aerodynamic interactions were beyond their scope of work. Wing wake effects were unconsidered as part of their evaluation for pitch stability. Based on this, the current work has filled this gap by providing an insight to wing wake-tail interactions under such forced harmonic pitch conditions.

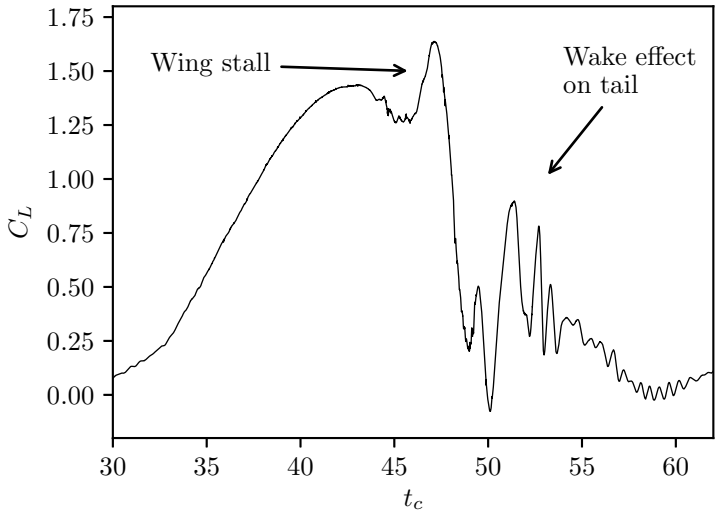

Figure 5.19: Close-up of one lift coefficient cycle for the coupled wing-tail configuration undergoing forced harmonic pitch oscillation, highlighting the synthesis of wing stall and its wake effects on the tail.

5.4 Chapter Closure

The current chapter demonstrates the potential effects of a wing wake shed downstream on to its tail. Additionally, the conditions imposed by the forced harmonic oscillation induces wing stall dynamics where the flow detaches and develops into LEV and TEVs. Despite being conducted under a relatively low Reynolds number with a moderate reduced frequency ($Re = 2.14 \times 10^4$, $k = 0.1$), it is observable that wake effects on the tail are readily apparent, and are distinguishable

from stall characteristics. This is evident from correlations drawn between the wing and tail lift coefficient time-histories. The computed tail lift forces show significant variances that strongly relate to those exhibited by wing wake shedding characteristics. This reveals that the source of these variances are a consequence of wing wake interaction.

As a dynamic motion is induced, the wing response as a result of pitch can be approximated with an empirical approach using the Theodorsen's function for unsteady aerodynamics. Similarly, it is shown that this can be applied on the tail, accounting for heave due to the tail moment arm. However, comparing the tail response with the Theodorsen's function neglects an additional component that accounts for wing wake interference effects. This suggests that the complete tail response including the effects of the wing wake could be approximated with an additional gust component adjusted with phase lag to account for the tail moment arm as a convective length. But prior to this, the present conditions should also be expanded to account for sensitivity studies.

For example, the harmonics of the problem can be used as a control variable to determine the sensitivity of the results in response to changes in tail length, pitch amplitude, and reduced frequency. This would affect heave rates of the tail, and subsequently its behaviour relative to the wing wake. Wing wake characteristics will be altered as its shedding dynamics are also a function of reduced frequency. Apart from the dynamics of the problem, span-wise effects are also neglected. Physical features such as wing-tip (vortices) and any geometric features, such as a Yehudi break (see Appendix A) might modify wake dynamics which interacts with the tail. Considering that these would vastly expand the scope of this chapter, they are therefore left for future discussions.

This dynamic case has captured the pitch hysteresis while identifying key aerodynamic behaviour. This includes stall dynamics for the wings, where characteristic LEV/TEVs are captured and observed to convect downstream towards the tail. Tail aerodynamics are also shown to respond to the wake, evident through its surface pressure distributions. The harmonic nature of the tail response therefore allows it to be predicted, while discrepancies in the approximation method are attributed to an additional gust component that could be used to account for wake effects. Distinct features in the total lifting response of the system are subsequently revealed to be the synthesis of wing stall and its wake interaction with the tail. These effects prove that wing-wake tail interactions are perceptible by the combined system.

Chapter 6

Conclusion

6.1 Key Outcomes & Findings

The engineering motivation for this work lies in the need for accurate wake capture and its consequential impact on downstream aerodynamics. Due to the highly turbulent and unsteady nature of wakes, a high fidelity turbulence modelling method is required to resolve the length scales and accurately represent wake physics before any interaction can be conducted thereafter. The computational framework that is used therefore validates the application of the DDES method on separated wakes. This process is accomplished as a flow over a bluff-body benchmark geometry supported by pre-existing data from the literature. Results for vortex shedding parameters such as the Strouhal number and drag statistics agree well with existing numerical and experimental counterparts ($+7.58\%$ over-prediction for Strouhal number and a 100-count precision for drag coefficient). Quantitative results in the wake with its time-averaged mean and fluctuating velocity profiles also compare well with published experimental data up to a downstream distance of $6x/D$. In addition, comparing the performance of the DDES method with RANS models for separated flows reinforces claims that RANS is unsuitable for such regimes, although it has been used for forced pitching at higher angles-of-attack among existing computational frameworks. Under the hierarchy of turbulence modelling techniques, this ascertains that minimally, hybrid RANS/LES methods (DES) are essential for capturing such flows. Using this technique is accompanied with only a marginal trade-off in computational costs for the increased fidelity it provides. Verifying these results successfully also expand the existing pool of numerical data available for benchmarking. This is useful especially for the public domain as it is achieved with the open-sourced CFD solver, OpenFOAM.

The validated wake on a wing-section located downstream is then investigated to reveal its impact on aerodynamics. This converts the bluff-body into a wake generator, analogous to flow obstacles inducing separated wakes—like those emanated from buildings, or shed from wings at high angles-of-attack. These conditions are subsequently shown to be significant to downstream aerodynamics. The oscillatory nature of the vortex shedding process induces massive flow sepa-

ration with lift responses and local flow fields that are characteristic of heave and gust dynamics. This is referenced to a wake-free case to draw such comparisons. The contrast in surface pressure distribution with the wake-free case (where the flow is attached), demonstrates the resultant effects of flow separation that occur periodically between alternating sides of the wing-section. With the reduced frequency of the wake generator, this corresponding response downstream can be compared with the Sear's function for gust loading and the Theodorsen's function for harmonic heave to predict these effects. However, the approximation methods are limited such that they neglect the underlying unsteadiness and turbulent spectra that are dominant in wake physics. The effects of the entire frequency content in the wake can only be captured either numerically, with the demonstrated techniques, or other accompanying experimental methods. There are therefore only suggested as approximations.

The computational framework considers a dynamic approach accomplished by expanding the methodology to include an overset grid technique. This is based on wing-tail aerodynamics where the wake interacts with the horizontal stabilizer under forced harmonic pitching motion. Wing pitch oscillation with a corresponding separated wake is induced, while the tail experiences a coupled pitch/heave motion due its moment arm. As it heaves and plunges in and out of the wing wake, the tail responds with large load variations, exceeding that of its own maximum lift coefficient from pitch displacement. The phase of this phenomenon strongly correlates to the timing of distinct wing wake features that are shed downstream. These features are captured with DDES, and identified as wing LEV/TEV pairs, where the TEV is evidently dominant as the rotation centre is imposed at the wing quarter chord point. While vortex cores are inherently low pressure, their effects translate to a suction force that interacts with the tail, evident in its pressure distribution while it coincides with the separated wing wake. Assessing the two systems independently have shown that their individual harmonic lift dynamics can be approximated reasonably well with the Theodorsen's function. This is with the exception of wing stall characteristics that are beyond theoretical prediction limits of the function, along with variances in tail lift due to the unsteady wake encounter. However, the periodicity and phase lag of the wake encounter by the tail suggests that a prediction method to consider this could be formulated. This could be achieved by accounting for wake effects with a gust component as a function of convective tail length.

Ultimately, insights on wake encounter effects are achieved with this computational framework. The results from Chapters 3 to 5 have demonstrated that these effects are significant, while revealing the developments and considerations that are essential to achieve this framework for wake encounter studies.

6.2 Thesis Contributions

A computational framework that provides novel insights on bluff-body wake encounters and tandem wing-tail dynamics under forced harmonic pitch is accomplished. The themes used to address these are referred to as the ***Static*** and ***Dynamic*** conditions which are also platforms to advance the understanding of wake interactions. The thesis contribution is achieved with two milestones:

- Under the ***Static*** conditions; the validity of the computational framework for using DDES on separated wake capture is ascertained. This is achieved with the validation against a library of aerodynamic benchmark flows modelled as a bluff-body wake (Chapter 3). Fulfilling this, the extent of numerical treatment on turbulence is further evaluated through statistical analyses, reinforcing the best practices for the capture of such flow regimes. Subsequently, wake effects on a wing-section downstream (Chapter 4) advances the observations on wake encounter aerodynamics that are inspired by Lefebvre and Jones [84], and Jiang et al. [85]. The additional developments for wake effects on downstream oscillations and flow separation is captured with the corresponding unsteady response and surface pressure distributions. Periodicity in its force time-history highlights the potential for the resulting behaviour to be predicted empirically. This is demonstrated by extending the Sear's and Theodorsen's functions to be applied for wake interactions.

- Under the ***Dynamic*** conditions; the framework is elevated to achieve a dynamic case (Chapter 5) that demonstrates the effects of a wing wake on its tail through dynamic grid motion under forced harmonic pitch oscillations. This bridges a gap among wake capture studies under the static conditions conducted by Waldmann et al. [52, 102], and the dynamic conditions but without any focus on wing wake-tail interactions for dynamic stability by Frink [62], Thompson et al. [63], and Hall et al. [104]. As these effects were generally beyond the scope of work for the dynamic cases, the work has shown that wake-tail effects are perceivable by the complete (wing-tail) system. Dynamic pitching cases also generally involve assessments at higher angles-of-attack, where it is also shown that the wing stall with its flow separated wake can induce distinct LEV/TEVs. These are observed to convect downstream and interact with the tail as low pressure vortex cores. The result of this are in the form of large amplitude fluctuations in the tail lift response, where under the conditions of the study, can exceed its maximum lift coefficient due to angle-of-attack alone.

Achieving the above milestones constitutes the overall contribution by this thesis. The computational framework successfully employed and advanced the best practices for the modelling of wake encounter on downstream aerodynamics. This fulfils the requirement for accurate modelling of wakes, supplemented with high-fidelity turbulence modelling and grid motion techniques.

6.3 Recommendations for Future Work

The findings and developments throughout the work have uncovered several fronts in the research that are worth exploring. This expands upon the various themes addressed in the thesis and are listed here as suggestions for future work:

1. The current level of uncertainty analyses is based on grid and turbulence modelling sensitivity studies (Section 2.2.1 and 2.4), but the overall extent of uncertainty quantification can be developed further. This can be conducted to ascertain the findings provided in Chapters 3 to 5. This includes the impact of numerical schemes as results here are limited to those outlined in Section 2.3.2 only. Potential numerical errors introduced by the overall computational framework can also be evaluated to a greater degree, as certain non-physicality in the presented results could exist [136]. Apart from solution parameters, sensitivity studies pertaining to dimensional analyses can also be explored further.

   (a) The solutions were 3-dimensional while the geometries are limited to infinite span with their widths spanning the entire domain. The results therefore were focused on the longitudinal plane only. The analyses can be expanded to consider the span-wise flows and its corresponding features. This is an important aspect as aerodynamic effects can be longitudinally and laterally coupled.

   (b) The findings in Chapter 4 are also limited to physically static conditions. This can be expanded to include the overset techniques demonstrated in Chapter 5 for the modelling of an obstacle approach or a wake encounter with a lateral maneuvre. The separation distance is a key control variable to further evaluate findings and aerodynamic relationships [84,85]. Taking a dynamic approach for control variables will provide insightful details to the problem.

   (c) While the overset method allows up to 6-DOF sub-zone mesh movements, it introduces numerical errors into the simulation. As a result, better grids can be designed to improve the background and sub-zone mesh interface. Detailed sensitivity studies at the interpolation fringe of sub-meshes can also be studied. This is key to tandem flows if disconnected sub-zone grids are used for the bodies, like the one designed in Chapter 5. Numerical information for the wake therefore passes through two interpolation fringes as a result of this design, which will lead to an increase in interpolation errors affecting accuracy. Uncertainty analyses needs to be performed in this regard as validation of free-shear flows across such regions may be challenging to accomplish with experiment, especially if the bodies are in proximity and motion is involved.

2. While it is demonstrated that DES is the minimum required for capturing separated flows, a detailed comparison with higher-fidelity turbulence modelling methods are worth con-

ducting. As the accuracy of wake capture is highly dependent on turbulence modelling technique, advances toward DNS for the bluff-body benchmark are already being made [79, 195]. This can be applied to consider downstream effects, which will further justify the behaviours observed especially in Chapter 4. Moreover, benchmarks constantly re-evaluate the hierarchy of turbulence modelling techniques relative to current advancements in computing power. The solution fidelity thus examines if the increase in resolution is worth the present-day computational expense in achieving simulation objectives.

(a) With regards to aerodynamic benchmarking, the current framework has demonstrated the potential of the square beam bluff-body as a platform for a wake generator. To expand this benchmark for downstream interactions, other novel methods for wake generation can also be explored. This is provided that the wake data can be substantially reproduced, as demonstrated by Chapter 3, which serves as a guideline.

3. As the tail is the primary contributor to pitch, assessing its ultimate effects on dynamic derivatives like pitch damping can only be addressed by expanding the computational framework to practical geometries. Further assessments on the effects of wing wake-tail interactions in Chapter 5 are limited to the isolated wing-tail geometry. Various benchmark models such as the General Transport Model (GTM) [63], or more recently, the NASA CRM [196] for dynamic stability (and control) analyses [104] can be considered. These geometries are designed to be representative of modern aircraft, and will provide increasingly meaningful details on the effects of wake interactions and ultimately on flight dynamics.

   However, the numerical implications grow with these geometries. Spatial and temporal scales become increasingly demanding to compute, especially on a dynamic grid with a sufficiently refined wake block and time-step to match [62]. An advanced meshing strategy is required, or an efficient approach needs to be taken. Such decisions have to be driven by the simulation objectives. With regards to wake-tail interactions, the spanwise impact of the wing wake on the HTP may only be limited to the inboard sections of the wing (See Appendix A). The magnitude of the problem is also compounded by flight Reynolds numbers, where a wider range of flow phenomena are expected to develop. The simulation of these conditions (grid motion, flight Reynolds numbers with manoeuvre, and full aircraft geometries) may be computationally prohibitive today, but is a targeted technology milestone within the next decade [43, 197].

Appendix A

Preliminary Study on Wing-Wake Relative to Tail

A.1 Details of Study

Results from Reynolds-Averaged computational studies of the span-wise flow field between the horizontal stabilizer and wing of the NASA CRM are explored here. It is observed early on that the horizontal stabilizer is engulfed at multiple post-stall angles due to the vertical extent of the wings wake. Discernible flow patterns can be observed such as an up wash and a weak inboard wake vortex that originates from the wing inboard section. The upwash in the wake can be attributed to the kink in the wing trailing edge, known as the Yehudi break, which also causes the wake to display characteristic features that are identified here. As the span-wise extent of the break's location is close to the stabilizer, results suggest levels of interaction between this up wash together with the weak inboard wake vortex. A shift in the inboard wake vortex can also be observed between the presented range of angles of attack. To offer insight on this, results present the velocity contours and vector fields of the wake through two post-stall angles-of-attack at 14° and 16°, just forward of the horizontal stabilizer and along two stream-wise stations in the region between the wing and tail.

The CRM (DPW-4 "Wing-Body-Tail" geometry) is used because it is the computational benchmark geometry for aircraft aerodynamics. It has a design cruise point of $M = 0.85$, $Re = 4.0 \times 10^7$, and a $C_L = 0.5$ at 37.000 feet AMSL [198]. Much work on it has been performed primarily for drag [199] and high-lift [200] prediction, but with more recent focus on its near wake [52]. The CRM wing plan form has a shape which deviates from a standard trapezoidal wing and is identifiable by a kink in its trailing edge, known as a Yehudi break. This break occurs at 37% wing semi-span which distinguishes between its inboard and outboard sections, and the HTP spans approximately 36.3% relative to the wing semi-span. Due to this proximity, flows leaving the wing from the break region is likely to interact with the HTP downstream. The HTP is of a conventional low-tail design that sits on the empennage. The CRM geometry variant

used here has a stabilizer incident to the freestream at 0° [196].

Low-speed post-stall conditions have been studied in terms of wing wakes for the CRM ($Re = 1.16 \times 10^7$, $M = 0.25$, $\alpha = 18°$) [52, 54]. At 18° angle-of-attack, results for profiles of time-averaged stream-wise velocity show a reduction of almost 60% relative to the freestream across its wake. As the HTP sits low on the empennage, it is highlighted that the wake largely passes over the HTP, but its vertical extent is adequately large, hinting some levels of interaction, which would be even greater at lower angles-of-attack. Focus on this interaction, however, was beyond the context of their work. It is demonstrated that PIV measurements are attempted and cross-validated with URANS and DDES methods focusing on stream-wise results. This includes time-averaged stream-wise velocities showing the wake profile and momentum deficit, as well as the spectral content of coefficient of pressure. Overall, scale-resolving techniques were generally favoured when compared to PIV-captured results, while the URANS demonstrated an under prediction of the wake velocity deficit by up to 20%. Although lacking in accuracy, the URANS model still manages to produce similar trends compared to results from both the experiment and scale-resolving techniques.

As the flow is 3-Dimensional, salient features would exist in the span-wise direction and this leaves much to be studied. This is aligned with observations from the discussed impact of the span-wise extent of the Yehudi break relative to the HTP. The break is known to provide both structural and aerodynamic benefits in terms of wing loads and is implemented in many existing aircraft wing designs. It allows a greater inboard thickness-to-chord ratio, alleviating structural stresses due to wing bending moments [42]. But as the break alters the plan-form shape of the wing, it is expected for it to have an impact on HTP characteristics through its wake, especially if it is exposed further to the freestream at higher angles of attack. Therefore, as the break gives the wing plan-form a characteristic shape, it is expected for it to produce characteristic wake features as well. Like empirical methods have highlighted, the aerodynamic contribution by the HTP is largely dependent on this wing-tail aerodynamic interaction. This phenomenon needs to be better understood as the benefits of the Yehudi break is mostly discussed from a structural standpoint but not on any consequent wake features that it may produce which can interact with the tail. This is especially so if the break spans at a location close to the HTP, such as seen on the CRM. Therefore, part of this work will reveal some potential aerodynamic interactions and wake considerations in terms of the wing wake due to this structural feature.

In the present work, similar conditions to Waldmann et al. [52] will be studied but at lower angles of attack ($< 18°$), where it is suggested that the wake effects on the HTP would be greater. In addition, as it was shown that the vertical extent of wake is large enough to blanket the HTP throughout a range of angles of attack, results will follow and assess the steady-state wake beginning first with a lower 16° and then 14° angle-of-attack. In terms of results, the Reynolds-Averaged velocity field just forward of the HTP will be used to initiate discussion and observations on the likelihood of any wake features and aerodynamic interaction(s) between the

wake generated because of the Yehudi break and the HTP. This is presented from a perspective looking downstream at stations defined by the span-wise station of the break, complementing pre-existing results which primarily focus on the stream-wise perspectives. Results presented from this perspective allows the properties of the wake with relation to the HTP span to be assessed.

Early on, discernible flow features exist when the wake velocity contours are observed. These are namely an up wash and a characteristic swirl aft of the wing inboard section. Studies of these features with computational methods are attempted, which are presently believed to be developed from the Yehudi break and the inboard wing-section. Focus will first be on the primitive variables of wake velocities and vorticity parallel to the x-normal plane, as well as iso-volumes of vorticity to visualize the flow in 3-Dimensions to obtain a model of the flow features involved just forward of the HTP. Subsequently, the result and effect of the turbulence model used will also be discussed showing effects of turbulent viscosity and Reynolds stresses. These will be able to provide some insight on the physics that are taking place across the wake which will impinge on the HTP thereafter.

A.1.1 Mesh Design

There are two parts to the fully unstructured mesh for the geometry and the flow domain. Meshing strategy is approached from the inside-out beginning from the aircraft surface. Regularly connected quadrants are used for the wing and HTP surface and triangles for the fuselage and wing and tail tip caps. Layers are then subsequently grown using prisms and hexahedrons for the existing surface triangles and quadrants at a rate of 1.2 times up to 20 layers, with the above flat plate estimations targeted for $y^+ = 60$. Subsequently, the flow domain is filled with rapidly growing tetrahedrons up to a far field boundary of 25 times the wing span. The enclosure is half-bullet shaped intersecting the aircraft symmetry plane. The geometry and mesh are shown in Figures A.1 and A.2.

As the lateral extent of the wake produced by the Yehudi break is unknown, the wake block is created to encompass the entire wing and stretches downstream to include the HTP. Cells in the block are equilateral tetrahedrons, with a cell edge size of 2% the reference chord. As this wake block spans the entire wing, the 2% reference chord cell resolution used here is relatively coarser to limit total cell count. The present mesh has a total of 44 million cells, of which 32 million are used in the wake block. No mesh sensitivity has been performed for the presented results due to the high element counts but the cell resolution used lies within the observed range of 1-3% the reference chord, although for DES-type scale-resolving techniques. The wake block is also ensured to be adequately large to enclose the vertical extent of the wake region for the angles of attack simulated.

As the wake refinement block does not focus on the wing tip vortex, a brief assessment of the wing tip vortex size is done to determine the profile of vortex tangential velocities towards

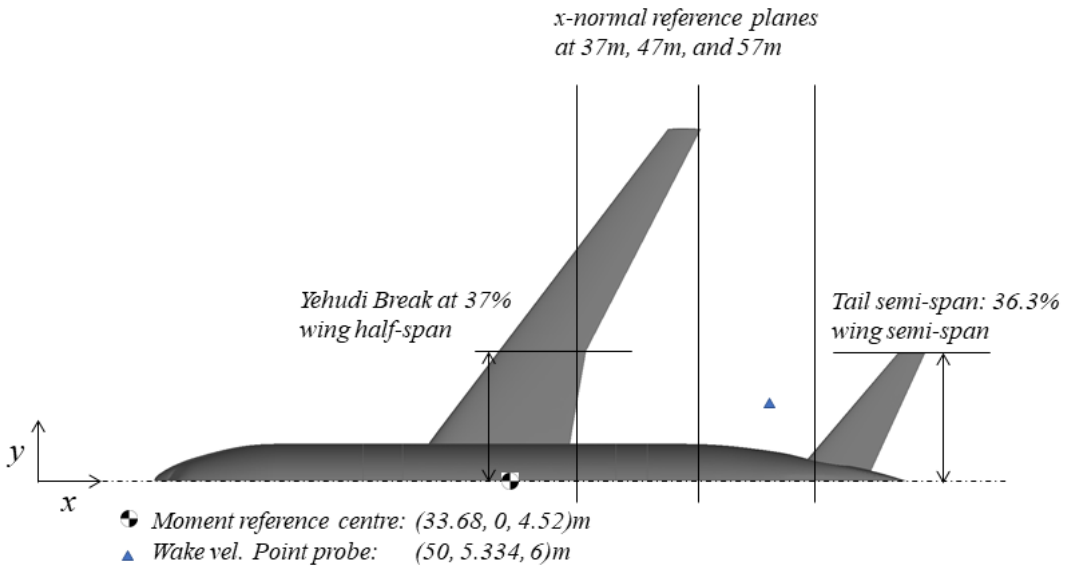

Figure A.1: Plan view of the Common Research Model showing moment reference centre and span-wise location of the Yehudi break (37% wing semi-span).

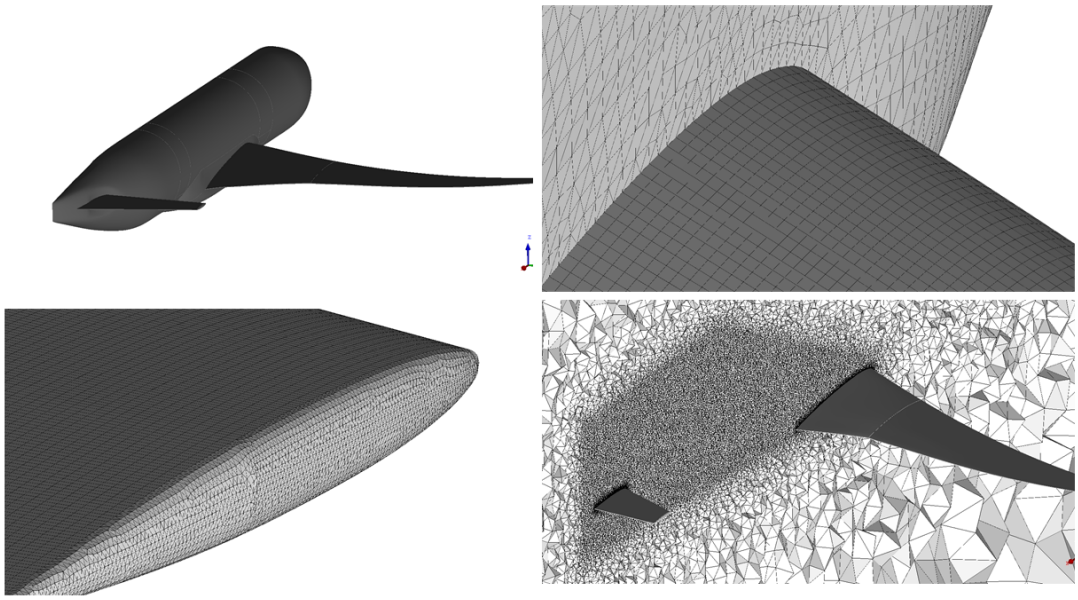

Figure A.2: Top left: the symmetrical CRM geometry. Top right: Surface mesh at the wing root. Bottom right: Wake block section mesh. Bottom left horizontal tailplane top cap surface mesh.

the tail. At this short stream-wise distance, it is likely that the tip vortex is still developing which will have little effect on the tail as any tangential velocities diminish exponentially [201] This can be inferred with the Biot-Savart law [202] relating the tangential velocity to a point at distance r from the vortex filament:

$$d\vec{V} = \frac{\Gamma}{4\pi}\frac{d\vec{l}\times\vec{r}}{|r^3|} \tag{A.1}$$

During meshing, the tail cone and the trailing edges of the wing and tail tip caps was a meticulous process due to the complexities of the geometry. The empennage tail cone meets the plane of symmetry forming a cusp. This causes cells, especially from layer generation, to form highly skewed faces which contributed to numerical instabilities. Improving the quality of the cells at this region required a crop along the cusp. Likewise, the trailing edges of the wing and tail tip caps are regions of high curvature. However, these areas did not require CAD modification but much higher levels of local mesh refinement.

The initial conditions of velocity and pressure internal fields are initialized by solving for potential flow first. Solution convergence is then determined by monitoring aerodynamic coefficients of total aircraft lift and moments stable to 1 count throughout a minimum of 50 iterations. In addition, a point probe in the wake region at (50, 5.334, 6)m from the CRM origin is used to monitor point velocity over the solutions iterations. This arbitrary point lies between the wing and HTP (Figure A.1). The wake velocity contours as presented in the results are also monitored across 500 iterations without any significant shift.

A.1.2 Interim Findings on Wing-Wake Relative to Tailplane

Results are presented for the 14°and 16°cases from Figure A.3 onwards. The cases are presented with their numerical results scaled for comparison to each other such that any insight on the wake differences between these attitudes and its development through these two angles of attack can be compared. Wake velocities are presented first in the form of contours and vector fields. This is then used to initiate further discussion on the up wash and inboard wake vortex where flow field variables such as turbulent viscosity and vorticity are used to obtain the modelled flow properties of the wake just forward of the HTP. These provide more information on the behavior of any interaction between them.

Figure A.3 shows the velocity magnitude contours limited to 98% freestream. A portion of the wake cross-section shows a velocity deficit of close to 50% relative to the freestream at the outboard section of the wing. This deficit agrees with what was suggested by existing literature. However, there is no attempt on evaluating this with the stream-wise wake profile with Waldmann et al.'s wake window [52]. A characteristic up wash in the wake following the Yehudi break can be observed. This also coincides with the approximate span of the HTP, where it can be observed by the same contours to be blanketed by a region of approximately 70% to

90% of the freestream. Compared to the 14°case, the wake profile is noticeably slimmer, which is expected due to a lower angle-of-attack. However, a distinct outboard shift in the wake profile can be seen at the inboard section of the wake as the angle-of-attack is decreased for the 14°case. This causes the wake to begin engulfing the HTP at greater levels towards it's tip indicating some levels of interaction close to the 10 m butt-line station (The absolute semi-span of the tail is at 10.67 m).

The breakdown of velocity magnitude in the form of planar velocity vector fields (v, w) is shown in Figure A.4. This provides insight on both the magnitude and direction of the local flow just forward of the HTP, again at the 57m downstream x-normal plane. An up wash of approximately 45% relative freestream can be seen towards the stabilizer tip, together with a hint of an inboard wake vortex that is relatively weak, of up to 10% freestream based on the contours. Comparing this planar velocity magnitude comprising of the vertical and span-wise velocities (v, w) with the 3-Dimensional magnitude in Figure A.3, it can be deduced that the impingement of the vortex on the HTP is dominated by the steam-wise flow. Furthermore, at 16°, the swirl is modelled to lie just above the HTP mid semi-span. But as the angle-of-attack decreases to 14°, the same outward lateral shift in the results can be observed to show this swirl approaching the stabilizer tip. Between the two cases, it can be said that the inboard wake tends to be drawn towards the fuselage at higher angles of attack. It is also likely that this is induced from the up wash generated by the freestream because of the wake being exposed through the Yehudi break. The observations on how the up wash is drawn inboard can be formed from the postulate that the inboard section of the wing has a higher thickness-to-chord (t/c) ratio which produces a higher profile drag and a lower inboard wake pressure. This leads to a convection of the wake inward. It can be observed that the up wash leading to a flex in the wake increases in height as the distance grows from the wing. This is as such that at this high relative angle-of-attack the wake is exposed to the freestream earlier due to the Yehudi break, deforming it, giving the wake its distinctive span-wise fold. However, it is uncertain if this up wash has any correlation with the inboard wake vortex as observed in the vector field in Figure A.4. This up wash also indicates that the problem at hand is 3-dimensional as the up wash would not exist if only a wing-section is modelled.

Relative levels of turbulent viscosity are used as an indicator of turbulence. This is in the form of turbulent viscosity taken relative to physical kinematic viscosity of the flow, as seen in Figure A.5. The lower 1% threshold of the contours are regarded as the freestream and are truncated from the figure. This 1% limit is based off the highest observable value of ν_t/ν in the 16°case, which has the highest between the two cases. Expectedly, it is evident that turbulent viscosity vastly dominates physical kinematic viscosity in the region towards the horizontal HTP indicating highly turbulent wake flow. But as RANS equations are limited to only the mean and large flow features, a higher-fidelity technique like DES or LES, may be needed to provide more insight on this portion of the flow, especially for the inboard wake section. In addition, is it also

notable that this viscosity ratio decreases substantially as the angle-of-attack decreases from 16°to 14°, with also the same observable outward shift.

The following flow feature of interest in the inboard wake vortex. To attempt at visualizing its source, absolute values of vorticity are depicted with iso-volumes but only limited from $10\,\mathrm{s}^{-1}$ to $15\,\mathrm{s}^{-1}$ in Figure A.6, and span-wise contours in Figure A.7 limited from $2/s$ to $22/s$. At 16°angle-of-attack the swirl lies just above the HTP but its size is adequately large to visually depict some interaction with the HTP, but with most of it passing over the upper surface. Based on the iso-volumes, the same lateral outboard shift in the wake can also be observed between these two attitudes. The 14°case shows the inboard wake vortex developing outwards, possibly coinciding with the HTP tip and its tip vortex. However, the mesh block and its refinement cells grow rapidly farther downstream, dissipating any useful results soon after the HTP trailing edge. Nevertheless, the iso-volumes provide valuable insight on this physical interaction, especially how the inboard vortex seems to coincide with the HTP tip. Looking closer at these results in Figure A.7, a core at the HTP of approximately 12/s with a diameter of approximately 5 m can be observed. These contours suggest that at 14°, the vortex core still does not strictly coincide with the HTP tip, and presently, it is unknown if it would at further lower attitudes. However, the trend between the two cases seem to suggest that this is likely.

A.1.3 Discussion

The results presented shows a preliminary model of the development of a wake from a wing with a Yehudi break. It is shown that this kink in the trailing edge of the wing can produce discernible and possibly characteristic flow features. From the results, it can be reasoned that the wing's wake impinging on the HTP is much more complex than just a blanketing of the HTP in a region of lower dynamic pressure hinted with a deficit in local velocity as suggested empirically. Based on these computational models, characteristic flow features can exist and interact with the HTP because of the existing Yehudi break, especially if its span-wise extent lies close to the stabilizer, such as in the case of the CRM. Since this physical feature usually lies close to the wing root, it could develop flow fields that propagate downstream to potentially interact with the HTP. However, determining the exact attitude at which the discussed features impinge on the HTP is challenging. This involves complicated flow fields as seen in the results presented here, which are also highly dependent on the flow conditions and geometry. Furthermore, the criteria that are used to define the impingement of the wake on the HTP needs to be determined before an exact angle-of-attack can be decided on. This coupled with the 3-dimensionality and inherently unsteadiness of the flow problem makes this definition challenging.

In terms of the potential impact of the inboard wake vortex, tangential velocity magnitudes in the x-normal plane are consistent to show a sub 10% reference velocity at the HTP. The impact of this relatively low velocity on the HTP is arguable as even at these magnitudes, the absolute local velocities might still be capable of altering the effective angle-of-attack of the HTP. More

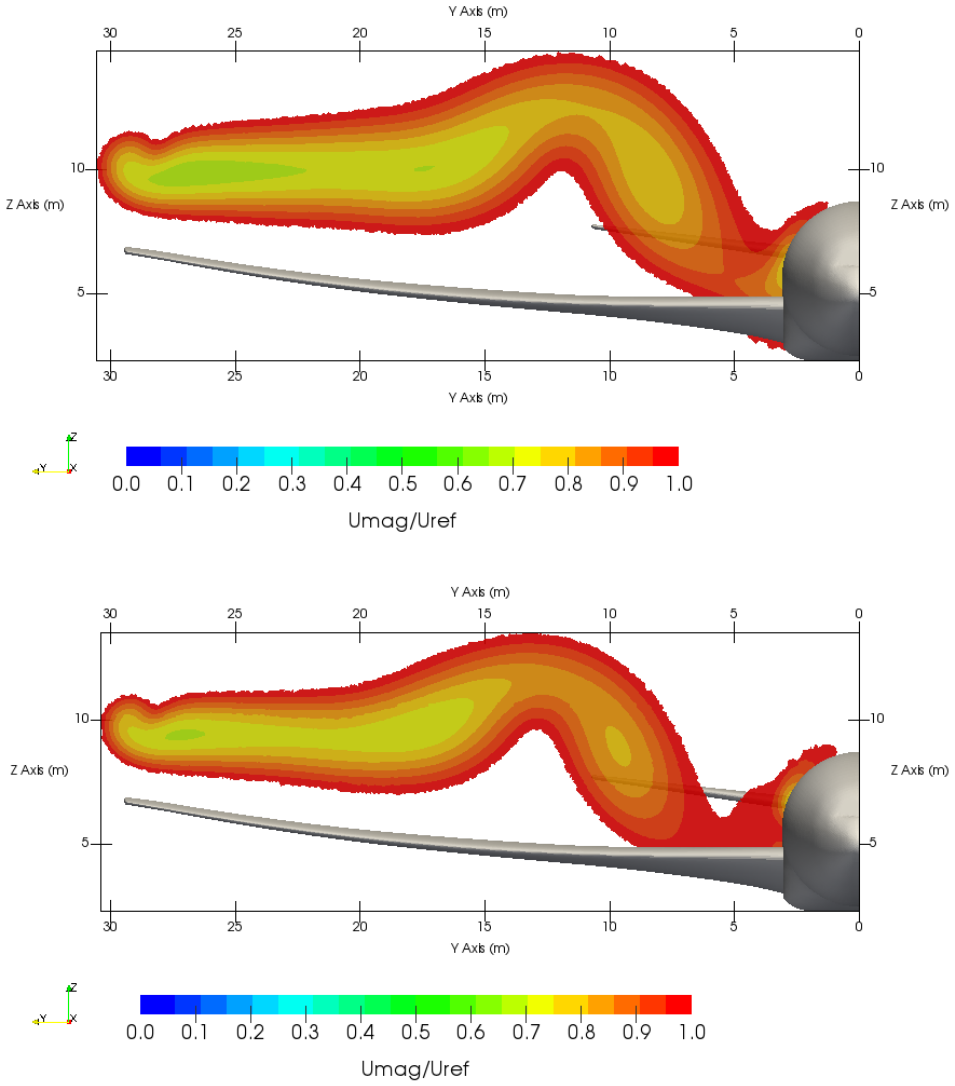

Figure A.3: Contours of velocity magnitude normalised to the freestream forward of the HTP for $\alpha = 16^\circ$ (top) and $\alpha = 14^\circ$ (Bottom). Contours are limited to an upper threshold of $0.98U_\infty$.

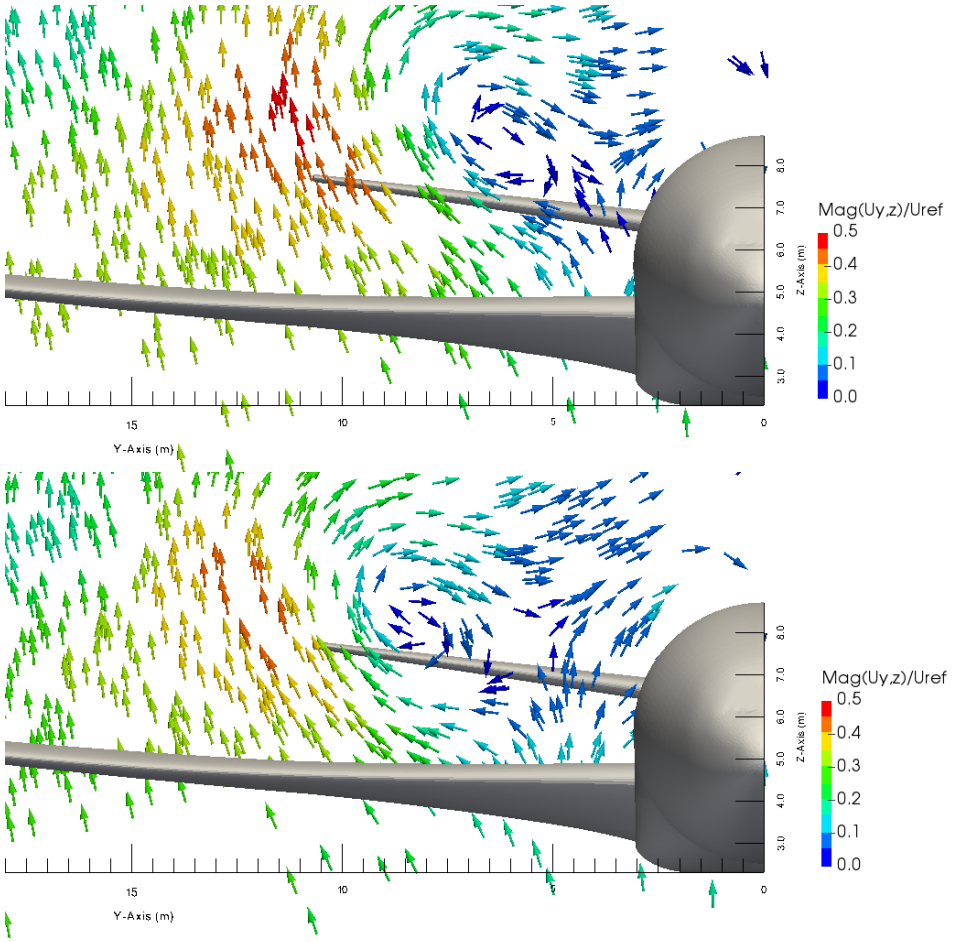

Figure A.4: velocity vector field normalised to the freestream forward of the HTP for $\alpha = 16°$ (top) and $\alpha = 14°$ (Bottom).

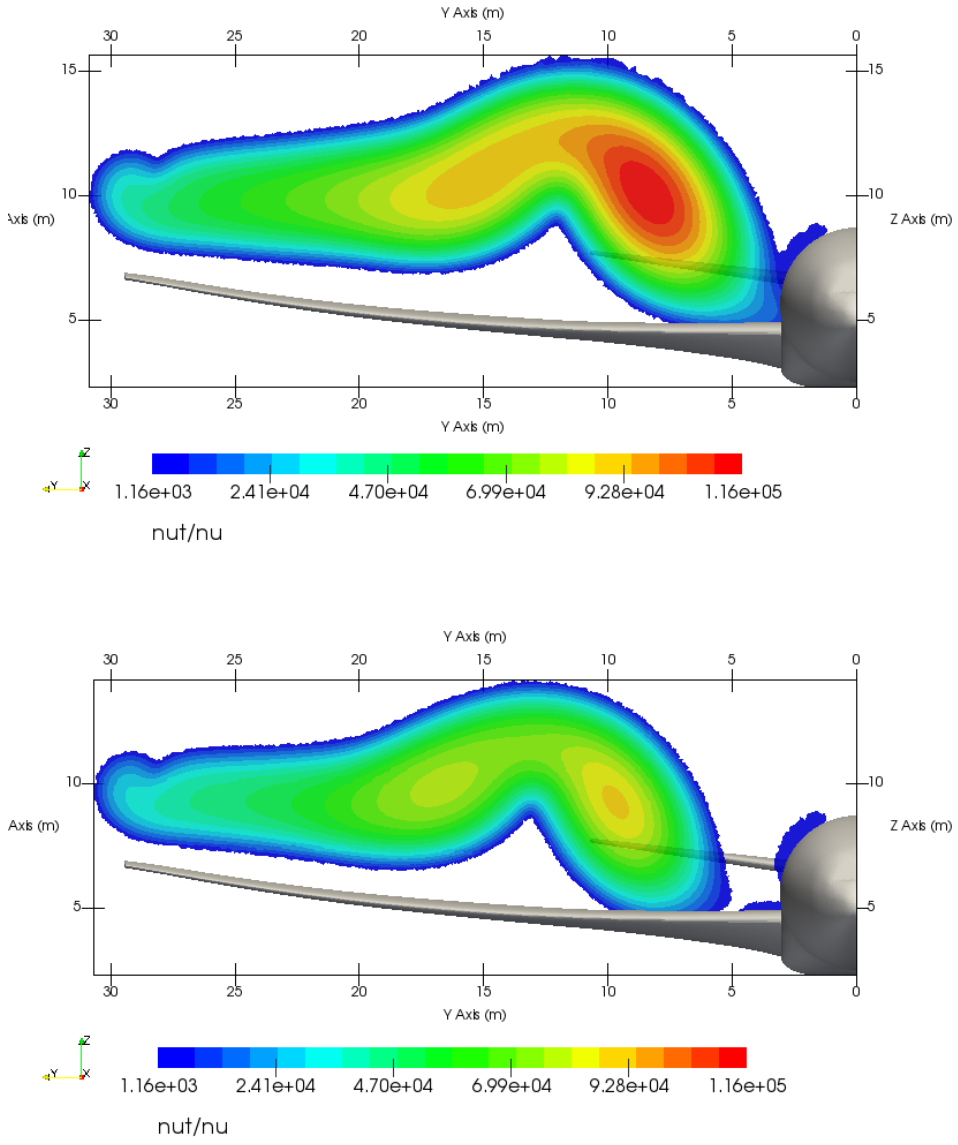

Figure A.5: Turbulent viscosity ratio in the solution forward of the HTP for $\alpha = 16°$ (top) and $\alpha = 14°$ (Bottom).

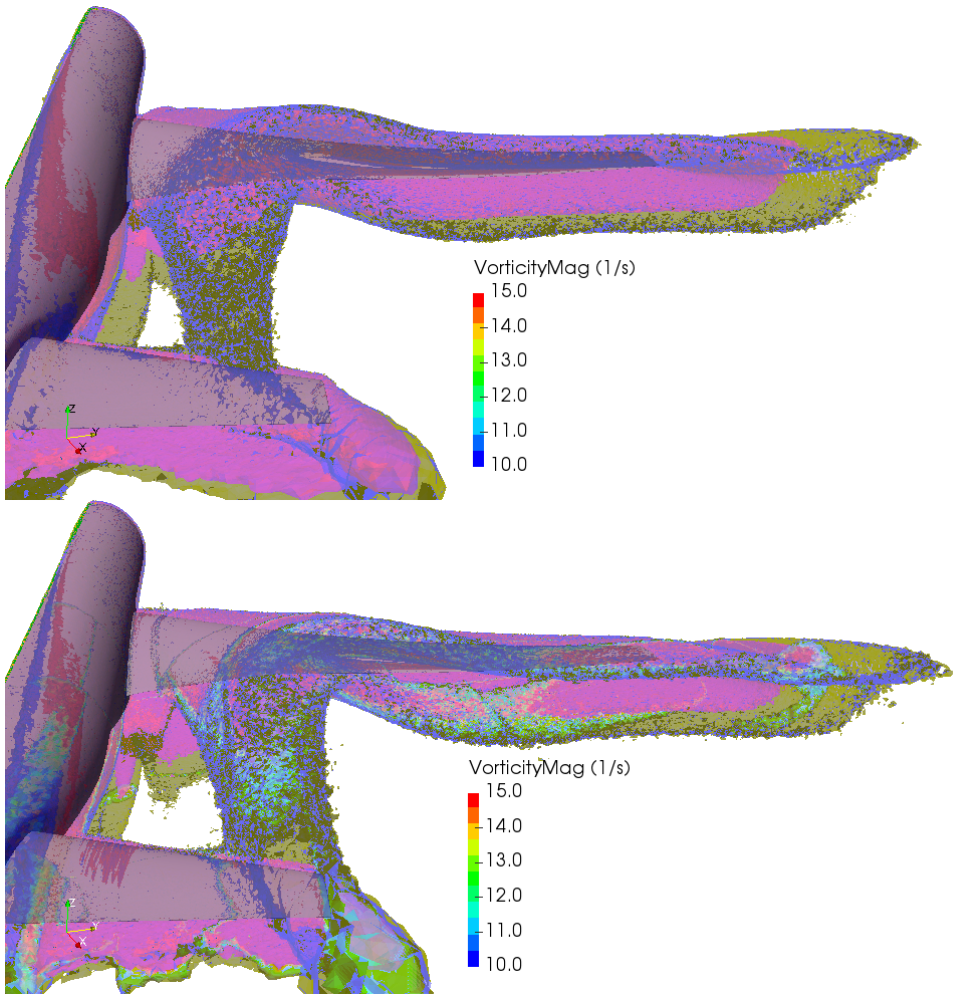

Figure A.6: Iso-volume of vorticity magnitude limited to a threshold of $10 \leq \omega \leq 15s^{-1}$. $\alpha = 16°$ (top) and $\alpha = 14°$ (Bottom).

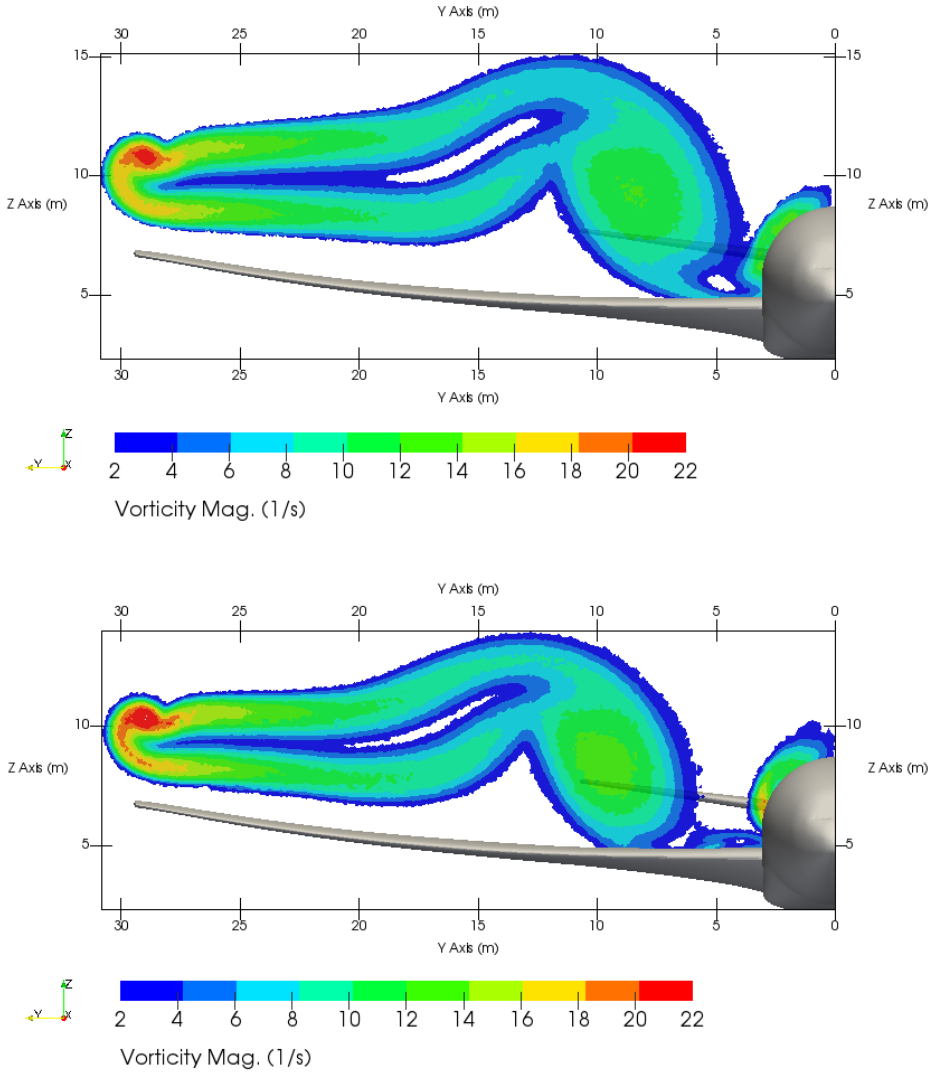

Figure A.7: Contours of vorticity magnitude forward of the HTP for $\alpha = 16^\circ$ (top) and $\alpha = 14^\circ$ (Bottom).

studies would be needed in determining the detailed properties of this vortex, such as its physical causes, its strengths at these flow conditions, and the attitude at which it impinges on the HTP directly. On the other hand, the up wash caused by the Yehudi break is significant, up to 50% relative freestream which resides close to the HTP tip. A better vortex identification method may be preferred in addition to vorticity such as the Q-criterion [203].

The flow is inherently unsteady although the present results model the mean development of the flow field across post-stall angles of attack. In addition, RANS is only capable of modelling the mean and large features and have been observed to inherently possess early wake dissipating characteristics. Judging based on trends observed by Waldmann et al. [52], it is arguable that the magnitude of results, especially for the velocities observed, is under-predicted, although trends would be similar compared to scale-resolving techniques and PIV experiments. It is therefore expected for results to be more pronounced, and potentially up to 20% relative to the freestream in the wake velocity deficit peak if the discrepancies are consistent. Therefore, the likelihood that the results are dissipated to a considerable degree is high. Because of this, the above discussed potential of the inboard wake vortex effect on the HTP need more work. Nevertheless, as RANS models being inherently dissipative of wake profiles are known [32, 204], they are still capable of providing insightful and acceptable results. Furthermore, the use of turbulence modelling to predict the effects of turbulence shown in terms of turbulent viscosity indicates that it dominates the wake towards the HTP, suggesting high levels of turbulence in the flow. Therefore, scale-resolving techniques such as DES may be preferred and will be explored in following work.

In terms of the mesh, the 3-dimensionality of a mesh block to model the wake requires an exorbitant number of cells for the wake capture shown here, as well as with past work. Having a spatial resolution of 2% the reference chord presently places total cell count in the order of 40 million. Moving towards a transient analysis would make the solution computationally expensive for the present resources. In addition, the present mesh could be improved. A handful of highly non-orthogonal elements still exist at junctions of the wing and tail root (fuselage joint) from layer generation (Maximum cell orthogonal angle at 77°). This process must be better controlled. An entirely structured grid may be unsuitable as the edge refinements for the wake block will propagate to corresponding parallel block edges, refining the domain unnecessarily. Alternatively, a multi-zone mesh hybrid which uses a structured body-fitted grid and an unstructured volume fill may be preferable instead. This allows better wall grid control over the entire geometry which the present mesh lacks and provides a convenient strategy for generating the wake block. The different type of cells used could also be considered. The wake block is presently filled with equilateral tetrahedrons that could be combined to form hexahedrons. This could aid in managing cell counts. Reassessing the span-wise extent of the wake block is also needed as refining the entire span of the wing wake may not be needed if focus is on the wake developed from the Yehudi break. This would allow the suggested spatial resolution of 1% the reference chord to be used for scale-resolving techniques.

Appendix B

Detailed Mesh Reports

The following are log extracts of mesh statistics obtained with the OpenFOAM mesh checker `checkMesh` utility.

B.1 Chapter 3 Grid Statistics for Square Beam Bluff-Body

The following reports the detailed mesh statistics for the grid used in Chapter 3, for the square beam bluff-body:

```
Mesh stats
    points:           4277560
    faces:            12654950
    internal faces:   12478474
    cells:            4188904
    faces per cell:   6
    boundary patches: 6
    point zones:      0
    face zones:       1
    cell zones:       1

Overall number of cells of each type:
    hexahedra:     4188904
    prisms:        0
    wedges:        0
    pyramids:      0
    tet wedges:    0
    tetrahedra:    0
    polyhedra:     0
```

```
Checking topology...
    Boundary definition OK.
    Cell to face addressing OK.
    Point usage OK.
    Upper triangular ordering OK.
    Face vertices OK.
    Number of regions: 1 (OK).

Checking patch topology for multiply connected surfaces...
    Patch               Faces    Points   Surface topology
    CUBE                15012    15120    ok
    INLET               15568    15820    ok
    OUTLET              15568    15820    ok
    TOP                 35028    35420    ok
    BOTTOM              35028    35420    ok
    FRONTANDBACK        60272    61108    ok

Checking geometry...
    Overall domain bounding box (-4 -0.7 0) (4 0.7 0.7)
    Mesh has 3 geometric (non-empty/wedge) directions (1 1 1)
    Mesh has 3 solution (non-empty) directions (1 1 1)
    Boundary openness
    (8.62312e-16 3.20389e-14 -8.77653e-17) OK.
    Max cell openness = 3.66402e-16 OK.
    Max aspect ratio = 100.007 OK.
    Minimum face area = 1.5096e-07.
    Maximum face area = 0.0139044.
    Face area magnitudes OK.
    Min volume = 7.60271e-10. Max volume = 7.00219e-05.
    Total volume = 7.833.  Cell volumes OK.
    Mesh non-orthogonality Max: 47.2125 average: 6.53999
    Non-orthogonality check OK.
    Face pyramids OK.
    Max skewness = 2.26167 OK.
    Coupled point location match (average 0) OK.

Mesh OK.
```

```
End
```

B.2 Chapter 4 Grid Statistics for Wing-In-Bluff-Body

The following reports the detailed mesh statistics for the grid used in Chapter 4, for the wing in bluff-body geometry:

```
Mesh stats
    points:           3840640
    faces:            11324700
    internal faces:   11129154
    cells:            3742309
    faces per cell:   6
    boundary patches: 8
    point zones:      0
    face zones:       1
    cell zones:       1

Overall number of cells of each type:
    hexahedra:     3742309
    prisms:        0
    wedges:        0
    pyramids:      0
    tet wedges:    0
    tetrahedra:    0
    polyhedra:     0

Checking topology...
    Boundary definition OK.
    Cell to face addressing OK.
    Point usage OK.
    Upper triangular ordering OK.
    Face vertices OK.
    Number of regions: 1 (OK).

Checking patch topology for multiply connected surfaces...
    Patch               Faces    Points   Surface topology
    BEAM                17064    17280    ok
    NACA0012            20224    20480    ok
```

```
    INLET               10033    10240    ok
    OUTLET              10033    10240    ok
    TOP                 21725    22080    ok
    BOTTOM              21725    22080    ok
    FRONT               47371    48008    ok
    BACK                47371    48008    ok

Checking geometry...
    Overall domain bounding box (-1.5 -0.7 -0.2) (2 0.7 0.2)
    Mesh has 3 geometric (non-empty/wedge) directions (1 1 1)
    Mesh has 3 solution (non-empty) directions (1 1 1)
    Boundary openness
    (4.55176e-15 -3.60274e-18 9.65312e-16) OK.
    Max cell openness = 4.24798e-16 OK.
    Max aspect ratio = 202.205 OK.
    Minimum face area = 2.95893e-09.
    Maximum face area = 0.00383838.
    Face area magnitudes OK.
    Min volume = 1.49819e-11. Max volume = 1.94348e-05.
    Total volume = 1.95563.  Cell volumes OK.
    Mesh non-orthogonality Max: 48.1789 average: 13.6625
    Non-orthogonality check OK.
    Face pyramids OK.
    Max skewness = 2.47161 OK.
    Coupled point location match (average 0) OK.

Mesh OK.

End
```

B.3 Chapter 5 Grid Statistics for Wing-Tail Overset Grid

The following reports the detailed mesh statistics for the grid used in Chapter 5, for the wing-tail overset grid:

```
Mesh stats
    points:           690352
    faces:            1980852
    internal faces:   1892460
```

```
    cells:            645552
    faces per cell:   6
    boundary patches: 9
    point zones:      0
    face zones:       2
    cell zones:       2

Overall number of cells of each type:
    hexahedra:     645552
    prisms:        0
    wedges:        0
    pyramids:      0
    tet wedges:    0
    tetrahedra:    0
    polyhedra:     0

Checking topology...
    Boundary definition OK.
    Cell to face addressing OK.
    Point usage OK.
    Upper triangular ordering OK.
    Face vertices OK.
   *Number of regions: 3
  <<Writing region information to "0/cellToRegion"
  <<Writing region 0 with 444000 cells to cellSet region0
  <<Writing region 1 with 100776 cells to cellSet region1
  <<Writing region 2 with 100776 cells to cellSet region2

Checking patch topology for multiply connected surfaces...
    Patch               Faces    Points   Surface topology
    OVERSETPATCH        5168     5440     ok
    INLET               2220     2352     ok
    OUTLET              2220     2352     ok
    BOTTOM              4000     4221     ok
    TOP                 4000     4221     ok
    BACK                32808    33392    ok
    FRONT               32808    33392    ok
    WING                2584     2720     ok
```

```
    TAIL                2584     2720     ok

Checking faceZone topology for multiply connected surfaces...
    FaceZone            Faces    Points   Surface topology
    int_WINGREGION      294440   108800   multiply connected
    int_TAILREGION      294440   108800   multiply connected
  <<Writing 216512 conflicting points to set nonManifoldPoints

Checking basic cellZone addressing...
    CellZone            Cells        Points       Volume
    WINGREGION          100776       108800       0.0069685067
    TAILREGION          100776       108800       0.0034145683

Checking geometry...
    Mesh has 3 geometric (non-empty/wedge) directions (1 1 1)
    Mesh has 3 solution (non-empty) directions (1 1 1)
    Boundary openness
    (-1.287536e-18 -1.7320551e-15 -1.773392e-14) OK.
    Max cell openness = 3.3059111e-16 OK.
    Max aspect ratio = 217.70095 OK.
    Minimum face area = 3.049504e-09.
    Maximum face area = 0.029761749.  Face area magnitudes OK.
    Min volume = 1.6052952e-11. Max volume = 0.00014880874.
    Total volume = 0.61038307.  Cell volumes OK.
    Mesh non-orthogonality Max: 40.408709 average: 5.2521193
    Non-orthogonality check OK.
    Face pyramids OK.
    Max skewness = 2.1225075 OK.
    Coupled point location match (average 0) OK.

Mesh OK.

End
```

References

[1] H. K. Versteeg and W. Malalasekera, *An Introduction to Computational Fluid Dynamics: the Finite Volume Method*. Harlow, Longman Scientific and Technical, 1995.

[2] H. J. Goett, "Experimental Investigation of the Momentum Method for Determining Profile Drag," Technical Report, NACA, 1939.

[3] A. Silverstein and S. Katzopf, "NACA Report 648: Design Charts for Predicting Downwash Angles and Wake Characteristics Behind Plain and Flapped Wings," Technical Report, NACA, 1939.

[4] M. Van Dyke, *An Album of Fluid Motion*. Parabolic Press Stanford, 1982.

[5] B. Etkin and L. D. Reid, *Dynamics of Flight: Stability and Control*, ch. 2, pp. 18–33. Wiley New York, 1996.

[6] D. Ball, "The Role of Computational Fluid Dynamics for Stability and Control; is it time?," in *COMSAC: Computational Methods for Stability and Control, NASA/CP-2004-213028/PT1, Proc. of NASA-Sponsored Symposium*, 2003.

[7] J. D. Anderson Jr., *Introduction to Flight*, ch. 2, pp. 642–643. WCB/McGraw-Hill Boston, MA, 2015.

[8] "Aviation Accident Reports - National Transportation Safety Board," May 2020.

[9] Aviation Week Network, "In The Wake of an A380: Dealing With Wake Turbulence." Available at `https://aviationweek.com/business-aviation/wake-a380-dealing-wake-turbulence`, 2017. Accessed: 2020-08-10.

[10] M. Pubby, "Wake Turbulence Led to C-130 J Aircraft Crash." Available at `https://indianexpress.com/article/india/india-others/wake-turbulence-led-to-c-130-j-aircraft-crash/`, 2014. Accessed: 2020-08-10.

[11] J. J. Robinson, "A Simulation-Based Study of the Impact of Aircraft Wake Turbulence Weight Categories on Airport Capacity," in *Advisory Group for Aerospace Research and Development (AGARD) Conference Proceedings*, p. 22, 1996.

[12] I. R. Cowan, I. P. Castro, and A. G. Robins, "Numerical Considerations for Simulations of Flow and Dispersion Around Buildings," *Journal of Wind Engineering and Industrial Aerodynamics*, vol. 67, pp. 535–545, 1997.

[13] T. Łusiak, A. Dziubiński, and K. Szumański, "Interference Between Helicopter and its Surroundings, Experimental and Numerical Analysis," *TASK Quarterly*, vol. 13, no. 4, pp. 379–392, 2009.

[14] P. Ruchała and K. Grabowska, "Problems of an Aerodynamic Interference Between Helicopter Rotor Slipstream and an Elevated Heliport," *Journal of KONES*, vol. 26, no. 3, pp. 189–196, 2019.

[15] D. Galway, J. Etele, and G. Fusina, "Modeling of Urban Wind Field Effects on Unmanned Rotorcraft Flight," *Journal of Aircraft*, vol. 48, no. 5, pp. 1613–1620, 2011.

[16] S. A. Raza and J. Etele, "Autonomous Position Control Analysis of Quadrotor Flight in Urban Wind Gust Conditions," in *AIAA Guidance, Navigation, and Control Conference*, p. 1385, 2016.

[17] J. S. Forrest, I. Owen, G. D. Padfield, and S. J. Hodge, "Ship-Helicopter Operating Limits Prediction Using Piloted Flight Simulation and Time-Accurate Airwakes," *Journal of Aircraft*, vol. 49, no. 4, pp. 1020–1031, 2012.

[18] G. Chirico, D. Szubert, L. Vigevano, and G. N. Barakos, "Numerical Modelling of the Aerodynamic Interference Between Helicopter and Ground Obstacles," *CEAS Aeronautical Journal*, vol. 8, no. 4, pp. 589–611, 2017.

[19] C. W. Murray and D. Anderson, "A CFD-based Procedure for Airspace Integration of Small Unmanned Aircraft Within Congested Areas," *International Journal of Micro Air Vehicles*, vol. 9, no. 4, pp. 235–252, 2017.

[20] J. Van Muijden, O. Boelens, J. van der Vorst, and J. Gooden, "Computational Ship Airwake Determination to Support Helicopter-Ship Dynamic Interface Assessment," in *21st AIAA Computational Fluid Dynamics Conference*, p. 3078, 2013.

[21] D. Galway, J. Etele, and G. Fusina, "Development and Implementation of an Urban Wind Field Database for Aircraft Flight Simulation," *Journal of Wind Engineering and Industrial Aerodynamics*, vol. 103, pp. 73–85, 2012.

[22] J. B. Barlow, W. H. Rae, and A. Pope, *Low-Speed Wind Tunnel Testing*. John Wiley & Sons, 1999.

[23] J. D. Anderson and J. D. Anderson Jr, *A History of Aerodynamics: and its Impact on Flying Machines*, vol. 8. Cambridge University Press, 1998.

[24] F. White, *Fluid Mechanics*. Mcgraw-Hill, New York, 2011.

[25] F. T. Johnson, E. N. Tinoco, and N. J. Yu, "Thirty Years of Development and Application of CFD at Boeing Commercial Airplanes, Seattle," *Computers & Fluids*, vol. 34, no. 10, pp. 1115–1151, 2005.

[26] G. E. Moore *et al.*, "Cramming More Components Onto Integrated Circuits," 1965.

[27] W. F. Philips, *Mechanics of Flight*. John Wiley & Sons Ltd, 2004.

[28] D. Drikakis, D. Kwak, and C. C. Kiris, "Computational Aerodynamics: Advances and Challenges," *Aeronautical Journal*, vol. 120, no. 1223, pp. 13–36, 2016.

[29] E. A. Pifer and G. Bramesfeld, "Measuring Wing Profile Drag Using an Integrating Wake Rake," *Technical Soaring*, vol. 36, no. 3, pp. 74–82, 2013.

[30] A. Betz, "A Method for the Direct Determination of Wing-Section Drag," *NACA Technical Memorandums*, 1925.

[31] B. M. Jones, *The Measurement of Profile Drag by the Pitot-Traverse Method*. HM Stationery Office, 1936.

[32] S. Mahon and X. Zhang, "Computational Analysis of Pressure and Wake Characteristics of an Aerofoil in Ground Effect," *Journal of Fluids Engineering*, vol. 127, no. 2, p. 290, 2005.

[33] A. Silverstein, "A Simplified Method for Determining Wing Profile Drag in Flight," *Journal of the Aeronautical Sciences*, vol. 7, pp. 295–301, May 1940.

[34] G. I. Taylor, *The Determination of Drag by the Pitot Traverse Method*. HM Stationery Office, 1937.

[35] D. E. Liarokapis, G. J. Grigoropoulos, and S. G. Perissakis, "Introducting a Seven-Hole Pitot Arrangement for Measuring Wake Flows in the Towing Tank," in *1st Intl. Conference on Advanced Model Measuremeent Techniques for the EU Maritime Industry*, 2009.

[36] G. Brune, "Quantitative Low-Speed Wake Surveys," *Journal of Aircraft*, vol. 31, no. 2, pp. 249–255, 1994.

[37] I. Yamaguchi, M. Takagi, K. Kurishima, and T. Mori, "Measurement of Wake Flow Fields, Including Reverse Flow, of Scale Vehicle Models Using a New 13-Hole Pitot Tube," Technical Report, SAE Technical Paper, 1996.

[38] W. Terra, A. Sciacchitano, F. Scarano, and B. van Oudheusden, "Drag Resolution of a PIV Wake Rake for Transiting Models," *Experiments in Fluids*, vol. 59, no. 7, p. 120, 2018.

[39] D. D. Baals, "Wind Tunnels of NASA." Available at `https://history.nasa.gov/SP-440/ch4-6.htm`, 2020. Accessed: 2020-08-14.

[40] P. Spalart and V. Venkatakrishnan, "On the Role and Challenges of CFD in the Aerospace Industry," *The Aeronautical Journal*, vol. 120, no. 1223, p. 209, 2016.

[41] H. Xiao and P. Cinnella, "Quantification of Model Uncertainty in RANS Simulations: A Review," *Progress in Aerospace Sciences*, vol. 108, pp. 1–31, 2019.

[42] Cummings, Russell M and Mason, William H and Morton, Scott A and McDaniel, David R, *Applied Computational Aerodynamics: A Modern Engineering Approach*, vol. 53. Cambridge University Press, 2015.

[43] CFD Vision 2030 Integration Committee, "The CFD Vision 2030 Study." Available at `http://www.cfd2030.com/`, 2020. Accessed: 2020-08-18.

[44] J. Zerihan and X. Zhang, "Aerodynamics of a Single Element Wing in Ground Effect," *Journal of Aircraft*, vol. 37, no. 6, pp. 1058–1064, 2000.

[45] X. Zhang and J. Zerihan, "Off-Surface Aerodynamic Measurements of a Wing in Ground Effect," *Journal of Aircraft*, vol. 40, no. 4, pp. 716–725, 2003.

[46] T.-H. Shih, W. W. Liou, A. Shabbir, Z. Yang, and J. Zhu, "A New Eddy Viscosity Model for High Reynolds Number Turbulent Flows," *Computers & Fluids*, vol. 24, no. 3, pp. 227–238, 1995.

[47] F. R. Menter, "Two-Equation Eddy-Viscosity Turbulence Models for Engineering Applications," *AIAA Journal*, vol. 32, no. 8, pp. 1598–1605, 1994.

[48] F. R. Menter, "Performance of Popular Turbulence Model for Attached and Separated Adverse Pressure Gradient Flows," *AIAA Journal*, vol. 30, no. 8, pp. 2066–2072, 1992.

[49] C. Rumsey, "NASA LaRC, Turbulence Modelling Resource." Available at `https://turbmodels.larc.nasa.gov/`, 2017. 2018-08-15.

[50] C. Rumsey, "CFL3D version 6.7." Available at `https://cfl3d.larc.nasa.gov/`, 2017. Accessed: 2018-08-15.

[51] NASA, "FUN3D, Fully Unstructured Navier-Stokes." Available at `https://fun3d.larc.nasa.gov/`, 2017. Accessed: 2018-08-15.

[52] A. Waldmann, P. P. Gansel, T. Lutz, and E. Krämer, "Unsteady Wake of the NASA Common Research Model in Low-Speed Stall," *Journal of Aircraft*, vol. 53, no. 4, pp. 1073–1086, 2015.

[53] P. P. Gansel, S. Illi, T. Lutz, and E. Krämer, "Numerical Simulation of Low Speed Stall and Analysis of Turbulent Wake Spectra," in *15th International Conference on Fluid Flow Technologies, Budapest, Hungary*, 09 2012.

[54] T. Lutz, P. P. Gansel, A. Waldmann, D.-M. Zimmermann, and S. Schulte am Hülse, "Prediction and Measurement of the Common Research Model Wake at Stall Conditions," *Journal of Aircraft*, vol. 53, pp. 501–514, Mar. 2016.

[55] M. Minguez, C. Brun, R. Pasquetti, and E. Serre, "Experimental and High-Order LES Analysis of the Flow in Near-Wall Region of a Square Cylinder," *International Journal of Heat and Fluid Flow*, vol. 32, no. 3, pp. 558–566, 2011.

[56] R. Courant, K. Friedrichs, and H. Lewy, "On the Partial Difference Equations of Mathematical Physics," *IBM Journal of Research and Development*, vol. 11, no. 2, pp. 215–234, 1967.

[57] P. Spalart, "Young-Persons Guide to Detached-Eddy Simulation Grids: NASA," Technical Report, CR-2001-211032): 1–18, 2001.

[58] M. Strelets, "Detached-Eddy Simulation of Massively Separated Flows," in *39th Aerospace Sciences Meeting and Exhibit*, p. 879, 2001.

[59] S. Göertz and Y. Le Moigne, "Detached-Eddy Simulations of a Full-span Delta Wing at High Incidence," in *21st AIAA Applied Aerodynamics Conference*, p. 4216, 2003.

[60] L. Schiavetta, K. Badcock, and R. Cummings, "Comparison of DES and URANS for Unsteady Vortical Flows over Delta Wings," in *45th AIAA Aerospace Sciences Meeting and Exhibit*, p. 1085, 2007.

[61] R. M. Cummings, S. A. Morton, and D. R. McDaniel, "Experiences in Accurately Predicting Time-Dependent Flows," *Progress in Aerospace Sciences*, vol. 44, no. 4, pp. 241–257, 2008.

[62] N. Frink, "Strategy for Dynamic CFD Simulations on SACCON Configuration," in *28th AIAA Applied Aerodynamics Conference*, p. 4559, 2010.

[63] J. Thompson, N. Frink, and P. Murphy, "Guidelines for Computing Longitudinal Dynamic Stability Characteristics on Subsonic Transport," in *28th AIAA Applied Aerodynamics Conference*, p. 4819, 2010.

[64] T. Von Kármán, "Mechanical Similitude and Turbulence," *Technical Memorandum*, 1931.

[65] H. Schlichting and K. Gersten, *Boundary-Layer Theory*. Springer, 2016.

[66] H. Nyquist, "Certain Factors Affecting Telegraph Speed," *Transactions of the American Institute of Electrical Engineers*, vol. 43, pp. 412–422, 1924.

[67] "European Research Community on Flow, Turbulence, and Combustion Database." Available at `http://cfd.mace.manchester.ac.uk/ercoftac/index.html`, 2020. 2020-04-20.

[68] D. Lyn, S. Einav, W. Rodi, and J.-H. Park, "A Laser-Doppler Velocimetry Study of Ensemble-Averaged Characteristics of the Turbulent Near Wake of a Square Cylinder," *Journal of Fluid Mechanics*, vol. 304, pp. 285–319, 1995.

[69] H. Bai and M. M. Alam, "Dependence of Square Cylinder Wake on Reynolds Number," *Physics of Fluids*, vol. 30, no. 1, p. 015102, 2018.

[70] H. Jiang and L. Cheng, "Flow Separation Around a Square Cylinder at Low to Moderate Reynolds Numbers," *Physics of Fluids*, vol. 32, no. 4, p. 044103, 2020.

[71] H. Jiang, L. Cheng, and H. An, "Three-Dimensional Wake Transition of a Square Cylinder," *Journal of Fluid Mechanics*, vol. 842, pp. 102–127, 2018.

[72] H. Jiang and L. Cheng, "Hydrodynamic Characteristics of Flow Past a Square Cylinder at Moderate Reynolds Numbers," *Physics of Fluids*, vol. 30, no. 10, p. 104107, 2018.

[73] W. Wood and W. Kleb, "Diffusion Characteristics of Upwind Schemes on Unstructured Triangulations," in *29th AIAA, Fluid Dynamics Conference*, p. 2443, 1998.

[74] Y. Q. Wang, "Effects of Reynolds number on Vortex Structure Behind a Surface-Mounted Finite Square Cylinder with AR= 7," *Physics of Fluids*, vol. 31, no. 11, p. 115103, 2019.

[75] M. Boudreau, G. Dumas, and J.-C. Veilleux, "Assessing the Ability of the DDES Turbulence Modeling Approach to Simulate the Wake of a Bluff Body," *Aerospace*, vol. 4, p. 41, Aug. 2017.

[76] A. Sohankar, L. Davidson, and C. Norberg, "Large Eddy Simulation of Flow Past a Square Cylinder: Comparison of Different Subgrid Scale Models," *Journal of Fluids Engineering*, vol. 122, no. 1, pp. 39–47, 2000.

[77] C. Fureby, G. Tabor, H. Weller, and A. Gosman, "Large Eddy Simulations of the Flow Around a Square Prism," *AIAA Journal*, vol. 38, no. 3, pp. 442–452, 2000.

[78] T. Uffinger, I. Ali, and S. Becker, "Experimental and Numerical Investigations of the Flow Around Three Different Wall-Mounted Cylinder Geometries of Finite Length," *Journal of Wind Engineering and Industrial Aerodynamics*, vol. 119, pp. 13–27, 2013.

[79] F. Trias, A. Gorobets, and A. Oliva, "Turbulent Flow Around a Square Cylinder at Reynolds Number 22,000: A DNS study," *Computers & Fluids*, vol. 123, pp. 87–98, 2015.

[80] C. J. Roy and M. F. Barone, "Evaluation of Detached Eddy Simulation for Turbulent Wake Applications," Technical Report, Sandia National Laboratories, 2005.

[81] S. Luo, M. G. Yazdani, Y. Chew, and T. Lee, "Effects of Incidence and Afterbody Shape on Flow Past Bluff Cylinders," *Journal of Wind Engineering and Industrial Aerodynamics*, vol. 53, no. 3, pp. 375–399, 1994.

[82] P. R. Spalart, "Comments on the Feasibility of LES for Wings, and on a Hybrid RANS/LES Approach," in *Proceedings of First AFOSR International Conference on DNS/LES*, Greyden Press, 1997.

[83] P. R. Spalart, S. Deck, M. L. Shur, K. D. Squires, M. K. Strelets, and A. Travin, "A New Version of Detached-Eddy Simulation, Resistant to Ambiguous Grid Densities," *Theoretical and Computational Fluid Dynamics*, vol. 20, no. 3, p. 181, 2006.

[84] J. N. Lefebvre and A. R. Jones, "Experimental Investigation of Airfoil Performance in the Wake of a Circular Cylinder," *AIAA Journal*, pp. 2808–2818, 2019.

[85] Y. Jiang, M.-L. Mao, X.-G. Deng, and H.-Y. Liu, "Numerical Investigation on Body-Wake Flow Interaction Over Rod-Airfoil Configuration," *Journal of Fluid Mechanics*, vol. 779, pp. 1–35, 2015.

[86] D. Lee, T. Nonomura, A. Oyama, and K. Fujii, "Comparison of Numerical Methods Evaluating Airfoil Aerodynamic Characteristics at Low Reynolds Number," *Journal of Aircraft*, vol. 52, no. 1, pp. 296–306, 2015.

[87] J. Winslow, H. Otsuka, B. Govindarajan, and I. Chopra, "Basic Understanding of Airfoil Characteristics at Low Reynolds Numbers," *Journal of Aircraft*, vol. 55, no. 3, pp. 1050–1061, 2018.

[88] B. Strom, N. Johnson, and B. Polagye, "Impact of Blade Mounting Structures on Cross-Flow Turbine Performance," *Journal of Renewable and Sustainable Energy*, vol. 10, no. 3, p. 034504, 2018.

[89] R. Kojima, T. Nonomura, A. Oyama, and K. Fujii, "Large-Eddy Simulation of Low-Reynolds-Number Flow Over Thick and Thin NACA Airfoils," *Journal of Aircraft*, vol. 50, no. 1, pp. 187–196, 2013.

[90] P. Balakumar, "Direct Numerical Simulation of Flows Over an NACA-0012 Airfoil at Low and Moderate Reynolds numbers," in *47th AIAA Fluid Dynamics Conference*, p. 3978, 2017.

[91] A. Travin, M. Shur, M. Strelets, and P. Spalart, "Detached-Eddy Simulations Past a Circular Cylinder," *Flow, Turbulence and Combustion*, vol. 63, no. 1-4, pp. 293–313, 2000.

[92] Y. Wang, D. Thompson, and Z. Hu, "Numerical Investigations on the Flow Over Cuboids with Different Aspect Ratios and the Emitted Noise," *Physics of Fluids*, vol. 32, no. 2, p. 025103, 2020.

[93] U. Cordes, G. Kampers, T. Meißner, C. Tropea, J. Peinke, and M. Hölling, "Note on the Limitations of the Theodorsen and Sears Functions," *Journal of Fluid Mechanics*, vol. 811, 2017.

[94] J. Wright and J. Cooper, *Introduction to Unsteady Aerodynamics*, vol. 20. John Wiley & Sons Ltd, Chichester, England, 2008.

[95] N. J. Wei, J. Kissing, and C. Tropea, "Generation of Periodic Gusts with a Pitching and Plunging Airfoil," *Experiments in Fluids*, vol. 60, no. 11, p. 166, 2019.

[96] J.-Z. Wu, X.-Y. Lu, A. G. Denny, M. Fan, and J.-M. Wu, "Post-stall Flow Control on an Airfoil by Local Unsteady Forcing," *Journal of Fluid Mechanics*, vol. 371, pp. 21–58, 1998.

[97] S. Yarusevych, J. G. Kawall, and P. E. Sullivan, "Separated-Shear-Layer Development on an Airfoil at Low Reynolds Numbers," *AIAA journal*, vol. 46, no. 12, pp. 3060–3069, 2008.

[98] S. Yarusevych and M. S. H. Boutilier, "Vortex Shedding of an Airfoil at Low Reynolds Numbers," *AIAA Journal*, vol. 49, no. 10, pp. 2221–2227, 2011.

[99] R. F. Huang and C. L. Lin, "Vortex Shedding and Shear-Layer Instability of Wing at Low-Reynolds Numbers," *AIAA Journal*, vol. 33, no. 8, pp. 1398–1403, 1995.

[100] J. H. Lienhard, *Synopsis of Lift, Drag, and Vortex Frequency Data for Rigid Circular Cylinders*, vol. 300. Technical Extension Service, Washington State University, 1966.

[101] A. Roshko, "On the Drag and Shedding Frequency of Two-Dimensional Bluff Bodies," *Technical Note 3169*, 1954.

[102] A. Waldmann, T. Lutz, and E. Kraemer, "Separated Wake Flow and Tail Loads of the Common Research Model in Low Speed Stall Conditions," in *AIAA Scitech 2019 Forum*, p. 2315, 2019.

[103] F. Pearce, "Wing Wake Effect on Longitudinal Stability," Technical Report, NACA, 1976.

[104] R. Hall, R. Biedron, D. Ball, D. Bogue, J. Chung, B. Green, M. Grismer, G. Brooks, and J. Chambers, "Computational Methods for Stability and Control (COMSAC): The Time Has Come," in *AIAA Atmospheric Flight Mechanics Conference and Exhibit*, p. 6121, 2005.

[105] A. Byrnes, W. Hensleigh, and L. Tolve, "Effect of Horizontal Stabilizer Vertical Location on the Design of Large Transport Aircraft," *Journal of Aircraft*, vol. 3, no. 2, pp. 97–104, 1966.

[106] R. C. Nelson *et al.*, *Flight Stability and Automatic Control*, vol. 2. WCB/McGraw Hill New York, 1998.

[107] W. Phillips, E. Anderson, J. Jenkins, and S. Sunouchi, "Estimating the Low-Speed Downwash Angle on an Aft Tail," *Journal of Aircraft*, vol. 39, no. 4, pp. 600–608, 2002.

[108] Lockheed, "Aerodynamic Data for Structural Loads: C-130," 1953.

[109] R. H. Liebeck, "Design of the Blended Wing Body Subsonic Transport," *Journal of Aircraft*, vol. 41, pp. 10–25, Jan. 2004.

[110] D. G. Murri and S. B. Grafton, "Low-Speed, Large Angle Wind Tunnel Investigation of a Subsonic Blended-Wing-Body Tri-jet Configuration," *NASA CDTM-10044*, 2004.

[111] S. P. Pao, R. T. Biedron, M. A. Park, C. M. Fremaux, and D. D. Vicroy, "Navier-Stokes Computations of Longitudinal Forces and Moments for a Blended Wing Body," in *AIAA Conference and Exhibit*, 2005.

[112] S. K. A. Silverstein and W. K. Bullivant, "NACA Report 651: Downwash and Wake Behind Plain and Flapped Airfoils," Technical Report, NACA, 1939.

[113] M. Breuer, N. Jovičić, and K. Mazaev, "Comparison of DES, RANS and LES for the Separated Flow Around a Flat Plate at High Incidence," *International Journal for Numerical Methods in Fluids*, vol. 41, no. 4, pp. 357–388, 2003.

[114] P. P. Gansel, S. A. Illi, S. Krimmer, T. Lutz, and E. Krämer, "Unsteady CFD Simulation of the NASA Common Research Model in Low Speed Stall," in *High Performance Computing in Science and Engineering '13*, pp. 439–453, Springer, 2013.

[115] J. Havas and G. Rabadan, "Prediction of Horizontal Tail Plane Buffeting Loads," in *International Forum on Aeroelasticity and Structural Dynamics Paper*, vol. 128, p. 2009, 2009.

[116] M. J. Whitney, T. J. Seitz, and E. L. Blades, "Low-Speed-Stall Tail Buffet Loads Estimation Using Unsteady CFD," in *International Forum on Aeroelasticity and Structural Dynamics (IFASD)*, 2009.

[117] H. Tennekes, J. L. Lumley, J. Lumley, *et al.*, *A First Course in Turbulence*. MIT press, 1972.

[118] U. Frisch and A. N. Kolmogorov, *Turbulence: The Legacy of AN Kolmogorov*. Cambridge University Press, 1995.

[119] S. B. Pope, "Turbulent Flows," 2001.

[120] J. H. Ferziger, "Simulation of Incompressible Turbulent Flows," *Journal of Computational Physics*, vol. 69, pp. 1–48, 1987.

[121] J. Boussinesq, "Theorie de L'ecoulement Tourbillant," *Mem. Acad. Sci.*, vol. 23, p. 46, 1877.

[122] B. E. Launder and D. B. Spalding, *The Numerical Computation of Turbulent Flows*. Elsevier, 1983.

[123] V. Yakhot and S. A. Orszag, "Renormalization Group Analysis of Turbulence. I. Basic Theory," *Journal of scientific computing*, vol. 1, no. 1, pp. 3–51, 1986.

[124] V. Yakhot, S. Orszag, S. Thangam, T. Gatski, and C. Speziale, "Development of Turbulence Models for Shear Flows by a Double Expansion Technique," *Physics of Fluids A: Fluid Dynamics*, vol. 4, no. 7, pp. 1510–1520, 1992.

[125] D. C. Wilcox *et al.*, *Turbulence Modeling for CFD*, vol. 2. DCW industries La Canada, CA, 1998.

[126] D. C. Wilcox, "Formulation of the k-omega Turbulence Model Revisited," *AIAA journal*, vol. 46, no. 11, pp. 2823–2838, 2008.

[127] P. Spalart and S. Allmaras, "A One-Equation Turbulence Model for Aerodynamic Flows," in *30th Aerospace Sciences Meeting and Exhibit*, p. 439, 1992.

[128] C. J. Roy, C. L. Rumsey, and E. N. Tinoco, "Summary Data from the Sixth AIAA Computational Fluid Dynamics Drag Prediction Workshop: Code Verification," *Journal of Aircraft*, pp. 1–14, 2018.

[129] S. R. Allmaras and F. T. Johnson, "Modifications and Clarifications for the Implementation of the Spalart-Allmaras Turbulence Model," in *Seventh International Conference on Computational Fluid Dynamics (ICCFD7)*, pp. 1–11, 2012.

[130] F. R. Menter, M. Kuntz, and R. Langtry, "Ten Years of Industrial Experience with the SST Turbulence Model," *Turbulence, heat and mass transfer*, vol. 4, no. 1, pp. 625–632, 2003.

[131] Deardorff, James W, "A Numerical Study of Three-Dimensional Turbulent Channel Flow at Large Reynolds Numbers," *Journal of Fluid Mechanics*, vol. 41, no. 2, pp. 453–480, 1970.

[132] Givi, Peyman, "Model-Free Simulations of Turbulent Reactive Flows," *Progress in Energy and Combustion Science*, vol. 15, no. 1, pp. 1–107, 1989.

[133] Moin, Parviz and Kim, John, "Numerical Investigation of Turbulent Channel Flow," *Journal of fluid mechanics*, vol. 118, pp. 341–377, 1982.

[134] J. H. Ferziger, "Large Eddy Simulation," *Simulation and Modeling of Turbulent Flows*, pp. 109–154, 1996.

[135] M. Shur, P. Spalart, M. Strelets, and A. Travin, "Detached-Eddy Simulation of an Airfoil at High Angle of Attack," in *Engineering turbulence modelling and experiments 4*, pp. 669–678, Elsevier, 1999.

[136] H. Jasak, A. Jemcov, Z. Tukovic, *et al.*, "OpenFOAM: A C++ library for Complex Physics Simulations," in *International Workshop on Coupled Methods in Numerical Dynamics*, vol. 1000, pp. 1–20, IUC, Dubrovnik, Croatia, 2007.

[137] H. Jasak, "OpenFOAM: Open Source CFD in Research and Industry," *International Journal of Naval Architecture and Ocean Engineering*, vol. 1, no. 2, pp. 89–94, 2009.

[138] C. J. Greenshields, "OpenFOAM User Guide," *OpenFOAM Foundation Ltd*, 2015.

[139] "OpenFOAM Supporters." Available at `https://openfoam.org/supporters/`, 2020. 2020-08-11.

[140] B. Zang, U. Vevek, H. Lim, X. Wei, and T. H. New, "An Assessment of OpenFOAM Solver on RANS Simulations of Round Supersonic Free Jets," *Journal of Computational Science*, vol. 28, pp. 18–31, 2018.

[141] The Free Software Foundation, "GNU General Public License." Available at `http://www.gnu.org/licenses/gpl-3.0.html`, 2007. Accessed: 2020-08-13.

[142] C. J. Greenshields, "OpenFOAM Programmer Guide," *OpenFOAM Foundation Ltd*, 2015.

[143] OpenMPI, "Open MPI: Open Source High Performance Computing." Available at `https://www.open-mpi.org/`, 2020. Accessed: 2020-08-13.

[144] B. Barney, "Message Passing Interface (MPI)." Available at `https://computing.llnl.gov/tutorials/mpi/`, 2020. Accessed: 2020-08-13.

[145] P. Lui, "Scalability Performance Analysis of OpenFOAM on Modern HPC Clustering Technologies." Available at `https://www.hpcadvisorycouncil.com/pdf/OpenFOAMConf2015_PakLui.pdf`, 2015. Accessed: 2020-08-13.

[146] S. Patankar, *Numerical Heat Transfer and Fluid Flow*. Taylor & Francis, 2018.

[147] C. Hirsch, "Numerical Computation of Internal and External Flows, Volume 1: Fundamentals of Numerical Discretization," *John Wiley and Sons*, vol. 9, p. 10, 1988.

[148] H. Jasak, "Error Analysis and Estimation for the Finite Volume Method with Applications to Fluid Flows.," *PhD Thesis*, 1996.

[149] M. Peric, "A Finite Volume Method for the Prediction of Three-Dimensional Fluid Flow in Complex Ducts," *PhD Thesis*, 1985.

[150] J. H. Ferziger, M. Perić, and R. L. Street, *Computational Methods for Fluid Dynamics*, vol. 3. Springer, 2002.

[151] H. Jasak, "Dynamic Mesh Handling in OpenFOAM," in *47th AIAA Aerospace Sciences Meeting Including the New Horizons Forum and Aerospace Exposition*, p. 341, 2009.

[152] I. Demirdžić and M. Perić, "Space Conservation Law in Finite Volume Calculations of Fluid Flow," *International journal for numerical methods in fluids*, vol. 8, no. 9, pp. 1037–1050, 1988.

[153] I. Gatin, V. Vukcevic, H. Jasak, and I. Lalovic, "Manoeuvring Simulations Using the Overset Grid Technology in foam-extend," in *32nd Symposium on Naval Hydrodynamics*, 2018.

[154] T. Petra, "Description of the Overset Mesh Approach in ESI version of OpenFOAM," in *A Course at Chalmers University of Technology*, 2019.

[155] J. F. Thompson, B. Soni, and N. Weatherill, "Handbook of Grid Generation CRC Press," *Boca Raton. Florida*, 1999.

[156] C. Windt, J. Davidson, D. D. Chandar, N. Faedo, and J. V. Ringwood, "Evaluation of the Overset Grid Method for Control Studies of Wave Energy Converters in OpenFOAM Numerical Wave Tanks," *Journal of Ocean Engineering and Marine Energy*, vol. 6, no. 1, pp. 55–70, 2020.

[157] OpenFOAM, "OpenFOAM: User Guide." Available at https://www.openfoam.com/documentation/guides/latest/doc/guide-overset.html, 2020. Accessed: 2020-08-12.

[158] D. Shepard, "A Two-Dimensional Interpolation Function for Irregularly-Spaced Data," in *Proceedings of the 1968 23rd ACM National Conference*, pp. 517–524, 1968.

[159] C. Rhie and W. L. Chow, "Numerical Study of the Turbulent Flow Past an Airfoil with Trailing Edge Separation," *AIAA journal*, vol. 21, no. 11, pp. 1525–1532, 1983.

[160] R. I. Issa, "Solution of the Implicitly Discretised Fluid Flow Equations by Operator-Splitting," *Journal of Computational Physics*, vol. 62, no. 1, pp. 40–65, 1986.

[161] J. W. Slater, "NPARC Alliance CFD Verification and Validation Website, Examining Iterative Convergence." Available at https://www.grc.nasa.gov/www/wind/valid/tutorial/iterconv.html, 2020. Accessed: 2018-08-12.

[162] P. J. Roache, *Verification and Validation in Computational Science and Engineering*, vol. 895. Hermosa Publishers, Albuquerque, NM, 1998.

[163] Microway Inc., "Detailed Specifications of the Intel Xeon E5-2600v4 Processors," 2018.

[164] "List of Solutions on Using General Purpose Graphical Processing Units (GPGPU) for OpenFOAM." Available at https://openfoamwiki.net/index.php/GPGPU, August 2019.

[165] ANSYS Inc., "ANSYS ICEM," *CFD User's Manual*, 2013.

[166] OPEN CASCADE, "The Open Source Integration Platform for Numerical Simulation." Available at https://www.salome-platform.org/, 2019. Accessed: 2019-06-06.

[167] The FreeCAD Team, "FreeCAD: Your Own 3D Parametric Modeler." Available at https://www.freecadweb.org/, 2019. Accessed: 2019-06-06.

[168] Dassault Systemes, "Solidworks." Available at https://www.solidworks.com/, 2019. Accessed: 2019-06-06.

[169] NASA, "OpenVSP: NASA Open Source Parametric Geometry." Available at http://openvsp.org/, 2017. Accessed: 2020-08-12.

[170] The OpenFOAM Foundation, "OpenFOAM." Available at https://openfoam.org/, 2019. Accessed: 2019-06-06.

[171] "The Open Sourced CFD Toolbox." Available at https://openfoam.com/, 2019. 2020-04-20.

[172] Kitware, "Paraview." Available at https://www.paraview.org/, 2019. Accessed: 2019-06-06.

[173] Python Software Foundation, "Python." Available at https://www.python.org/, 2019. Accessed: 2019-06-06.

[174] Matplotlib, "Matplotlib." Available at https://matplotlib.org/, 2019. Accessed: 2019-06-06.

[175] NumPy developers, "NumPy." Available at https://www.numpy.org/, 2019. Accessed: 2019-06-06.

[176] The SciPy Community, "Discrete Fourier Transformation (numpy.fft) - NumPy Manual." Available at https://docs.scipy.org/doc/numpy-1.15.1/reference/generated/numpy.fft.fft.html, 2017. Accessed: 2019-02-20.

[177] Pandas, "Python Data Analyses Library." Available at https://matplotlib.org/, 2019. Accessed: 2019-06-06.

[178] D. B. Spalding, "A Novel Finite Difference Formulation for Differential Expressions Involving Both First and Second Derivatives," *International Journal for Numerical Methods in Engineering*, vol. 4, no. 4, pp. 551–559, 1972.

[179] S. B. Lee, "A Study on Temporal Accuracy of OpenFOAM," *International Journal of Naval Architecture and Ocean Engineering*, vol. 9, no. 4, pp. 429–438, 2017.

[180] M. Leschziner, "Practical Evaluation of Three Finite Difference Schemes for the Computation of Steady-State Recirculating Flows," *CMAME*, vol. 23, pp. 293–312, 1980.

[181] "The OpenFOAM Foundation," May 2020.

[182] L. Davidson, "Large Eddy Simulations: How to Evaluate Resolution," *International Journal of Heat and Fluid Flow*, vol. 30, no. 5, pp. 1016–1025, 2009.

[183] R. Camussi, M. Felli, F. Pereira, G. Aloisio, and A. Di Marco, "Statistical Properties of Wall Pressure Fluctuations Over a Forward-Facing Step," *Physics of Fluids*, vol. 20, no. 7, p. 075113, 2008.

[184] J. Jeong and F. Hussain, "On the Identification of a Vortex," *Journal of Fluid Mechanics*, vol. 285, pp. 69–94, 1995.

[185] K. J. B. Tan, H. Hesse, and P. C. Wang, "Numerical Capture and Validation of a Massively Separated Bluff-Body Wake," in *AIAA Aviation Forum 2020*, p. 2713, 2020.

[186] D. Caraeni, "A Third-Order Residual Distribution Method for Steady/Unsteady Simulations: Formulation and Benchmarking Including LES," *Lecture Series-von Kármán Institute for Fluid Dynamics*, vol. 1, p. 8, 2006.

[187] "NASA Langley Research Center: Turbulence Modeling Resource," August 2019.

[188] E. Laitone, "Wind Tunnel Tests of Wings at Reynolds Numbers Below 70,000," *Experiments in Fluids*, vol. 23, no. 5, pp. 405–409, 1997.

[189] T. Ohtake, Y. Nakae, and T. Motohashi, "Nonlinearity of the Aerodynamic Characteristics of NACA0012 Aerofoil at Low Reynolds Numbers," *Japan Society of Aeronautical Space Sciences*, vol. 55, pp. 439–445, 2007.

[190] M. K. Chauhan, S. Dutta, B. S. More, and B. K. Gandhi, "Experimental Investigation of Flow Over a Square Cylinder with an Attached Splitter Plate at Intermediate Reynolds number," *Journal of Fluids and Structures*, vol. 76, pp. 319–335, 2018.

[191] Y. C. Fung, *An Introduction to the Theory of Aeroelasticity*. Courier Dover Publications, 2008.

[192] The OpenFOAM Guide, "The PIMPLE Algorithm in OpenFOAM." Available at `https://openfoamwiki.net/index.php/OpenFOAM_guide/The_PIMPLE_algorithm_in_OpenFOAM`, 2018. Accessed: 2020-08-21.

[193] S. Lemaire, G. Vaz, and S. Turnock, "On The Need for Higher Order Interpolation With Overset Grid Methods," *22nd Numerical Towing Tank Symposium*, 2019.

[194] M. Amiralaei, H. Alighanbari, and S. Hashemi, "An Investigation into the Effects of Unsteady Parameters on the Aerodynamics of a Low Reynolds Number Pitching Airfoil," *Journal of Fluids and Structures*, vol. 26, no. 6, pp. 979–993, 2010.

[195] Heat and Mass Transfer Technological Center (CTTC), "Results from DNS of Turbulent Flow Around a Square Cylinder at Re=22000." Available at `http://www.cttc.upc.edu/downloads/SqCyl22K/`, 2020. Accessed: 2020-08-18.

[196] NASA, "The NASA Common Research Model." Available at `https://commonresearchmodel.larc.nasa.gov/`, 2017. 2018-08-15.

[197] J. Slotnick, A. Khodadoust, J. Alonso, D. Darmofal, W. Gropp, E. Lurie, and D. Mavriplis, "CFD Vision 2030 Study: A Path to Revolutionary Computational Aerosciences," *NASA Technical Reports*, 2020.

[198] J. Vassberg, M. Dehaan, M. Rivers, and R. Wahls, "Development of a Common Research Model for applied CFD Validation Studies," in *26th AIAA Applied Aerodynamics Conference*, p. 6919, 2008.

[199] E. N. Tinoco, O. P. Brodersen, S. Keye, K. R. Laflin, E. Feltrop, J. C. Vassberg, M. Mani, B. Rider, R. A. Wahls, J. H. Morrison, *et al.*, "Summary Data from the Sixth AIAA CFD Drag Prediction Workshop: CRM Cases," *Journal of Aircraft*, vol. 55, no. 4, pp. 1352–1379, 2018.

[200] NASA, "3rd AIAA CFD High Lift Prediction Workshop (HiLiftPW-3)." Available at `https://hiliftpw.larc.nasa.gov/`, 2017. 2018-08-15.

[201] F. Proctor, "Numerical Simulation of Wake Vortices Measured During the Idaho Falls and Memphis Field Programs," in *14th Applied Aerodynamics Conference*, p. 2496, 1996.

[202] J. D. Anderson Jr, *Fundamentals of Aerodynamics*. Tata McGraw-Hill Education, 2010.

[203] V. Holmén, "Methods for Vortex Identification," *Master's Thesis in Mathematical Sciences*, 2012.

[204] N. Subaschandar and A. Prabhu, "Turbulent Near-Wake Studies Behind an Infinitely Swept Wing," *Journal of Aircraft*, vol. 39, no. 2, pp. 290–295, 2002.